Multiscale Imaging of Evapotranspiration

Daniel Sousa

Submitted in partial fulfillment of the
requirements for the degree of
Doctor of Philosophy
in the Graduate School of Arts and Sciences

COLUMBIA UNIVERSITY

2019

© 2019

Daniel Sousa

All rights reserved

ABSTRACT

Multiscale Imaging of Evapotranspiration

Daniel Sousa

Evapotranspiration (ET; evaporation + transpiration) is central to a wide range of biological, chemical, and physical processes in the Earth system. Accurate remote sensing of ET is challenging due to the interrelated and generally scale dependent nature of the physical factors which contribute to the process. The evaporation of water from porous media like sands and soils is an important subset of the complete ET problem. Chapter 1 presents a laboratory investigation into this question, examining the effects of grain size and composition on the evolution of drying sands. The effects of composition are found to be 2-5x greater than the effects of grain size, indicating that differences in heating caused by differences in reflectance may dominate hydrologic differences caused by grain size variation. In order to relate the results of Chapter 1 to the satellite image archive, however, the question of information loss between hyperspectral (measurements at 100s of wavelength intervals) laboratory measurements and multispectral (≤ 12 wavelength intervals) satellite images must be addressed. Chapter 2 focuses on this question as applied to substrate materials such as sediment, soil, rock, and non-photosynthetic vegetation. The results indicate that the continuum that is resolved by multispectral sensors is sufficient to resolve the gradient between sand-rich and clay-rich soils, and that this gradient is also a dominant feature in hyperspectral mixing spaces where the actual absorptions can be resolved. Multispectral measurements can be converted to biogeophysically relevant quantities using spectral mixture analysis (SMA). However, retrospective multitemporal analysis first requires cross-sensor calibration of the mixture model. Chapter 3 presents this calibration, allowing multispectral image data to be used interchangeably throughout the Landsat 4-8 archive. In

addition, a theoretical explanation is advanced for the observed superior scaling properties of SMA-derived fraction images over spectral indices. The physical quantities estimated by the spectral mixture model are then compared to simultaneously imaged surface temperature, as well as to the derived parameters of ET Fraction and Moisture Availability. SMA-derived vegetation abundance is found to produce substantially more informative ET maps, and SMA-derived substrate fraction is found to yield a surprisingly strong linear relationship with surface temperature. These results provide context for agricultural applications. Chapter 5 investigates the question of mapping and monitoring rice agricultural using optical and thermal satellite image time series. Thermal image time series are found to produce more accurate maps of rice presence/absence, but optical image time series are found to produce more accurate maps of rice crop timing. Chapter 6 takes a more global approach, investigating the spatial structure of agricultural networks for a diverse set of landscapes. Surprisingly consistent scaling relations are found. These relations are assessed in the context of a network-based approach to land cover analysis, with potential implications for the scale dependence of ET estimates. In sum, this thesis present a novel approach to improving ET estimation based on a synthesis of complementary laboratory measurements, satellite image analysis, and field observations. Alone, each of these independent sources of information provides novel insights. Viewed together, these insights form the basis of a more accurate and complete geophysical understanding of the ET phenomenon.

Contents

List of Figures viii

List of Tables xi

Acknowledgements xii

Dedication xiii

Introduction 1

1. Effects of Grain Size and Composition on the Thermal and Optical Evolution of Evaporating Porous Media 7

Abstract 7

Introduction 8

Materials & Methods 10

Laboratory Apparatus 10

Sands 13

Laboratory procedure 17

Caveat – packing 18

Observations 19

Definition of Extinction and Skin Depths 19

Generalized drying progression 20

Justification for using 1440 nm reflectance 23

Reflectance and Surface Temperature Time Series 24

Interpretation 32

Overview of the salient features of the drying trajectories 32

Transition 1 33

Matrix Evaporation 34

Transition 2 34

Discussion 35

A. How much variability exists in the drying process among sands and grain sizes, how does the magnitude of this variability compare to variability caused by fluctuations in ambient air temperature and relative humidity, and how does this variability compare between optical and thermal domains? 35

B. Do variations in grain size and mineralogy have impacts of comparable amplitude on the evolution of temperature and reflectance? If not, which physical parameter has a greater effect, and by how much? 36

C. To what extent do grain size and mineralogy systematically the impact timing and amplitude of specific optical and thermal transitions? 38

Possible physical processes – Albedo, composition, and grain size 38

Possible physical processes – Surface roughness 40

Possible physical processes – Skin layer thickness 40

Contribution to the existing body of knowledge 43

Conclusions 44

2. Multisensor Analysis of Spectral Dimensionality and Soil Diversity in the Great Central Valley of California 46

Abstract 46

Introduction 47

Background 49

Measuring Spectral Variability 49

Spectral Variability and the Spatial Dimension 51

Spectral Variability of the Plane of Substrates 53

Materials and Methods 54

Results 60

Discussion 69

Conclusions 75

3. Global cross-calibration of Landsat spectral mixture models 77

Abstract 77

Introduction 78

Background 81

Implications of Spectral Band Positioning 81

Spectral Mixture Models and Linear Spectral Unmixing 84

Scientific Context and Limitations of the Study 85

Data & Methods 88

Analysis 89

Discussion 102

Conclusions 107

4. Spectral Mixture Analysis as a Unifying Framework for the Remote Sensing of Evapotranspiration 109

Abstract 109

Introduction 110

ET Model Overview 115

Models Relying on V vs T 115

Models Relying on α vs T 116

Spectral Mixture Analysis 117

Materials and Methods 121

Data 121

Spectral Mixture Analysis 122

ET Estimation Using the Triangle Method 123

Study Area 126

Results 127

Vegetation Metric Comparison 128

Dark Fraction and Albedo 136

Substrate Fraction, Temperature, and ET 141

Discussion 143
Application Examples 143
Evaluation 149
ET Partitioning 154
Thermal EM Selection 155
Clustering in Fraction vs ET Parameter Space 156
The SVD Approach as a Unifying Framework 157
Conclusions 159
5. Mapping and Monitoring Rice Agriculture with Multisensor Temporal Mixture Models 160
Abstract 160
Introduction 161
Background – Study Area 165
Regional Thermal Setting 165
Rice in the Sacramento Valley 168
Materials and Methods 169
Data Acquisition & Preprocessing 169
Spectral Mixture Analysis of Optical Data 170
Emissivity Estimation 172
Atmospheric Correction of Thermal Data 173
Effect of emissivity estimation and atmospheric correction 175

Spatiotemporal Analysis and Temporal Mixture Models 178
Results 182
Vegetation Phenology 182
Thermal Phenology 186
Characterization – EOF analysis and tEM selection 187
Modeling 197
Near-Realtime Monitoring & Field Validation 198
Discussion 204
Harvest Forecasts 205
Intra-field Variability: Weed and Nutrient Management 205
Pest Management 206
Evapotranspiration and Water Use 206
View Angle and Flooding Presence 209
Integration of New Data Streams 209
Conclusions 210
Appendix: Field Validation 212
6. Spatial Structure and Scaling of Agricultural Networks 217
Abstract 217
Introduction 218
Background 222

Rank-size Plots and Heavy-Tailed Distributions 222

Scale-Free Networks and Constrained Networks 224

Data & Methods 226

Analysis 233

Landsat 233

Sentinel-2 237

IKONOS 242

Practical Example – Disruption by Node Removal 244

Discussion 245

Conclusion 251

References 255

List of Figures

Figure 1. Laboratory setup.. 13

Figure 2. Micrographs. 16

Figure 3. A. Example time series of coincident mass, surface temperature, and reflectance measurements. 21

Figure 4. 1440 nm reflectance versus time. 25

Figure 5. 1440 nm reflectance versus fractional mass loss. 26

Figure 6. Surface temperature versus time. 27

Figure 7. Surface temperature versus fractional mass loss. 28

Figure 8. Material comparison for each grain size.. 29

Figure 9. Grain size comparison for each material.. 30

Figure 10. Northern California AVIRIS flight lines used in this analysis. 55

Figure 11. False color composite images of the five AVIRIS flight lines used in this study. 57

Figure 12. Spectral band comparison for Landsat 7/8, Sentinel 2, and AVIRIS 58

Figure 13. Partition of variance for AVIRIS (left) and Landsat (right) 60

Figure 14. Low dimensional feature space comparison. 62

Figure 15. Spectral feature space and endmembers for the rock and soil substrate spectra from the JHU spectral library 65

Figure 16. AVIRIS and Landsat substrate EM variability. 66

Figure 17. Spectral diversity in a 9 × 15 km region of intensive agriculture in the Great Central Valley of California 69

Figure 18. Intraband and interband spectral dimensionality of AVIRIS in comparison to individual infrared bands of Landsat OLI 73

Figure 19. Illustration of the effect of changes in spectral response functions for Landsat 8 OLI and Landsat 7 ETM+ 82
Figure 20. The spectral response functions are generally wider for ETM+ (solid thin lines) than OLI (dashed lines)..... 83
Figure 21. Locations of 30 near-simultaneous Landsat 7/8 scene pairs from which the 100 subscenes for this analysis were chosen. 89
Figure 22. Comparison of 100 OLI subscenes chosen from the near-simultaneous Landsat 7 and Landsat 8 acquisitions from Figure 21..... 90
Figure 23. The Landsat 8 spectral mixing space derived from 80,910,343 broadband spectra.... 93
Figure 24. SVD fraction intercomparison for 80,910,343 Landsat 8 spectra by unmixing with old (Small & Milesi 2013) global EMs and the new 2016 OLI EMs 96
Figure 25. Intercomparison of SVD fractions from 80,910,343 near-simultaneous ETM+ and OLI spectra using the new underflight ETM+ and OLI EMs.. 99
Figure 26. Vegetation index intercomparison. NDVI, EVI, and SAVI relative to vegetation fraction of the same 80,910,343 OLI spectra..... 101
Figure 27. Calculation of EVI for theoretical pixels containing every possible integer combination of subpixel soil, vegetation and shadow. 105
Figure 28. Calculation of NDVI for theoretical pixels containing every possible integer combination of subpixel soil, vegetation, and shadow 106
Figure 29. True color (UL), false color (UR), fraction abundance (LL) and thermal (LR) images of a diverse northern CA landscape as imaged by Landsat 8 on June 19, 2013..... 120
Figure 30. Vegetation metric comparison..... 131
Figure 31. Vegetation metrics vs EF..... 132

Figure 32. Vegetation metrics vs Mo. 134
Figure 33. Dark and Substrate Fractions vs EF and Mo. 138
Figure 34. Dark fraction (D), albedo (α), and Substrate (S) vs normalized temperature (T*) ... 140
Figure 35. Composite relationship between S and T. 142
Figure 36. S, V & D fractions, along with EF & Mo, for a sample 15 × 50 km area imaged on August 14, 2016. 146
Figure 37. Example ET comparison. 148
Figure 38. Four met stations are maintained in the study area by the California Irrigation Management Information System (CIMIS). 152
Figure 39. Comparison to ground observations. 153
Figure 40. Thermal Phenology of the Western United States of America. 167
Figure 41. Effect of atmospheric correction and emissivity estimation on T estimates. 176
Figure 42. The primary rice producing region of California. 181
Figure 43. Multisensor evolution of land cover and temperature. 185
Figure 44. F_v vs LST 2016 temporal feature space (TFS) comparison. 194
Figure 45. Joint 2016 & 2017 F_v vs LST TFS comparison.. 196
Figure 46. Temporal mixture model comparison. 199
Figure 47. 2018 stress test. 201
Figure 48. Mid-season TMM for 2018. 204
Figure 49. Relationship between vegetation and soil LST throughout the study period. 207
Figure 50. Comparison of field and satellite spectra. 215
Figure 51. Photos from July 2018 field validation campaign. 216

Figure 52. Global comparison of agricultural land cover products (top) and corresponding rank size distributions of agricultural land area (bottom). 220
Figure 53. Illustration of network progression with threshold. 229
Figure 54. Agricultural landscapes used for scaling analysis. 234
Figure 55. Rank-Size distributions for Fv from the 9 Landsat scenes shown in Figure 54. 235
Figure 56. Slope of Rank-Size distribution versus threshold for the nine Landsat scenes used in the preceding two figures. 236
Figure 57. Comparison of Landsat- and Sentinel-derived networks from a 30 km x 30 km agricultural region in Abbruzzo, Italy. 239
Figure 58. Same as Figure 57, but for a 30 km x 30 km region in Bavaria, Germany. 240
Figure 59. Same as Figure 57 and Figure 58, but for a 30 km x 30 km agricultural region in Centre-Val de Loire, France. 241
Figure 60. Successive thresholding of vegetation fraction for a 39 km^2 IKONOS image of Anhui, China. 243
Figure 61. Disruption of agricultural networks by erosion. 245

List of Tables

Table 1. Generalized Triangle Method coefficients used to estimate EF and Mo. From Carlson (2007). 125

Acknowledgements

The following thesis is a direct product of intensive collaboration with my advisor, Chris Small. Useful feedback and additional insights from my committee members, Upmanu Lall and Bill Menke, provided much appreciated guidance and support at pivotal junctures along the way. Additional conversations with Jeff Bowles, Tim Crone, Mary Kappus, Andy Kwarteng, Alberto Malinverno, Doug Martinson, Son Nghiem, Andrew Spalton, and Andrea Taramelli were both informative and enjoyable. Weston Anderson, Dan Bishop, Max Cunningham, Josh Russell, and Yen Joe Tan were always available to provide both scientific and nonscientific feedback over the years. Any merit in the following pages is largely attributable to those listed above; any faults are entirely my own.

Dedication

Caroline;

Anna, Emily, Betty, and Frank;

Frisbee, Reilly, Auggie, and Abbee;

Our parents, their parents, and all those who came before us:

During the dry years, the people forgot about the rich years, and when the wet years returned, they lost all memory of the dry years. It was always that way.
John Steinbeck

The only wisdom we can hope to acquire
Is the wisdom of humility: humility is endless.
T.S. Eliot

τοῦ λόγου δὲ ἐόντος ξυνοῦ ζώουσιν οἱ πολλοί
ὡς ἰδίαν ἔχοντες φρόνησιν
Heraclitus

Ekam Sat. Vipra bahuda vadanti.
Rig Veda

1 Corinthians 13

γνῶθι σεαυτόν
Temple of Apollo at Delphi

Introduction

Earth's lithosphere, atmosphere, and biosphere are unified by the movement of water. Evapotranspiration (ET; the sum of evaporation and transpiration) is a central mechanism in this exchange, and accordingly plays a major role in Earth's surface energy balance. However, despite the pivotal role that ET plays in the Earth system, a number of outstanding questions remain in our fundamental physical understanding of the process. For instance, a recent review found that over 50 models currently exist to compute ET, and model choice can impact ET estimates by over 25% (Fisher et al., 2011). Uncertainty in ET estimation propagates into to Earth system models and has direct implications for our ability to monitor and predict changes to fundamental processes such as the speed and amplitude of the water cycle, the location and movement of biomes, and the partitioning of the global surface energy balance. This uncertainty is, at least in part, a result of insufficient observations to resolve ambiguities in the assumptions underlying each model.

One critical component of these models is the evaporation of water from soil, sediment, and rock substrates. Despite the importance of experimental constraints to an understanding of the underlying mechanisms, surprisingly few laboratory investigations exist documenting the evaporation of water from porous media. Those experiments that do exist focus on measurements of either the optical (Lobell and Asner, 2002; Small et al., 2009; Tian and Philpot, 2015a; Zhang and Voss, 2006) or thermal (Smits et al., 2012, 2011, 2010) evolution alone, without explicit consideration for the potential complementary information that could be provided by the other data stream. This knowledge gap is particularly remarkable given that the remote sensing of ET generally relies on coincident measurements of both reflectance and surface temperature.

Chapter 1 of this thesis presents the results of a suite of laboratory experiments designed to provide constraints on one component of ET models. These experiments observe the simultaneous optical and thermal evolution of drying sands of varying composition and grain size. While all the sands are observed to undergo the same stages during the drying process, important differences in the timing, rate of change, and amplitude of change observed in each stage are also observed. The relationship between the differences in drying trajectories and the variations in grain size and composition is explored. In addition to being of interest on its own, the content of this chapter provides important physical and conceptual framework underlying the chapters which follow.

While laboratory measurements are critical to understanding the underlying physics, the ultimate objective for many ET studies is landscape-scale mapping and monitoring. Satellite imagery can be useful for landscape-scale ET studies because it provides low cost, rigorously calibrated, quantitative time series measurements nearly simultaneously over broad (>100 km) spatial extents. However, the decades-long multispectral Landsat archive is collected at broadband (>100 nm) spectral intervals. In order to understand how the hyperspectral (3-12 nm resolution) laboratory measurements of Chapter 1 can be expected to relate to multispectral satellite imagery, the question of hyperspectral-to-multispectral information loss – or preservation – must be considered.

Chapter 2 investigates this question. Hyperspectral images collected by the AVIRIS sensor are compared to same-day multispectral images collected by Landsat. These images were selected on the basis of maximum diversity of substrate materials such as sediment, soil, rock, and non-photosynthetic vegetation. The results indicate that the spectral continuum measured by Landsat is sufficient to resolve the gradient between sand-rich and clay-rich soils. This gradient

is also found to be a dominant feature in hyperspectral mixing spaces where the actual absorptions can be resolved. This is encouraging news for the potential application of laboratory results such as those of Chapter 1 to landscape-scale soil mapping and ET monitoring.

In order to relate laboratory measurements to landscape-scale processes, the issue of scale must also be considered. One reason that estimates of ET are so variable is that the physical quantities on which they rely (e.g. temperature, humidity deficit, wind speed, stomatal conductance) operate at different spatial scales. As a result, surface energy balance equations generally scale nonlinearly in heterogenous areas (Brunsell and Gillies, 2003a). The effects of this nonlinear scaling are so pernicious that subgrid variation of latent heat exchange has been shown to produce bias errors in surface-vegetation-atmosphere-transfer (SVAT) models often exceeding 100%, and sometimes up to 300% (Baldocchi et al., 2005).

Maps of ET are generally derived from a combination of data from satellite imagery and ground based weather stations. Spatially explicit SVAT models which leverage spatial and/or temporal differences in the thermal radiance field are inverted to estimate thermal inertia and evapotranspirative cooling. Because of the nonlinearity in the surface energy balance equations, the spatial structure of ET maps obtained in this way are scale-dependent and can vary widely between sensors. This has been the subject of a considerable body of recent work (e.g. (Brunsell and Anderson, 2011; Ershadi et al., 2013; McCabe and Wood, 2006; Sharma et al., 2016)).

The vast majority of ET models rely, at least in part, on spectral vegetation indices as inputs to provide critical constraints on land surface properties such as vegetation abundance and leaf area index. Vegetation indices generally have nonlinear scaling properties (Christopher Small, 2001; Small and Milesi, 2013; Sousa and Small, 2017a). This nonlinearity is particularly severe for the most commonly used index, the Normalized Difference Vegetation Index (NDVI;

(Rouse et al., 1974)). Nonlinear scaling in such a critical input parameter can have obvious implications for ET estimation.

Spectral mixture analysis (SMA; (Adams et al., 1986; Gillespie et al., 1990; Smith et al., 1985)) is a simple, physically based approach to the estimation of areal abundance of spectrally distinct Earth materials from satellite imagery. For the purposes of mapping the areal abundance of subpixel vegetation, SMA has been shown to have strongly linear scaling properties (Christopher Small, 2001; Small and Milesi, 2013). Independent field validations using traditional estimation methods have shown the accuracy of SMA to be superior to spectral indices when estimating the amount and density of vegetation, particularly in cases of sparse, open canopy vegetation cover (Elmore et al., 2000; Smith et al., 1990). The linear scaling that SMA provides clearly has the potential to yield obvious benefits for understanding a scale-dependent process like ET.

A globally standardized approach to SMA was developed by (Small, 2004) for the Landsat 7 ETM+ sensor. However, Landsat 8, launched in 2013, carries a substantially redesigned imaging sensor. Because of differences in spectral bandpass between the two sensors, cross-calibration is required in order to allow the globally standardized model to operate on data from the two sensors interchangeably. Fortunately, an underflight of the two satellites was performed soon after the launch of Landsat 8, enabling this cross-calibration using image pairs collected < 2 min apart. Chapter 3 presents this cross-calibration, as well as a theoretical explanation for the superior scaling properties of SMA fraction estimates versus spectral indices. The result is a standardized approach which permits effectively interchangeable treatment of data throughout the Landsat 4-8 archive.

At landscape scales, the tradeoff between vegetation abundance and surface temperature has long been recognized to result in a generally triangular distribution on scatterplots of simultaneously imaged land surface temperature versus vegetation abundance (J. C. Price, 1990). This has led to a popular approach to ET estimation deemed the Triangle method (Carlson et al., 1994). However, Triangle Method-based studies to date have based their vegetation abundance estimates on spectral indices. The improvement to Triangle Method-based ET estimation obtained by estimating vegetation abundance using SMA instead of spectral indices is examined in Chapter 4. In addition, the Substrate and Dark EM fraction maps are examined in the context of surface temperature. The relationships between all three EMs and the derived parameters of ET Fraction and Moisture Availability are also are examined in detail, using an agriculturally diverse region of substantial economic and environmental interest in the Sacramento Valley of California.

Chapter 5 focuses on leveraging optical and thermal satellite image time series to improve the mapping and monitoring of rice agriculture in this same geographic region. However, instead of using multitemporal optical and thermal image data as inputs to a landscape-scale ET model, time series of each parameter are considered separately. Optical image time series are shown to provide superior ability to estimate differences in crop phenology, but thermal image time series are shown to be capable of more accurately distinguishing rice from non-rice crops. Taken together, the results of Chapters 4 and 5 have clear implications for the application of geophysical methods to problems with clear human relevance.

Finally, Chapter 6 also focuses on agricultural applications, but from a more global perspective. The scaling properties of agricultural landscapes are investigated. The land surface

of the Earth can be considered a mosaic of competing spatial networks of land cover types (Small and Sousa, 2015). Agriculture is one of the most spatially pervasive and economically important of these land cover types. A diverse global sample of agriculturally intensive landscapes is examined and surprisingly similar scaling properties are observed. These properties are found to be similar to those of global agricultural maps, as well as estimates of forest cover and human settlements. This unity in scaling properties and connectivity structure across land cover types is suggestive of a single, general mechanism for the nucleation, growth, and connection of bounded spatial networks (Small and Sousa, 2015). If this relationship also holds for variables such as ET fraction and surface moisture availability, these scaling properties could provide useful new constraints for improved ET estimation.

1. Effects of Grain Size and Composition on the Thermal and Optical Evolution of Evaporating Porous Media

Abstract

Evaporation from porous substrates (e.g. sediments and soils) is a critical component of global energy and water budgets. Sediments and soils generally change both optically and thermally throughout the drying process. However, the mechanisms by which the physical properties of a porous medium influence the timing and amplitude of these changes remain poorly understood. This is partially due to the large number of potentially relevant, interrelated parameters which are generally needed to characterize porous media. Sieved sands offer a natural basis for experimental investigation because they do not possess several of the most challenging of these parameters (e.g. wide range of grain sizes, clay-sized particles, organic matter). While experiments have been previously conducted using either optical or thermal measurements alone, to my knowledge no study has yet been published documenting the joint optical and thermal evolution of drying sieved sand samples. The results of previous optical laboratory experiments have variously suggested linear, exponential, or multiphase progressions of brightness with moisture content. Previous thermal experiments suggest more complex evolutions with dependence on boundary conditions. This chapter uses a set of laboratory experiments to document the simultaneous optical and thermal evolution of naturally occurring sand samples. The three sands used in this chapter vary widely in composition. The sands are sieved to grain sizes corresponding to fine, medium, and coarse sand grades. Differences among compositions and grain sizes are documented in order to address questions of within- vs between-sample variability, relative effect of grain size vs composition on drying trajectory, and impact of both grain size and composition on timing of transitions in the drying process. The results indicate that the effects of composition are 2-5x greater than the effects of grain size for both optical and

thermal measurements throughout the drying process. This suggests that differences in heating caused by differences in reflectance may dominate hydrologic differences caused by grain size variation, at least for sands in the 125-1000 μm range. A set of hypotheses is developed addressing the potential to leverage differences in optical and thermal skin depths to infer the slope of the vertical moisture gradient at a particular stage in the drying process. If these hypotheses are validated by future experimental studies, a new method of characterizing near-surface hydrological properties of porous media using only remotely sensed measurements could be developed.

Introduction

The optical and thermal properties of porous media like sediments and soils change when wetted. In the optical domain, the addition of water generally results in darkening. In the thermal domain, a complex interaction takes place involving flow of both sensible (temperature) and latent (evaporation) heat. Optical and thermal processes are interrelated through the physical properties of the medium. Two of the most widely variable and geophysically relevant properties of sediments and soils are mineralogic composition and grain size. Both mineralogy and grain size influence albedo (optical), which influences heating (thermal) by determining the fraction of incident radiation that is absorbed by the material. Despite fundamental importance to a complete understanding of the evaporation process, the relative contributions of the physical properties of porous media to the timing, range, and rate of change of their optical and thermal drying trajectories remain poorly understood.

Evaporation from the land surface is often considered in the context of surface energy balance. This approach relies on the principle of conservation of energy: energy reaching the Earth surface (i.e. solar radiation + atmospheric emission) must balance the sum of energy

partitioned into outgoing radiation (reflection and emission) and both sensible (temperature increase) and latent (evaporation) heating. While conceptually simple, this approach can be difficult to implement in the case of porous media because of the coupling between terms. Material properties impacting radiative and sensible heat flow such as the albedo, surface temperature, emissivity, and conductance all change with surface moisture content, which in turn changes with latent heat flow. Optical changes in material properties of wetted porous media are largely due to the moisture darkening phenomenon, which has been recognized in the geophysical literature since at least 1925 (Ångström, 1925), subject to considerable theoretical and experimental investigation ever since (e.g. (Bablet et al., 2018; Lekner and Dorf, 1988; Philpot, 2010; Sadeghi et al., 2017; Tian and Philpot, 2015a; Twomey et al., 1986; Zhang and Voss, 2006)). Previous studies have found results suggesting both linear (Idso et al., 1975) and exponential (Lobell and Asner, 2002) reflectance variations in soils, as well as multiphase transitions in sands (Small et al., 2009). Thermal changes have also been the subject of considerable study (e.g. (Smits et al., 2013, 2012, 2011, 2010; Vanderborght et al., 2017)). Despite the importance of experimental constraints to an understanding of the underlying mechanisms, surprisingly few laboratory investigations exist documenting the evaporation of water from porous media. Those experiments that do exist focus on measurements of either the optical (Lobell and Asner, 2002; Small et al., 2009; Tian and Philpot, 2015a; Zhang and Voss, 2006) or thermal (Smits et al., 2012, 2011, 2010) evolution alone, without explicit consideration for the potential complementary information that could be provided by the other data stream. To my knowledge, no investigation has yet been published which uses simultaneous optical and thermal time series measurements to constrain how fundamental physical properties of porous media can impact the evaporation process.

This chapter presents a set of experiments designed to address this knowledge gap by characterizing the impact of two fundamental geophysical properties – grain size and mineralogic composition – on the optical and thermal evolution of drying sands. Three natural samples spanning a wide range of provenance and transport history were partitioned into grain size fractions corresponding to fine, medium, and coarse sand. These samples were then wetted and subsequently allowed to dry while observed under laboratory conditions. Simultaneous time series measurements of reflectance, surface temperature, and mass were recorded. These data were then used to address the following set of questions:

- *How much variability exists in the drying process among compositions and grain sizes, how does the magnitude of this variability compare to variability caused by fluctuations in ambient air temperature and relative humidity, and how does this variability compare between optical and thermal measurement domains?*
- *Do variations in grain size and mineralogy have impacts of comparable amplitude on the evolution of temperature and reflectance? If not, which physical parameter has a greater effect, and by how much?*
- *To what extent do grain size and mineralogy systematically impact timing and amplitude of specific optical and thermal transitions in the drying process?*

The observations made in this chapter, while limited in scope, provide microscale geophysical context for the evaporation component of the surface energy balance, and for the landscape-scale optical and thermal analyses in the chapters to follow.

Materials & Methods

Laboratory Apparatus

Geophysical measurements of the drying progression were simultaneously obtained by the following instruments arranged in the laboratory setup illustrated by Figure 1. Illumination was provided by an Ushio Halogen 30V 200 W bulb, run at a constant 20 V using a BK Precision 9131B Triple Output Programmable DC power supply. The bulb was mounted in a

Lowell Pro lamp at a distance of 85 cm, directed at the target from an elevation angle of 45º. Spectral reflectance measurements were obtained over the full visible through shortwave infrared (350-2500 nm) spectrum using an ASD FieldSpec Pro JR spectroradiometer mounted with an 8º foreoptic. The instrument is comprised of three separate spectrometers: one 512 channel silicon photodiode array providing Full Width Half Maximum (FWHM) spectral resolution of 3 nm across the visible through near infrared (VNIR, 350 to 1050 nm) spectral range, and two indium gallium arsenide (InGaAs) detectors providing FWHM spectral resolution of 10 to 12 nm across the shortwave infrared (SWIR, 700 to 2500 nm) spectral range. After collection, spectra were oversampled to 1 nm wavelength intervals throughout the entire 350-2500 nm spectral range. Reflectance measurements were recorded at the sampling rate of 1 / min or faster for every experiment conducted. Each recorded spectrum represents the average of 10 individual scan spectra collected over the interval of 1 sec. Calibration against a Spectralon® white standard was performed at the beginning and end of each experiment and used to estimate the drift of the spectrometer over the 4-5 hour duration of each experiment. Drift at a given wavelength was observed to be on the order of +/- 0.005 reflectance units for SWIR wavelengths and +/- 0.02 for VNIR wavelengths. Drift was observed to be greatest towards the ends of the wavelength ranges of each of the 3 spectrometers, and least towards the center. Spectra were subsequently corrected for drift by subtraction, assuming linearity with respect to time.

Thermal measurements were made using a Heitronics CT09.K6 8-14 μm pyrometer and a FLIR A35 f=9 mm thermal camera with SC kit (60 Hz). The pyrometer was factory calibrated to have measurement error of +/- 1 ºC + 0.6% of the difference between the target and sensor head temperature. The thermal camera was factory calibrated to have measurement error of +/- 5 ºC or 5% of the target temperature. The pyrometer, thermal camera, and spectrometer foreoptic were

all mounted at a distance of approximately 17.5 cm from the sample. Tests of the collocation of the pyrometer and spectrometer fields of view (FOVs) were conducted using high intensity localized thermal and visible sources. The FOVs of both instruments were determined to be centered within 1 cm of each other. The total widths of the spectrometer and pyrometer FOVs were approximately 2.5 cm and 0.7 cm, respectively.

Measurements of mass were made using a Scientech Zeta Z500 mass balance and recorded at 1 sec intervals. While the data were output by the instrument to 0.001 g precision, drift was observed over the course of the experiments on the order of 0.005 g. Drift in the mass balance measurements was estimated by differencing the initial and final masses. Mass balance measurements were corrected for drift by subtraction, assuming linearity with respect to time.

Ambient temperature and relative humidity (RH) were measured at the beginning and end of each experiment using an Ambient Weather WS-3000-X3 Thermo-Hygrometer Wireless Monitor. Macro photos of drying stages were obtained using a Lumix GX85 μ4/3 camera with an Olympus M Zuiko ED 60mm f/2.8 macro lens.

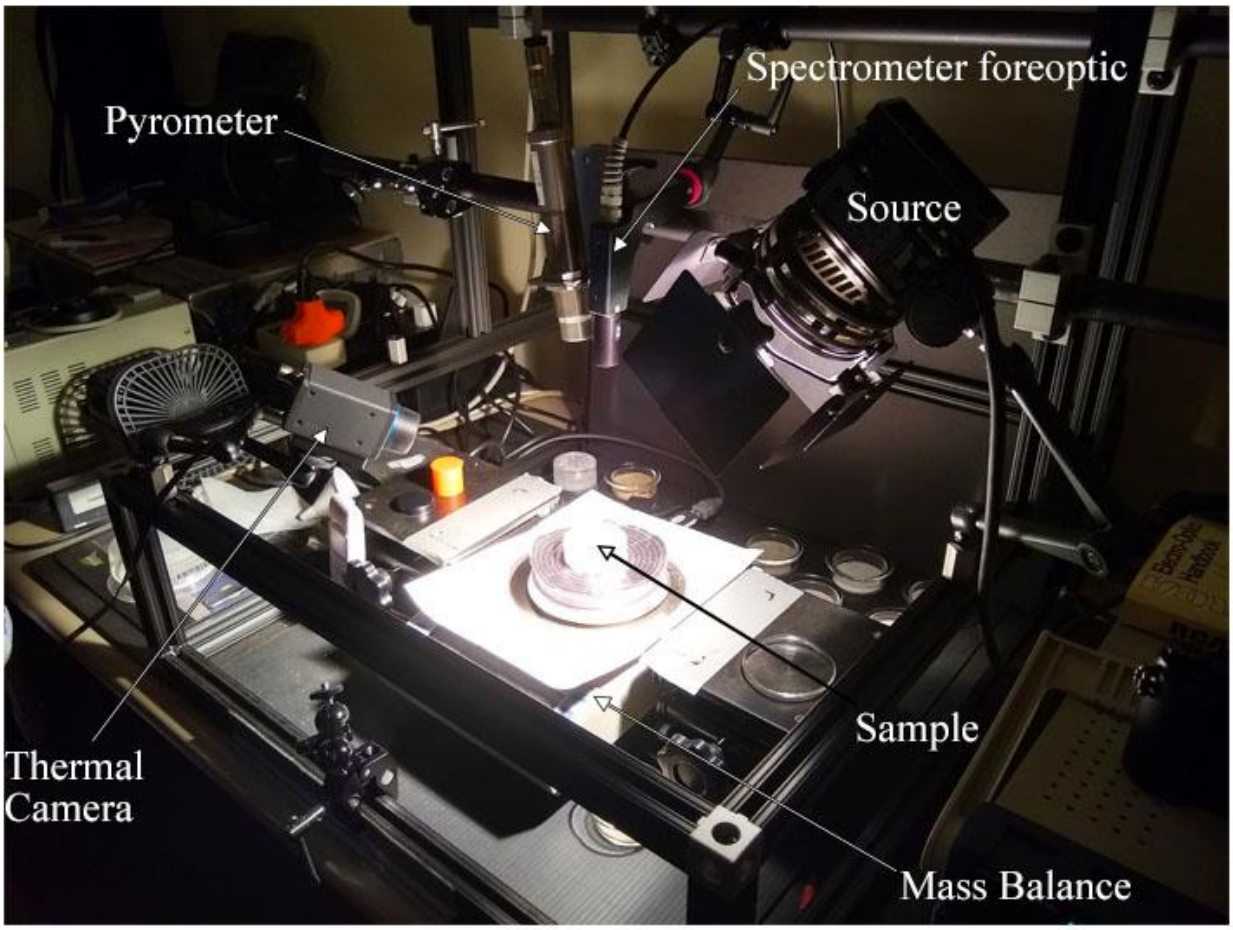

Figure 1. Laboratory setup. Each sample was centered on the mass balance and illuminated by the halogen lamp at 45 degree elevation angle. The spectrometer foreoptic, pyrometer, and thermal camera were all focused on the center of the sample. The spectrometer was nadir-looking and the pyrometer was oriented near-nadir (approx. 10 degrees) in the principal plane. The camera was positioned obliquely outside the principal plane.

Sands

The 3 sands used for this analysis are described below. Each sand was sieved into the following size fractions: < 63 μm (silt & clay), 63-125 μm (very fine sand), 125-250 μm (fine

sand), 250-500 μm (medium sand), 500-1000 μm (coarse sand), and > 1000 μm (very coarse sand). Because of the grain size distributions of the samples, the analysis focuses on 125-250 μm, 250-500 μm, and 500-1000 μm size fractions. Micrographs, grain size distributions, and reflectance spectra of each sample are shown in Figure 2.

The *Cam Ranh* (CR) sand was obtained from a coastal dune deposit in southeast Vietnam. The CR sample is dominated by semi-rounded to rounded milky quartz, with trace metallic oxides, pyroxene, calcite, zircon, and plant debris. CR is the brightest of the three sands (dry albedo (α) = 0.65). Micrographs of the sample demonstrate minimal mineralogic variability among size fractions. Grains appear generally homogenous in color. The rounding of the grains is consistent with distance from provenance and moderately high energy depositional environment. Sufficient material existed in the CR sample to obtain 25 g samples for each of the 125-250 μm, 250-500 μm and 500-1000 μm size fractions. Micrograph histograms indicate only minor variability in grayscale brightness among grain sizes for the CR sands, consistent with the nearly monomineralic nature of the sample.

The *Cape Cod* (CC) sand was obtained from the Provincetown Dunes in Cape Cod National Seashore. The CC sample is primarily composed of rounded quartz, with rare feldspar are trace rounded lithics, glauconite, hornblende, and detrital carbonate. CC grains are more variable in color than CR grains, resulting in a lower overall sample albedo (α = 0.54). The grain size distribution of the CC sand is skewed toward coarser size fractions, consistent with dunes deposited in a subaqueous environment and subsequently subject to aeolian erosion. The dominance of rounded grains is in accord with the long sediment age and transport distance of the CC sand. Given the grain size distribution, 25 g samples were only able to be obtained of the 250-500 μm and 500-1000 μm size fractions. Micrograph histograms reveal the 500-1000 μm

sample to be shifted toward darker grains relative to the 250-2500 μm sample, suggesting nonnegligible covariability of mineralogy with grain size.

The *Brahmaputra* (BR) sand was obtained from a transient sediment deposit (*char*) in the floodplain of the Brahmaputra River in Bangladesh. The char was deposited underwater during monsoonal high water and subsequently exposed to the air as water levels fell in the dry season. The BR sample is characterized by abundant angular quartz grains, with a trace amount of lithic grains, micas, and a wide range of heavy minerals. The relative abundance and diversity of heavy minerals results in its darker appearance and low overall albedo ($\alpha = 0.38$). The grain size distribution for the BR sample is skewed toward finer size fractions, reflecting its position in a relatively low energy depositional microenvironment within the char. The angularity of the BR grains is consistent with proximity to sediment source. 25 g samples of the BR sand were obtainable for the 125-250 μm and 250-500 μm size fractions. Micrograph histograms reveal the 250-500 μm sample to be shifter toward brighter grains than the 125-250 μm sample, again suggesting nonnegligible covariability of mineralogy with grain size.

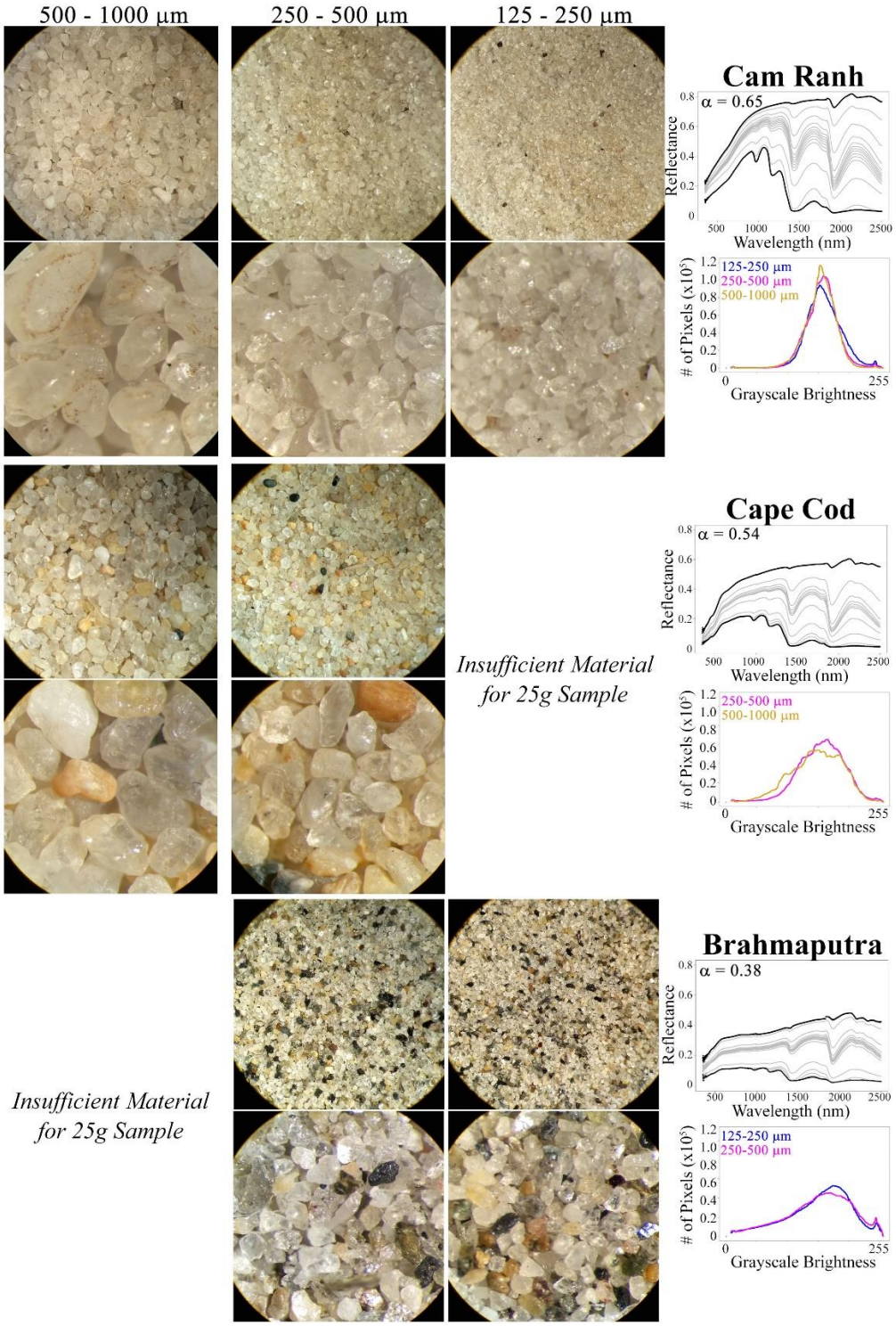

Figure 2. Micrographs. The Cam Ranh, Cape Cod, and Brahmaputra sands were sieved into fine sand (125 – 250 mm), medium sand (250 – 500 mm), and coarse sand (500 – 1000 mm) size

fractions. Micrographs of each size fraction were acquired at 1x and 4x magnification using Leica MS5 stereomicroscope. Histograms of the micrographs are shown to the right. Representative dry and wet sample reflectance spectra are shown in black. Reflectance spectra of intermediate stages of drying are shown in gray at 15 minute intervals. Sufficient material was present for the Cam Ranh sand to partition 25 g samples of each of the three size grades, but only two size grades were available for each of the other two sands.

Laboratory procedure

For each experiment, the 25 g sample was measured into a glass petri dish 60 mm in diameter. A white reference measurement was taken, and the petri dish containing the sample was placed into position on the mass balance within the fields of view of the spectrometer and pyrometer. The sample was placed on a dark background to minimize the effects of stray light. The dry sample was left in position for at least 30 minutes prior to the beginning of the experiment in order to 1) provide baseline measurements of mass and reflectance, and 2) standardize the thermal state of the sample prior to the addition of water, minimizing the effect of fluctuations in ambient conditions of the climate-controlled building in which the experiments took place.

A reservoir of *Milli-Q* purified water was maintained in the lab at ambient temperature. After the initial heating, water was drawn from this reservoir and added to the samples using a micropipette. 8 mL of water was sufficient to saturate the CR and CC samples, but 10 mL were required for the BR samples due to their lower density. Both the air temperature and RH of the room were observed to vary substantially during the experiments. The lowest ambient temperature recorded was 23.1 ºC and the highest was 31.7 ºC, with a maximum temperature fluctuation of 3.9 ºC and minimum fluctuation of 0.4 ºC within a single experiment. The lowest

ambient RH recorded was 4% and the highest was 28%, with a maximum RH fluctuation of 9% and minimum fluctuation of < 1% within a single experiment. Each experiment was conducted in triplicate to provide an estimate of the effect of these (and other) sources of variability in the ambient environment.

Evaporation was then allowed to proceed until complete. The beginning and end of the time period reported in subsequent figures as "experiment duration" were determined using the time water was added and the time mass loss dropped below the measurement error of the mass balance, respectively. The sample was left in place for at least 30 minutes of additional heating after mass loss had ceased in order to allow the sample to more closely approach thermal equilibrium and to provide post-experiment observations of reflectance and mass for the linear drift corrections.

Caveat – packing

Differences in packing among samples were unavoidable. Micrographs of both sieved and unsieved samples (Figure 2) demonstrate that significant differences in angularity and pore structure are to be expected among the samples. The most prominent evidence of significant variations in packing is that an additional 2 mL of water were necessary to saturate the BR sample than the CR and CC samples. This is consistent with the hypothesis that the more angular material (BR) packs less closely, has greater volume of pore spaces, thus requires more water to saturate than the more rounded materials.

The potential for improvement in consistency by mechanically enhanced settling was investigated by vibration of the 500-1000 μm CC samples at 38 Hz for 60 seconds both before and after the addition of water. The results of this experiment were inconclusive and vibration

was not applied to the remainder of the samples. Observations of the vibrated samples are plotted in gray on the figures that follow.

Observations

Definition of Extinction and Skin Depths

Before the general features of the drying progression are examined, it is important to consider the portion of the sample observed by each sensor. The mass balance measurements are integrated throughout the volume of the sample. The optical and thermal measurements are not. The fraction of the sample to which these sensors are sensitive is determined by the depth to which light penetrates into the medium. This depth, referred to as the *extinction depth*, is wavelength- and material-dependent and can be expected to vary with physical properties such as packing structure, transmittance, and emissivity. The spectrometer and pyrometer are sensitive to the optical and thermal *skin depths*, respectively. For a given wavelength, the skin depth is generally shallower than the extinction depth because two-way paths must be considered. The extinction and skin depths can be considered to form surface layers which will be referred to for the remainder of this chapter as the *extinction layer* and *skin layer*, respectively.

In soils, the optical skin layer has long been recognized as having a thickness of < 20 mm (Idso et al., 1975). It is likely that the thickness of the optical skin layer for these sediment samples may reach or exceed this 20 mm threshold given the 1 mm (1000 μm) size of the largest grains, the transmissivity of the grains, and the amount of pore space visible in the micrographs from Figure 2. Because of the relatively small samples being used in this experiment, verification that the samples are optically thick (at least to two-way transits) is important before the observations can be interpreted.

Optical thickness of all the samples measured in this experiment was tested by measuring spectra of each dry sample on both dark (reflectance < 0.06 for all wavelengths in the 350-2500 range) and bright (Spectralon® white standard) backgrounds. The backgrounds were measured to be within +/- 1 mm in height to ensure consistent illumination. The difference between spectra collected on bright and dark backgrounds was computed for each wavelength. The median difference was found to be 0.5% or less for each sample, on the order of measurement error of the spectral measurements. For 3 of the 8 samples the median difference was positive (sample on dark background brighter than sample on light background). These observations support the notion that the 350 – 2500 nm skin depth for all the samples measured in this chapter is less than the thickness of the samples. The thermal skin layer can be expected to be substantially thinner than the optical skin layer given the strong thermal absorptivity of water and most sediments.

Generalized drying progression

Figure 3 demonstrates the generalized progression of the drying experiments using an individual run of the CC 250-500 μm sample (A), along with representative reflectance spectra for each stage of the drying process (B) and a cartoon highlighting salient features of the physical state of the sample at each stage in the drying process (C). The experiment begins as the sample is heated before water is added (t < 0 hr). The state of the sample at this initial stage closely resembles the state of the sample at the termination of the experiment (t > 3.7 hr). The surface temperature of the sample is near maximum (≈ 67 ºC), the mass of the sample is minimum (+ 0 g relative to dry), and the 1440 nm reflectance is near maximum (0.56).

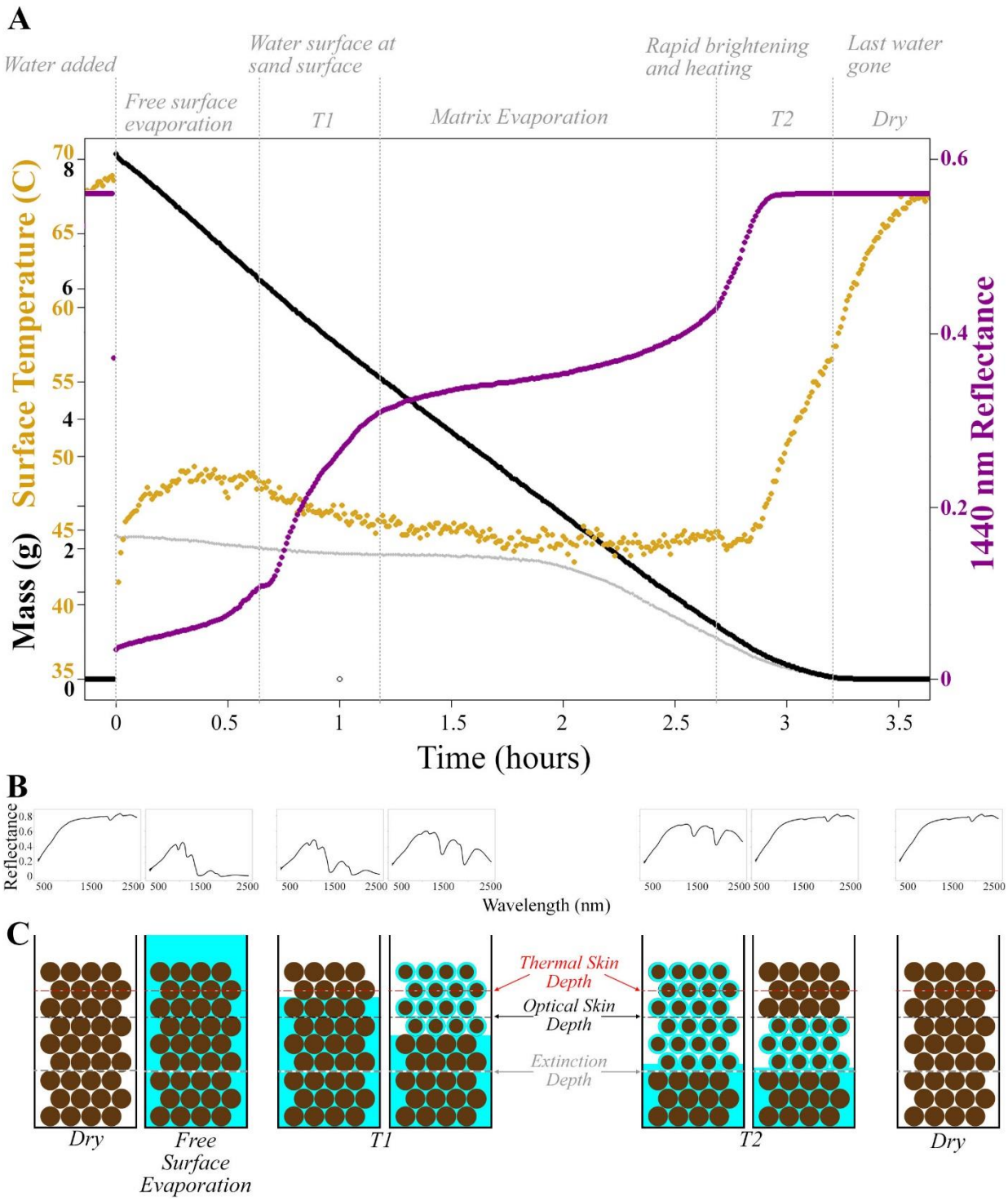

Figure 3. A. Example time series of coincident mass, surface temperature, and reflectance measurements. Hourly mass loss rate is computed continuously and plotted in gray. B.

Reflectance spectra measured at each stage. C. Cartoon illustrating the physical progression of the sample associated with the phases identified in A. The sample begins dry, hot, and bright. When water is added, the sample gains mass, cools, and darkens. The first stage is reached when sufficient water exists to form a free surface above the sand sample. This then transitions to a second stage as water evaporates from the matrix of pore spaces. Optical and thermal surface properties return to the dry state as the optical and thermal skin layers dry.

The addition of room temperature water at t = 0 results in abrupt changes to the state of the sample. The mass increases by 8 g (or 10 g, in the case of the BR samples) to its maximum value, then begins to immediately monotonically decrease as evaporation progresses. The reflectance drops to its minimum value (< 0.1), then begins to immediately monotonically increase as water absorption diminishes with evaporation. The surface temperature drops to its minimum (< 40 ºC), then rapidly increases to an initial steady state temperature of ≈ 45 ºC. The state reached immediately after the addition of water is referred to as *free surface evaporation* because standing water is present above the top layer of sand grains. This stage generally persists for ≈ 1/4 of the duration of the experiment, but significant differences exist between sediment samples.

Free surface evaporation terminates when the water level drops sufficiently to approach the surface of the sand. Once this occurs, the source of evaporating water evolves from a reservoir above the sand grains towards the matrix of interstitial spaces among the sand grains. For the remainder of the chapter, this new stage will be referred to as *Matrix Evaporation*, and the transition into it will be referred to as *Transition 1 (T1)*. The surface temperature during matrix evaporation reaches a gradually cooling plateau which is ≈ 3 to 5 ºC cooler than during the free surface evaporation stage, reaching a minimum at the end of the matrix evaporation

stage. Reflectance increases rapidly by ≈ 1/3 of its range during T1, then monotonically increases at an increasing rate throughout matrix evaporation. Mass loss continues monotonically throughout both the T1 and matrix evaporation stages.

The rate of matrix evaporation drops precipitously when water availability becomes limited. Near this time, 1) the surface temperature rapidly increases because the grains in the thermal skin layer change from being dominated by latent heat flow (evaporation) to sensible heat flow (temperature change), and 2) reflectance increases rapidly as the liquid water absorption ceases on the dry grains. Both surface temperature and reflectance approach the dry states that were observed before the water was added. The transition from matrix evaporation to the final dry state will be referred to as *Transition 2 (T2)* for the remainder of this chapter.

The features listed above are common to all of the drying experiments. These common features provide context with which the effects of sample-to-sample variations in grain size and composition can be interpreted. Systematic effects of grain size and composition on the timing and amplitude of the transitions discussed above, as well as the overall range of values and rates of change, will be examined in detail in the following subsections – after a brief caveat.

Justification for using 1440 nm reflectance

While the optical and thermal properties of porous media are each of sufficient complexity to warrant their own detailed analyses, this chapter is designed to examine their joint evolution in the context of evaporation. In order to focus the analysis on the most salient features, the thermal properties of the sample are reduced to the single variable of surface temperature. In the same way, the principal relevant information present in the 350-2500 nm

reflectance continuum will be extracted using the reflectance at a single wavelength – 1440 nm. This wavelength was chosen on the basis of the absorption spectrum of liquid water.

Liquid water is well known to have strong infrared absorption features at 970, 1160, 1440, and 1930 nm wavelengths. The depth of these absorptions increases with wavelength, so that the 1930 nm absorption is the most intense and the 970 nm absorption is the least intense (Kou et al., 1993). Wet sediments have been observed to monotonically increase in brightness as evaporation proceeds, with the rate of brightening systematically varying with wavelength in accord with the absorption spectrum of liquid water (Tian and Philpot, 2015b). The 1930 nm absorption feature was not chosen because it is so deep as to result in the complete absorption of all detectable light in the initial stages of the experiment. For the purposes of this experiment, 1440 nm thus has the greatest dynamic range of the infrared water absorption features measured by the spectrometer.

Reflectance and Surface Temperature Time Series

Figure 4 shows the evolution of 1440 nm reflectance versus time for each experiment.

Figure 5 shows the same reflectance measurements plotted against fractional mass loss (Fm).

Figure 6 and Figure 7 show complementary time series of surface temperature versus time and Fm, respectively. The duration of each experiment from the addition of water to the cease of mass loss is labeled on Figures 4 and 6. During two of the experiments (CR 250-500 μm #2 and CC 250-500 μm #3), the spectrometer experienced a read/write error. As a result, time

series of surface temperature and mass are available for all runs but time series of reflectance were not collected for these two runs.

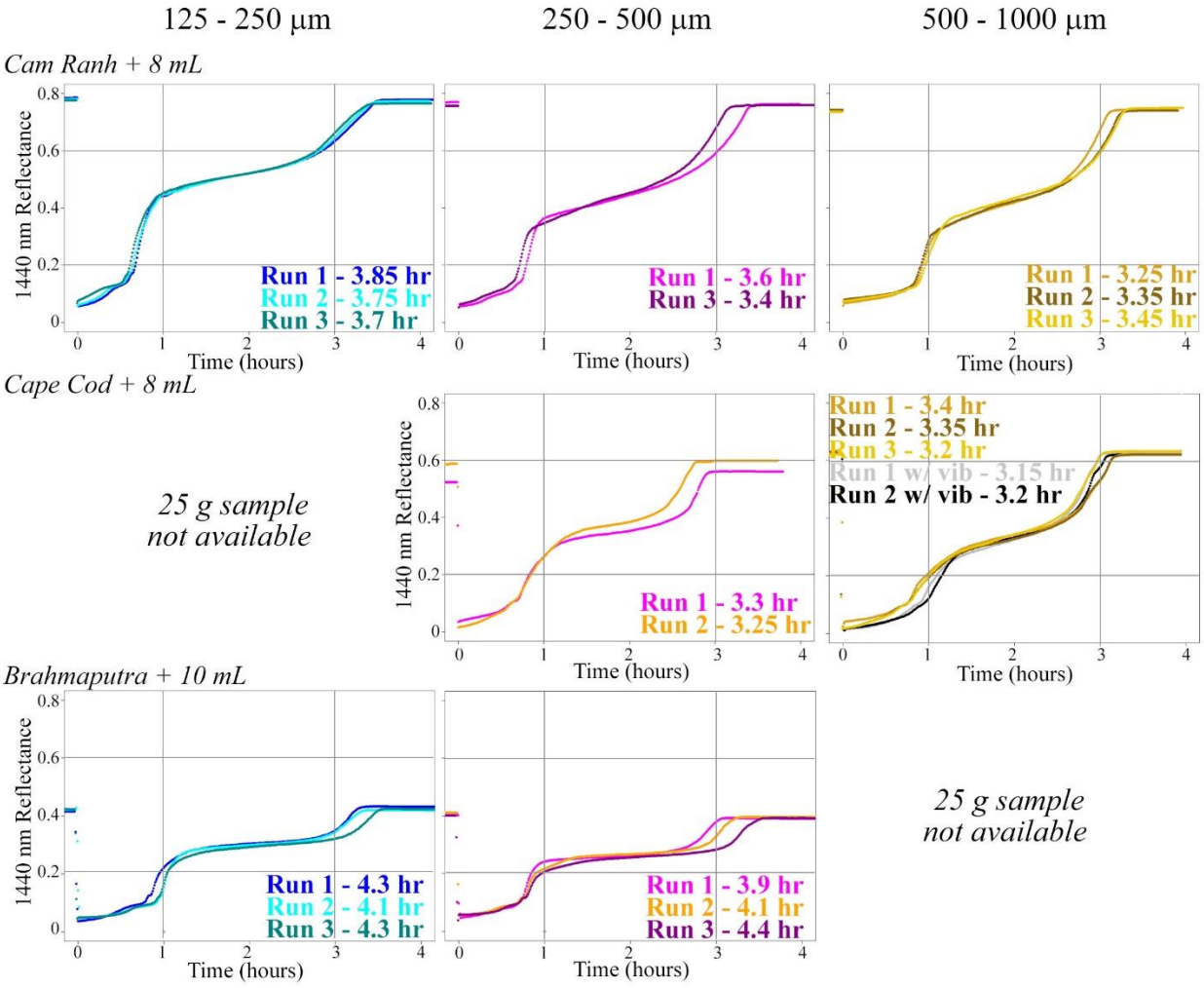

Figure 4. 1440 nm reflectance versus time. Run duration is based on termination of mass loss (not shown). The experimental runs are segregated by grain size and material composition. Substantial intra-sample variability is observed for each sample, largely due to fluctuations in ambient environmental conditions. The normalization by fractional mass (

Figure 5) reduces this variability considerably.

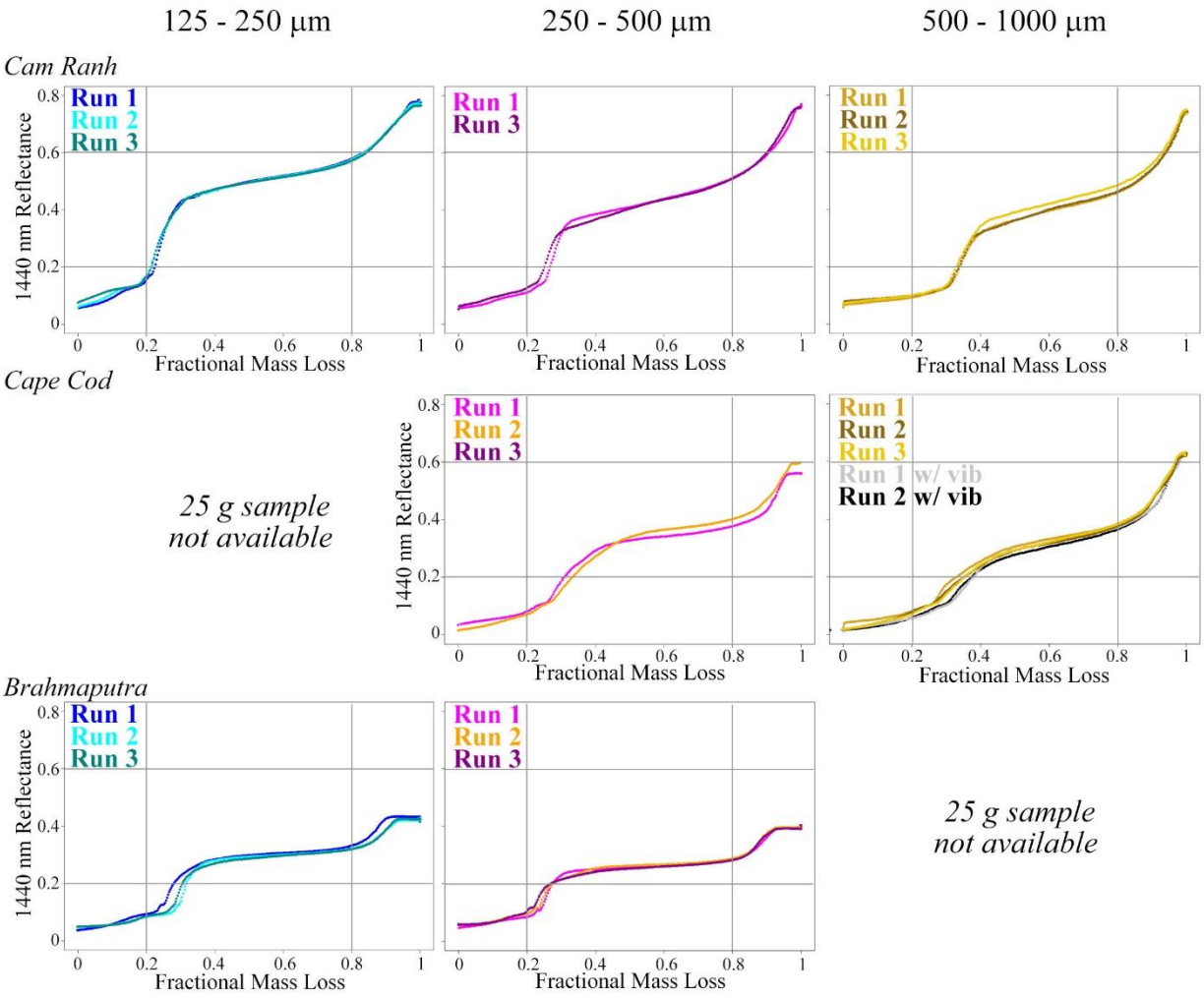

Figure 5. 1440 nm reflectance versus fractional mass loss. Same as Figure 4, but with the time axis replaced by fractional mass loss. This has the effect of (partially) collapsing variations in evaporation rate due to changes in ambient environmental conditions. The cause of remaining intra-sample variability is considered to be variations in packing configuration, mineralogical distribution within the skin layer, and/or measurement error.

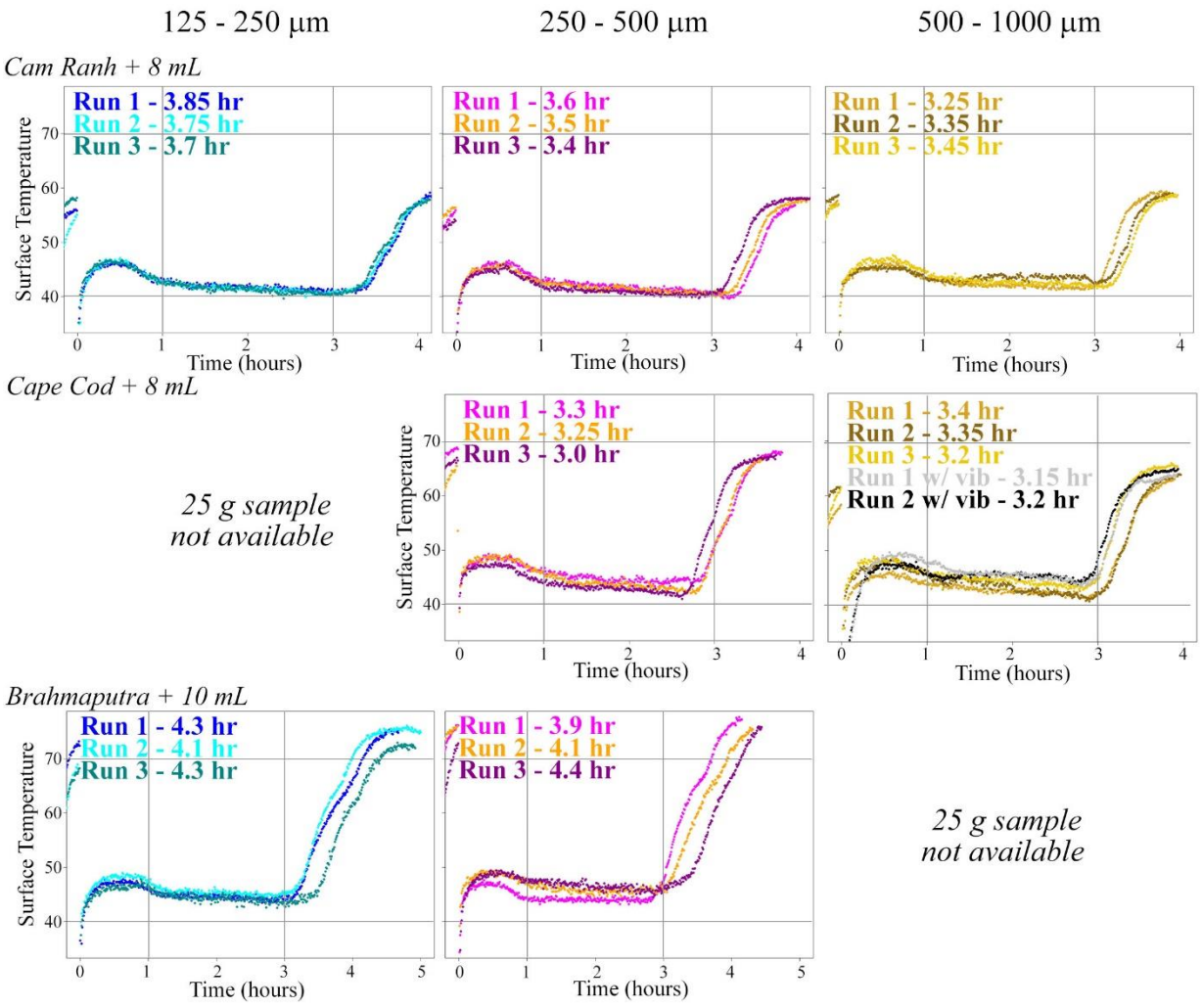

Figure 6. Surface temperature versus time. Same as Figure 4, but showing surface temperature instead of reflectance. More pronounced intra-sample variability is observed for surface temperature than for reflectance.

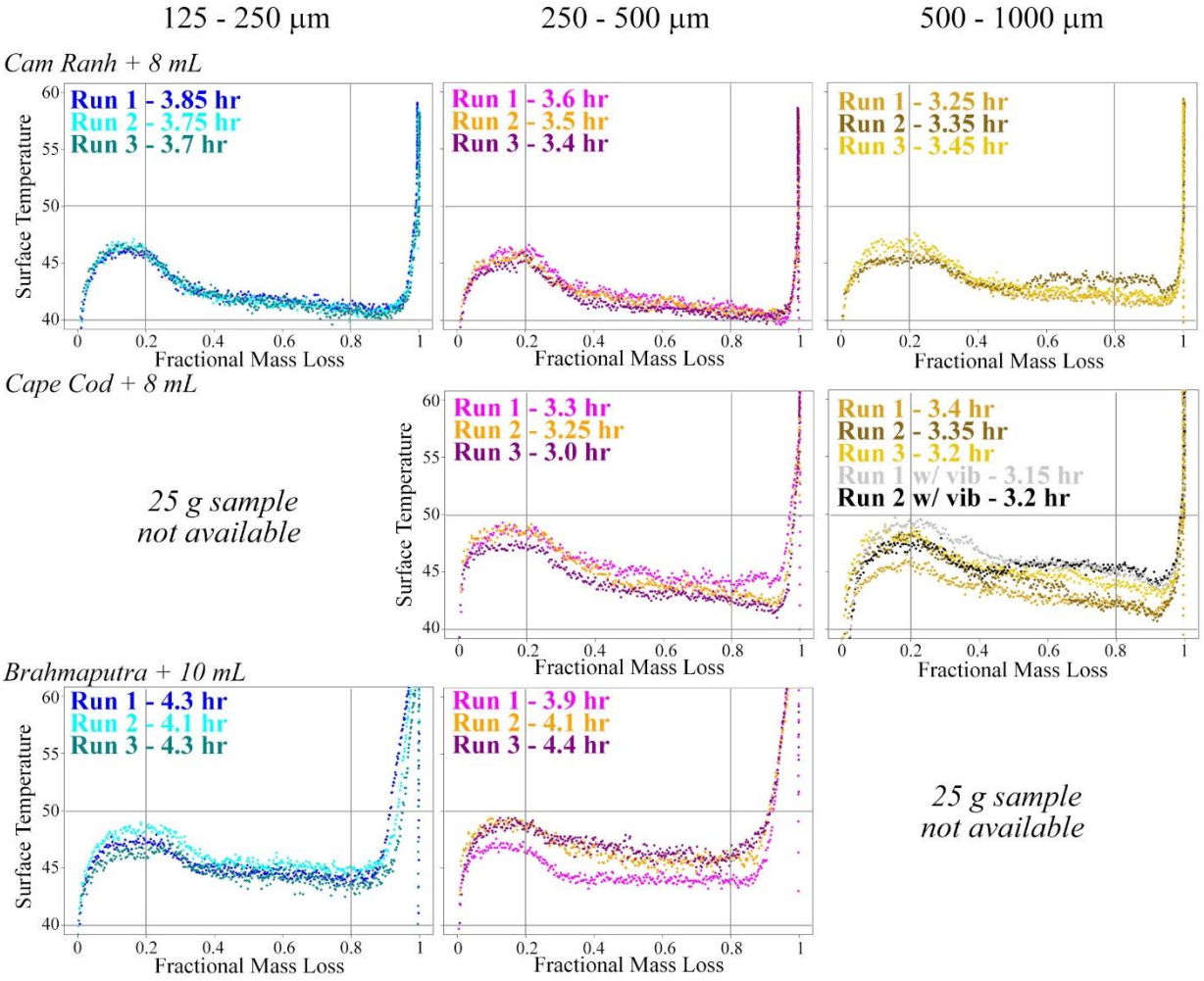

Figure 7. Surface temperature versus fractional mass loss. Same as Figure 5, but showing surface temperature instead of reflectance. Again, the fractional mass normalization accounts for some of the variability between runs, but substantial differences remain. Temperature variations between runs of the same sample are likely due to variations in ambient relative humidity resulting in higher or lower steady state evaporation temperatures. Despite the intra-sample variability, consistent differences between samples are still observed.

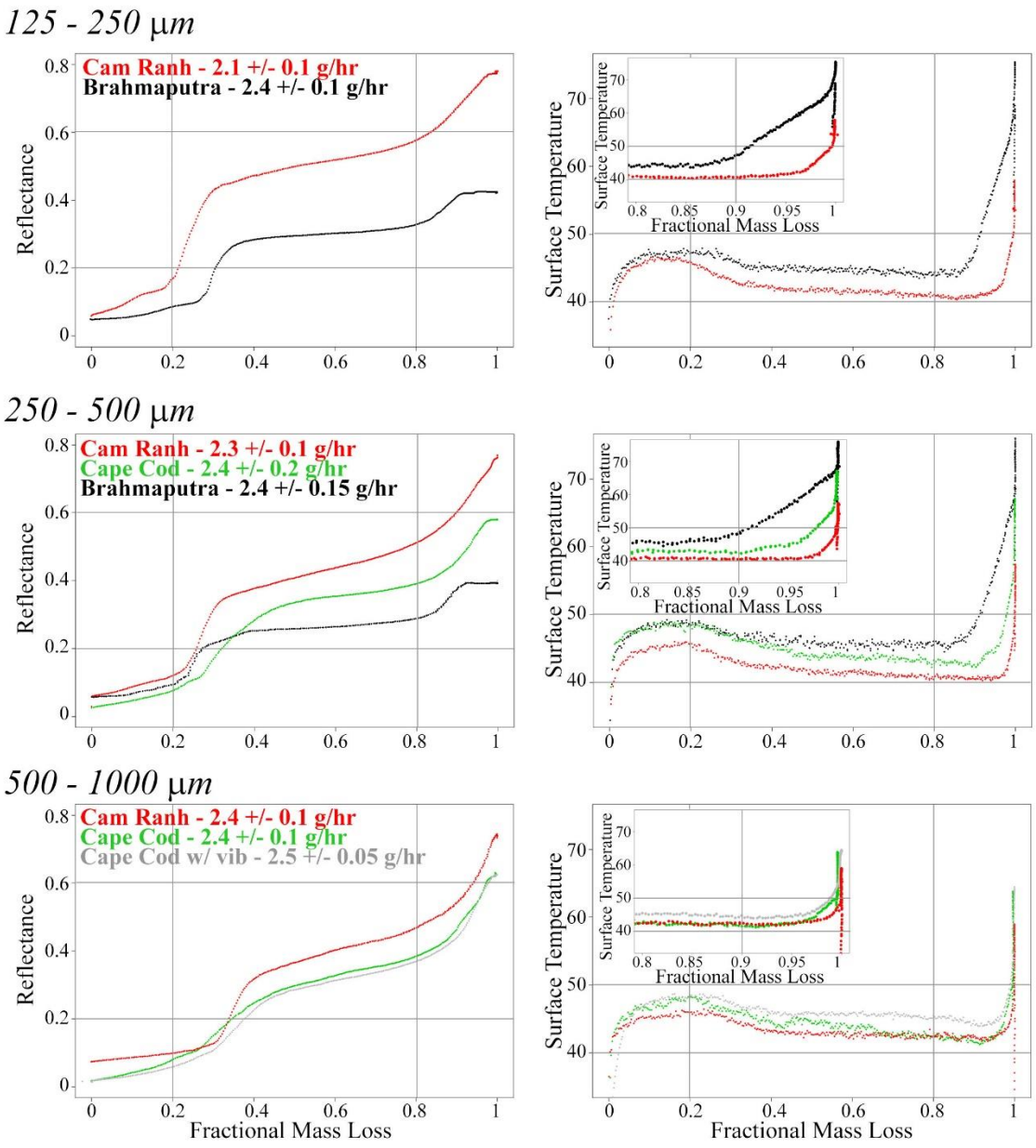

Figure 8. Material comparison for each grain size. Clear differences emerge among the drying trajectories of the three materials in terms of both reflectance and surface temperature. CR is consistently brightest and coolest, and BR is consistently darkest and hottest. CC is intermediate, with a more delayed onset of T1. The onset of T2 as measured by surface temperature is earliest for BR, latest for CR, and intermediate for CC. The termination of T2 as measured by reflectance is also earliest for BR, latest for CR, and intermediate for CC.

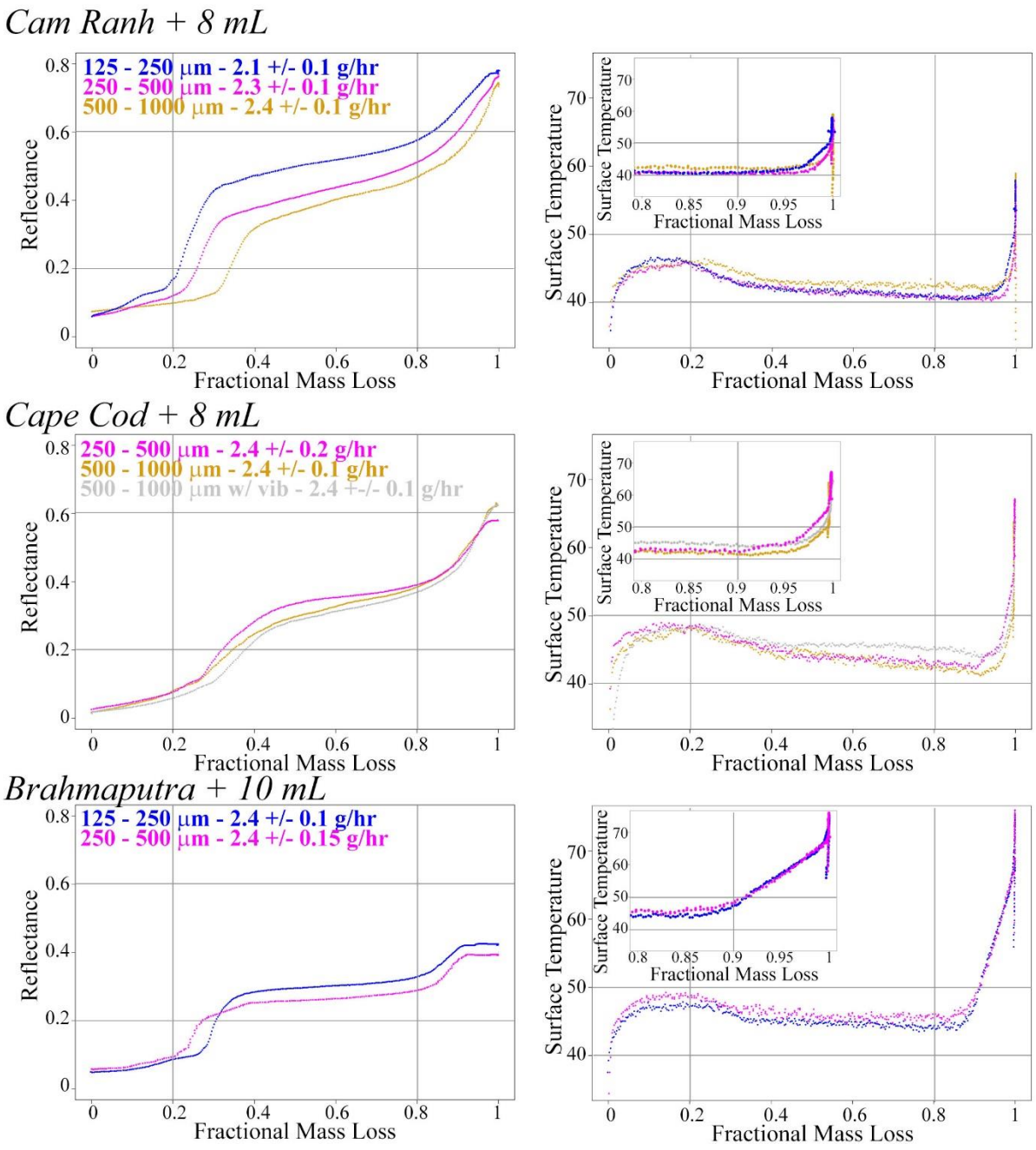

Figure 9. Grain size comparison for each material. The differences among grain sizes for each material are more subtle than the material-to-material differences, but still evident. Finer grained samples are consistently brighter than coarser grained samples. Finer grained samples have earlier T2 onset and earlier T2 termination than coarser grained samples. Deviations from this relationship exist but are minor.

The common features shown in Figure 3 are present in each time series. Substantial intra-sample variability is observed when plotted against time. The portion of the variability present in the time domain that collapses in the Fm domain is interpreted to be a function of differences in ambient atmospheric conditions and not relevant to the material properties of interest to this study. The residual intra-sample differences in reflectance and surface temperature versus Fm for each sample give interpreted to give an indication of both natural variability in packing and measurement error. Differences between materials and between grain sizes clearly exceed within-sample variability, and provide the sought-after information about the relevance of grain size and composition to the drying process. In order to more clearly identify these differences, the medians of each triplicate (or duplicate) set of samples are grouped by grain size (Figure 8) and by material (Figure 9). On these figures, experiment duration has been converted to an average mass loss rate (median +/- MAD) to account for the greater amount of water added to the BR samples than the CC or CR samples.

Reflectance differences between materials at constant grain size are evident in Figure 8. Albedo differences are clearly manifest in the overall amplitude of the reflectance trajectories. The BR samples (black) are characterized by roughly half the reflectance of the CR samples (red) for all but the earliest experimental stages. The CC sample has intermediate reflectance for most experimental stages. Differences in timing of the experimental progression are also clearly present. For instance, T1 is earliest and most abrupt in CR, latest and most gradual in CC, and intermediate in BR. On the other hand, the opposite trend is observed for T2.

Surface temperature differences are also evident among materials. These differences are particularly pronounced during T2. As expected, the low albedo BR samples are hottest, the high albedo CR samples are coolest, and the intermediate CC samples plot in between. Interestingly, a

consistent difference is also evident in the onset of T2 heating in terms of Fm. This difference is consistent across grain sizes.

Reflectance differences between grain sizes are also present (Figure 9). As expected, finer grained samples are generally brighter than coarser grained samples for each material throughout the drying progression. Two exceptions are visible. One is the BR samples at the early stage of the experiment. This may be explained due to differences in packing between the samples resulting in less pore space in the finer grained sample, causing a greater fraction of the water added to pool above the sand and extend the duration of the free surface evaporation stage. The second exception is the dry reflectance of the CC samples. This may be explained by differences among the grain size distributions of the minerals comprising the sample. This interpretation is supported by the differences in micrograph histograms between the 250-500 μm and 500-1000 μm grain size fractions of the CC sample.

Finally, surface temperature differences between grain sizes are also present, although much less pronounced than the differences between materials. The initiation of T2 is observed to occur at a slightly earlier Fm stage for finer grained materials than coarser grained materials. Interpretation of the potential causes and implications of the differences highlighted above will be discussed below.

Interpretation

Overview of the salient features of the drying trajectories

The broad consistency observed in the time series of mass loss, reflectance, and surface temperature is suggestive of potential generality in the stages introduced in Figure 3, at least for similarly conducted drying experiments of sieved sediment samples in the 125-1000 μm range of

grain sizes. However, the purpose of this study is to investigate the sensitivity of the drying process to differences in matrix properties. The fundamental questions central to this study can be addressed by an examination of the systematic covariability among samples between matrix properties and specific features of the drying trajectories.

At least three prominent features emerge from the trajectories of both reflectance and surface temperature: Transition 1 (T1), the Matrix Evaporation stage, and Transition 2 (T2). T1 is characterized by the cooling of the sample from the initial surface temperature maximum that occurs during free surface evaporation, along with a concomitant abrupt increase in 1440 nm reflectance. The Matrix Evaporation stage is characterized by gradual but consistent decrease in surface temperature and increase in 1440 nm reflectance. T2 is characterized by the heating of the sample from the surface temperature minimum that occurs at the end of the Matrix Evaporation stage, along with a second abrupt increase in 1440 nm reflectance. The timing, amplitude, and slopes of these three features covary in consistent ways from sample to sample, and may provide useful information about the fundamental questions under consideration.

Transition 1

One clear difference that emerges among samples of varying composition is the abruptness of the onset and termination of T1. For both the CR and BR samples, the increase in 1440 nm reflectance gives abrupt and unambiguous signals bounding T1. The same is not true for the CC sample, which is characterized by a gradual onset and even more gradual termination. Grain size variation is observed to result in a more modest, but still consistent effect. Finer grained samples of a given material have visibly steeper and higher amplitude T1 reflectance increases, and less prominently but consistently steeper and more abrupt surface temperature decreases. This is consistent for all three materials.

Matrix Evaporation

The slope of both reflectance and surface temperature during the Matrix Evaporation stage vary considerably among samples of variable composition. Again, the BR sample forms one endmember, with minimal slope in both the reflectance and surface temperature trajectories. The CR sample forms the other endmember in terms of reflectance, increasing by more than 0.1, but the CC sample forms the other endmember in terms of surface temperature, dropping by more than 6 ºC over this period. The duration of the Matrix Evaporation stage is controlled by the timing and slope of T1 and T2. Again, consistent but more modest impacts of grain size on this stage are also observed. Coarser grained materials have consistently steeper reflectance increases than finer grained materials. In contrast, no reliable grain size effect can be discerned from the surface temperature measurements during the Matrix Evaporation stage.

Transition 2

Surface temperature and reflectance measurements of the timing and onset of T2 show consistent relationships for a given sample, and these parameters are also observed to covary consistently among samples. Compositionally, the BR samples form one endmember, heating earliest (Fm ≈ 0.85) and also reaching terminal 1440 nm reflectance earliest (Fm ≈ 0.9). The CR samples form another endmember, heating latest (Fm ≈ 0.95) and also reaching terminal reflectance latest, near complete mass loss (Fm ≈ 1.0). The CC samples are intermediate, heating at Fm ≈ 0.9 and reaching a plateau near Fm ≈ 0.95 for the finer grained samples, but not terminating until complete mass loss for the coarser grained samples. Again, grain size-based variations are observed to be more subtle but persistent. Finer grained materials are observed to heat earlier and reach dry 1440 nm reflectance earlier than coarser grained materials of the same composition.

Discussion

The observations and interpretation described above can be used to address the fundamental questions raised in the Introduction. Each of these questions is considered in turn.

A. *How much variability exists in the drying process among sands and grain sizes, how does the magnitude of this variability compare to variability caused by fluctuations in ambient air temperature and relative humidity, and how does this variability compare between optical and thermal measurement domains?*

One parameter relevant to this question is overall experiment duration. For the CR samples, the range in experiment duration among runs of the same grain size never exceeded 0.2 hr. In contrast, the difference between median duration of the 125-250 μm and 500-1000 μm samples was 0.4 hr, and even the difference between 125-250 and 250-500 μm was 0.25 hr. For the CC and BR samples, however, within-sample variability was higher (0.2-0.5 hr in all cases), and the effect of grain size variability was lower (0.05 hr for CC and 0.2 hr for BR). Comparing across samples requires the use of mass loss rates. For the 125-250 μm samples, the BR sample clearly lost mass at a higher rate than the CR sample, as expected given the lower albedo. For the other grain sizes, the results are inconclusive, with within-sample variability meeting or exceeding between-sample variability in every case. In many (but not all) cases, intra-sample differences in experiment durations and mass loss rates are consistent with differences in ambient T and RH. As noted above, experiment duration and overall mass loss rate are the least consistent of the measurements made because of their sensitivity to ambient environmental conditions.

Observations of the salient features of the reflectance and surface temperature curves offer a stark contrast to the overall experiment duration and average mass loss rate. Material-specific variability clearly exceeds intra-sample variability in every parameter measured: the

timing, amplitude, and slope of T1; the slope of the Matrix Evaporation stage; and the timing, amplitude and slope of T2. This is true for both optical and thermal measurements.

This result can be illustrated by examining pairs of samples. Optically, one metric to use is the increase in reflectance associated with T1. Among materials, this parameter can exceed 4x the intra-sample variability. Among grain sizes, it can exceed 2x intra-sample variability.[1] Thermally, one metric to use is the Fm associated with T2 onset. While the surface temperature measurements do show more intra-sample variability than the optical measurements, variations associated with material and grain size generally exceed even this uncertainty, sometimes by as much as 5x.[2]

B. Do variations in grain size and mineralogy have impacts of comparable amplitude on the evolution of temperature and reflectance? If not, which physical parameter has a greater effect, and by how much?

The effect of composition is consistently observed to be greater than the effect of grain size. The relative magnitude of compositional effects and grain size effects is observed to be 2x-5x, depending on the parameter. Similar relative amplitudes of composition versus grain size are observed in a wide range of optical and thermal parameters. Optically, this signal is present in the amplitude of T1 brightening[3], the overall reflectance increase during the matrix evaporation

[1] See (CR vs BR 125-250 μm) and (CR 125-250 vs 500-1000 μm). Intra-sample range in amplitude of the T1 reflectance increases: < 0.05 in every case. Difference between materials: 0.2 (CR vs BR 125-250 μm). Difference between grain sizes: 0.1 (CR 125-250 vs 500-1000 μm)

[2] See (CR vs BR 125-250 μm). Intra-sample ranges in Fm associated with T2 onset: 0.02 (CR) and 0.05 (BR). Difference between materials: 0.1

[3] 2x material effect vs 0.2x grain size effect. Material effect: 0.3 vs 0.15 for CR vs BR 125-250. Grain size effect: 0.3 vs 0.25 for CR 125-250 vs 500-1000 μm

stage[4], and the Fm at which terminal reflectance is reached[5]. Thermally, the signal is observed in the amplitude of cooling during the Matrix Evaporation stage[6] and the Fm at which T2 heating begins[7].

This result suggests that the overall effect of systematic differences in packing, arrangement of pores, or other physical structure that occur as a result of grain size variations in the 125-1000 μm range on the hydrologic properties of the medium has substantially lower amplitude than the overall effect of changes in reflectance due to mineralogical composition. The closest samples in albedo (CC and CR) consistently showed greater difference than the furthest samples in grain size (125-250 vs 500-1000 μm). However, fine grained materials such as silts and clays are well known to have much longer, more complex drying trajectories. While it seems reasonable to expect the results found in this study to extend to coarser grain size fractions (e.g. very coarse sand; 1000-2000 μm), the same is not true of finer grain sizes. Ultimately, this begs questions such as: What is the functional form of the relationship tying grain size to drying trajectory? What is the lower limit on grain size before changes in the physical structure of the medium cause effects of comparable intensity to those caused by changes in albedo? And how does this limit compare to the capillary length of water?

[4] 3x material effect vs 0.5x grain size effect. Material effect: 0.03 vs 0.1 for BR vs CR 125-250. Grain size effect: 0.1 vs 0.15 for CR 125-250 vs 500-100 μm

[5] 9% material effect vs 2% grain size effect. Material effect: 0.9 vs 0.98 for BR vs CR 125-250. Grain size effect: 0.98 vs 1.0 for CR 125-250 vs 500-1000 μm

[6] Material effect 5x grain size effect. Material effect: 2 vs 7 ºC for BR vs CC 250-500 μm. Grain size effect: 2 vs 3 ºC for CR 125-250 vs 500-1000 μm.

[7] Material effect 5x grain size effect. Material effect: 0.85 vs 0.95 for BR vs CR 125-250 μm. Grain size effect: 0.97 vs 0.99 for CR 125-250 vs 500-1000 μm.

C. *To what extent do grain size and mineralogy systematically the impact timing and amplitude of specific optical and thermal transitions in the drying process?*

This question can be addressed by the relative timing of the T1 and T2 features. Fm is used instead of absolute time (hours) because it is more useful for a physical understanding of the system and is less sensitive to environmental parameters. For the 250-500 μm grain size, the time between the termination of T1 and the onset of T2 is observed to vary between materials by approximately 0.15 Fm. This time varies for the BR 125-250 and 250-500 μm samples approximately 0.03 Fm. The timing of T2 is perhaps the most diagnostic of the features, with large variations on the order of 0.15 Fm in both the onset of heating and the reaching of dry 1440 nm reflectance due to composition. These differences covaried with albedo, with the darkest sample characterized by the earliest T2, and the brightest sample characterized by the latest T2.

Possible physical processes – Albedo, composition, and grain size

In the idealized case, every sample would have constant energy input for the duration of the experiment. In reality, energy input varies with time due to fluctuations in the emission of the bulb, ambient environmental conditions, and other uncontrollable factors. In this analysis, these are considered to be higher order factors considered to contribute to experimental uncertainty and intra-sample variability. Regardless of these complexities, the vast majority of energy reaching the sample comes in the form of radiation from the halogen bulb. Some fraction of this incident radiation is absorbed by the sample, and some is reflected. The reflectance spectrum of the sample determines the fraction of shortwave incident energy that is absorbed at each wavelength. The matrix materials used in these experiments vary in reflectance by approximately a factor of 2 (Figure 2) due to differences in mineralogic composition. Differences in the fraction of incident longwave radiation absorbed (absorptivity) between samples are expected to be minor for all but the latest stages of the experiment because of the presence of water. Therefore, all else

equal, lower albedo samples can thus be expected to absorb a greater fraction of incident energy, heat to higher temperatures, and evaporate water more rapidly, than higher albedo samples. This simple physical mechanism is sufficient to explain the observed relationship between albedo and overall temperature.

Additionally, for grain sizes much greater than the wavelength of light, finer grained materials are expected to demonstrate brighter volume scattering than coarser grained materials when single-scattering albedo is derived from first principles (if all else is equal) (Hapke, 2012). This explanation is sufficient to explain the observation that finer size fractions of a given material are generally more reflective than coarser size fractions throughout the course of the experiments. Two primary exceptions are present in the data. One exception is due to the T1 brightening of the 250-500 μm BR sample occurring earlier (i.e. at lower fractional mass loss) than the T1 brightening of the 125-250 μm BR sample. While the coarser of the two samples is temporarily brighter than the finer, it reaches a darker steady state for the remainder of the experiment and so does not violate the physical explanation. The other exception is the 500-1000 μm CC sample reaching a greater final brightness than the 250-500 μm CC sample. The observations that that 1) this occurs in the dry sample, 2) the difference between the fine and coarse samples varies throughout the experiment, and 3) the difference has a small amplitude relative to the other grain size and compositional differences suggests that this may be due to minor compositional heterogeneity between the two size fractions of the same material, especially given that small absorptive impurities can produce outsize effects of aggregate reflectance (Hapke, 2012). This highlights the reality that grain size and composition are unlikely to vary independently in many real-world geophysical systems, adding further emphasis to the

outsized impact of composition relative to grain size on the drying process as observed by these sensors.

Possible physical processes – Surface roughness

Considerable variation is observed among samples in the shape of T1. One potential explanation for this observed variability can be phrased as a hypothesis: *1) Irregularities in the sample surface prolong T1 by broadening the effective vertical thickness of the surface layer of grains*. If Hypothesis 1 were true, a hypothetical, perfectly flat sediment surface would be expected to have a maximally sharp T1 and a highly irregular sediment surface would be expected to have a maximally gradual, ambiguous T1. Hypothesis 1 is consistent with the observation that the vibrated 500-1000 μm CC samples have a (slightly) less ambiguous T1 than the unvibrated 500-1000 μm CC samples. To test Hypothesis 1, the spatial arrangement of grains within the skin layer could be systematically varied at the beginning of the experiment.

Possible physical processes – Skin layer thickness

Reflectance and surface temperature are derived from measurements of the amount of optical and thermal radiance upwelling from the sample, respectively. For this reason, both are indicators of physical conditions in the optical and thermal skin layers (and not the full sample volume), as described above. In contrast to reflectance and surface temperature, however, the mass balance measures a property of the entire volume of the sample. Material-specific relationships between mass and surface temperature or reflectance may thus provide potentially useful information about geophysical sediment properties such as depth of penetration of light and permeability of water through the optical and thermal skin layers.

The observation that the 1440 nm reflectance stops changing before mass loss is complete suggests that the optical skin layer observed by the spectrometer does not encompass the full volume of the sample. This inference is consistent with the observed lack of difference in reflectance between samples placed on dark versus bright backgrounds. If true, this suggests a second hypothesis: *2) The sands are able to support a vertical moisture gradient sufficiently steep to allow for the drying of the optical skin layer before the deepest water evaporates.* The thickness of the optical skin layer could be tested by differencing reflectance spectra of samples with systematically varying thickness lying above reflective and absorptive backgrounds. The vertical gradient could be tested using small sensors able to measure a moisture profile on the scale of the sample.

Hypothesis 2 is consistent with the observed variations in T2 with grain size. Finer grained samples consistently reach their maximum 1440 nm reflectance at lower fractional mass loss than coarser grained samples. In the context of Hypothesis 2, this suggests two further hypotheses: *3) the optical skin layer is thinner for the finer grained samples than the coarser grained samples*, and *4) differences in pore size distribution result in vertical differences in water distribution with grain size as a result of capillarity effects*. If hypothesis 3) were true, this would suggest that coarser grained sands would be sensitive to deeper moisture than finer grained sands because their lower density of scattering interfaces would allow deeper penetration of light into the medium. If hypothesis 4) were true, this would suggest that water (relatively) deep in the sediment column would be held longer in finer grained materials than coarser grained materials. The same variable thickness experiments and small sensors described above could test hypotheses 3 and 4, respectively.

Hypotheses 2, 3 and 4 all suggest that the Fm of T2 termination could be a particularly informative parameter. Hypothesis 2 predicts that this parameter would vary with 2 properties of the sample: thickness of the optical skin layer and slope of the vertical moisture gradient. If true, these hypotheses suggest the following inference: If the skin depth were determined using the method described above, then the slope of the moisture gradient would be the only remaining parameter. Once characterized for a wide range of natural samples, this could provide a potentially valuable constraint on hydrologic parameters of the medium such as vertical hydraulic conductivity and capillary strength – using only remotely sensed observations.

In addition, the surface temperature increase associated with T2 termination suggests a final hypothesis: *5) T2 termination represents the drying of the thermal skin layer*. The time lag between the temperature and reflectance increases of T2 might then be leveraged to give an indication of the difference in optical and thermal skin depths. In combination with the approach outlined above, exploration of this hypothesis may also be an additional avenue for future work. Once the optical skin depth was determined by the sequential thickness experiments described above, the thermal skin depth could be constrained using the time lag between optical and thermal. This set of observations could potentially be used to answer a host of questions with potentially significant implications for landscape-scale surface energy balance of such as: *Does shallow subsurface water contribute more to the skin temperature and reflectance of coarser sands than finer sands? Can the degree of covariability between SWIR and thermal observations be used to infer physical properties of sediments and soils from satellite images of drying landscapes acquired days apart? Under what range of conditions can dry optical spectra be used to predict hot (dry) surface temperatures?* This third question has particularly significant

implications for the combined use of optical + thermal satellite observations (e.g. Landsat) with data from optical-only sensors (e.g. Sentinel-2)

Contribution to the existing body of knowledge

The monotonic progression in reflectance observed in this experiment is generally consistent with the findings of previous optical laboratory drying experiments. The progression of reflectance spectra observed in this work bears obvious similarity to the previous experimental results of drying sands found by (Small et al., 2009; Tian and Philpot, 2015c; Zhang and Voss, 2006). The primary way that the experiments presented here extend previous work in the optical domain is by the addition of coincident measurements of surface temperature. The surface temperature informs the reflectance measurements by providing contextual information about skin layer thickness and energy balance.

Much of the previous work in the thermal domain has focused on variations in thermal conductivity (Smits et al., 2013, 2010) and fluid flow through the porous medium involving long (>1 m) columns (Smits et al., 2012, 2011, 2010). The experiments presented here cannot approach the level of laboratory control and complexity achieved in this robust body of work, and cannot address the factors of heat flow and vertical temperature profile through the sample. However, detailed borehole measurements are also unavailable for the vast majority of spaceborne, airborne, and field-based remote sensing applications. The radiometric measurement of surface temperature is much more common. Laboratory focus on this measurement has the potential to leverage the coincident, spatially explicit measurements of surface temperature and reflectance which are available globally for over 35 years.

Conclusions

This chapter presents the results of laboratory experiments documenting the simultaneous optical and thermal evolution of drying porous media. Sands with three distinct compositions were sieved into fine, medium, and coarse sand size grades; saturated; and allowed to dry under strong illumination comparable to solar intensity. The drying process was monitored with time series measurements of mass, reflectance, and surface temperature. Ambient environmental conditions were also monitored, and each sample was observed in triplicate in order to quantify intra-sample variability for each variable. More variability was present in surface temperature than reflectance, but systematic variations were observed among compositions and grain sizes that exceeded the intra-sample variability for both measurements. Two clear transitions were identified in the drying process, for which differences in the associated reflectance increase, timing, and temperature change were identified as consistent properties of specific grain size-composition pairs. Composition was consistently found to produce greater variability than grain size by a factor of 2-5x, suggesting that, for the drying of sands, differences in heating caused by differences in reflectance may dominate hydrologic differences caused by grain size variation, at least in the 125-1000 μm range. Hypotheses, along with possible means of testing, were developed regarding the potential connection between these transitions and the arrangement of grains within the optical skin layer (roughness), as well as the relative thickness of the optical and thermal skin layers. If supported, these hypotheses could potentially lead to the development of a novel metric to remotely estimate a physically meaningful property of drying porous media. The experimental results presented in this chapter are directly relevant to geophysical applications requiring spaceborne optical and thermal image data, and thus to the thesis chapters which follow.

2. Multisensor Analysis of Spectral Dimensionality and Soil Diversity in the Great Central Valley of California

Abstract

Planned hyperspectral satellite missions and the decreased revisit time of multispectral imaging offer the potential for data fusion to leverage both the spectral resolution of hyperspectral sensors and the temporal resolution of multispectral constellations. Hyperspectral imagery can also be used to better understand fundamental properties of multispectral data. In this analysis, we use five flight lines from the Airborne Visible/Infrared Imaging Spectrometer (AVIRIS) archive with coincident Landsat 8 acquisitions over a spectrally diverse region of California to address the following questions: (1) How much of the spectral dimensionality of hyperspectral data is captured in multispectral data?; (2) Is the characteristic pyramidal structure of the multispectral feature space also present in the low order dimensions of the hyperspectral feature space at comparable spatial scales?; (3) How much variability in rock and soil substrate endmembers (EMs) present in hyperspectral data is captured by multispectral sensors? We find nearly identical partitions of variance, low-order feature space topologies, and EM spectra for hyperspectral and multispectral image composites. The resulting feature spaces and EMs are also very similar to those from previous global multispectral analyses, implying that the fundamental structure of the global feature space is present in our relatively small spatial subset of California. Finally, we find that the multispectral dataset well represents the substrate EM variability present in the study area – despite its inability to resolve narrow band absorptions. We observe a tentative but consistent physical relationship between the gradation of substrate reflectance in the feature space and the gradation of sand versus clay content in the soil classification system.

Introduction

The availability of hyperspectral data for scientific purposes is rapidly increasing. The recent opening of the AVIRIS (Green et al., 1998) and HICO (Lucke et al., 2011) data archives offers scientists a wealth of high quality observations. Planned satellite missions such as HyspIRI (Lee et al., 2015), EnMAP (Stuffler et al., 2007), and HYPXIM (Michel et al., 2011) promise to offer even greater spatial and temporal coverage of narrowband imaging observations in the coming years.

These newly available and planned hyperspectral datasets complement the existing wealth of public multispectral satellite observations. The Landsat archive offers over 35 years of rigorously intercalibrated multispectral data (Wulder et al., 2016). The recent and planned launches of the Sentinel satellite constellation promise to add considerably to this collection (Drusch et al., 2012), substantially decreasing the revisit time between subsequent multispectral observations (Li et al., 2017).

The future availability of systematic global archives of both hyperspectral and short revisit time multispectral observations is expected to offer significant potential for studies that leverage both the spectral resolution of hyperspectral sensors and the temporal resolution of multispectral sensors. A growing number of data fusion techniques attempt to explicitly merge hyperspectral and multispectral data (e.g., (Wei et al., 2015; Zhou et al., 2017)). More generally, hyperspectral imagery can be used to better understand fundamental properties of multispectral data. Regardless of the specific application, any combined use of hyperspectral and multispectral data will benefit from a better understanding of a fundamental question: How much of the spectral dimensionality of hyperspectral data is captured in multispectral data?

As first recognized by the pioneering work of (Kauth and Thomas, 1976), multispectral observations generally form a three-dimensional pyramidal feature space. Subsequent global analyses of Landsat (Small, 2004; Small and Milesi, 2013; Sousa and Small, 2017a) confirm this finding on spatially extensive, spectrally diverse sets of data and show that these spaces generally contain >97% of their variance in the first three dimensions. Consistent global endmembers (EMs) can be identified from the apexes of the space representing soil and rock substrates, photosynthetic vegetation, and dark targets such as shadow and water. However, most analyses are regional and sample only a small fraction of the diversity of land covers present on the surface of the Earth. Another fundamental question is thus: Is the characteristic pyramidal structure of the multispectral feature space also present in the low order dimensions of the hyperspectral feature space at comparable spatial scales?

Finally, the majority of the EM variability observed in global multispectral analyses is in the substrate EM (Crist and Cicone, 1984; Kauth and Thomas, 1976; Small, 2004). This is due to the wide range of soil and rock compositions that cover the land surface of the earth. It is likely that the global availability of hyperspectral imagery will add additional constraints to the properties of multispectral substrate EMs. A third fundamental question is thus: How much of the variability in Substrate EMs present in hyperspectral data is captured by multispectral sensors?

In this analysis, we use coincident AVIRIS and Landsat 8 acquisitions to address these three fundamental questions. We find the nearly identical partition of variance, low order feature space topology, and EM spectra for the hyperspectral and multispectral cases. The resulting feature spaces and EMs are also very similar to those found in previous global multispectral analyses, implying that the relatively simple pyramidal structure of the broadband feature space

also represents the low order dimensions of the hyperspectral feature space. Finally, we find that the multispectral dataset well represents the basic structure of the plane of substrates found in the hyperspectral data, despite the fact that AVIRIS resolves a wide range of absorptions indistinguishable to Landsat OLI. Our results also suggest a novel, potentially useful method for mapping sand versus clay soil composition–from both hyperspectral and multispectral observations–on the basis of the location of soil EMs on the plane of substrates.

Background

We provide a background for each of the three central questions of the paper in order:

Measuring Spectral Variability

A reflectance spectrum is a characteristic of a material. Reflectance is the continuous, wavelength dependent function which describes the fraction of incident light which is reflected in a given direction. One profitable way of conceptualizing a Visible to Shortwave Infrared (VSWIR) reflectance spectrum is as a composite of two signals: the continuum and the absorptions (Gillespie et al., 1990). Hyperspectral imagers generally oversample the reflectance spectrum, allowing for the analysis of both continuum and absorptions. Broadband instruments undersample the spectrum unevenly, often blurring together the continuum with the absorptions.

One way of quantifying the variability of reflectance (or radiance) vector sets is through their covariance matrix. For an image with n spectral bands, the spatial variance and covariance of each pair of bands forms an n square positive semi-definite matrix with n eigenvectors, representing uncorrelated modes of spectral variability, and n eigenvalues, representing the fraction of total variance described by each eigenvector and its corresponding spatial Principal Component, or PC.

Because of spatial and spectral redundancy in large numbers of reflectance measurements, the actual dimensionality of the spectral feature space may be less than the number of spectral dimensions provided by the sensor. The uncorrelated modes of spectral variability given by the eigenstructure of the covariance matrix generally contribute unequally to the total variance of the data. As a result, the most important modes (i.e. those contributing the most variance) can be used to represent the underlying structure of the spectral feature space. This provides an optimal representation of the diversity and interrelationships (e.g. mixing) of the most disparate spectral patterns in the data. In this context, spectral dimensionality refers to the distinction between the most informative dimensions, describing the physically meaningful structure of the spectral feature space, and the remaining dimensions that describe stochastic variance like sensor noise, atmospheric effects (or correction artifacts), and natural spectral variability with a less straightforward physical meaning than that represented by the lower dimensions.

This technique has been used to estimate the information content of hyperspectral imagery (Asner et al., 2012; Boardman and Green, 2000; Price, 1975; Thompson et al., 2017), as well as to describe the information loss when reflectance spectra are undersampled by multispectral imagers (Price, 1997, 1994). Eigenvalues have also been used to directly quantify the dimensionality of multispectral data without reference to hyperspectral imagery (Crist and Cicone, 1984). Finally, the approach has also been used in the spatiotemporal analysis of image time series (Piwowar et al., 1998; Small, 2012; Townshend et al., 1985).

The key assumption behind the use of this approach to estimate data dimensionality is that variance directly corresponds to information. As noted by (Boardman and Green, 2000), this is a key limitation for its use with hyperspectral data because the location and depth of specific

absorptions provide substantial information in a small amount of overall variance. Despite this limitation, we use this method in our analysis because it is a reliable, well-understood tool with both precedent and broad applicability. The purpose of this work is to present a comparative analysis of the characteristics of coincident hyperspectral and multispectral observations of a wide range of diverse land covers.

Spectral Variability and the Spatial Dimension

Image dimensionality is an attempt to measure the spectral diversity captured by a dataset. However, the spectral diversity of the Earth surface is spatially heterogeneous. The local variations that can exist in Earth surface reflectance, as well as the dimensionality of a large, diverse set of hyperspectral data, are well illustrated by the recent study of (Thompson et al., 2017).

One might expect imagery with a higher spatial resolution to resolve more spectral diversity because of fewer mixed pixels. While this is generally true, the increase in spectral diversity (and dimensionality) with spatial resolution depends on the characteristic spatial scale of the reflectance of the landscape relative to the resolution of the sensor. This dependence of dimensionality on spatial resolution and SNR has long been recognized (Green and Boardman, 2000; Price, 1997; C. Small, 2001; Woodcock and Strahler, 1987). While it is not the focus of this study, it is noteworthy that the AVIRIS data we use have roughly half the Full Width at Half Maximum (and thus four times the spatial resolution) of the Landsat data.

All else equal, more spatially extensive image domains might also be expected to include a wider range of reflectance spectra and so have higher dimensionality -- up to a point. As with spatial resolution, the dependence of spectral diversity on domain size depends on the

characteristic spatial scale of the landscape reflectance. However, if the spectral diversity within an area approaches the global spectral diversity of the Earth, imaging a larger area should not add additional dimensionality.

The total area of land surface required to approach the level of global spectral diversity is clearly location dependent. However, the relationship between spatial resolution, extent of spatial domain, and the characteristic spatial scale of Earth's spectral diversity is important because it determines which combination of extent and resolution may provide the most informative depiction of the spectral feature space as imaged by the sensor. This is important because the spectral feature space provides a physically-based depiction of the properties of a landscape that a given sensor is able to distinguish.

Part of the answer to this question lies in the overall global spectral diversity of the Earth. Previous work has attempted to address this. A global analysis of total Earth radiance as measured by the hyperspectral Scanning Imaging Absorption Spectrometer for Atmospheric Cartography (SCIAMACHY) was conducted by (Roberts et al., 2011), finding 99.5% of variance explained in six dimensions. However, the spatial resolution of ~30 km attenuates much of the spectral variability of interest by spectral mixing. Due to the current absence of systematic global hyperspectral imagery of the land surface, no analog exists to these studies. The largest area study of Earth surface hyperspectral imagery to date was performed by (Thompson et al., 2017). This study used 15 m resolution AVIRIS imagery of a wide range of land cover types in California and estimated the overall spectral dimensionality at 50 dimensions. The broadband spectral dimensionality of a wide range of environments has been characterized for six-band multispectral Landsat imagery (Small, 2004; Small and Milesi, 2013). Because Landsat resolves only the spectral continuum, it can represent 99% of its spectral variability in only three

dimensions. The structural similarities of the low order feature spaces in Boardman and Green's 2000 analysis of 510 AVIRIS scenes and Small's 2004 analysis of 100,000,000 Landsat spectra suggest that multispectral and hyperspectral feature spaces may share a common structure, despite the vastly greater information content of hyperspectral data. The analysis of 2.5 × 109 AVIRIS spectra by Thompson et al. suggests that the spectral diversity observable within California can represent all of the canonical land cover types included in the global MODIS land cover classification. In the present study, we use near coincident acquisitions of AVIRIS and Landsat 8 OLI to compare the spectral feature spaces and EMs in a pedologically diverse range of environments in the Great Central Valley of California.

Spectral Variability of the Plane of Substrates

Linear mixture models (Adams et al., 1986; Gillespie et al., 1990; Smith et al., 1985) are a common way to represent multispectral and hyperspectral data as linear combinations of spectral EMs. The three most common endmembers used for these models are soil and rock substrates, green vegetation, and dark or unilluminated materials (e.g., (Roberts et al., 1993)). Non-photosynthetic vegetation is also commonly added as a fourth EM.

Of these EMs, the majority of the multispectral variability on a global scale is observed in the substrate (Crist and Cicone, 1984; Small, 2004). This is due to the wide range of physical, chemical, biological, and textural properties present in soil, sediment, and rock. Reflectance spectroscopy of substrates is complex. Substrate reflectance spectra can vary in at least three ways: in continuum shape, in broad absorptions (e.g., Fe), and in narrow absorptions (e.g., some clays). Broadband imagery can only be expected to capture the coarsest of these features. For a comprehensive treatment of soil reflectance (a complex subset of the plane of substrates), see the

seminal work of (Baumgardner et al., 1986), more recent analyses by (Palacios-Orueta and Ustin, 1998, 1996), and reviews by (Ben-Dor et al., 2009; Wulf et al., 2014).

Early work on the hyperspectral dimensionality of the plane of substrates focused on full range Visible to SWIR (VSWIR) laboratory spectra (J. Price, 1990) and Visible to NIR (VNIR) field spectra of soils. Further laboratory VNIR characterization of a wide range of soils was performed by (Brown et al., 2006), although the dimensionality of the dataset was not discussed. The question of how the full diversity of hyperspectral VSWIR substrates (including soil, rock, and sediment) are represented in the spectral feature space, as well as how the signal is degraded when undersampled by a multispectral imager, remains open. The present study addresses this question by directly comparing substrate spectra from simultaneously acquired VSWIR hyperspectral and multispectral data, as well as by presenting a parallel analysis of 161 soil and rock laboratory spectra.

Portions of these three questions have been investigated previously. The questions of data dimensionality and generality of the feature space have been addressed independently for hyperspectral and multispectral datasets, but not simultaneously for both. Variability of the plane of substrates has been studied by the analysis of libraries of laboratory and field spectra. However, to our knowledge, none of these three questions have been addressed using simultaneous, independently imaged multispectral and hyperspectral observations over large areas of a spectrally diverse landscape.

Materials and Methods

Figure 10 shows the study area for this analysis in northern and central California, USA. This region was chosen because of the confluence of data availability from the recently opened

AVIRIS hyperspectral image archive (https://aviris.jpl.nasa.gov/alt_locator/) and high-quality soil maps maintained by the UC Davis California Soil Resource Lab (https://casoilresource.lawr.ucdavis.edu/). The study area spans an unusually wide range of soil orders, textures, and chemical properties. A diversity of soil provenances is also present as a result of the geologic diversity of the region. Six of the nine soil orders in California are sampled in this study.

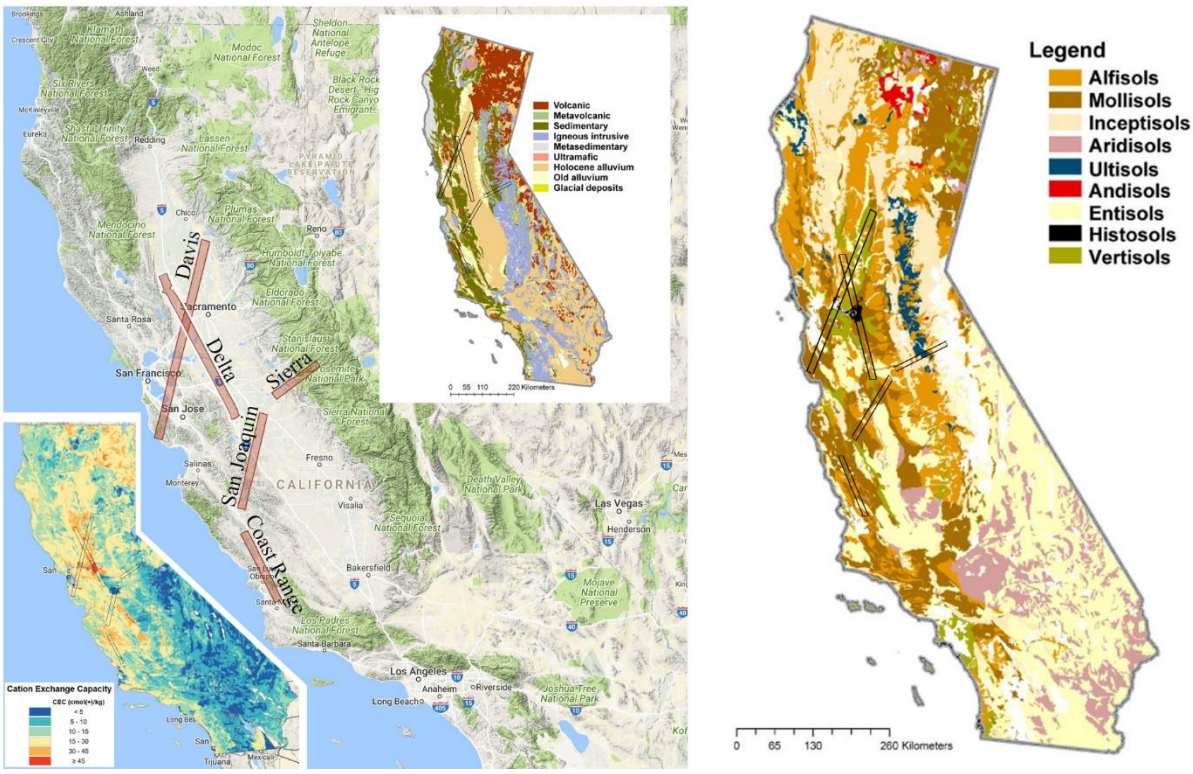

Figure 10. Northern California AVIRIS flight lines used in this analysis. Five lines were selected from the AVIRIS classic data archive on the basis of pedologic and agricultural diversity. Landsat 8 acquisitions were collected on the same day as each of the five flight lines. Simplified maps showing soil orders (right), as well as lithologic provenance (inset, upper right), and cation exchange capacity (inset, lower left) illustrates the complexity of soil properties in the study area. Six of the nine soil orders are represented in these flight lines. Soil maps from the UC

Davis California Soil Resource Lab (https://casoilresource.lawr.ucdavis.edu/). Map data © 2017 Google INEGI

Five AVIRIS flight lines were selected for use in this analysis on the basis of pedologic and spectral diversity (Figure 11). Critically, all five flight lines were acquired on the same day as coincident Landsat 8 acquisitions, allowing for a direct comparison of the effect of spectral resolution on dimensionality, as well as the opportunity for a direct comparison of AVIRIS and Landsat standard surface reflectance products. A diversity of agricultural and natural vegetation, settlements, bare soils, and water is present in the dataset. Some geological diversity is present in crystalline basement and sedimentary rock outcrops within the Sierra and Coast Range flight lines. Wetlands are present in the San Francisco Bay-Delta, as well as the San Joaquin River National Wildlife Refuge.

All AVIRIS images were downloaded as Level 2 Atmospherically Corrected Reflectance from the AVIRIS Data Portal at https://aviris.jpl.nasa.gov/alt_locator. Coincident Landsat 8 LaSRC modeled surface reflectance products were downloaded from the USGS at https://earthexplorer.usgs.gov.

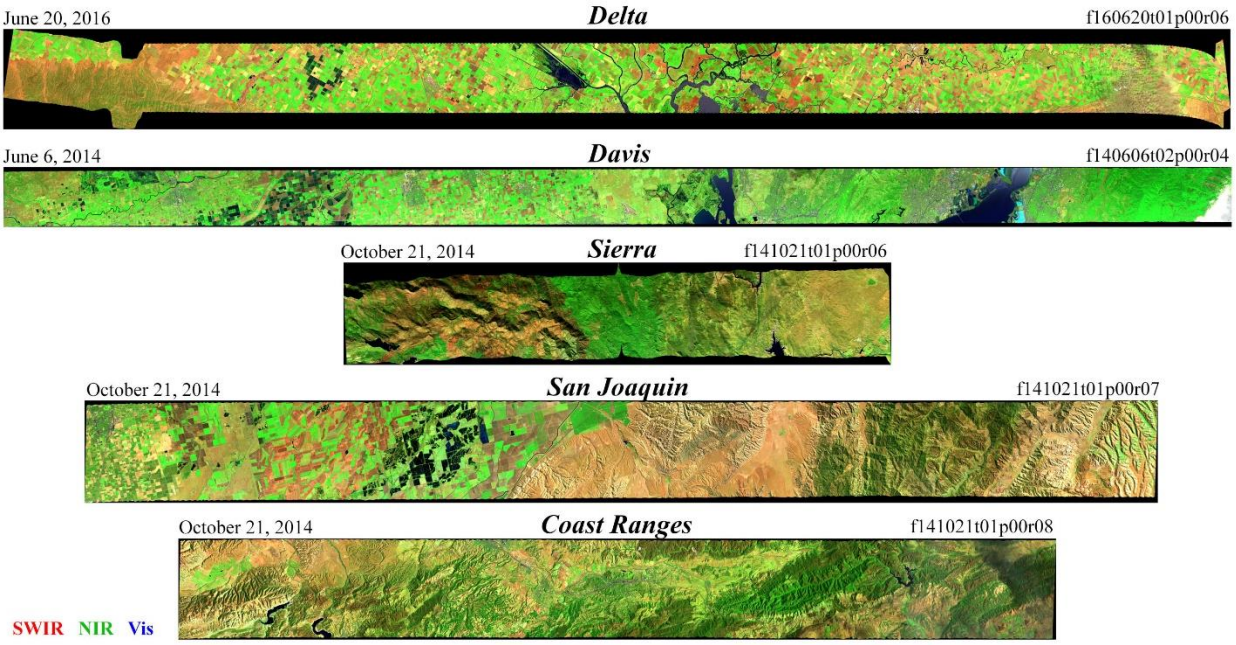

Figure 11. False color composite images of the five AVIRIS flight lines used in this study. A wide range of agriculture in the Great Central Valley of California is sampled in both summer and fall. Bare rock substrates are present in the Sierra and Coast Ranges. Non-photosynthetic vegetation (NPV) is present in both agricultural and natural land cover regimes. Cloud contamination near the ends of the Delta, Davis, and Coast Ranges lines was excluded from the remainder of the analysis. Wetlands are sampled in the Delta line and the San Joaquin line. Spectrally complex salt ponds are present in the South Bay portion of the Davis line. Sun glint is present in some water bodies.

Figure 12 shows a comparison of sensor resolutions for Landsat 8 OLI and AVIRIS, as well as the older Landsat 7 ETM+ and newer Sentinel 2 MSI sensors. The AVIRIS sensor images the Earth in 224 channels over the full VSWIR 365 to 2500 nm spectral range at a 10 nm spectral resolution. In comparison, multispectral sensors such as Landsat and Sentinel 2 collect a much smaller number of spectral bands with much wider bandpasses. As of the date of publication of (Green et al., 1998), the signal-to-noise ratio (SNR) of AVIRIS was approximately

1000 for the VNIR, 700 for SWIR1, and 250 for SWIR2. In contrast, the Landsat 8 OLI SNR ranges between 201 and 367 for the bands used in this study (Morfitt et al., 2015). AVIRIS oversamples most features in the reflectance spectrum and is therefore also able to resolve physical parameters about spectral slope and narrow band absorptions which are averaged together by OLI.

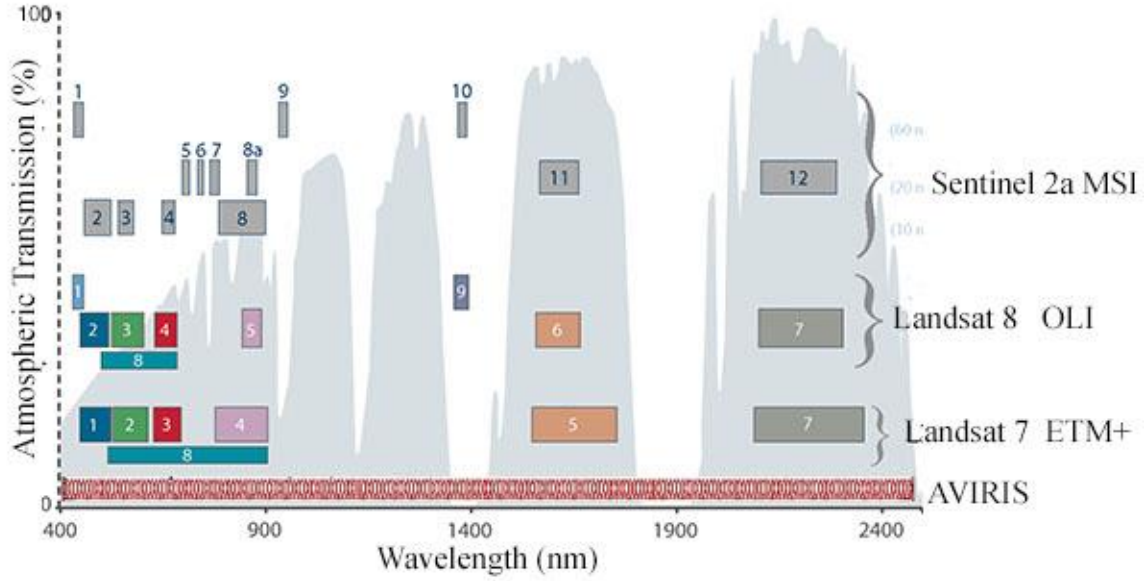

Figure 12. Spectral band comparison for Landsat 7/8, Sentinel 2, and AVIRIS. The AVIRIS hyperspectral sensor has 224 bands with 10 nm FWHM in the 365 to 2500 nm range. Spatial resolution of the AVIRIS IFOV depends on flight altitude. Modified from https://landsat.gsfc.nasa.gov.

The five AVIRIS flight lines were subdivided into seven spatial subsets of 5000 × 700 pixels each. Coincident multispectral Landsat images were coregistered to match the hyperspectral subsets using nearest neighbor spectral resampling. All individual AVIRIS pixels were preserved without pixel averaging or interpolation. Because the spatial resolution of the

AVIRIS data used in this study is somewhat higher (15 m to 17 m) than the 30 m resolution of Landsat 8, no direct pixel-to-pixel comparisons are attempted. Fortunately, the spatial scale of the land cover features of interest is generally coarse enough to allow a comparison of multipixel means of homogenous targets. The total areal coverage of the seven spatial subsets is approximately 9800 km2.

Bad and no data pixels present in either dataset were flagged and removed from the analysis. AVIRIS channels 108–133 (1363 to 1423 nm), 154–167 (1827 to 1927 nm), and 223–224 (2480 to 2500 nm) were excluded from subsequent analysis because of a large number of pixels with nonphysical reflectance values (i.e., high amplitude positive and negative spikes). Landsat 8 OLI coastal aerosol and cirrus bands (1 and 9) were excluded from this analysis because land cover is the focus of this study. The Landsat 8 panchromatic band was not used.

Image statistics were then computed for the remaining 181 channels of the AVIRIS image and PC rotations of all the AVIRIS spectra were computed based on both the image covariance and correlation matrices. Eigenvalues were normalized by their sum to compute the fraction of variance present in each dimension. The same procedure was repeated for the six band Landsat 8 pixels. A Maximum Noise Fraction (MNF) transform (Green et al., 1988) was also used for comparison, but yielded similar EMs to the PC-derived feature space.

For comparison with pure substrate EMs, 161 laboratory spectra of rocks and soils from the Johns Hopkins University (JHU) spectral library were used for a PC analysis, as described above. For more details on the JHU spectral library, see: https://speclib.jpl.nasa.gov/documents/jhu_desc.

Results

Figure 13 shows the low order partition of variance for each of the 5000 × 700 pixel AVIRIS subsets (light gray), as well as the full 5000 × 4900 pixel image composite (black). While some variability is observed in the partition of variance for individual spatial subsets of both the AVIRIS and Landsat datasets, the first three or four dimensions clearly contain nearly all of the variance in all cases. Cumulative variance for the first three dimensions of the AVIRIS and Landsat composite images is 97% and 99%, respectively. As expected, inset correlation matrices illustrate three or four relatively distinct spectral regimes (Visible, NIR, SWIR1, and SWIR2). A more complex correlation structure is evident within the AVIRIS NIR spectral regime, illustrating the added value of the hyperspectral sensor.

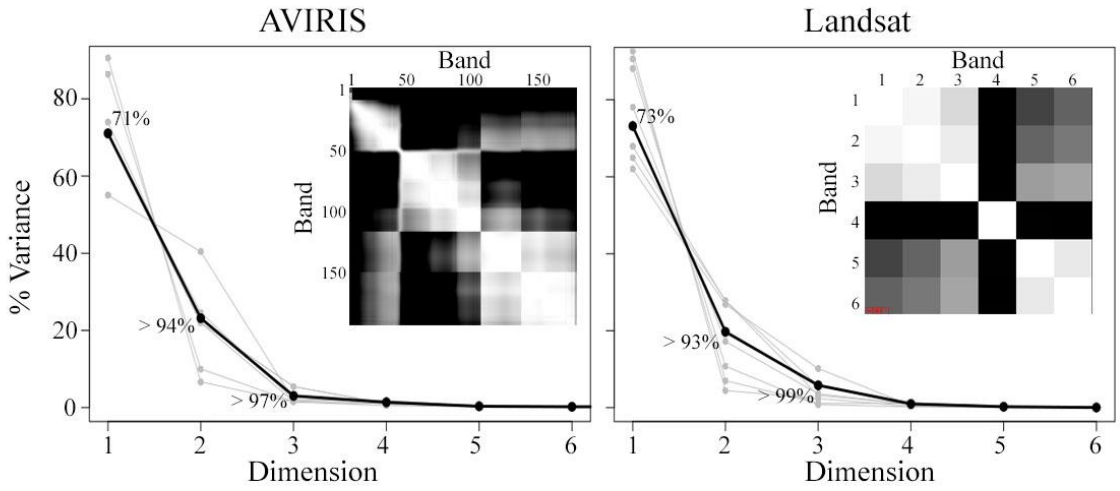

Figure 13. Partition of variance for AVIRIS (left) and Landsat (right). Result are shown for each 5000 × 700 pixel spatial subset (gray), as well as for the combined dataset (black). While the dimensionality of each spatial subset is variable, the combined dataset shows the first three dimensions clearly separated from the continuum that follows. Cumulative variance is labeled for the first three dimensions, showing that 97% or more of the total variance in contained in the

first three dimensions of each dataset. Correlation matrices (inset) clearly show three or four distinct spectral regimes which capture the majority of the variance in the dataset.

Figure 14 shows projections of the first three dimensions of the spectral feature spaces for the AVIRIS and Landsat datasets of this study (top) in comparison to the much more extensive spatial sampling of previous studies by (Small, 2004; Small and Milesi, 2013; Sousa and Small, 2017a). The first three dimensions of the AVIRIS and Landsat feature spaces show striking similarity to each other, despite the roughly 30x greater spectral sampling of the AVIRIS. Both covariance- and correlation-based transforms were performed. Because the resulting feature spaces were nearly identical, only the feature space from the covariance-based transform is shown here.

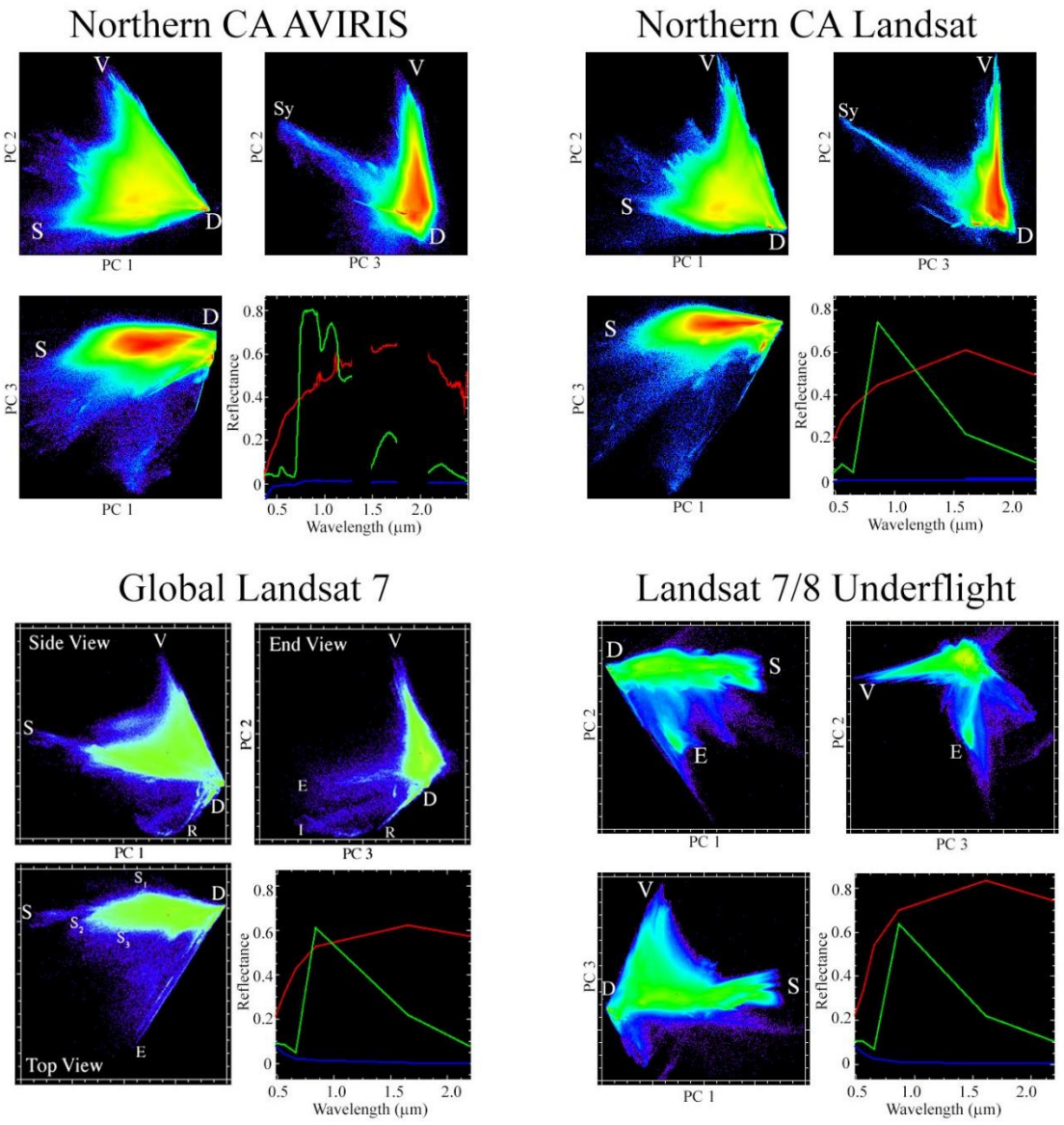

Figure 14. Low dimensional feature space comparison. Northern CA AVIRIS and Landsat used in this study both show similar low-order feature space topology to the much wider range of land covers sampled in the global Landsat 7 analysis of Small & Milesi (2013), as well as the Landsat 7/8 underflight comparison analysis of Sousa & Small (2017). Substrate (S), Vegetation (V), and Dark (D) EMs are also broadly consistent across all four studies, in spite of the substantial disparities in both spectral resolution and spatial extent. Differences in topology are predominantly due to variations in sampling of relatively rare land covers such as evaporites (E)

and synthetic materials (Sy). Substrate EMs show the greatest variability, as expected given the diversity in the shape of the reflectance continuum of rock and soil.

In addition, both of the feature spaces of this study are remarkably similar to the global Landsat feature spaces. This observation is especially noteworthy given the differences between the studies in data preprocessing. Substrate, Vegetation, and Dark EM spectra show comparable spectral shapes despite the relatively minimal sampling of crystalline basement or large scale sedimentary deposits.

The most prominent differences between the feature spaces of this study and previous studies involve the sampling of evaporites and synthetic materials. This study does not sample any large deposits of evaporitic minerals such as Halite or Gypsum. These minerals are spectrally distinct from other soil and rock substrates and they plot separately from the main point cloud that represents the vast majority of land surface reflectance spectra. This study does, however, contain a relatively large fractional area of settlements with synthetic roofs and tarped fields. These relatively exotic spectra do not have appreciable global abundance and so are not present in the previous studies focusing on terrestrial targets.

Multispectral green vegetation and dark EMs are generalizable globally with spectral shapes consistent with physical and biological properties. However, as has been noted in numerous previous studies (e.g., (Boardman and Green, 2000; Gillespie et al., 1990; Price, 1975)), rock, sediment, and soil substrates demonstrate a diversity of spectral shapes. Local substrate EMs are generally used for more accurate spectral unmixing results because they can take into account this regional pedologic and geologic diversity. These EMs can be selected directly from the spectral feature space.

For comparison with pure substrate EMs spanning a wider range of rocks and soils than that found in the study area, we rendered a spectral feature space from laboratory spectra of rock and soil samples. Using the Johns Hopkins University (JHU) spectral library, we compiled 161 laboratory rock and soil reflectance spectra. The spectra span a wide range of soil and rock types, including 67 igneous rocks, 55 metamorphic rocks, 14 sedimentary rocks, and 25 soils.

PCA of the JHU substrate spectra reveals the first three dimensions account for 85.8%, 10.5%, and 2.2%, respectively. The first three dimensions thus account for over 96% of the overall variance of this diverse library of substrate spectra. The spectral feature space in Figure 15 shows that the 25 soils cluster in a relatively confined subset of this substrate space. The soil spectra are observed to deviate from each other in much less pronounced ways than rocks vary both within and between the igneous, metamorphic, and sedimentary classes. Given the dominance of agricultural land cover in our study area, it is this relatively narrow range of soil spectra which we would expect to dominate as the substrate EM in our Landsat-AVIRIS analysis.

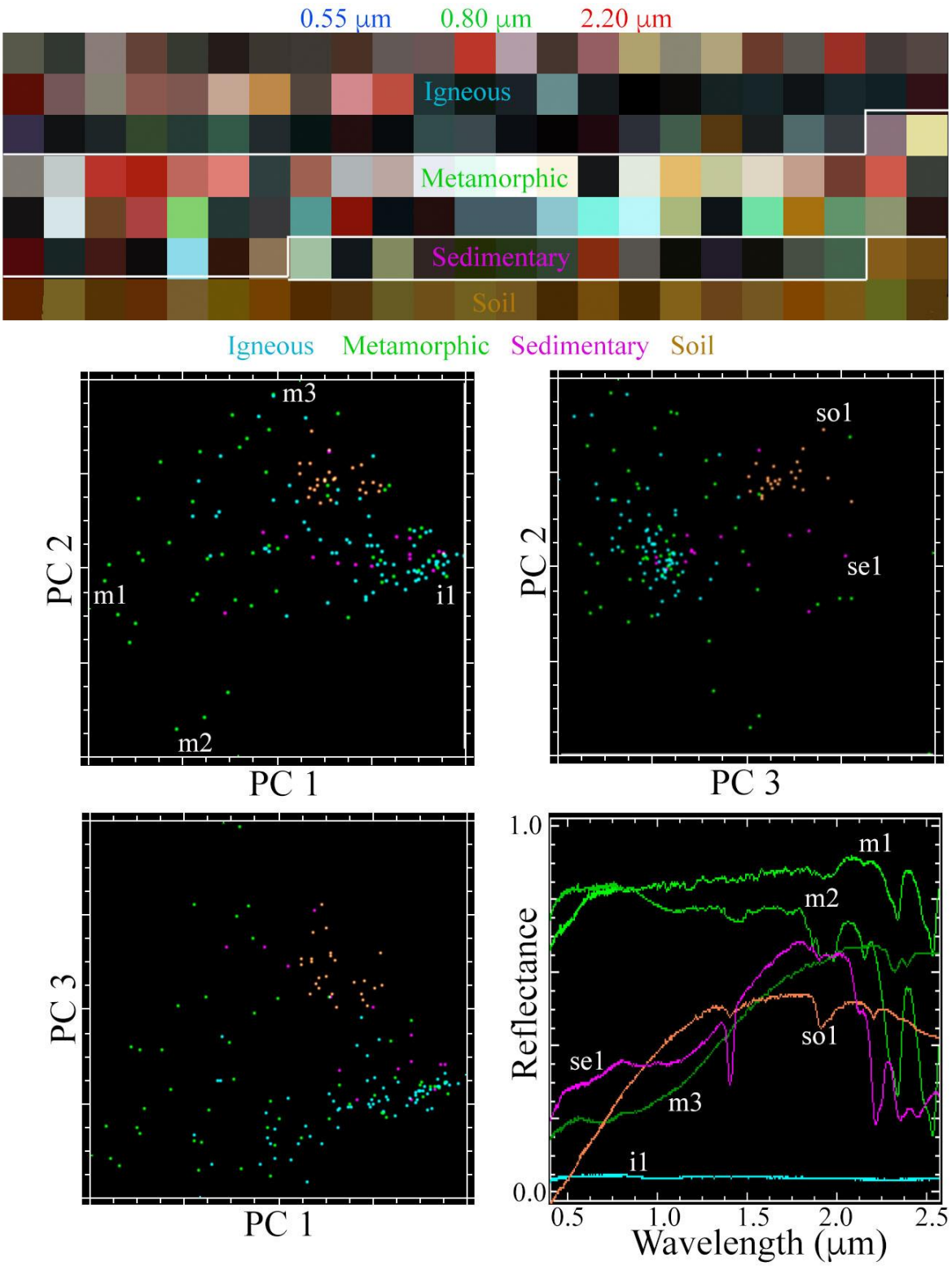

Figure 15. Spectral feature space and endmembers for the rock and soil substrate spectra from the JHU spectral library. Visible/NIR/SWIR false color composite (top) gives some indication of

the spectral diversity in three principal wavebands. Three orthogonal projections of the spectral feature space (bottom), along with example endmember spectra from the periphery of the space, illustrate the broad diversity of metamorphic spectra compared to the more continuous soil spectra.

The range of substrate EMs actually present in this analysis is shown in Figure 16. In order to clearly identify these substrate EMs, the fourth dimension of the spectral feature space is used. While accounting for less than 2% of the total variance in either dataset, PC 4 proves to be useful in this case for distinguishing between the shapes of soil and rock spectra.

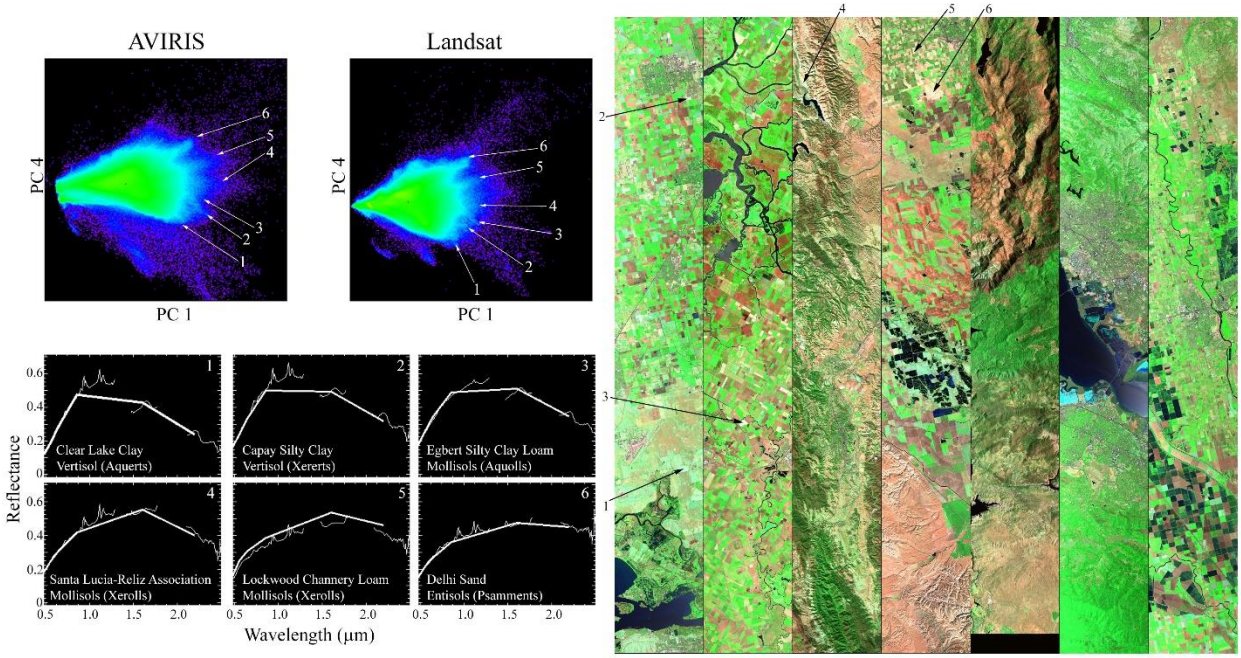

Figure 16. AVIRIS and Landsat substrate EM variability. The PC 1 vs. 4 projection is useful in both transforms as a means of discriminating between the spectral shape of substrate EMs. The remarkable topological similarity between the AVIRIS and Landsat feature spaces (upper left) extends into the fourth dimension. The bright (high PC1) edge of the point cloud splays out in both AVIRIS and Landsat to reveal a continuum of rock and soil substrate EM spectra.

Multipixel mean spectra for each of these EMs (lower left) are displayed as observed by both Landsat and AVIRIS. The locations of the spectra are indicated on the AVIRIS flight lines (right). USDA-NCSS soil survey data were used to find the soil type at the location of each EM. The order and suborder of each soil are shown on the EM spectra plots. The spectral variability captured by the EM continuum corresponds to consistent soil property variations. From EM1 to EM6, the soil types are characterized by a tradeoff between decreasing clay content and increasing sand content.

Six substrate EMs are identified from the PC 1 vs. 4 projection of the feature space. The clear visual similarity in feature space topologies and EM spectra between the hyperspectral and multispectral datasets continues through the fourth dimension. This similarity is unsurprising given the dominance of the spectral continuum (rather than narrowband or broadband absorption features) in the reflectance spectra of these soil EMs.

Each EM corresponds to a spatial cluster of points in a bare (or senescent) agricultural field or a spatially extensive sedimentary deposit. The locations of the EMs are indicated on both the feature space and the false color composite of the flight line subsets. USDA-NCSS soil survey data were acquired for the location of each spectral EM using the California Soil Resource Lab SoilWeb browser (https://casoilresource.lawr.ucdavis.edu/gmap/). The map unit name is given for each EM (e.g., Clear Lake Clay), as well as its order (e.g., Vertisol) and suborder (e.g., Aquerts).

Notably, the spectral properties of the continuum of substrate EMs appear to correspond to a continuum of soil grain sizes and textures. The soil at EM 1 is classified as a Clay, with surface composition of the dominant series (Clear Lake) of roughly 60% clay and 15% sand. In contrast, the soil at EM 6 is classified as a Sand with typical surface composition of its dominant

soil series (Delhi) of roughly 4% clay and 95% sand. EM 3 is classified as a Silty Clay Loam, and the surface composition of its dominant series (Egbert) lies in between, with 38% clay and 18% sand fractions. While preliminary, these results suggest that some soil compositional properties may be sufficiently spectrally distinct to be mapped using their position in the feature space–at least in this study area.

Figure 17 illustrates the complexity that can be measured by hyperspectral imagery on even a relatively small spatial scale. The spatial subset shown in this figure is only 9 × 15 km. Even this small spatial area exhibits considerable diversity in vegetation and substrate spectra. Substantially more prominent clustering is notable within the AVIRIS feature space than within the Landsat feature space, as the subtle spectral differences between fields are better resolved by the hyperspectral sensor than the multispectral sensor. The full complexity of these spectra could not be captured in any three band false color composite image, or resolved with the six-band Landsat or even 11-band Sentinel-2 sensors. Individual pigment and mineral absorptions are distinguishable that would be lost completely in multispectral data. Notably, despite the severely limited spatial domain of this subset, spectra are identifiable (e.g., 2 and 5) that are again remarkably similar to global EMs.

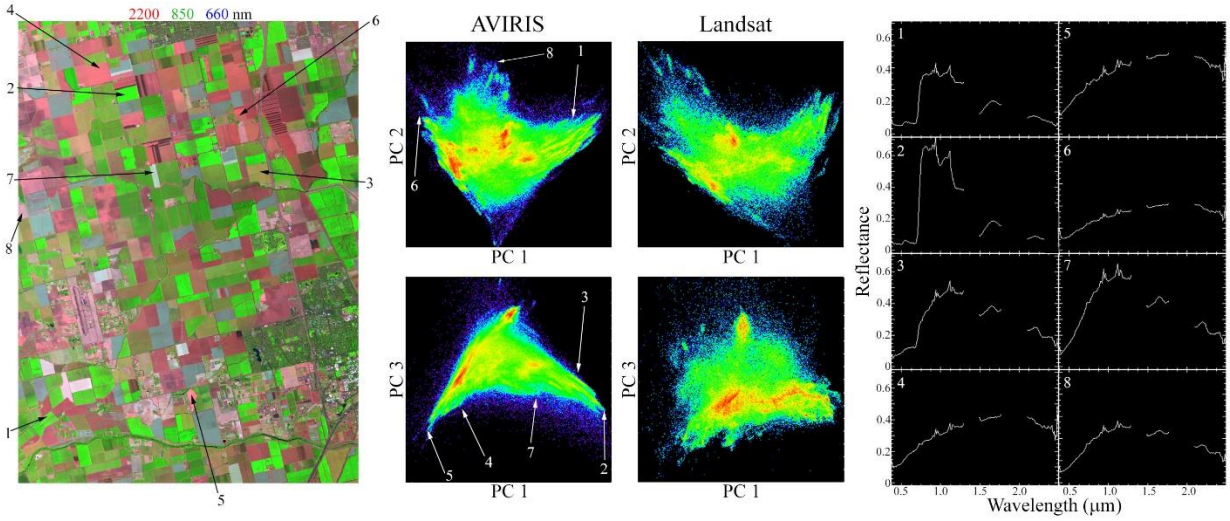

Figure 17. Spectral diversity in a 9 × 15 km region of intensive agriculture in the Great Central Valley of California. Considerably more spectral diversity is present in this hyperspectral dataset than can be adequately represented by any false color composite image Locations of spectra a-h are shown on the AVIRIS feature space and on the image. (A). The AVIRIS feature space for this spatial subset (B, left column) clearly shows more prominent clustering than the Landsat feature space (B, right column). Green fields are characterized by a wide range of red edge and absorption properties (C1 and C2). Bare or senescent fields are characterized by an even greater range of spectral shapes (C3-C8). This high concentration of spectral diversity is consistent with the similarity in dimensionality and feature space topology between the limited area of this study and the much more extensive global studies of Small & Milesi (2013) and Sousa & Small (2017).

Discussion

This work addresses three questions:

1. How much of the dimensionality of hyperspectral data is captured in multispectral data?

2. Is the characteristic pyramidal structure of the multispectral feature space also present in the low order dimensions of the hyperspectral feature space at comparable spatial scales?

3. How much variability in Substrate EMs present hyperspectral data is captured by multispectral sensors?

The first question of this study is addressed quantitatively by the hyperspectral and multispectral partitions of variance given in Figure 4. It is further addressed qualitatively through the topologies of the low-order feature spaces shown in Figures 5 and 6. The spectral feature spaces show a striking similarity in the dimensionality, topology, and EM spectra of the coincident hyperspectral and multispectral datasets used in this study. This is observed despite a factor of 4 difference in the sensor spatial resolution, a factor of 30 difference in the spectral resolution, and further differences in atmospheric correction procedures between the products. At least 97% of the variance in each dataset is present in the first three dimensions and >99% is present in the first four dimensions for both sensors.

This result is in accord with the multispectral findings of (Small, 2004). It suggests a substantially lower dimensionality than the previous hyperspectral studies of (Green and Boardman, 2000; C. Small, 2001; Thompson et al., 2017), but this is because our metrics for dimensionality differ. A primary purpose of dimensionality estimation by these previous AVIRIS studies was to quantify the number of unique materials that the hyperspectral sensor can image above noise level. This is not our purpose. Rather, we seek to describe the number of independent dimensions in which the majority of the spectra reside when decomposed by variance, the number of EMs which bound the space, and the way in which these EMs trade off. This is a fundamentally different question and is why we examine the topology of the point cloud so closely in addition to the partition of variance.

The information content of a dataset is not a trivial quantity to estimate. We are in full accord with (Boardman and Green, 2000) in the opinion that "measuring dimensionality in multivariate data sets is a slippery slope and an approximation at best." We also agree with the findings of (Thompson et al., 2017), that the overdetermined nature of hyperspectral imaging "is highly desirable since it offers numerical leverage while also providing the capability to measure unexpected phenomena and falsify modeling assumptions". It is additionally clear that much of the value of hyperspectral data resides in the precise measurement in the location, depth, and breadth of absorption features. This analysis shows that these features are not well-represented in dimensionality estimates given by the PC transform, nor by deviations in the topology of the point cloud, at least in the first four dimensions. Variance is an imperfect metric for information content, especially in hyperspectral imagery.

While difficult to estimate, the question of dimensionality is important because it places in context the aggregate landscape-scale measurements of a sensor. The observation of the similarity of the multispectral and hyperspectral feature spaces suggests that, even with hyperspectral observations, the shape and amplitude of the spectral continuum dominates the variance structure of the data, but does not fully determine its information content. It is upon the structure of this low-order spectral feature space that the narrowband absorptions and other fine spectral features are superposed. Our results suggest that these information-rich fine spectral features do not appreciably change the fundamental low-order structure of the feature space. This finding has potential implications for the future synergistic use of multispectral and hyperspectral data.

Figure 18 shows an additional way of visualizing information content present in these fine spectral features. In this figure, each of the NIR, SWIR 1, and SWIR 2 Landsat bands are

shown individually for a single spatial domain. Because there is only one band for each of these spectral regimes, the Landsat dimensionality for each spectral subset is 1 and must be shown as a grayscale image. However, over 40 AVIRIS channels are present for each of these spectral regimes. Adjacent to each Landsat band is a tricolor composite showing the three low order PC images for the AVIRIS spectral subset corresponding to each spectral regime. Substantially greater information is obviously present in each spectral regime for the hyperspectral cube than the multispectral dataset. The dimensionality of AVIRIS is clearly at least two in each of these spectral regimes, yielding intraband feature spaces with a considerable structure and physically meaningful EMs.

The results of this study do not imply that the AVIRIS data cube only images three or four spectrally distinct quantities, nor that the information contained in the hyperspectral cube can be captured by a multispectral instrument. Rather, they demonstrate that, when decomposed linearly using the PC transform, the variance of both datasets is partitioned into a nearly identical number of fundamental dimensions and the relationship between the spectra follows a similar geometric relationship. It might have been expected that substantially different EMs would arise from the differences in spatial and spectral resolutions of the sensors. This was not the case. Furthermore, it might have been expected that a low-order dimension would emerge in the hyperspectral dataset which differed substantially from the multispectral dataset. This was not the case either. Rather, despite the significant variations in absorption features–most notably in the plane of substrates–the EMs were arranged in a nearly identical configuration. The implications of this result for multitemporal analyses are substantial, as they suggest that pixel trajectories in multispectral feature space correspond to nearly identical trajectories in low-order hyperspectral feature space.

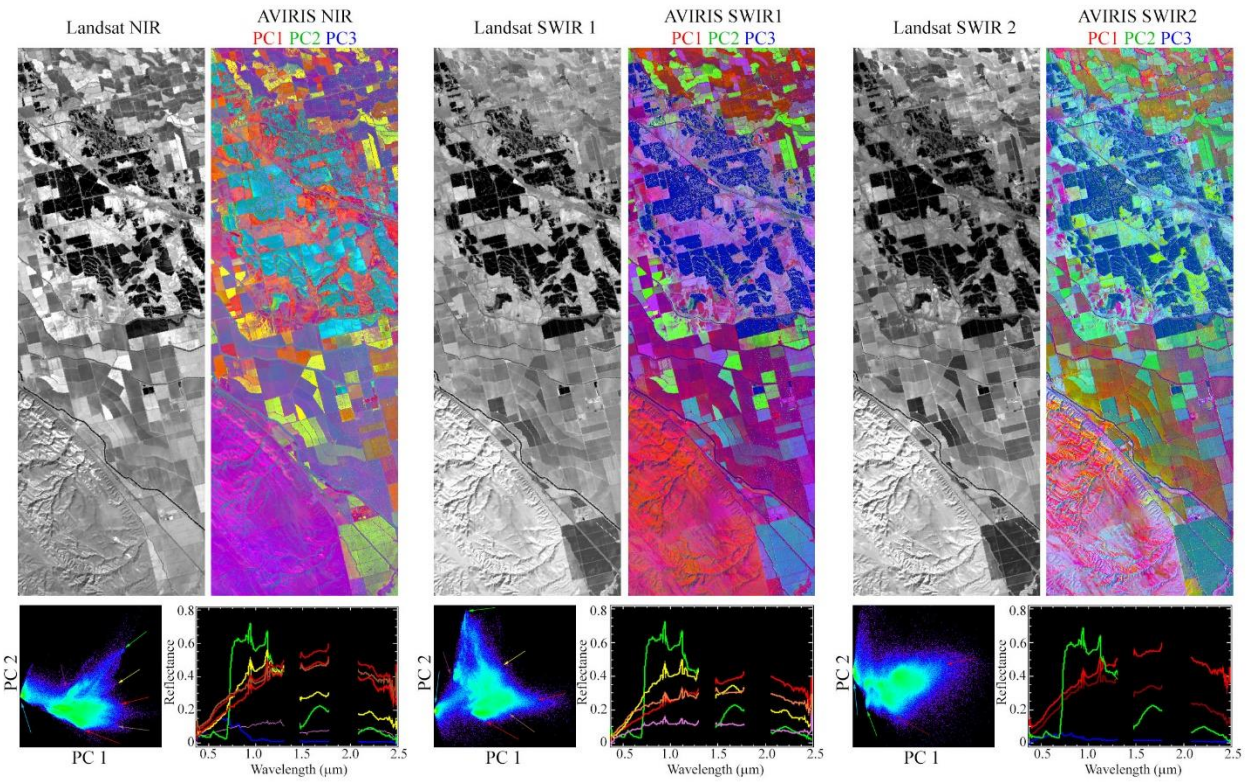

Figure 18. Intraband and interband spectral dimensionality of AVIRIS in comparison to individual infrared bands of Landsat OLI. OLI is one dimensional in each of the NIR, SWIRl, and SWIR2 spectral regimes because the sensor only collects in one band for each. In contrast, AVIRIS collects in over 40 channels for each of the three spectral regimes. The spectral dimensionality of the hyperspectral imagery is apparent in the color images of the three lowest-order Principal Components for the channels within each regime, as well as in the structure for the corresponding spectral feature spaces. Dark and vegetation EMs are similar for each feature space but substrate EMs differ because of distinct absorptions. EM locations are indicated on each feature space by colored arrows.

The second question of this study is addressed quantitatively through the partitions of variance in Figure 13 and qualitatively by the feature spaces in Figure 14 and Figure 15. Both the hyperspectral and multispectral partitions of variance, feature spaces, and EMs found in this

study are remarkably similar to those found in previous analyses of Landsat data sampling much more spatially extensive regions. These results suggest that a substantial fraction of global multispectral diversity can be sampled in a local spatial extent. Notably, the entire area used in this analysis, 9800 km^2, is roughly 1/3 of the 34,000 km^2 area covered by a single Landsat scene and less than 0.01% of the ice-free global land area. Similar EM spectra were even present within the very small 180 km^2 region of Figure 16.

Finally, the third question of this study is directly addressed by Figure 15. Not only are the relative positions of the substrate EMs nearly identical, a consistent physical relationship is also observed between their position in the PC 1 vs. 4 projection of the feature space and the soil properties of the locations from which they are derived. This was observed in both the hyperspectral and multispectral datasets using independent rotations. While there is clearly more information to be gained from hyperspectral imagery than the topology of the point cloud, it is important that the multispectral and hyperspectral sensors distinguish between the same broad soil features in the same way. The similarity of the spectral feature spaces suggests significant potential for inferring properties of full soil reflectance spectra from multispectral observations. As indicated by Figure 6, this is not true for rock spectra in general. While soil spectra have generally similar shapes, rock spectra often have very distinct narrowband absorptions related to the crystal structure of specific minerals not generally preserved in soils. This consistency in the structure of the plane of substrates has the potential to substantially inform analyses in studies where a temporally or spatially sparse set of hyperspectral observations complement a wealth of multispectral observations.

Variability in grain size and textural properties of the underlying soils is a physically plausible explanation for the spectral variability observed in the feature space. The potential for

soil-specific information in PC 4 has been previously documented by (Crist and Cicone, 1984), but was only briefly mentioned and was not tied directly to specific compositional properties. To our knowledge, the question has not yet been further elucidated. Although our results for this subject are preliminary, as this was not the primary focus of the study, they are encouraging. One critical complicating factor moving forward will be controlling for the presence of non-photosynthetic vegetation.

While beyond the scope of this study, further investigation of the relationship between soil type and reflectance presents an attractive avenue for future work. In a pedologically diverse region such as California with quality soil maps and abundant hyperspectral observations, the potential exists to use hyperspectral feature spaces to determine which soil properties can and cannot be reliably determined from hyperspectral and multispectral imagery. The range of reflectance spectra corresponding to each soil class could be documented and a repeatable, systematic classification system (expanding upon the Munsell color chart) could potentially be developed on the basis of reflectance spectroscopy. The tools of the visible could be extended into the infrared.

Conclusions

We analyze the spectral dimensionality of five hyperspectral flight lines and coincident multispectral satellite images over a region of considerable pedologic and agricultural diversity. The partition of variance, spectral feature spaces, and EM spectra for each dataset bear remarkable resemblance to each other. Comparable similarity with earlier global multispectral analyses is also observed. These results demonstrate 1) that the multispectral and hyperspectral feature spaces share a fundamental low order structure, and 2) that the global multispectral feature space can be reasonably represented in a relatively small spatial domain.

In addition, a nearly identical continuum of substrate EMs is observed in both the multispectral and hyperspectral datasets. Comparison with a soil map shows that variability in soil composition strongly covaries with the position of EMs in the feature space. Our (local) success in discriminating between soil classes with variable sand vs. clay fractional compositions suggests considerable potential for a novel method for improving the mapping of soils with optical remote sensing.

3. Global cross-calibration of Landsat spectral mixture models

Abstract

Data continuity for the Landsat program relies on accurate cross-calibration among sensors. The Landsat 8 Operational Land Imager (OLI) has been shown to exhibit superior performance to the sensors on Landsats 4-7 with respect to radiometric calibration, signal to noise, and geolocation. However, improvements to the positioning of the spectral response functions on the OLI have resulted in known biases for commonly used spectral indices because the new band responses integrate absorption features differently from previous Landsat sensors. The objective of this analysis is to quantify the impact of these changes on linear spectral mixture models that use imagery collected by different Landsat sensors. The 2013 underflight of Landsat 7 and Landsat 8 provides an opportunity to cross calibrate the spectral mixing spaces of the ETM+ and OLI sensors using near-simultaneous acquisitions of radiance measurements from a wide variety of land cover types worldwide. We use 80,910,343 pairs of OLI and ETM+ spectra to characterize the Landsat 8 OLI spectral mixing space and perform a cross-calibration with Landsat 7 ETM+. This new global collection of Landsat spectra spans a greater spectral diversity than those used in prior studies and the resulting Substrate, Vegetation, and Dark (SVD) spectral endmembers (EMs) supplant prior global Landsat EMs. We find only minor ($-0.01 < \mu < 0.01$) differences between SVD fractions unmixed using sensor-specific endmembers. Root mean square (RMS) misfit fractions are also shown to be small (<98% of pixels with <5%RMS), in accord with previous studies using standardized global endmembers. Finally, vegetation is used as an example to illustrate the empirical and theoretical relationship between commonly used spectral indices and subpixel fractions. We include the new global ETM+ and OLI EMs as Supplementary Materials. SVD fractions unmixed using global EMs thus provide

easily computable, linearly scalable, physically based measures of subpixel land cover area which can be compared accurately across the entire Landsat 4-8 archive without introducing any additional cross-sensor corrections.

Introduction

The Landsat program provides the longest continuous record of satellite imaging of the Earth available to the scientific community (Wulder et al., 2016). One great strength of this record lies in data continuity provided by the generally excellent cross-calibration between the sensors on board the different satellites (Markham and Helder, 2012). To extend this continuity into the future, the Operational Land Imager (OLI) onboard Landsat 8 must be intercalibrated with the rest of the archive. Over the 3+ years since launch, the OLI has been shown to exhibit superior performance to previous Landsat sensors with respect to radiometric calibration (Mishra et al., 2016; Morfitt et al., 2015), signal to noise (Knight et al., n.d.; Morfitt et al., 2015; Schott et al., 2016), and geolocation (Storey et al., 2014).

One of the applications enabled by such a deep archive of high quality Earth observation data is multitemporal analysis to study long-baseline changes (Vogelmann et al., 2016). However, concern has recently emerged over the direct intermixing of data collected by both the OLI and older TM/ETM+ instruments onboard Landsats 4-7 because of the changes in band placement introduced with Landsat 8 (Holden and Woodcock, 2016). Statistical corrections and corresponding transfer functions have been introduced to correct for these differences (Roy et al., 2016). Considerable work has been done to examine the effect of these discrepancies and corrections in the context of spectral indices. The implications of these changes for spectral mixture analysis (SMA) are different than for spectral indices. The implications for multi-sensor and multi-temporal SMA have been investigated on the regional scale by (Flood, 2014), but, to

our knowledge, no attempt has been made to address these implications for globally standardized spectral mixture models.

The purpose of this study is to characterize the global Landsat 8 OLI spectral mixing space and cross-calibrate it with the Landsat 4-7 TM/ETM+ spectral mixing space. Previous work has shown the TM and ETM+ sensors to provide globally consistent results for Substrate, Vegetation, and Dark (SVD) subpixel fraction estimates using SMA (Small, 2004; Small and Milesi, 2013). Extending this cross-calibration to include imagery from the OLI onboard Landsat 8 could thus extend this consistency across the entire 30+ year archive of Landsat 4-8 imagery. In order to develop a cross calibration suitable for multi-sensor SMA, it is necessary to compare spectral mixing spaces for both sensors and identify comparable spectral endmembers that span both spaces. Under ideal circumstances, this would require spectrally diverse collections of TM/ETM+ and OLI spectra where both sensors image the same targets simultaneously.

Before Landsat 8 was placed into its final orbit, it was maneuvered into underflight configuration below Landsat 7 for one day: March 30 (Julian Day 89) 2013. While the two satellites were positioned in this way, they imaged a diversity of land cover spanning a wide range of spectral reflectance signatures. Each pair of ETM+/OLI images was collected approximately 2-5 minutes apart. The short temporal baseline between image pairs minimizes changes in solar illumination, surface processes and atmospheric effects. The underflight imagery thus provides a rare, nearly ideal opportunity for cross-calibration of the OLI and ETM+ sensors.

However, while the underflight dataset is nearly ideal for this purpose in many ways, there are some caveats. Standard LaSRC surface reflectance is not available for the OLI underflight data, so this analysis is limited to exoatmospheric reflectance with no atmospheric

correction attempted. Furthermore, this analysis is both retrospective and global in extent, limiting the results of this study to that of an intercomparison and cross-calibration, but not a full field validation. We suggest that the unique, near-synchronous imaging geometry of the underflight data provides valuable information that is worth exploring despite these limitations.

In this study, we use 80,910,343 unsaturated broadband spectra imaged nearly simultaneously by Landsat 7 and Landsat 8 while flown in underflight configuration to address the following question: How reliably can subpixel Substrate, Vegetation and Dark (SVD) fractions be used interchangeably between ETM+ and OLI?

We find that the subscenes chosen for this analysis span an even greater range of the Landsat spectral mixing space than previous (Small, 2004; Small and Milesi, 2013) studies. We suggest that endmembers (EMs) generated for this study can thus effectively replace previous global EMs. While the new Dark (D) EM does not differ substantially from previous EMs, small differences in the Vegetation (V) EM and larger differences in the Substrate (S) EM are apparent. The overall behavior of the model is consistent with the findings of (Flood, 2014). The differences in the Vegetation EM are consistent with the findings of (Holden and Woodcock, 2016; Roy et al., 2016) as being a result of band placement. The differences in the Substrate EM are likely due to the wider range of global substrates present in this study than in any previous global study and constitute an improvement upon previous global models.

As a result, we find that subpixel estimates of SVD fractions for Landsat 8 using the old and new EMs display strong linear relations, with estimates of subpixel V fraction essentially unchanged and with easily correctible biases for S and D. When compared with the new EMs, all three SVD fractions scale linearly between the sensors with minimal (μ = -0.01 to 0.01) bias.

Root-mean-square (RMS) misfit to the SVD model for both the old and the new EMs is generally small, with > 98% of all pixels showing < 5% error.

Finally, we use vegetation as an example to show the relationship between commonly used spectral indices and subpixel EM fractions produced by SMA of Landsat 8. We suggest that fractions estimated by SMA from global EMs provide easily computable, linearly scalable, physically based measures of subpixel land cover which can be compared accurately across the entire Landsat 4-8 archive without introducing any additional cross-sensor corrections.

Background

Implications of Spectral Band Positioning

The spectral response function of a sensor quantitatively defines its sensitivity to different wavelengths of light. The radiometric design of the Landsat 8 OLI featured an improvement on the previous TM/ETM+ sensors by modifying its spectral response function to narrow and slightly relocate several of the spectral bands. This has the effect of reducing the impact of common atmospheric absorptions which impede imaging the land surface (Mishra et al., 2016). However, it also has the effect of subtly changing the broadband spectrum imaged by OLI for any object which is not spectrally flat over the wavelengths for which the spectral response function was modified.

Figure 19 and Figure 20 shows the effect of the different spectral responses of the OLI and ETM+ sensors. Four sample green vegetation spectra (column 1) are shown, as well as four sample mineral spectra (column 3) from the USGS spectral library. The response functions of the two Landsat sensors are plotted as well to demonstrate the portions of the spectrum over which

they are sensitive. The narrowing and slight adjustment to the position of the NIR and SWIR bands

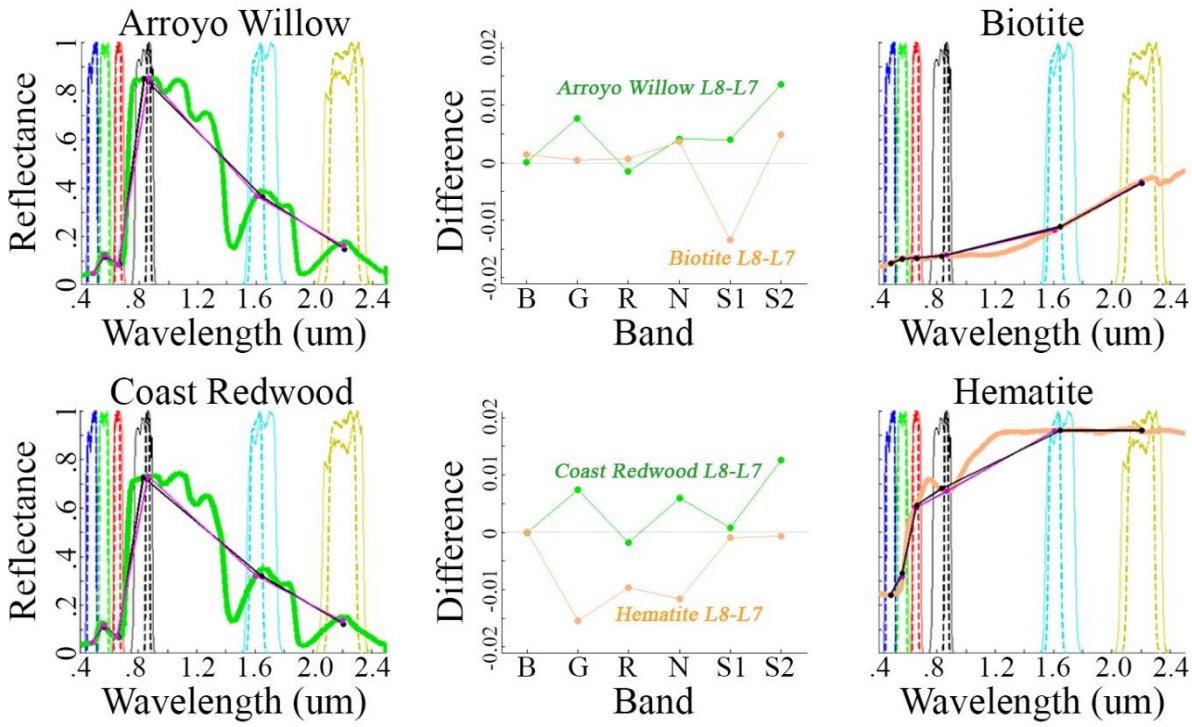

Figure 19. Illustration of the effect of changes in spectral response functions for Landsat 8 OLI and Landsat 7 ETM+. Laboratory spectra from the USGS spectral library for sample vegetation (column 1) and minerals (column 3) are convolved with the spectral response functions of OLI and ETM+. The simulated reflectance for each sensor is shown in thick lines (L7 = black, L8 = magenta).

(black, cyan, and gold) are evident. Superimposed on each of these spectra are simulated Landsat 7 and 8 broadband spectra computed by convolving the reflectance spectra with the response functions of the sensors as described above.

Column 2 shows the difference between the OLI and ETM+ reflectances derived from the laboratory spectra. The essential shape and fundamental characteristics of the spectra are all

very similar, but perceptible differences in the spectra are detectible. While the differences in aggregate are generally <0.01 reflectance units (<5%), the differences can approach 0.02 reflectance units (10%) for individual bands in some cases.

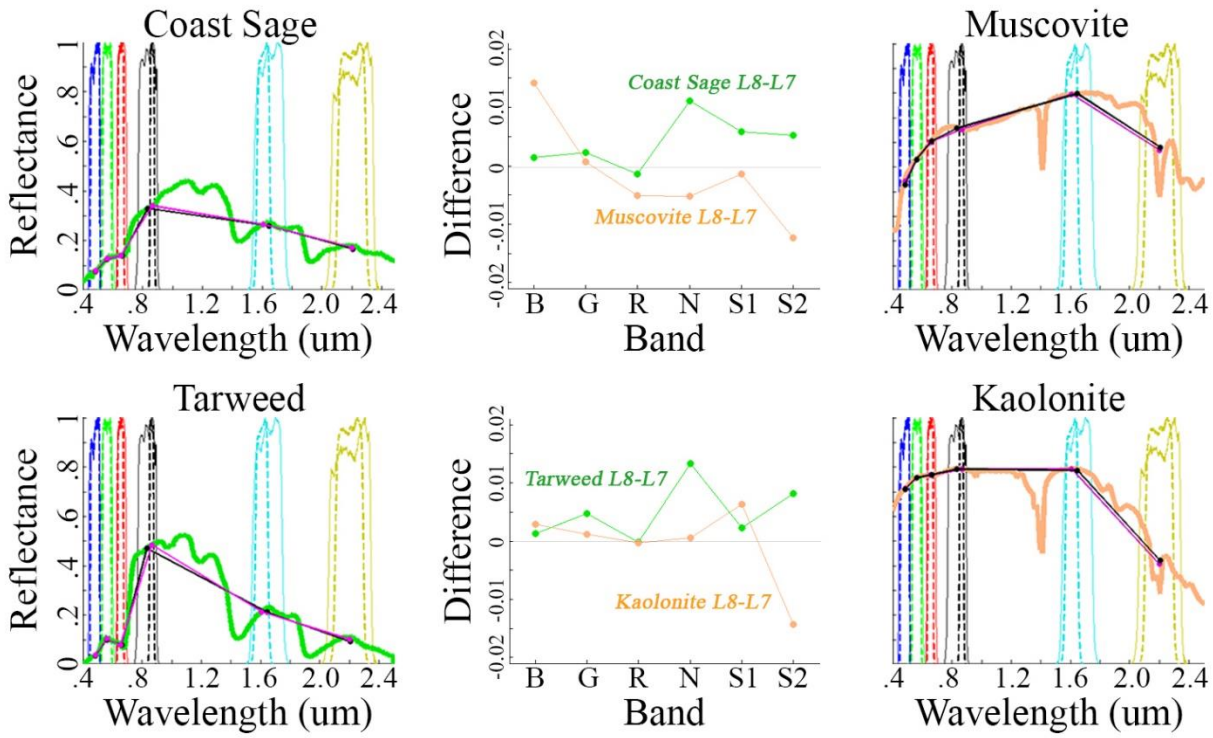

Figure 20. The spectral response functions are generally wider for ETM+ (solid thin lines) than OLI (dashed lines). Differences in broadband reflectance as observed by ETM+ and OLI (center) depend on both overall albedo and on the depth, width and location of absorptions. While both sensors record similar spectra, band-to-band differences can be nearly 0.02 reflectance units, sometimes, exceeding 10% of the value of an individual band.

Spectral Mixture Models and Linear Spectral Unmixing

At the scale of the 30 m Landsat pixel, most landscapes are spectrally heterogeneous. As a result, most pixels imaged by Landsat sensors are spectral mixtures of different materials (e.g. soils, vegetation, water, etc) with varying amounts of subpixel shadow. The continuum of aggregate radiance spectra imaged by a sensor forms a spectral mixing space in which each pixel occupies a location determined by the relative abundance of material reflectances imaged in the Ground Instantaneous Field Of View (GIFOV) of the pixel. In situations where multiple scattering among subpixel targets is small compared to single scattering from each subpixel target to the sensor, the aggregate response of the sensor often varies in proportion to the relative abundance of the spectrally distinct materials (Singer and McCord, 1979).

The topology of the full space of radiance (or equivalently reflectance) spectra reveals the linearity of mixing and the composition of the spectral endmembers and mixtures that bound the space of all other observed spectral mixtures (Boardman, 1993). In the case of decameter resolution sensors like those on the Landsat satellites, the combination of spatial and spectral resolution, and positioning of the spectral bands, resolves characteristics of reflectance spectra that distinguish the most spectrally distinct materials commonly found in landscapes. Ice, snow, rock and soil substrates, vegetation, and water each represent a general class of reflectance spectra that are clearly distinguishable with broadband sensors at decameter spatial scales (Small, 2004). Of these, the aggregate broadband reflectances of most landscapes can be represented accurately as linear mixtures of substrate (S), vegetation (V) and dark (D) endmembers. The dark endmember corresponds to either absorptive, transmissive or non-illuminated surfaces and typically represents either shadow or water. As a result, linear

combinations of these three spectral endmembers can represent the aggregate reflectance of a very wide range of landscapes at meter to decameter scales (Small and Milesi, 2013).

By identifying the SVD endmember spectra that bound the spectral mixing space, it is possible to use these endmembers together with a linear spectral mixture model to project the 6D feature space of the Landsat sensors onto a simpler 3D mixing space bounded by spectrally and functionally distinct components of a wide range of landscapes (Adams et al., 1986). Inverting a simple three endmember linear spectral mixture model using the SVD endmembers yields estimates of areal abundance of each endmember for each pixel in an image. Using standardized spectral endmembers that span the global mixing space of spectra allows for intercomparison of fraction estimates derived from different sensors across space and time. Standardized spectral endmembers confer all of the benefits of spectral indices, with the added benefit of using all of the spectral information available while simultaneously representing multiple spectral contributions to the mixed pixel.

Scientific Context and Limitations of the Study

The approach taken in this paper is to calibrate global spectral mixture models of Landsat ETM+ and OLI imagery using the novel global collection acquired during the Landsat 7 and 8 underflight. While this has not previously been accomplished, a regional study in Australia examining the continuity of ETM+ and OLI performance in a multiple linear regression model, a spectral mixture model, and a spectral index was performed by (Flood, 2014). In the analysis of (Flood, 2014), the problem is approached in a different way: ETM+ and OLI imagery from subsequent overpasses (8 days apart) were bias corrected band-by-band before being input into biophysical models. Orthogonal Distance Regression was used to cross-calibrate the imagery, which was then used to a) predict overstorey foliage projective cover, (an areal estimate of

vegetation), using top of atmosphere (TOA) reflectance; b) predict fractional vegetation cover with a linear mixture model of bare soil, photosynthetic, and non-photosynthetic vegetation, using modeled surface reflectance; and c) compute NDVI. Large systematic changes were reported in the Near Infrared and Shortwave Infrared 2 bands, with surprisingly little change in the Shortwave Infrared 1 band. The approach of (Flood, 2014) corrected for these differences well, resulting in regression slopes equal to 1.00 and good agreement between ETM+ and OLI fractional land cover.

The collection of Landsat 7/8 underflight data undersamples the surface of the Earth in both space and time. Notably, there are unfortunately no cloud-free acquisitions over dense tropical forests. The season of the overpass (late March) results in imaging of senescence of many high latitude boreal forests. However, this is unlikely to result in appreciable variability in either the vegetation or dark EMs because, as shown previously (Small and Milesi, 2013), these two EMs show negligible change on a global scale when compared even with the limited global subset of (Small, 2004). That the ETM+ vegetation and dark EMs from this study are very similar to those found by the two previous studies mentioned here is further evidence that undersampling of vegetation and dark EMs is not an appreciable source of uncertainty in this analysis.

However, representation of an unusually diverse subset of the global substrates is a strength of this collection. The plane of substrates was shown previously to be spectrally diverse. Greater sampling of this portion of the space than was achieved in previous studies further supports the linear mixing hypothesis in the substrate-rich (and vegetation-sparse) region of the mixing space, and yielded a new global substrate EM which provides the most complete bound on the global Landsat mixing space to date.

This study is performed with TOA reflectance in order to provide a direct comparison with previous studies and to minimize the complexity of the analysis. As mentioned in the introduction, standard LaSRC surface reflectance processing is not available for pre-WRS2 Landsat 8 data (USGS, 2016a), and modeling of surface reflectance was not attempted. Furthermore, the retrospective nature of the study precludes true field validation. The global extent of the study and the remote location of many of the subscenes precludes precise knowledge of atmospheric or BRDF parameters at the time of the overpass.

The clear atmospheric conditions present in the subscenes we chose for the analysis was fortuitous and minimizes the contamination by atmospheric effects that is common in satellite imaging. Mixture models cannot correct for most atmospheric contamination problems and surface reflectance should be used whenever well constrained atmospheric corrections are available.

The unique nature of the near-simultaneous acquisitions in the underflight dataset greatly reduces the problems of imaging geometry and atmospheric change which surface reflectance is designed to overcome. The level of mixture model agreement given by TOA reflectance in this study allows us to take a conservative stance on the level of data preprocessing. We do this in order to avoid introducing unnecessary sources of uncertainty that can result from using an unjustifiably complex model. However, a similar analysis characterizing the global Landsat mixing space with modeled surface reflectance and field validation would be a valuable line of inquiry in the future.

Data & Methods

All data used in this study were acquired from the USGS Earth Resources Observation and Science Center at http://glovis.usgs.gov/. Landsat 8 data were acquired from the "Landsat 8 OLI Pre-WRS 2" collection. Data were processed from DN to radiance (L) using the following expression:

$$L_\lambda = Gain * DN + Bias$$

Exoatmospheric reflectance (Chander and Markham, 2003) was then computed using the following expression:

$$\rho_\lambda = \frac{\pi L_\lambda d^2}{ESUN_\lambda \sin\theta}$$

where ρ_λ is the reflectance at a given wavelength, d is the earth-sun distance, $ESUN_\lambda$ is the solar irradiance, and θ is the sun elevation in degrees. We manually selected a set of 100 30 x 30 km subscenes from the spatial overlap between the Landsat 7 and 8 acquisitions on the basis of maximum spectral diversity. Nearly all of the subscenes were cloud-free, although some subscenes which contained land cover with unusually diverse spectral properties were included even if minor cloud contamination was present. Both Landsat 7 and 8 analyses were performed only on pixels unaffected by the SLC-off gaps. No saturated pixels were used in this analysis.

Linear spectral unmixing represents each pixel reflectance factor (R) as a linear combination of the input spectral EMs (M) weighted by their areal fractions (f) plus misfit (□□ as R = fM + □. A unit sum constraint is often used, which amounts to adding an additional equation that the fraction estimates sum to unity (□f = 1). This set of equations is overdetermined and the coefficients for the optimal linear combination of EMs to represent each

pixel under the L2 norm can be directly computed using Weighted Least Squares, where the relative weight of the unit sum constraint is a tunable parameter. All unmixing was performed with unit sum constraints with weight = 1.

Analysis

Figure 21 shows the locations of the 30 Landsat 7 and 8 scene pairs used in this analysis. All scene pairs were collected in underflight configuration. The time difference between Landsat 7 and 8 overpasses was < 6 minutes for every scene pair. The scenes span a remarkable geographic diversity of land cover given the short time in which they were collected. Five continents are represented. Although several images were acquired over mainland Europe (Path 198), unfortunately all except the one covering Ibiza, Spain were too cloudy for the purposes of this analysis.

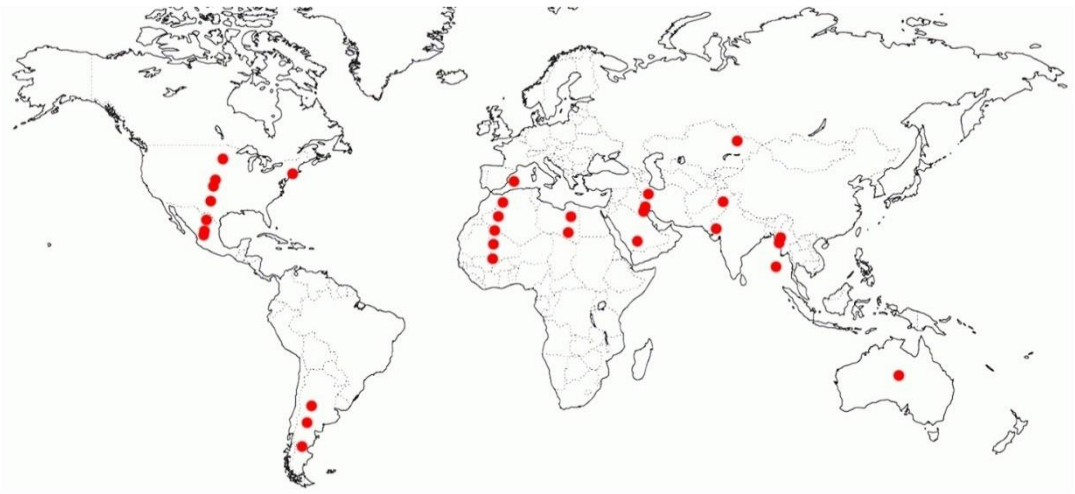

Figure 21. Locations of 30 near-simultaneous Landsat 7/8 scene pairs from which the 100 subscenes for this analysis were chosen. For every scene pair, Landsat 7 and Landsat 8 overpass times were within 6 minutes of each other. All scenes were imaged while Landsat 8 was performing its pre-WRS2 underflight of Landsat 7 on March 30 (JD 89), 2013.

From these 30 image pairs, 100 subscenes of 1,000,000 spectra each were chosen on the basis of spectral diversity (Figure 22). Subscenes are shown both with a common linear stretch (TOA reflectance = 0 to 0.7) and subscene specific 2% linear stretches in an attempt to show the spectral diversity and complexity included in this sample. Shallow and deep water are each represented in both coastal and inland water bodies. Natural and managed vegetation are both present over a wide range of climate zones and soil types. Geologic diversity includes both mafic and felsic bedrock, Quaternary alluvium, and sand dunes with variable grain size and lithology. One large evaporite pan near Kuwala, India was included to demonstrate the performance of spectrally complex minerals in the global SVD model. Despite several cloud-free acquisitions at high northern latitudes, snow and ice was minimized due to its minor areal coverage within the terrestrial ecoregions of the world (Olson et al., 2001) and the fact that a larger sample would be required to accurately represent its true spectral diversity. When pixels in the SLC-off gaps of Landsat 7 are removed, a total of 80,910,343 coregistered ETM+ and OLI spectra remain.

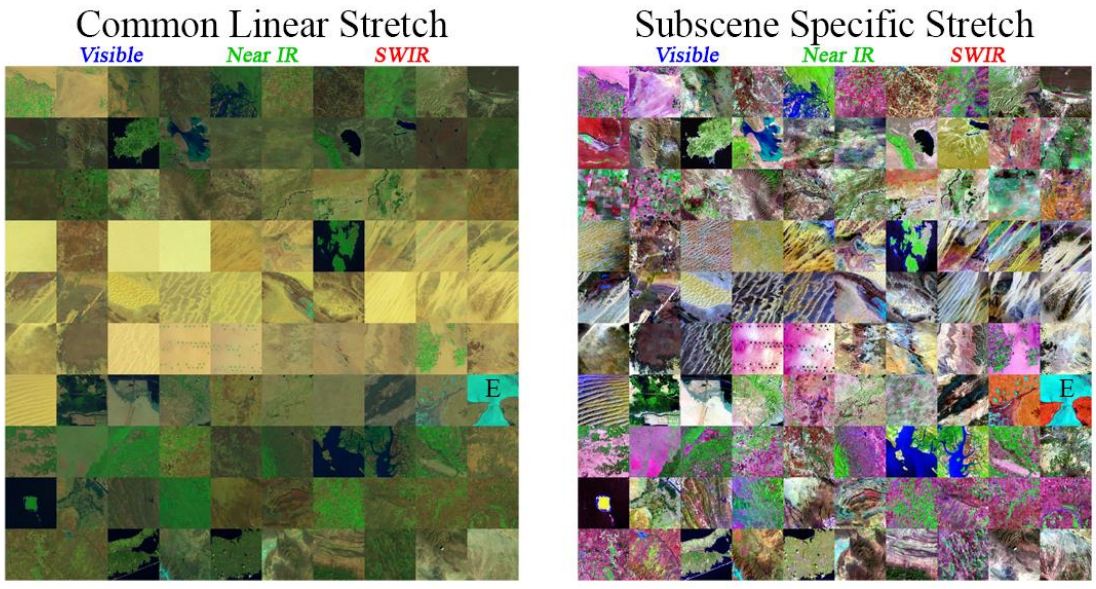

Figure 22. Comparison of 100 OLI subscenes chosen from the near-simultaneous Landsat 7 and Landsat 8 acquisitions from Figure 21. Each 30 x 30 km subscene is shown with both a common

linear stretch (reflectance = 0 to 0.7) and subscene-specific 2% linear stretches to illustrate the spectral diversity of the scenes chosen. The subscenes sample a range of evergreen and deciduous natural vegetation, agriculture, lithologically variable soil, sediment, and rock substrates, as well as standing water (both deep and shallow). With the exception of the evaporite pan in western India (labeled E), all subscenes are composed of varying mixtures of rock and soil substrates, vegetation, water, and shadow.

Principal Component (PC) analysis was then performed independently on both the Landsat 7 and Landsat 8 subscene mosaics. Landsat 8 Coastal/Aerosol and Cirrus bands were not included in the analysis in order to facilitate a direct comparison between the sensors. The resulting Landsat 8 spectral mixing space with corresponding single pixel EMs is shown in Figure 23. The Landsat 7 mixing space is not shown, as it is visually indistinguishable from the Landsat 8 space. As found in previous work, the space is characterized by sharp, clear apexes corresponding to Vegetation and Dark EMs, but substantial complexity near the Substrate EM. This complexity reflects the diverse range of rocks and soils spanning the plane of substrates. Sharp linear edges connecting (D,V) and (D,S) EMs (clearly visible in the projection showing PC 1 and PC 3) indicates binary linear mixing. Concavity on the edge connecting (S,V) suggests that Substrate and Vegetation rarely trade off completely without any subpixel shadow. The elongate cluster of pixels spectrally distinct from the global mixing space corresponds to the Evaporite pan (E) in India. The inclusion of these evaporites allows an opportunity to illustrate the behavior of the model to materials which are not linear combinations of substrate, vegetation, or dark targets in broadband visible-IR spectra. Inclusion of these evaporites in the PC rotation does not affect the other fractions because EMs were manually chosen from the other apexes of the space.

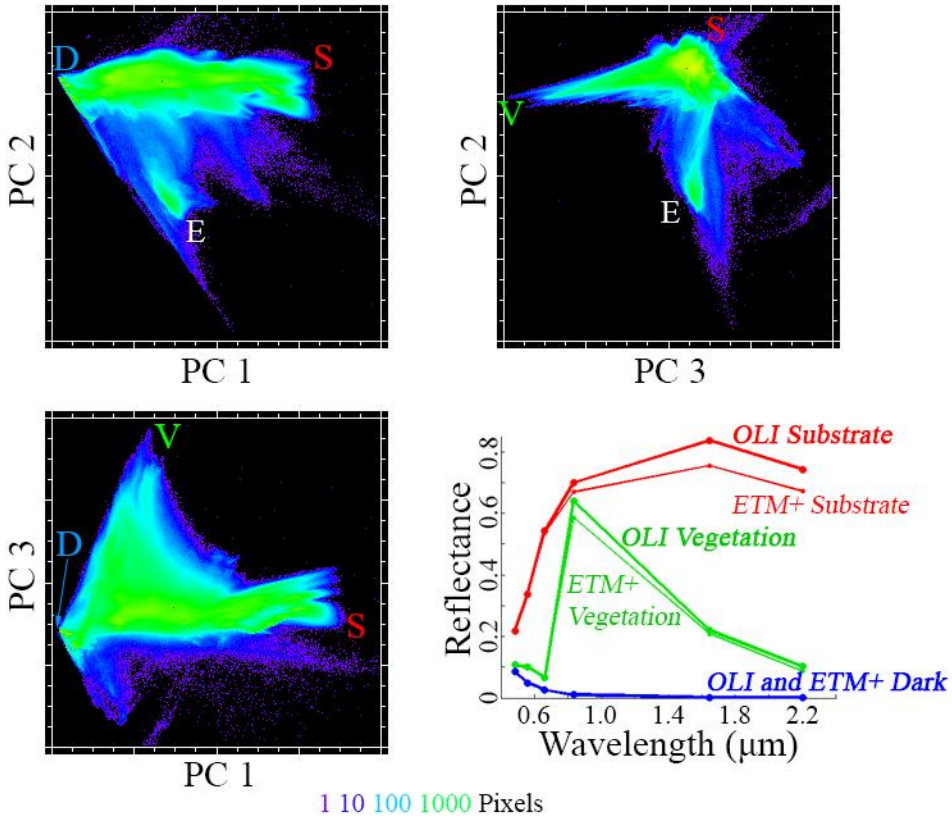

Figure 23. The Landsat 8 OLI spectral mixing space derived from 80,910,343 broadband spectra. The Landsat 7 ETM mixing space (not shown) of the near-simultaneous Landsat 7 acquisitions is visually indistinguishable. EM spectra (lower right) selected from the apexes of the scatterplot correspond to the same geographic locations and so represent the same materials – within uncertainty in the coregistration of each OLI/ETM+ image pair. The prominent cluster with distinct PC 2 values (E) corresponds to an evaporite pan near Kuwala, India.

Substrate (red), Vegetation (green) and Dark (blue) global EM spectra are shown in Figure 23. The differences between the ETM+ and OLI EM spectra are a result of the changes in spectral response functions between the sensors. These pairs of spectra represent identical geographical locations imaged at nearly the same time. The Substrate EM corresponds to a field of sand dunes in the Libyan Sahara (p184r044), the Vegetation EM corresponds to a homogenous agricultural field in central Texas (p029r038), and the Dark EM corresponds to deep water off the Atlantic coast of Long Island, New York (p013r032). While the dark EM is nearly identical for the two sensors, the Landsat 8 substrate and vegetation EMs are brighter than the Landsat 7 EMs in all IR wavelengths, most prominently in the NIR and SWIR 1. Text files with EM spectra for both ETM+ and OLI sensors are included as supplementary materials.

As expected, the geometry of the mixing space shown here, as well as the ETM+ spectra of the resulting Vegetation and Dark EMs, are similar to those found by previous studies (RMS differences with (Small and Milesi, 2013) of 0.02 and 0.00 for V and D, respectively). However, the Substrate EM is substantially brighter across all wavelengths than found previously (RMS differences with (Small and Milesi, 2013) of 0.14 for the new OLI EM and 0.10 for the new ETM+ EM). The plane of substrates found in this study is inclusive of the spectral range found by prior studies, but also contains substantially greater variability in bright sands. This extension of the plane of substrates is likely a result of the range of diversity of sands and soils included in this analysis. The newly identified substrates represent an improvement over previous models as they are more general and inclusive of the range of landscapes present on the surface of the Earth.

The newly identified global EMs were used to unmix the collections of both OLI and ETM+ underflight spectra. Figure 24 shows the comparison of SVD fraction estimates from

Landsat 8 OLI spectra as unmixed using the previous (Small and Milesi, 2013) global EMs and the new underflight OLI EMs. As expected given the new, more reflective substrate EM, substrate fractions are substantially lower and dark fractions are substantially higher with the new EMs than with the old. Note that the x-axes of the Substrate and Dark plots are truncated at upper bounds of 1.2 and lower bounds of -0.2, respectively. A substantial number of pixels have substrate fractions as high as 1.4 and dark fractions as low as -0.4 when unmixed with the old EMs. This is expected as a result of the significantly higher SWIR reflectance of the new OLI substrate EM. The new EMs more effectively span the global mixing space and result in the physically plausible bounds of 1.0 and 0.0 for these fractions. By extending the apexes of the Substrate and (to a lesser degree) Vegetation EMs, the new OLI & ETM+ mixing spaces encompass the earlier mixing spaces bounded by the older EMs.

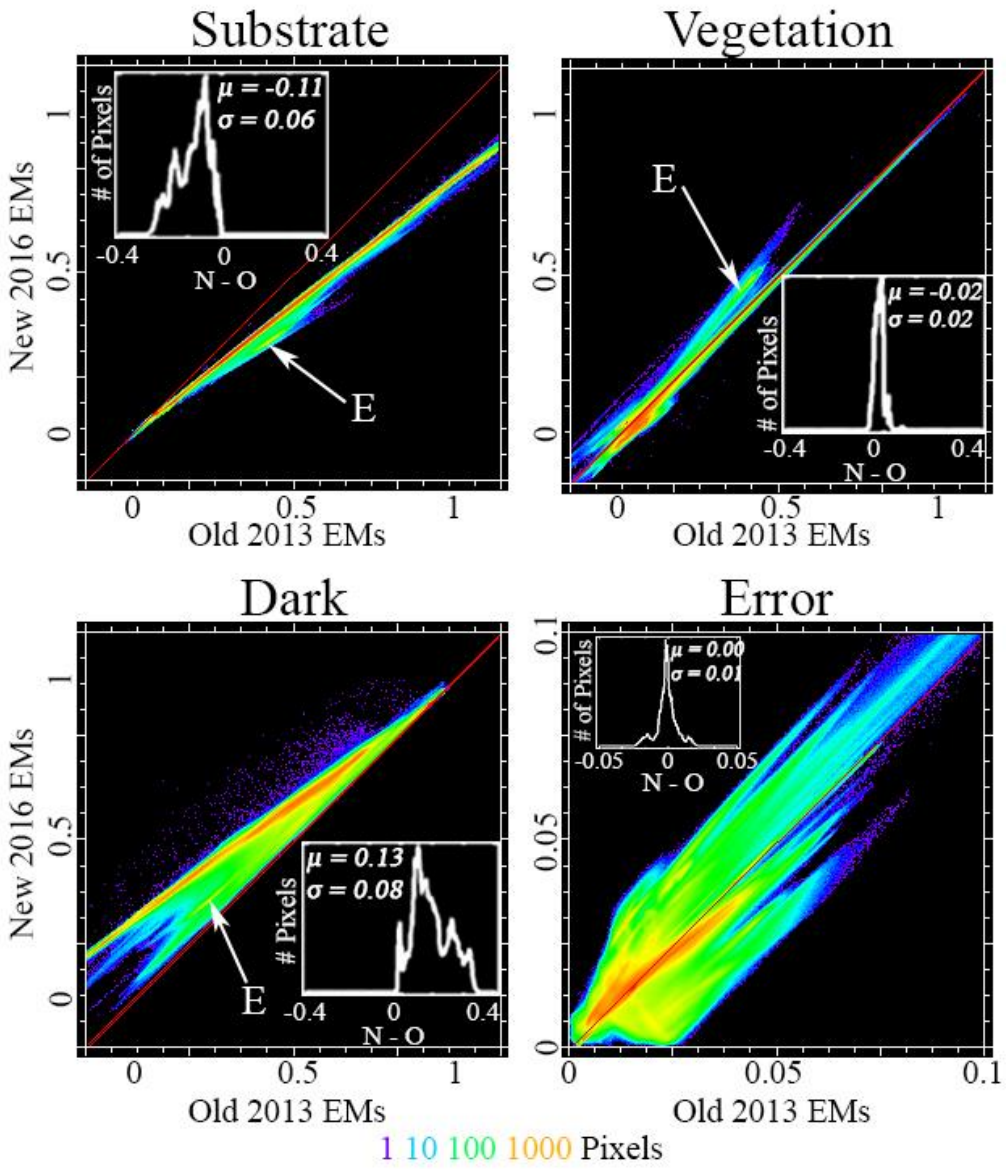

Figure 24. SVD fraction intercomparison for 80,910,343 Landsat 8 spectra by unmixing with old (Small & Milesi 2013) global EMs and the new 2016 OLI EMs. OLI fractions unmixed with both sets of EMs are strongly linear – even though the EMs were derived from independent global collections of spectra. Unmixing with old EMs shows a clear bias toward higher substrate (μ = -0.11) and lower dark fractions (μ = +0.13) than using the new EMs. Vegetation fraction shows a small bias (μ = +0.02). Error fractions are slightly lower for the new EMs than the old EMs,

but > 98% of all pixels have error < 5% for both models. The cluster of pixels distinctly plotting off the linear S, V, and D relations corresponds to evaporites (E) which are not well represented by either simple 3 EM model. Histogram insets show fraction difference (New – Old) between the two models.

The vegetation fractions in Fig. 5 plot close to the 1:1 line, indicating that vegetation estimates are essentially unchanged between the old and new sets of EMs. RMS error magnitudes are essentially unchanged between the two sets of EMs, with > 98% of all pixels showing error < 5%. As expected, the evaporites plot distinctly off the 1:1 line for all fractions, showing reduced S, increased V, and reduced D fractions relative to the rest of the global space. These values are clearly erroneous and reflect the inability of the SVD model to represent evaporite reflectance accurately. The evaporite EM is not included in the SVD model because evaporites represent a small fraction of Earth's surface and lie outside the primary SVD hull that represents most landscapes. However, the quasi-linear binary mixing trend between the evaporite and dark EMs suggests that a linear mixture model might be useful for mapping variations in moisture content of evaporites. We do not include an evaporite EM here because our single acquisition is not necessarily representative of the true diversity of evaporites and range of moisture contents. We omit ice and snow EMs for the same reason.

Figure 25 shows the cross comparison between Landsat 8 underflight fractions unmixed using the new OLI global EMs (thick lines from Figure 23) and Landsat 7 underflight fractions unmixed using the corresponding new global ETM+ EMs (thin lines from Figure 23). Biases for all fractions are small ($-0.01 < \mu < 0.01$) and all fractions cluster tightly around the 1:1 line ($\sigma = 0.03$ for all fractions and $\sigma = 0.00$ for error). The small number of pixels plotting substantially off the 1:1 line can generally be visually identified as either: 1) movement of macroscale clouds, 2)

microscale atmospheric parameters such as aerosol or water vapor content which changed over the 1-6 minutes between satellite overpasses or 3) land cover types poorly fit by the global SVD model such as snow/ice or shallow/turbid water. The evaporite cluster remains clearly distinct as a reminder of the limits of the model. Some of the dispersion about the 1:1 line may also be attributed to spatial misregistration between Landsat 7 and 8, although visual comparison shows qualitatively excellent coregistration in most cases. This suggests that subpixel displacements between the Landsat 7 and Landsat 8 acquisitions may introduce fraction differences of several percent in some cases, although the majority of pixels agree to well within 3%. Pixels from the evaporite pan are included in the calculation of the descriptive statistics listed here. Exclusion of the evaporite pan would result in a minor reduction in the bias, dispersion, and overall RMS misfit reported here. We choose to include the evaporites in our statistics in order to provide a more conservative estimate of the power of the model on a global scale. The linearity, lack of bias, and tight clustering of these scatterplots suggest TM/ETM+ and OLI imagery can be safely used interchangeably when unmixed using these global EMs. Although subtraction of the fraction bias values given here might improve agreement between TM/ETM+ and OLI fractions, the bias in each case is significantly smaller than the 0.03 to 0.07 fraction estimate uncertainty found in vicarious validations of Landsat SVD fractions with aggregated SVD fractions from near simultaneous WorldView2 acquisitions (Small and Milesi, 2013).

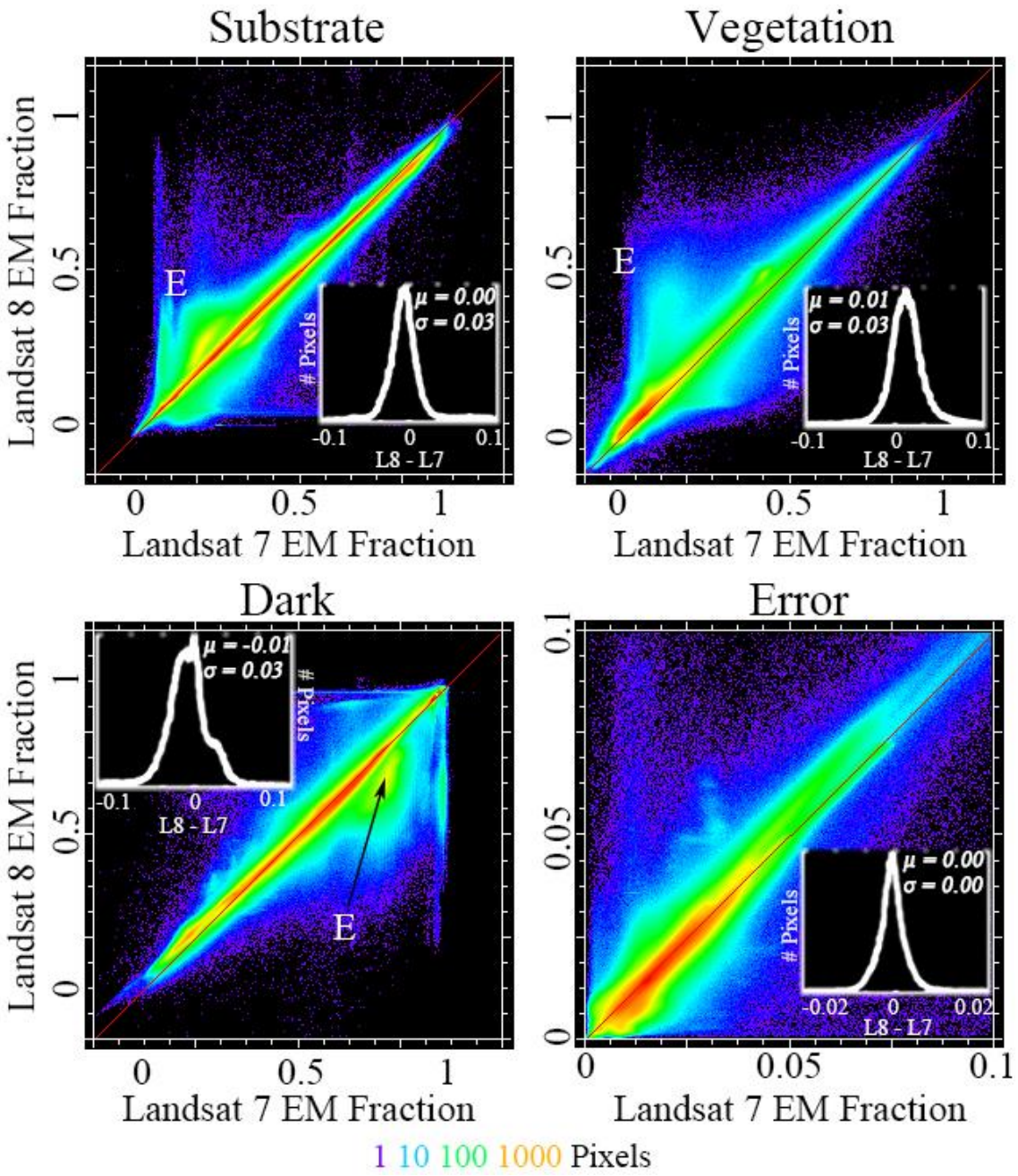

Figure 25. Intercomparison of SVD fractions from 80,910,343 near-simultaneous ETM+ and OLI spectra using the new underflight ETM+ and OLI EMs. All fraction (including error) show minimal bias (≤ 1%). Scatter corresponds to pixels with changing atmosphere in the 1-6 minutes between satellite overpasses or subpixel displacements between images. Evaporites (E) are not well represented by the SVD model so they also plot off axis. Inset histograms show fraction difference distributions. All three SVD fractions show > 95% of all pixels with differences in the

range +/- 5%. Error differences show 98% of all pixels have < 1% change across sensors for the SVD model.

As discussed by (Holden and Woodcock, 2016), differences in the OLI and ETM+ spectral responses have implications for comparability of spectral indices. Vegetation indices are a class of commonly used spectral indices with a direct relationship to one of the land cover fractions (i.e. vegetation fraction). While the relationship between indices for Landsat ETM+ has already been shown (Small and Milesi, 2013), this relationship may change on the global scale for OLI due to changes in NIR band positioning resulting in small changes in the intensity of the red edge. To illustrate the new relationship for OLI and the new global EMs from this study, we compare three commonly used vegetation indices with vegetation fraction estimates for the diversity of Landsat 8 OLI spectra in the underflight collection. Figure 26 shows the relation between subpixel vegetation fraction (Fv) as estimated with the new global SVD EMs and three commonly used vegetation indices: Normalized Difference Vegetation Index (NDVI, (Rouse et al., 1974)), Enhanced Vegetation Index (EVI, (Huete et al., 2002)), and Soil Adjusted Vegetation Index (SAVI, (Huete, 1988)).

The equation used for NDVI is:

$$\frac{NIR - V_r}{NIR + V_r}$$

The equation used for EVI is:

$$2.5 * \frac{NIR - V_r}{NIR + 6 * V_r - 7.5 * V_b + 1}$$

The equation used for SAVI is:

$$1.5 * \frac{NIR - V_r}{NIR + V_r + 0.5}$$

The relationship between SAVI and Fv is relatively linear for most pixels with Fv > 0.2, although a substantial bias is present and variance is wide at low values. The relationship between EVI and Fv is also linear, although with considerable variability and positive offset from the 1:1 line. The relationship between NDVI and Fv is substantially more complex and shows the well-known saturation effect at high vegetation fractions.

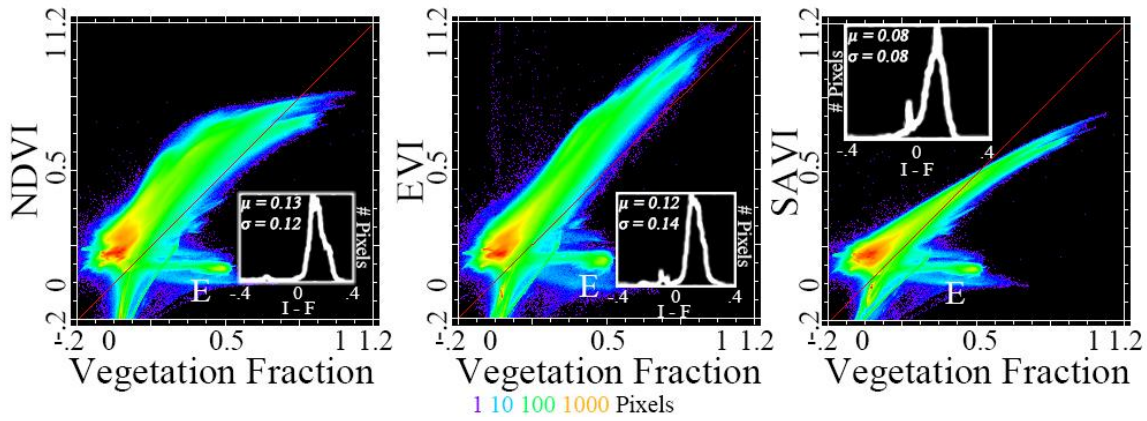

Figure 26. Vegetation index intercomparison. NDVI, EVI, and SAVI relative to vegetation fraction of the same 80,910,343 OLI spectra. SAVI and EVI are quasi-linear functions of vegetation fraction, but with varying dispersion and slope. NDVI shows nonlinear saturation above 0.5 with considerable dispersion at all fractions.

Discussion

The complex relationships of the vegetation indices shown in Figure 26 may not be intuitive given their arithmetic simplicity. This complexity is not a function of the geographic limitation of the study or of the limitations of SMA. Instead, the complexity can be shown to have a simple physical explanation.

To illustrate the basis for the complexity of these relations, we simulate the effects of subpixel soil reflectance, shadow and atmospheric scattering on these vegetation indices, compared to true vegetation fraction. Consider a hypothetical 30 x 30 m Landsat pixel filled with some amount of green vegetation and some amount of exposed soil and some amount of shadow. Based on the solar geometry illuminating the pixel, there will be some variable amount of area (viewed from directly above) of subpixel shadow cast by the roughness of the soil and the height and geometry of the vegetation. Areas in deep shadow are illuminated only by diffuse scattering with a spectrum dominated by Rayleigh scattering in the atmospheric column between the ground and sensor – as illustrated by the Dark EM. Between deep shadow and illuminated substrate and vegetation is a continuous triangular plane of spectral mixtures. This plane includes 100% illuminated vegetation with no soil or shadow, 100% illuminated soil with no vegetation or shadow, and 100% deep shadow (Rayleigh scattering only) – as well as all combinations thereof. In the case of single scattering, the sensor essentially integrates these continuous endmember spectra as a linear sum into a single 6-element broadband spectrum. We use the atmospherically corrected LEDAPS surface reflectance EMs from (Small and Milesi, 2013) with the linear spectral mixture model to simulate all possible integer mixtures of substrate, vegetation and shadow, then compute vegetation indices (NDVI and EVI) for each simulated mixed pixel.

Figure 27 and Figure 28 show the results of a Monte Carlo simulation for every possible mixture of vegetation, soil and shadow in 1% increments, resulting in 5050 simulated Landsat spectra. This simulation is run for 3 different levels of atmospheric "noise" (in the form of adding an increasingly opaque Rayleigh scattering spectrum as the dark EM) based on the expected analytical relationship between scattering of light by particles much smaller than the wavelength ($r \alpha \lambda^{-4}$). The simulation is also run for 3 different background soils (produced by varying the amplitude of the soil spectrum as the substrate EM). A common vegetation spectrum was used for all runs and was chosen to represent a sample broadband spectrum of healthy photosynthetic vegetation.

Fv, NDVI and EVI are then computed for all of these simulated mixed pixels. As expected, inversion of the linear SVD model yields accurate results for Fv, with minimal bias and scatter (in all cases $\mu < 0.5\%$ and maximum error of any pixel < 2.5%), with nearly uniform dispersion across the full range of values. The correlation between "true" input fractional vegetative cover and Fv estimated by unmixing using SMA in this model is 0.9999.

However, the behavior of the vegetation indices is more complex. Varying the amplitude of atmospheric noise or the spectrum of the soil substrate can substantially alter the bias and curvature of the indices. Over a wide range of soils, EVI exhibits substantial linearity with Fv, although it consistently plots above the 1:1 line for all but the brightest soil. EVI is also shown to deviate more strongly from linearity with more severe atmosphere, especially at high vegetation fractions. NDVI demonstrates its well-known saturation at high values and greatly variable nonlinear dependency on the soil spectrum.

This range of values for spectral indices with small variations in atmospheric and soil parameters is a result of the functional form of the equations used in the computation of the

indices. NDVI is a simple ratio of the sum and difference of 2 bands. EVI introduces the visible blue band in order to account for atmospheric variability, and exhibits substantially enhanced stability over a range of conditions as a result. Fv uses the full information content of all 6 bands in the spectrum and explicitly accounts for the contributions of both soil and shadow. This results in enhanced theoretical stability of fraction estimates over indices based on only 2 or 3 bands – stability which also applies to any systematic perturbations which affect all pixels equally that may be introduced by the changes in spectral response between ETM+ and OLI.

To the extent that the perturbations affect the EMs in the same way they would affect any other pixel, selection of new EMs will adjust the model and correct the subpixel fraction estimates accordingly. This illustrates two fundamental strengths of the linear mixture model relative to indices that use a subset of bands and do not account for other factors contributing to the mixed pixel reflectance. The use of standardized global endmembers extends these benefits by making fraction estimates intercomparable across time and space. We note that the availability of standardized global endmembers in no way reduces the utility of locally derived, application-specific endmembers. Given the ease with which fraction estimates are obtained, analyses can easily include fractions from both local and global endmembers for comparison. In fact, given the spectral diversity of the plane of substrates, we advocate the use of local substrate endmembers which may often be more suitable for substrate-oriented analyses than the very bright substrate endmember given here.

Importantly, we also note that this stability also only extends to systematic perturbations which propagate into the EMs. For instance, linear mixture models are not able to correct for perturbations to the reflectance spectrum produced by spatially and temporally localized atmospheric variability. The global linear mixture model presented here, and indeed no linear

mixture model at all, can fully resolve most atmospheric effects – or any similar effects which are not systematic perturbations to the spectral mixing space. This is particularly the case when the effects are nonlinear.

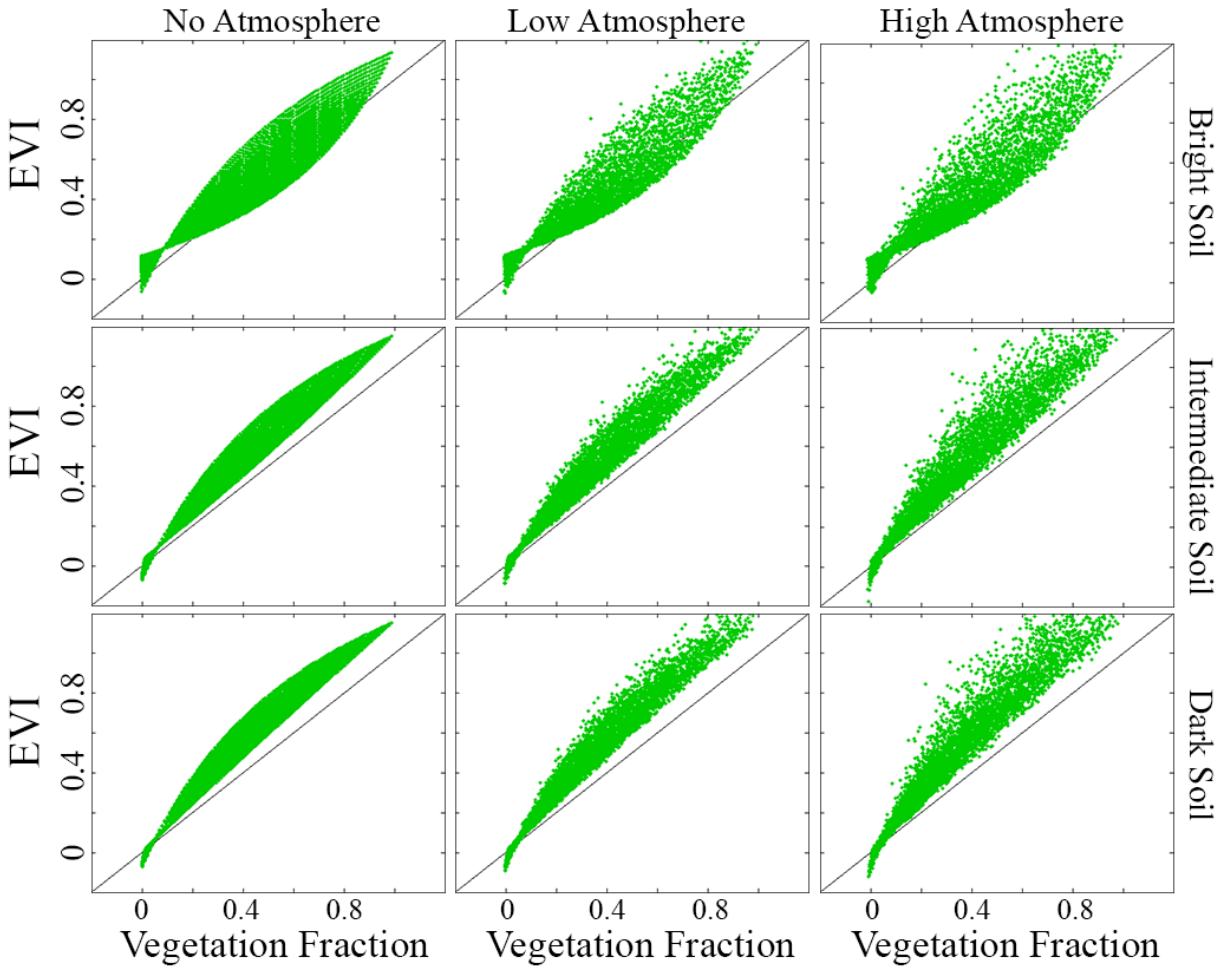

Figure 27. Calculation of EVI for theoretical pixels containing every possible integer combination of subpixel soil, vegetation and shadow. EVI exhibits more linearity over a wider range than NDVI. High values of EVI show sensitivity to atmospheric perturbations.

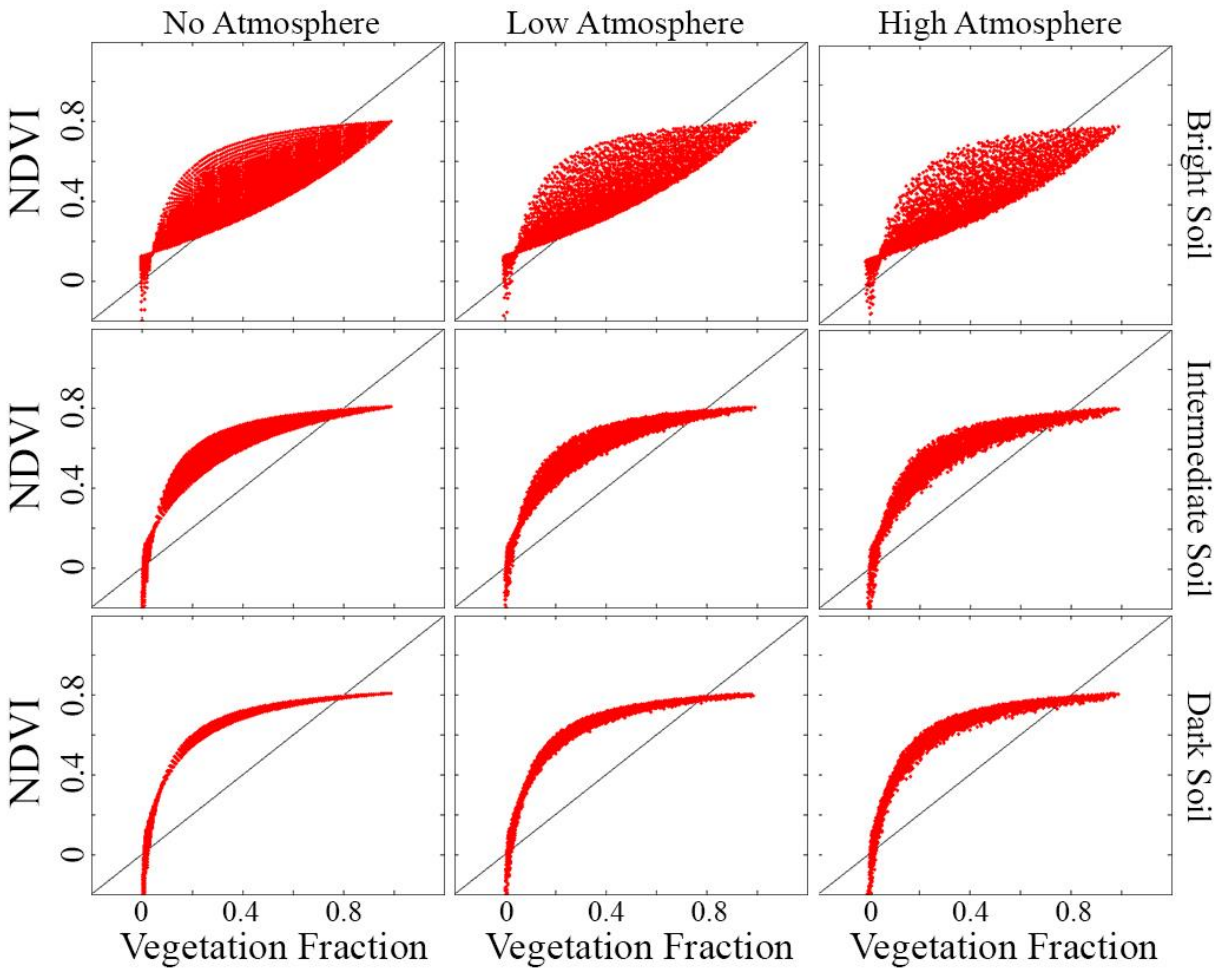

Figure 28. Calculation of NDVI for theoretical pixels containing every possible integer combination of subpixel soil, vegetation, and shadow. Slight variations in the amount of atmospheric perturbation (simulated as Rayleigh scatter times a small random number) and brightness of the soil substrate can yield substantial differences in the value of the index.

Conclusions

Subpixel EM fractions for Landsats 7 and 8 imaged in underflight configuration over a wide range of land cover show considerable agreement and can be well-characterized by the simple 1:1 relation with minimal bias or scatter. RMS misfit for both sensors using these new models remains < 5% for > 98% of the > 80 million pixels, as good or better than the previous EMs. It is also notable that no atmospheric correction was attempted for this study (beyond the selection of subscenes which appeared to be cloud-free). The increasing availability of standardized surface reflectance products should only improve upon this result. The agreement found in this study is testament to the work done by those at NASA, the USGS, and all those who are responsible for the design and implementation of the radiometric cross-calibration of these sensors.

The results of the EM fraction comparison suggest that the differences in bandpasses between the two sensors can effectively be taken into account by the use of new EMs based on the near-simultaneous imaging of the same geographical locations by the two sensors – with no additional radiometric correction. In addition, these EMs now more fully span the global mixing space than previous EMs due to the inclusion of additional bright sands which extend the plane of substrates beyond previous studies. We suggest that these new global EMs supplant the EMs from previous studies. These EMs are freely available online at: www.LDEO.columbia.edu/~small/GlobalLandsat/ and are included here as supplementary materials in plain text format.

However, the behavior of spectral indices, as already noted by others, is substantially more complex and may require cross-calibration beyond direct download of L1T imagery from

the USGS archive if such indices are to be used operationally to compare TM/ETM+ and OLI imagery, as discussed by (Holden and Woodcock, 2016) and (Roy et al., 2016).

4. Spectral Mixture Analysis as a Unifying Framework for the Remote Sensing of Evapotranspiration

Abstract

This study illustrates a unified, physically-based framework for mapping landscape parameters of evapotranspiration (*ET*) using spectral mixture analysis (SMA). The framework integrates two widely used approaches by relating radiometric surface temperature to subpixel fractions of substrate (*S*), vegetation (*V*), and dark (*D*) spectral endmembers (EMs). Spatial and temporal variations in these spectral endmember fractions reflect process-driven variations in soil moisture, vegetation phenology, and illumination. Using all available Landsat 8 scenes from the peak growing season in the agriculturally diverse Sacramento Valley of northern California, we characterize the spatiotemporal relationships between each of the *S, V, D* land cover fractions and apparent brightness temperature (*T*) using bivariate distributions in the *ET* parameter spaces. The dark fraction scales inversely with shortwave broadband albedo ($\rho < -0.98$), and show a multilinear relationship to *T*. Substrate fraction estimates show a consistent ($\rho \approx 0.7$ to 0.9) linear relationship to *T*. The vegetation fraction showed the expected triangular relationship to *T*. However, the bivariate distribution of *V* and *T* shows more distinct clustering than the distributions of Normalized Difference Vegetation Index (*NDVI*)-based proxies and *T*. Following the Triangle Method, the *V* fraction is used with *T* to compute the spatial maps of the *ET* fraction (*EF*; the ratio of the actual total *ET* to the net radiation) and moisture availability (*Mo*; the ratio of the actual soil surface evaporation to potential *ET* at the soil surface). *EF* and *Mo* estimates derived from the *V* fraction distinguish among rice growth stages, and between rice and non-rice agriculture, more clearly than those derived from transformed *NDVI* proxies. Met station-based reference *ET* & soil temperatures also track vegetation fraction-based estimates of *EF* & *Mo* more closely than do *NDVI*-based estimates of *EF* & *Mo*. The proposed approach using S, V, D

land cover fractions in conjunction with T (SVD+T) provides a physically-based conceptual framework that unifies two widely-used approaches by simultaneously mapping the effects of albedo and vegetation abundance on the surface temperature field. The additional information provided by the third (Substrate) fraction suggests a potential avenue for *ET* model improvement by providing an explicit observational constraint on the exposed soil fraction and its moisture-modulated brightness. The structures of the *T*, *EF* & *Mo* vs SVD feature spaces are complementary and that can be interpreted in the context of physical variables that scale linearly and that can be represented directly in process models. Using the structure of the feature spaces to represent the spatiotemporal trajectory of crop phenology is possible in agricultural settings, because variations in the timing of planting and irrigation result in continuous trajectories in the physical parameter spaces that are represented by the feature spaces. The linear scaling properties of the SMA fraction estimates from meter to kilometer scales also facilitate the vicarious validation of *ET* estimates using multiple resolutions of imagery.

Introduction

Water is critical to life on Earth: metabolic pathways rely on the chemistry of aqueous solutions, plant physiology requires cooling through stomatal water loss, and landscape-scale patterns in ecological communities often develop around the availability of near-surface water (or lack thereof). The movement of water between components of the Earth system therefore connects the biosphere with the lithosphere and the atmosphere. Evapotranspiration (*ET*; the sum of evaporation and transpiration) is a central mechanism in this exchange, describing the directional transfer of water from the Earth's surface to its atmosphere. In addition to its importance for global biogeochemical cycles, *ET* also plays a major role in Earth's surface energy balance (SEB). The thermodynamic implications of *ET* in the SEB result in its

fundamental importance in the climate system, where clear global teleconnections are observed between *ET* and phenomena such as the El Niño–Southern Oscillation (Miralles et al., 2013), in addition to direct relationships between soil moisture and temperature (Miralles et al., 2012). The sheer variety of biogeophysical systems that are impacted by *ET* demonstrate the importance of accurate global distributions of the components of *ET* (Miralles et al., 2011) and characterization of multidecadal trends (Zhang et al., 2016) for our understanding of, and ability to predict changes in, fundamental aspects of the Earth system.

In addition to its importance for understanding fundamental Earth system processes, *ET* also has clear practical applications. *ET* has long been recognized as a practical indicator of plant water stress (Idso et al., 1977; Jackson et al., 1981, 1977). In agricultural settings, *ET* monitoring has been used for water resource regulation and planning in water-limited regions such as the western United States (Allen et al., 2005) as well as to improve estimates of irrigation need (Bastiaanssen et al., 2005; Farahani et al., 2007). In natural environments, *ET* has been used for global biodiversity assessments (Fisher et al., 2011; Gaston, 2000) as well as to assess regional water consumption by invasive species (Shafroth et al., 2010). For recent reviews of the potential applications of *ET* monitoring, as well as outstanding unresolved questions, see (Anderson et al., 2012).

Despite its centrality to such a wide range of fundamental Earth systems, accurate and consistent estimation of *ET* remains a challenge. For instance, a recent analysis found that over 50 models currently exist to compute potential *ET*, and that model choice can impact flux estimates by over 25% (Fisher et al., 2011). Uncertainty in *ET* estimation has substantial implications for our ability to manage agriculture and to monitor wildlands, as well as for our understanding of deeper questions about the Earth system, such as the amplitude of global water

and energy fluxes. This uncertainty is, at least in part, a result of differences in the data streams, underlying assumptions, and conceptual approaches that are used by each model. The more that these disparities can be integrated into a single framework, the more that it will be possible to reduce the overall uncertainty in *ET* estimation.

Algorithms that estimate *ET* parameters on landscape scales generally rely on observations from optical and thermal remote sensing. For *ET* studies, remote sensing observations are most commonly used to provide direct estimates of fractional vegetation cover (*V*), surface temperature (*T*), and albedo (α). The relationships among these three quantities can be understood in the context of their bivariate distributions. The distribution of *V* vs *T* gives information about plant-based evapotranspirative cooling and is fundamental to the physical basis of many popular *ET* models (e.g., (Allen et al., 2007; Bastiaanssen et al., 1998; Carlson and Boland, 1978; Moran et al., 1994)). Leaf area index (*LAI*) is an additional parameter that has been shown to have a significant impact on *ET* partitioning (Wang et al., 2014), and it is often used as an input in *ET* models. However, remote sensing is generally used to estimate *LAI* using a direct empirical relationship with *V*. Because of this intrinsic dependence between the remote sensing estimates of *LAI* and *V*, the *LAI* vs *T* and *V* vs *T* relationships contain fundamentally similar information. The distribution of α vs *T* has also been long recognized (Menenti et al., 1989), and provides information about soil moisture ((Ångström, 1925; Idso et al., 1975)) and roughness (Matthias et al., 2000). α vs *T* has been incorporated into a popular *ET* model by (Roerink et al., 2000). Recent work by (Merlin et al., 2014) has developed a model based on fusion of both the *V* vs *T* and α vs *T* relationships, with encouraging results.

For the vast majority of current *ET* estimation algorithms and associated Surface–Vegetation–Atmosphere Transfer (SVAT) models, vegetation abundance is computed with a

spectral index. The specific index used varies from model to model, but all spectral indices use only part of the information present in multispectral imagery. Many models (e.g., (Jiang and Islam, 1999; Kustas et al., 2003)) rely directly upon the Normalized Difference Vegetation Index (*NDVI*). *NDVI* has a number of known flaws, including scaling nonlinearities ((Elmore et al., 2000; J. C. Price, 1990; Christopher Small, 2001)), sensitivity to both soil background and atmospheric effects ((Small and Milesi, 2013; Smith et al., 1990)), and saturation effects over a wide range of vegetation fractions (Small and Milesi, 2013). In an attempt to mitigate these problems, *NDVI* is often normalized using linear (e.g., (Choudhury et al., 1994)) or quadratic (e.g., (Carlson, 2007; Carlson and Ripley, 1997; Sun, 2016)) transformations. Each spectral index, transformed or untransformed, gives different estimates of vegetation abundance, which then result in differences in the estimated *ET*. If these metrics could be improved and standardized, *ET* models could be made more accurate, and cross-model standardization could be more effective. One recent study (Li et al., 2018) has recognized the impact of subpixel heterogeneity on *ET* model accuracy and used a spectral mixture model to estimate subpixel fractions of different agricultural crops with different *ET* characteristics. These crop fractions were used as inputs to the SEBAL and SEBS models, resulting in improved accuracies of between 7% and 18% for different crop types.

Spectral Mixture Analysis (SMA; (Adams et al., 1986; Gillespie et al., 1990; Smith et al., 1985)) is a physically-based method that uses the full reflectance spectrum, rather than a subset of bands, to estimate *V* simultaneously with fractions of other spectral endmembers within each pixel's field of view. SMA can explicitly account for illumination effects, as well the reflectance of the soil and non-photosynthetic vegetation (NPV) background, substantially improving estimates at low vegetation abundance (Smith et al., 1990). Because SMA relies on the area-

weighted linear mixing of radiance from materials within the pixel, *V* estimates are relatively insensitive to sensor spatial resolution, and they have been shown to scale linearly from 2 m to 30 m (Christopher Small, 2001; Small and Milesi, 2013), as well as from meter-scale field measurements (Elmore et al., 2000). This simple linear scaling could be a key advantage for *ET* studies, given the widely recognized scaling nonlinearities of many *ET* estimates (e.g., (Baldocchi et al., 2005; Brunsell and Anderson, 2011; Brunsell and Gillies, 2003b; Ershadi et al., 2013; McCabe and Wood, 2006; Sharma et al., 2016)). SMA fraction estimates are sensitive to the spectra of the endmember (EM) materials, but previous work has characterized the global multispectral mixing space and proposed standardized generic EMs, which well-describe the majority of the Earth's land environments, and are calibrated across sensors ((Small, 2004; Small and Milesi, 2013; Sousa and Small, 2017a)).

In addition to providing enhanced estimates of *V*, SMA simultaneously provides accurate estimates of two additional physically meaningful quantities: (1) the subpixel areal abundances of soil, rock, and NPV substrates (*S*), and (2) dark features (*D*) such as shadow, water, and low-albedo surfaces. These estimates are made at subpixel resolution and with trivial computational cost. Dark fraction estimates represent the effects of albedo (α), illumination geometry (flux density), atmospheric opacity, and soil moisture content, thereby modulating the overall amplitude of the reflectance signal. Substrate fraction estimates provide information about the compositional properties of the soil, and NPV substrate background at each pixel. To our knowledge, the simultaneous estimation of vegetation fraction, soil+NPV background, and albedo provided by standardized SMA has not yet been incorporated into *ET* estimation approaches. This could represent a missed opportunity. When compared against coincident *T* measurements, SVD fractions can provide a unifying framework which incorporates two major

existing approaches to *ET* estimation (*V* vs *T* and α vs *T*), and also includes a novel, potentially useful supplement (*S* vs *T*). By estimating *S, V,* and *D* fractions simultaneously, SMA automatically provides information on their respective contributions to the aggregate reflectance spectrum of each pixel. Therefore, multitemporal SVD fractions provide a self-consistent measure of the time-varying tradeoff between illuminated vegetation and soil fractions and moisture-modulated soil albedo—two of the primary factors determining the combined evaporative and transpirative processes that control the surface temperature field.

The primary purpose of this analysis is to explore the SVD model as a conceptual framework for *ET* estimation. While the *V* vs *T* relationship has been long recognized in *ET* studies (Carlson et al., 1994; J. C. Price, 1990), to our knowledge it has been only investigated using *NDVI* and its transformations, not by *V* as estimated by standardized SMA. Similarly, the α vs *T* relationship has already been explored, but only by estimating α through forward modeling. The connection between the α vs *T* and *D* vs *T* relationships has not yet been documented. In addition, to our knowledge, the relationships between *S, V, D,* and the *ET* Fraction (*EF*) and Moisture Availability (*Mo*) estimates have not yet been characterized. Finally, we evaluate the *EF* and *Mo* estimates using weather station data, and discuss the implications of this approach for improving the accuracy and consistency of *ET* estimates, informing flux partitioning, and providing an optimized, unifying approach to extract maximum value from coincident multispectral and multiresolution optical and thermal imagery.

ET Model Overview

Models Relying on V vs T

The combined use of optical and thermal imagery for *ET* monitoring has been the focus of extensive previous work. A plethora of physical and statistical models have been built to

approach the problem. One of the first approaches ((Carlson et al., 1994; J. C. Price, 1990) and subsequent publications; reviewed by (Carlson, 2007)) was based on the observed triangular (or trapezoidal (Moran et al., 1994)) relationship in the vegetation index vs temperature space for many landscapes. The physical basis for this triangular relationship is the evapotranspirative cooling that occurs in dense well-watered vegetation, and which may or may not occur in unvegetated areas, depending on the moisture availability.

Other popular approaches, such as the Surface Energy Balance Algorithm for Land (SEBAL) (Bastiaanssen et al., 1998) and Mapping EvapoTranspiration at high Resolution with Internalized Calibration (METRIC) (Allen et al., 2007), are primarily based on the information contained in the spatial variability of the temperature field across a landscape. Another class of approaches, most notably the ALEXI/DisALEXI model ((Anderson et al., 2011, 2004, 1997)), rely on the time differencing of the thermal field to capture variations in the diurnal temporal trajectory of different land covers. Recently, a modification of the Two-Source Energy Balance (TSEB) model to include contextual vegetation information has been shown to yield encouraging results (Nieto et al., 2018). Despite their different sets of assumptions and governing equations, all of these models generally require vegetation abundance estimates in one form or another (even if only for initial roughness estimates), and they rely on spectral indices to provide them.

Models Relying on α vs T

Early work based in north Africa observed a strong relationship between the overall surface reflectance (albedo) and *ET* (Menenti et al., 1989). This relationship was interpreted in the context of the governing equations for surface energy balance. Four models were presented that could potentially describe the physical meaning of the relationship. These were later brought into a single framework by (Roerink et al., 2000). This model decomposes the α vs *T* relationship

into evaporation-controlled and radiation-controlled regimes. The evaporation-controlled regime is active at lower albedos, and is characterized by an increase in T with increasing α, as is physically explained by the moisture darkening of soils. Once the soils are sufficiently dry for the effects of moisture darkening to become negligible, the sign of the relation reverses, and T decreases with increasing α. The physical explanation for this is the decreased absorption of incident radiation at higher albedos. Comparative studies of the α and T and V vs T relations (e.g., (Galleguillos et al., 2011; Yang and Wang, 2011)) can provide insights into the relative strength of the physical processes underlying each conceptual framework. More recently, Ref. (Merlin et al., 2014) have developed an integrated approach which unites the V vs T and α vs T relations into a single model.

The above summary of models is not intended to be comprehensive. Rather, it is designed to present the reader with a sampling of the range of ET estimation methods that are extant in the literature, and to show the ways in which V, α, and T are incorporated into ET estimation algorithms. For more comprehensive reviews of these methods (and more), see (Carter and Liang, 2018; Kalma et al., 2008; Petropoulos et al., 2009).

Spectral Mixture Analysis

Multispectral satellite imaging sensors generally measure reflectance in 4 to 12 optical wavelength intervals. Vegetation indices are generally based on only two or three of these wavelengths, leveraging the distinctive visible-near infrared (NIR) “red edge” that makes vegetation abundance one of the strongest signals that are present in multispectral data. The information present in the surface reflectance at other visible and IR wavelengths, unused by spectral indices, can provide significantly more information than vegetation abundance alone.

SMA (Adams et al., 1986; Gillespie et al., 1990; Smith et al., 1985) is a well-established, physically-based way to retrieve this additional information.

SMA assumes area-weighted linear mixing of upwelling radiance within the Instantaneous Field of View (IFOV) of each multispectral pixel. While not always a valid assumption, linear mixing has been shown by (Johnson et al., 1983; Singer, 1981; Singer and McCord, 1979) to have a solid theoretical and observational basis for practical applications. SMA treats each pixel spectrum as a linear combination of pure EM spectra, and inverts a set of linear mixing equations to accurately estimate the subpixel abundance of each EM material.

Theoretically, as many materials could be mapped as wavelengths measured by the multispectral imager (4 to 12). In practice, however, 6-band Landsat spectra have been shown to essentially represent only three distinct land cover types on ice-free land surfaces ((Kauth and Thomas, 1976; Small, 2004)) corresponding to substrate, vegetation, and dark surfaces (S, *V*, and *D*). Similar EMs emerge from diverse mixing spaces of higher dimensional 12-band Sentinel-2 imagery (Small, 2018), and 224-band hyperspectral AVIRIS flight line composites (Sousa and Small, 2018a). These studies suggest that an approach based on estimation of three materials from multispectral imagery is likely to be generally applicable across most terrestrial surfaces relevant to *ET* analysis.

Reflectance spectra of the three global SVD EMs for Landsat 8 are shown in the lower left corner of Figure 29. Substrate fractions represent materials such as soil, rock, and non-photosynthetic vegetation. Vegetation fractions represent illuminated photosynthetic vegetation. Dark fractions can variously represent shadow, water, or low albedo surfaces such as mafic rocks and some impervious surfaces. The spectral mixing space spanned by the bounding *S*, *V*, and *D* EMs encompasses (nearly) the full global range of multispectral diversity of the Earth surface.

Subpixel mixtures of rock and soil substrates, and different classes of vegetation with varying structural shadow and illumination conditions, as well as substrate and vegetation types with distinct lower amplitude reflectances, all plot as various mixtures of these three generic EMs (Small, 2004). Snow, ice, evaporate materials, and shallow marine substrates occupy distinct limbs of the global mixing space, and are not well-represented by these three EMs, but they are generally not considered in *ET* studies, and will not be discussed in this analysis.

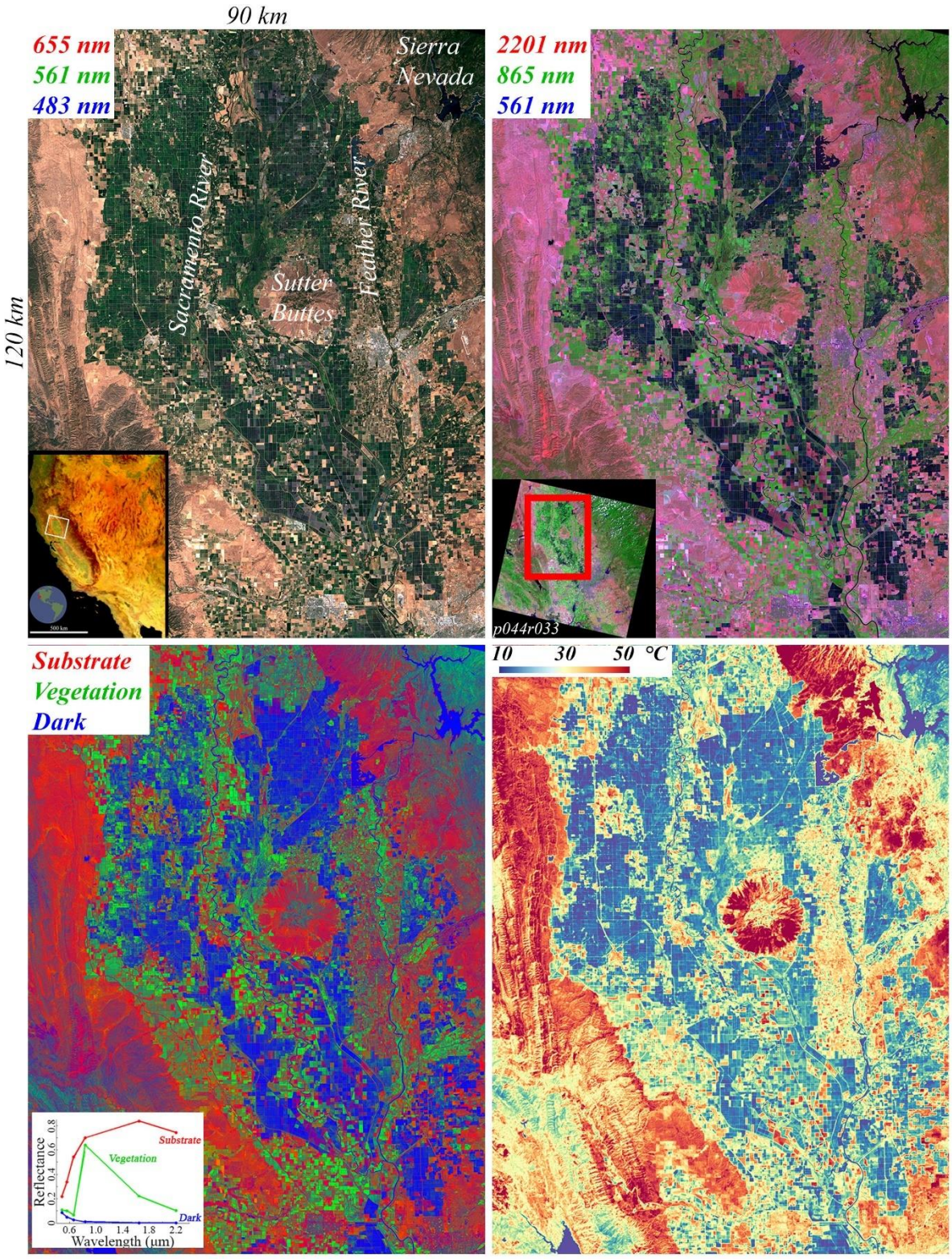

Figure 29. True color (UL), false color (UR), fraction abundance (LL) and thermal (LR) images of a diverse northern CA landscape as imaged by Landsat 8 on June 19, 2013. Green fields are

generally distinct from fallow fields and grasslands in the visible, but infrared bands shown in the false color composite allow superior discrimination. At this time of year, nearly all flooded fields are rice and nearly all green, not flooded fields are row crops & orchards. S, V, D subpixel abundances are estimated using a 3 EM spectral mixture model. Visual agreement between the S fraction and T images suggests that regions dominated by S fraction are generally hotter than regions dominated by V or D fractions.

Materials and Methods

Data

This analysis relies on optical data from the Operational Land Imager (OLI) and thermal data from the Thermal Infrared Sensor (TIRS) instruments onboard Landsat 8. Landsat data were downloaded free of charge as digital numbers (DNs) from the USGS GloVis download hub (http://glovis.usgs.gov) (USGS, 2018). Optical and thermal image data were calibrated to exoatmospheric reflectance and apparent brightness temperature, respectively, using the standard calibration procedures described in the Landsat Data Users Handbook (USGS, 2016b). All data were downloaded with Collection 1 preprocessing, which incorporates the standard correction (Gerace and Montanaro, 2017) to the well-known TIRS stray light problem (Montanaro et al., 2014). Where indicated, 30 m OLI bands were convolved with a 21 × 21 low pass Gaussian kernel to simulate the larger 100 m IFOV of the TIRS.

While optical Landsat 8 OLI imagery is now available on-demand with the standard Landsat Surface Reflectance Code (LaSRC) atmospheric correction, standard atmospherically-corrected thermal Landsat 8 TIRS imagery is not yet available. In order to provide the study with maximum generality, we do not apply atmospheric correction to either the optical or thermal images used in the study. We also include images with minor atmospheric effects to note their

potential impact on *ET* estimation. This allows for more direct comparisons with historical studies involving Landsats 4–7, which do not have the benefit of the LaSRC correction, and are forced to rely on the less accurate Landsat Ecosystem Disturbance Adaptive Processing System (LEDAPS) correction. It also allows for the use of global EMs, which are cross-calibrated to account for the differences in band positioning between the optical imaging instruments on Landsats 7 and 8 (Sousa and Small, 2017a). The study area used has the additional benefit of atmospheric dynamics, which are generally favorable for satellite imaging during the primary growing season, resulting in a relatively large number of cloud-free images.

Spectral Mixture Analysis

All OLI images were unmixed into *S*, *V*, and *D* fraction images using the global *S*, *V* and *D* EMs from (Sousa and Small, 2017a). As suggested in (Small, 2004; Small and Milesi, 2013; Sousa and Small, 2017a), local SVD EMs were also selected from the apexes of the convex hull of the image point cloud in low-order feature space, and compared against the global EMs. The local *V* and *D* EMs were nearly indistinguishable from the global EMs, but the local substrate EM was substantially darker than the global EM, as expected given the difference between the soils that are present in the study area and the sand from the Libyan Sahara identified from the global analysis. The local *S* EM was then used in conjunction with the global *V* and *D* EMs for unmixing.

Linear spectral unmixing considers the multispectral reflectance of each pixel to be an area-weighted linear sum of the constituent EM reflectances. The subpixel areal abundances of each EM are estimated through the inversion of a system of linear equations of the form:

$$f_S E_{S,\lambda_i} + f_V E_{V,\lambda_i} + f_D E_{D,\lambda_i} = R_{\lambda_i}$$

where f_S, f_V, f_D, are the relative subpixel areal abundances of the *S*, *V*, and *D* EMs; $E_{S,\lambda i}$, $E_{V,\lambda i}$, $E_{D,\lambda i}$, are the reflectances of the *S*, *V*, and *D* EMs at each wavelength; and $\lambda_i \in$ {482 nm; 561 nm; 655 nm; 865 nm; 1609 nm; 2201 nm}, corresponding to bands 2–7 of Landsat 8 OLI, respectively. A unit sum constraint was imposed with weight = 1 on the physical basis that the subpixel areal abundances are expected to sum to unity.

ET Estimation Using the Triangle Method

Because the primary purpose of this analysis is to illustrate the relationship between *S*, *V*, *D* fractions and *ET* parameters, we chose the simple and popular Triangle Method for *ET* parameter estimation. The Triangle Method fundamentally relies on the bivariate distribution of vegetation abundance and temperature. The physical principles underlying the method are: (1) soil with a high surface water content exhibits more evaporative cooling than soil with low surface water content, and (2) regions with abundant (non-water-stressed) vegetation exhibit more evapotranspirative cooling than regions with sparse (and/or water-stressed) vegetation. Regions with dense vegetation ($V \approx 1$) have a tight distribution of (relatively low) temperatures, because cooling is maximal. Unvegetated regions ($V \approx 0$) have a broad distribution of temperatures, from cool (wet soil, maximal cooling from *ET*) to hot (dry soil, no cooling from *ET*). This results in a triangular shape of the bivariate distribution of *V* vs *T*.

Following the procedure of (Carlson, 2007), a SVAT model was then used to compute expectations of *EF* and *Mo* for any arbitrary combination of *V* and *T*. *EF* is defined as:

$$EF = \text{——}$$

where LE is total actual surface ET (vegetation + soil), and R_n is the surface net radiation. Mo is defined as:

$$Mo = \frac{LEs}{}$$

where LE_s is the total actual soil evaporation, and ET_{os} is the potential ET at the soil surface radiant temperature. Mo can alternately be understood as the ratio of soil water content to that at field capacity, or the ratio of soil surface resistance to the soil surface plus atmospheric resistance.

EF and Mo are thus both relative measures of ET. EF quantifies spatially explicit information about the fraction of net radiation that is used by total surface ET. Mo quantifies spatially explicit information about the availability of water near the soil surface to participate in the ET energy exchange.

While a number of SVAT models exist, model-to-model variations generally result in only small changes in outputs in V vs T space. Regardless of SVAT model choice, a triangular pattern of EF and Mo are generated. For this analysis, we use the generalized Triangle method coefficients proposed by (Carlson, 2007) and shown in Table 1. While not specifically tailored to the landscape studied here, the general coefficients are expected by (Carlson, 2007) to yield satisfactory results in most cases, and are sufficiently accurate for the illustrative purposes of this study.

$(EF) = \sum_{i=0}^{3} \sum_{j=0}^{3} a_{ij} T^{*i} Fr^{j}$ r^2=0.9993, RMSE=0.017

a_{ij}	j=0	j=1	j=2	j=3
i=0	0.8106	-0.5967	0.4049	-0.0740
i=1	-0.8029	0.7537	0.0681	0.2302
i=2	0.4866	1.2402	-0.9489	-0.8676
i=3	-0.3702	-1.3943	-0.7359	0.3860

$(Mo) = \sum_{i=0}^{3} \sum_{j=0}^{3} a_{ij} T^{*i} Fr^{j}$ r^2=0.9994, RMSE=0.0079

a_{ij}	j=0	j=1	j=2	j=3
i=0	2.058	-1.644	0.850	-0.313
i=1	-6.490	1.112	-3.420	-0.062
i=2	7.618	3.494	10.869	4.831
i=3	-3.190	-3.871	-6.974	-16.902

Table 1. Generalized Triangle Method coefficients used to estimate EF and Mo. From Carlson (2007).

Table 1. Generalized Triangle Method coefficients used to estimate EF and Mo. From Carlson (2007).

The triangular shapes of these model outputs are then fit to the observed *V* vs *T* distribution of each image. This is done by normalizing both the observed *T* and *V* values to the range 0 to 1. *T* was normalized (to *T**) by using the linear transformation suggested in (Carlson, 2007):

$$T = \frac{T - T_{min}}{T_{max} - T_{min}} \quad \textbf{(Error! No sequence specified.)}$$

The bounding values of T_{min} and T_{max} used for all scenes were 285 K and 335 K, respectively. While *ET* estimates could be more accurate if scene-to-scene differences in air temperature were accounted for by using scene-specific T_{min} and T_{max} values, we used consistent bounding values to facilitate intercomparison between scenes. After normalization, *T** values fall in the 0 to 1 range that is expected by the SVAT model.

Theoretically, *V* estimates should not need normalization, since they directly represent a physical quantity that varies from 0 to 1, and that has been shown to scale linearly. SMA-derived *V* estimates are satisfactory in this regard, and they were not further normalized in this analysis. These estimates were compared against *NDVI* computed using the standard relation:

$$NDVI\ NDVI\ \frac{NIR-}{NIR+}$$

NDVI is well known to frequently both yield negative values and roll off well below the value of 1. For this reason, it is recommended to be transformed to fit the 0 to 1 range for the purposes of the Triangle Method. We compare two normalizations. The first normalization is *NDVI**, computed using the linear relation popularized by (Gutman and Ignatov, 1998):

$$NDVI \quad = \frac{NDVI - NDVI_{min}}{NDVI_{max} - NDVI_{min}}$$

The second normalization is $NDVI^{*2}$, computed using the quadratic transformation suggested by (Carlson, 2007):

$$NDVI \quad ^{2} = \left(\frac{NDVI - NDVI_{min}}{NDVI_{max} - NDVI_{min}}\right)^{2}$$

For this analysis, $NDVI_{min}$ and $NDVI_{max}$ values were identified to be 0.15 and 0.85, respectively, for all scenes. Finally, albedo calculations were performed using the shortwave broadband albedo coefficients from (Liang, 2001).

Study Area

The study area used for this analysis is a 120 × 90 km region comprising the Sacramento Valley of California and its surrounding foothills. The region hosts a broad diversity of soils and vegetation types. The valley is flat and dominated by high intensity agriculture. Rice is commonly grown in the clay-rich soils away from the Sacramento and Feather River channels. A diverse mix of row crops and orchards is grown in the sandier soils closer to the river channels and valley edges. The foothills of the Coast Ranges (west of the valley), Sierra Nevada (east of the valley), and Sutter Buttes (center of the valley) rise above the valley floor, and are generally

covered with mixed rainfed grasslands, which are predominantly used for grazing. The northeast and southwest corners of the scene capture coniferous and deciduous forests, which are common at higher elevations surrounding the study area. Spatially extensive human settlements are present in the southeast (Sacramento/Davis/Woodland) and central east (Marysville/Yuba City) portions of the scene. The deep reservoirs of Lake Berryessa (southwest corner) and Lake Oroville (northeast corner) are also present. The climate of the region is classified as Hot Summer Mediterranean (Köppen *Csa*), with hot, dry summers and cool, wet winters.

Figure 29 shows the region as imaged by Landsat 8 on 19 June 2013. The natural color composite image (upper left) allows for broad discrimination between the foothill grasslands, valley agriculture, and upland forests. However, substantially more information is provided by the infrared bands shown in the false color composite (upper right). Here, broad diversity is apparent in soil and NPV background reflectance, as well as enhanced discrimination between flooded rice fields (black) and non-flooded row and orchard crops (green/brown/red). The SVD fraction image (lower left) shows the subpixel areal abundance of each globally standardized EM (inset, from (Sousa and Small, 2017a)), which is estimated from the multispectral reflectance data by SMA. Vegetation indices provide an approximation of only the green channel of this image. The red channel of this image (*S* fraction abundance) shows substantial visual similarity to the hot (red) values recorded by the thermal image (lower right). The similarity between these two spatial patterns provides qualitative visual evidence suggesting a strong *S* vs *T* relationship, further explored below.

Results

The main body of results are presented as bivariate distributions in a series of density-shaded scatterplots comparing the SVD land cover fractions and transformed vegetation indices

with the *ET* parameters (Mo and EF), and brightness temperature. Because of differences in the timing of planting and irrigation of individual fields in the study area, each Landsat acquisition captures a wide variety of crops at varying stages of their phenological cycles, in addition to a diversity of fallow soils with varying moisture contents and tillage conditions. Therefore, all of the images used in this study contain nearly the full range of vegetation abundance, soil exposure, and soil moisture contents. The most pronounced differences in the bivariate distributions from date to date are related to the phenological progression of the rice crop through the peak growing season, varying somewhat from year to year. The trajectories of the clusters within the distributions are related to the evolving land cover mosaic and its effect on the surface energy balance that controls the structure of the distributions.

Vegetation Metric Comparison

We begin our analysis with a comparison of the vegetation metrics because of their centrality to *ET* estimation. The left panel of Figure 30 shows bivariate distributions of *NDVI*, *NDVI**, and *NDVI**^{2} against SMA-derived vegetation fraction (*V*) for the five most informative June Landsat 8 images in the archive. Images are arranged from top to bottom by increasing the Julian Day irrespective of year to illustrate the general features of the seasonal phenology of the region. *NDVI* shows a nonlinear relationship with *V*, overestimating at most values and rolling off prominently. The roll-off of the top of the distribution begins below 0.5 and truncates near 0.85, while the roll-off on the bottom appears to be continuous. The consistency of the $NDVI_{max}$ and $NDVI_{min}$ values of 0.85 and 0.15 across all 10 images (including five not shown in Figure 30) justifies the use of a single set of normalization bounds for all images. The residual values of 0.15 in the unvegetated areas is largely due to the positive slope between visible red and near infrared wavelengths that are generally present in bare soil spectra. *NDVI** better fills the

physically meaningful 0 to 1 range that is expected of fractional vegetation cover, but it still has notable overestimation and roll-off effects. $NDVI^{*2}$ is even more linear than *NDVI**, but the distribution is compressed towards smaller values, because squaring numbers that are smaller than 1 reduces their value. In addition, a long tail at negative *NDVI** values (truncated in Figure 30) is a result of dark materials having a smaller spectral slope than the $NDVI_{min}$ values that are representative of bare soil. When the square transform is applied, these values are projected up towards large positive $NDVI^{*2}$ values, resulting in erroneous estimates of high (sometimes over 0.5) vegetation abundance in these totally unvegetated areas. Overall, the general effect of these rescalings of *NDVI* appears to be to increase the degree of underestimation at low vegetation fractions, while retaining the overestimation at higher vegetation fractions. Notably, the saturation at high *NDVI* values, though reduced by the rescalings, still remains after squaring is applied. As a result, a wide range of vegetation fractions are placed near $NDVI^{*2}_{\max}$. The effects described here are consistent for our study area throughout the entire June Landsat 8 archive.

Bivariate distributions of *NDVI**, $NDVI^{*2}$, and *V* versus *T** are shown in the right panel of Figure 30. The density-shaded bivariate distribution for each date is shown in color, superimposed on the silhouette of the combined distribution of all dates in black. All three metrics show the expected triangular relationship, but considerably more information is evident using *V* than either of the spectral indices, visible in the form of internal clustering. Because *NDVI** generally overestimates *V*, a pronounced density of points near the upper bound ("warm edge") of the triangle in *NDVI** vs *T**

space is present. $NDVI^{*2}$ overcompensates for this effect, compressing the vegetation abundance distribution toward 0 values, and leaving the upper portion of the space sparsely populated, scattered, and concave. In comparison, *V* retains considerable structure across low,

intermediate, and high *V* values. Physically meaningful clusters are clearly identifiable in the *V* vs *T* space, which are not distinct in either of the spaces of the spectral indices. One example of this is the paddy rice, which plots at low *V* and *T* values on the 3 June 2013 image, and then progressively migrates toward higher *V* values in later images, as the crop matures and its canopy closes. Note that the rice clusters around the intermediate (0.5–0.7) vegetation fraction at the later dates, but near the maximum of the transformed *NDVI* distributions. Due to its erectophile structure, the rice canopy does not attain full closure until the end of its growing cycle, so that a substantial fraction of underlying soil or water contributes to the aggregate reflectance. In contrast, leafy vegetable crops attain more complete canopy closure at this time, and therefore occupy the upper tail of the vegetation fraction distribution.

Structure (or lack thereof) in the *V* vs *T* distribution maps onto the structure in the *ET* parameter space. Figure 31 shows this for the *ET* fraction (*EF*) using each of the *NDVI**, *NDVI**^{2}, and *V* vegetation metrics. Every image examined generally forms a triangular distribution in *EF* vs vegetation space, regardless of the vegetation metric. Pixels with high vegetation abundances converge to a single, high *EF* value, but pixels with low vegetation abundances can have either high (flooded fields or lakes) or low (dry soil or impervious surface) *EF* values. However, the amount of structure within the pixel envelope varies considerably from metric to metric. The least clustered structure is visible in the *NDVI** distribution, and the most clustered structure is visible in the *V* distribution. The compression of *NDVI**^{2} down toward small values results in a broad base to the triangular cloud, but sparse and scattered intermediate estimates. In contrast, the *V* vs *EF* plots show considerable pixel density throughout the range of *V* values, with broad clusters corresponding to physically meaningful land covers. Flooded rice paddies are clearly distinct from green (non-rice) agricultural fields, which are clearly distinct

from dry soils. These distinctions in the *EF* vs vegetation space are much more clearly represented by *V* than *NDVI** or *NDVI**^{2}.

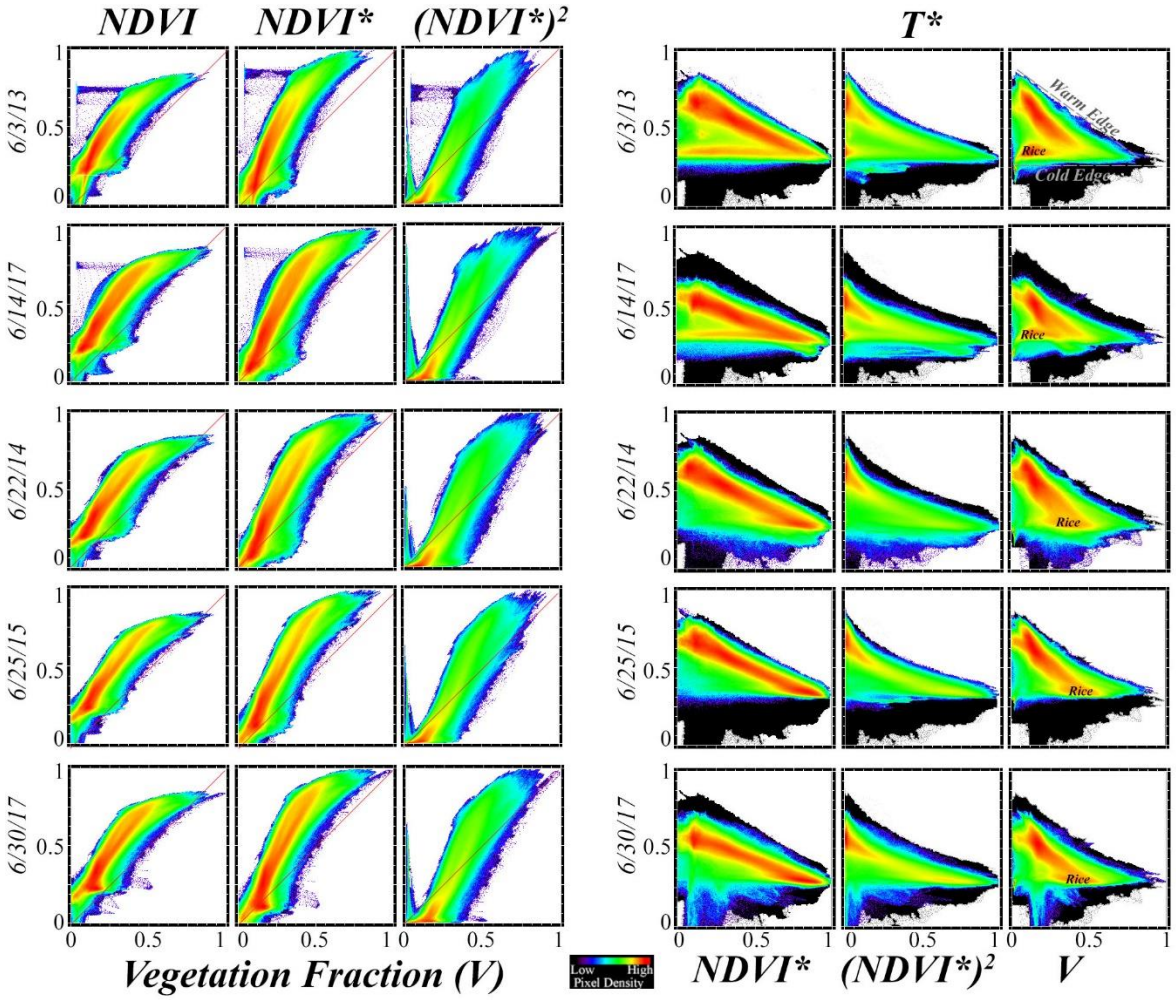

Figure 30. Vegetation metric comparison. L: Raw and transformed Normalized Difference Vegetation Index (NDVI, y-axis) vs SMA-derived vegetation fraction (V, x-axis). All three indices overestimate V at intermediate values and roll-off at high values. R: Bivariate distributions of vegetation metrics vs T all form triangular distributions. However, considerably more structure is evident in the V vs T* distributions than in the index distributions. In early June (top rows), flooded, young rice paddies form a cluster in the V vs T* distributions that is not distinguished by either index, illustrating the inaccuracy of NDVI for sparse vegetation.*

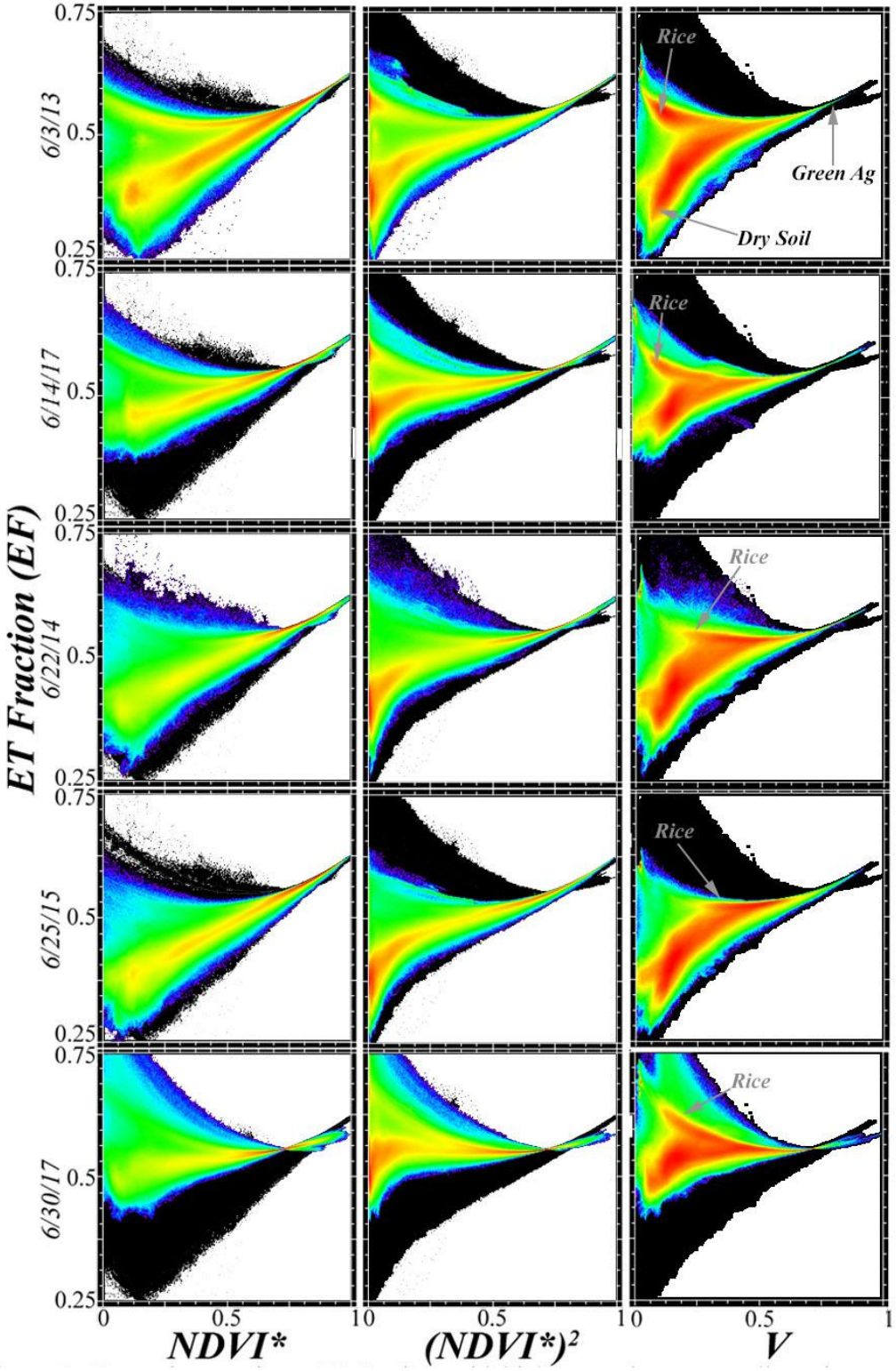

Figure 31. Vegetation metrics vs EF. Regions with high vegetation cover collapse into a tight range of EF. Regions with low vegetation can have high or low EF. For images earlier in June,

the abundance of flooded rice paddies results in a cluster at high EF but low T. This cluster migrates to higher V later in June as the rice canopy fills. Again, NDVI shows the least structure, NDVI*^{2} is intermediate, and V shows the most structure.*

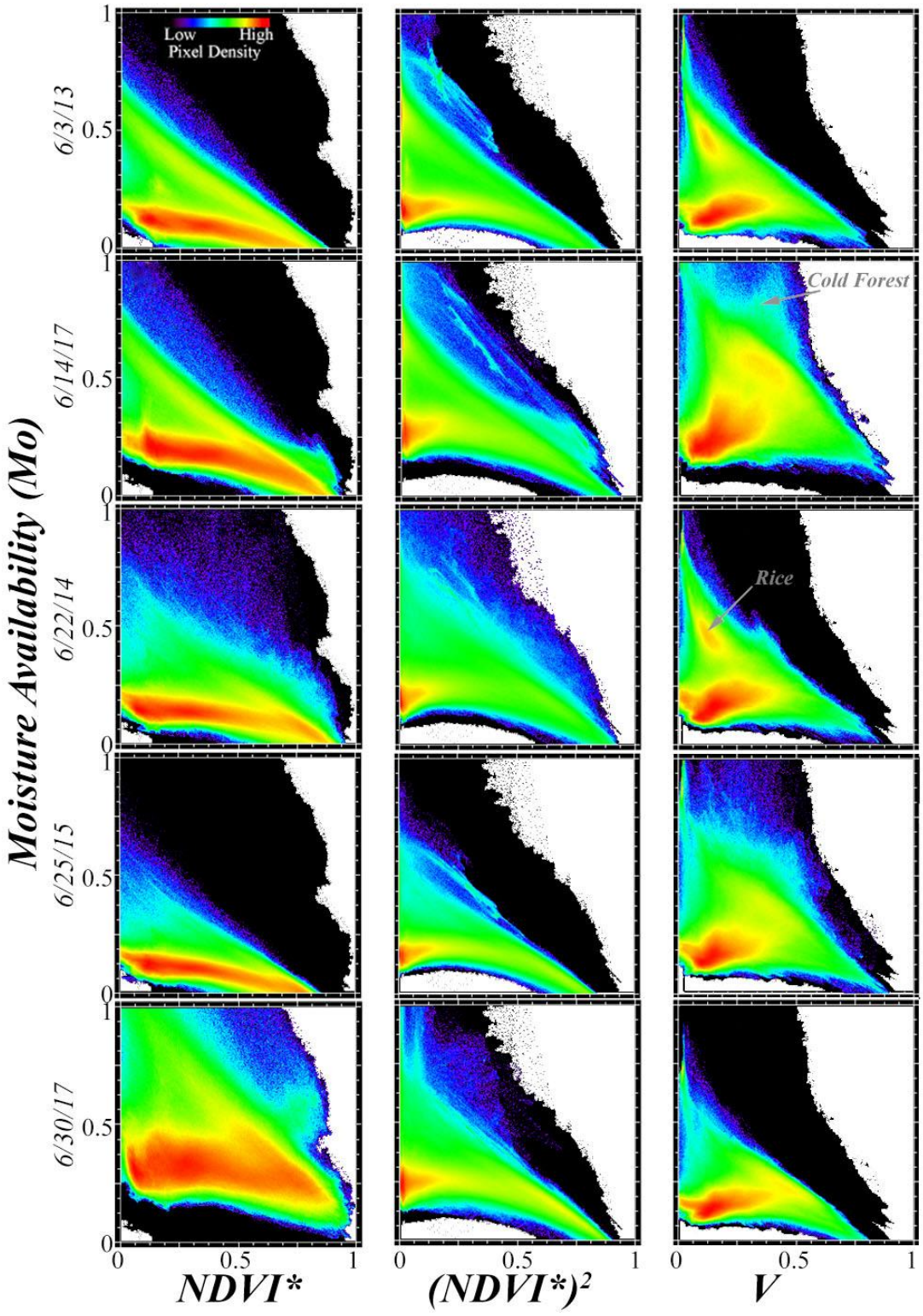

Figure 32. Vegetation metrics vs Mo. Regions with high vegetation cover converge into a tight range of low Mo. Regions with low cover can have high or low Mo. In some scenes, forests at

higher elevation in the NE corner of the image are colder than that rest of the image and so record anomalously high Mo. With V, the rice paddy cluster is again separate in early June, then moves to high V and low Mo values as the canopy fills. This cluster is barely distinguishable, and the structure much less clear, using either spectral index.

The *Mo* vs vegetation space, shown in Figure 32, can be interpreted similarly. In all cases, a clear triangular structure to the space is again evident. All pixels with high vegetation abundances are associated with low *Mo*, but pixels with low *V* values can be associated with high *Mo* (flooded areas & lakes) or low *Mo* (dry soil & impervious surface). In some scenes, higher-elevation forests in the Sierra Nevada form a distinct cluster in *V* vs *Mo* space because they are substantially colder than the rest of the scene. Again, significant differences in internal structure are apparent from metric to metric, with the most complex and informative structures being apparent in the *V* vs *Mo* space.

SMA-derived *V* fraction has long been recognized as a more accurate metric of vegetation abundance than spectral indices like *NDVI*. Taken together, Figure 31 and Figure 32 demonstrate how the inaccuracies in *NDVI* propagate through a simple *ET* model to clearly result in substantial information loss in estimates of *EF* and *Mo*. Evaluation of *NDVI**, *NDVI**^{2}, and *V*-based estimates of *ET* parameters using field measurements from agriculturally met stations, described in the Discussion, confirms that the greater information content of *V*-based estimates results in improved agreement between satellite and field measurements. While linear and quadratic transformations of *NDVI* do somewhat linearize the distributions and rescale their ranges, they cannot recover the structure of the bivariate distribution, which is simply not captured by the 2-band normalized difference. When spectral indices are used in more complex *ET* models, the error propagation may be even more severe.

Dark Fraction and Albedo

The *D* fraction provided by SMA also yields information relevant to *ET* estimation. Bivariate distributions of the *D* fraction against *EF* and *Mo* estimates are shown in the first and third columns of Figure 33. *D* vs *EF* spaces show similar overall structures from scene to scene, with a considerably more complex pixel distribution than that of the *V* vs *EF* & *Mo* spaces. Information about the phenological progression of the rice crop is present within this complexity. In early June, rice paddies reside in a consistent cluster at high *D* and high EF. This cluster is prominently separated from the remainder of the point cloud. As the growing season progresses, *D* decreases as *V* increases, and the cluster migrates to join the other green (non-rice) agriculture in the upper left corner of the point cloud at high *EF* values, but at low *D* fractions. Dry soil and NPV occupies the lower curvilinear bound of the space, with variable *D* fraction corresponding to illumination, substrate albedo, roughness, and the fractional cover of the NPV vs soil.

The overall envelope of the *D* vs *Mo* distributions (third column of Figure 33) is more triangular than that of the *D* vs *EF* distributions. This reflects the propensity for surfaces with high *D* fractions to have high moisture contents (standing water, saturated soil) or deep shadows. Rice paddies again reside in a consistently isolated cluster in early June, with high values of both *D* and *EF*, and migrate toward the remainder of the point cloud as the growing season progresses. Non-rice land cover resides in a more amorphous cluster with intermediate dark fractions and relatively low *Mo*.

The left and center columns of Figure 34 show the bivariate distribution of *D* vs *T** and α vs *T** for each image, respectively. The two distributions have obvious visual similarity, and they give similar information ($\rho < -0.98$ for all scenes). Clearly, the *D* fraction well represents broadband shortwave albedo in these images. Pixels with high *D* fractions and low α values

generally have low T^* values, generally corresponding to standing water. Pixels with intermediate D fractions or intermediate α, however, can possess any of the full range of T^* values. This is because these pixels can correspond to a wide range of land covers, including green crops, forests, dry fields, and impervious surfaces. The two subparallel diagonal limbs in the D vs T^* space correspond to variations in crop canopy structural shadow and plant spacing.

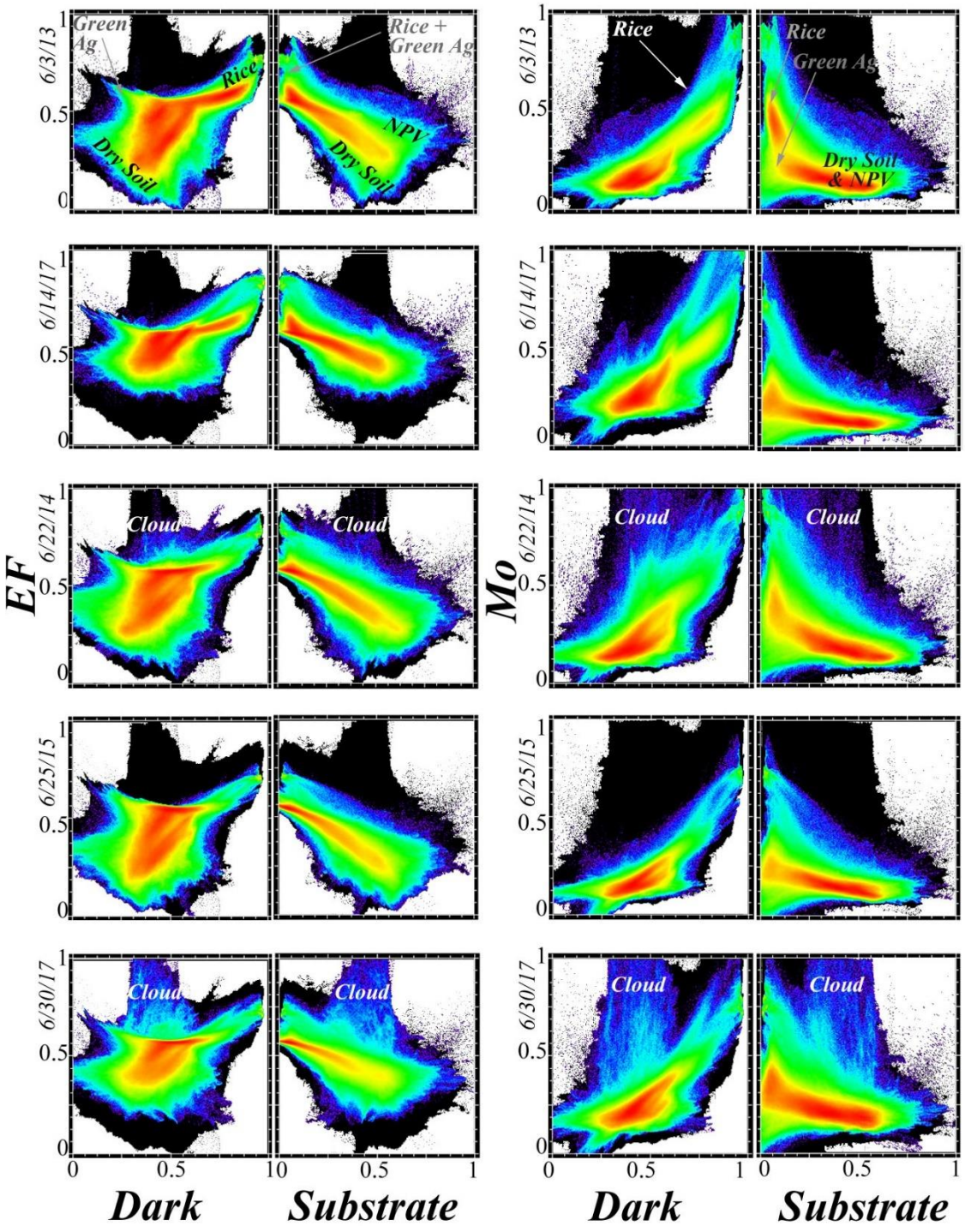

Figure 33. Dark and Substrate Fractions vs EF and Mo. Corresponding α vs EF and Mo spaces are not shown because nearly indistinguishable from the mirror image of the D vs EF and Mo

spaces. The rice paddy cluster is present in both D vs EF and D vs Mo spaces, but only weakly in S vs Mo. High EF values are partitioned between green (non-rice) agriculture at low D & low S values and rice paddies at high D and low S values. D vs Mo distributions generally show increasing Mo with increasing D. S vs EF and MO distributions show decreasing EF and MO with increasing S.

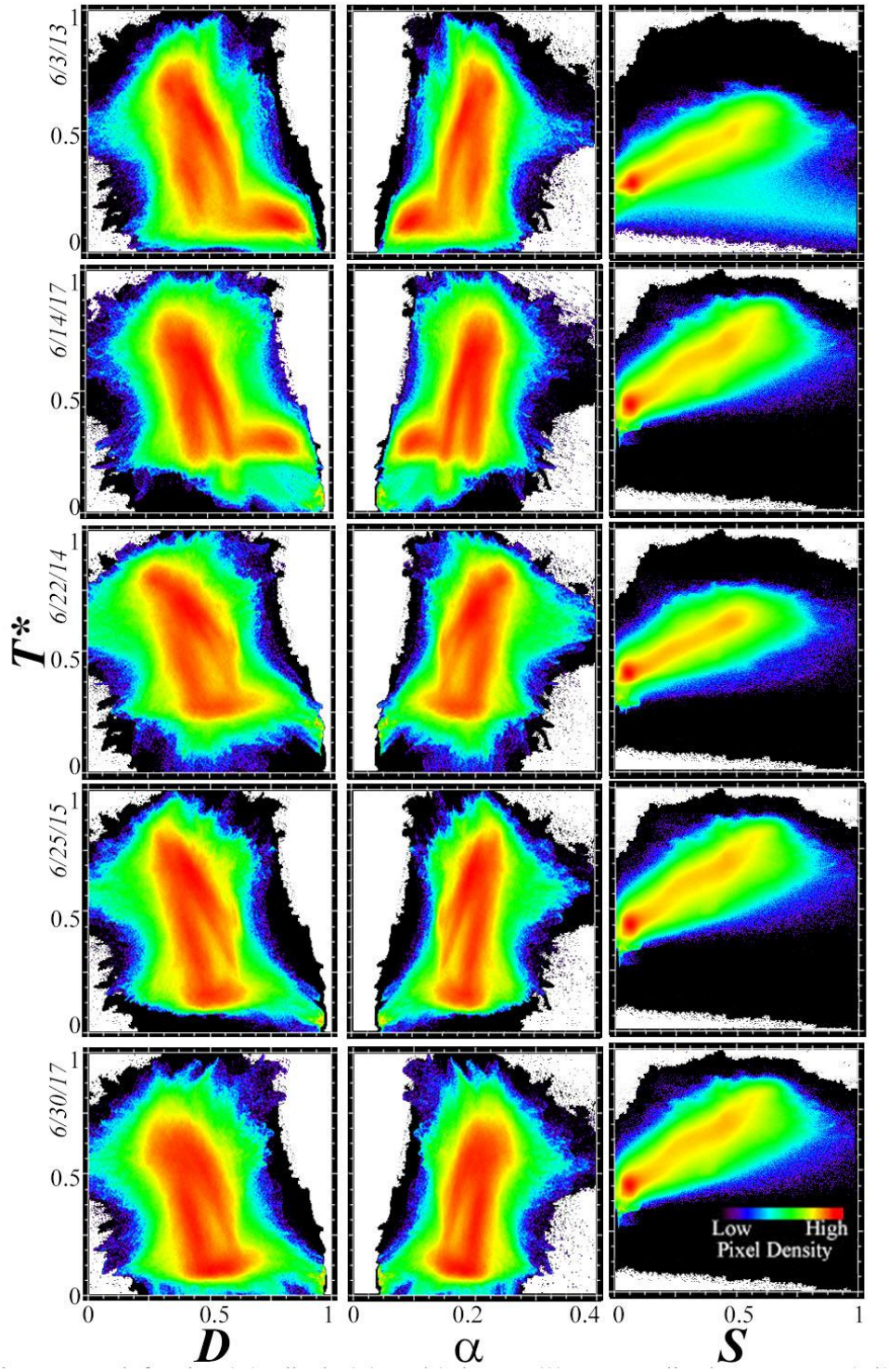

Figure 34. Dark fraction (D), albedo (α), and Substrate (S) vs normalized temperature (T). The D vs T* relation is similar to the α vs T* relation (with a sign flip). In contrast, the S vs T*

relation is highly linear. Pixels which are cooler than the main S vs T relation are generally covered with NPV and pixels hotter generally correspond to low albedo soils.

Substrate Fraction, Temperature, and ET

The third complementary piece of information given by the SVD approach is contained in the *S* fraction. The distributions of *S* versus *EF* & *Mo* are examined in the second and fourth columns of Figure 33. Again, broad similarities in structure are observed between scenes. *EF* shows a consistent inverse relationship to *S*, fanning out at higher *S* values in correspondence to the spectral ambiguity between soil and NPV. In contrast, the relationship between *S* and *Mo* is generally triangular, and it has some visual similarities to the relationship between *V* and *Mo*, shown in Figure 32. Pixels with high *S* values uniformly have low *Mo* values, accurately representing the low moisture content of bright, dry soils and NPV. However, pixels with low *S* values can have either high or low *Mo* values, corresponding to standing water or dense vegetation, respectively. In some scenes, the sporadic clouds intentionally carried through the analysis distort these relationships by yielding spuriously high *S* values, low *T* values, and high *EF* and *Mo* values. This illustrates the effect that uncorrected atmospheric effects can have on both SMA-derived fractions and *ET* estimates.

In contrast to the complexity of the *V* vs *T* and *D* vs *T* distributions, the relationship between *S* and *T* is remarkably straightforward in this study area, as shown in the right column of Figure 34. For all 10 June Landsat 8 images in the archive, *S* fraction shows a simple linear relationship to *T*. When all the single date spaces are combined into a single multi-date composite space, as shown in Figure 35, this relationship is masked because scene-to-scene variations in air temperature and illumination geometry result in shifts in absolute position of the point cloud in T—but not in its structure. Correlation coefficients for each coincident *S* vs *T*

image pair, also shown in Figure 35, quantify the strength of this relationship in the 0.7 to 0.9 range, which is substantially stronger than the (negative) relationship between *V* and *T*. Because the relationship between *S* and *T* is so strong, the relationship between *S* and *V* is similar to the relationship between *T* and *V*. The potential implications of this observation could be considerable, given that *S* is quantified using information from the optical bands alone.

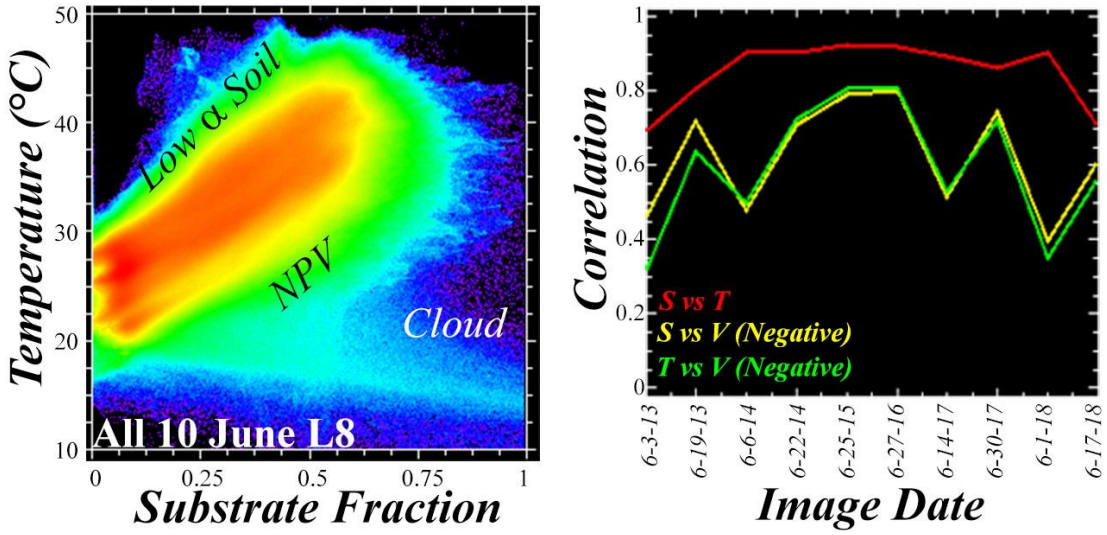

Figure 35. Composite relationship between S and T. Left: A consistent linear relationship between S and T is observed for nearly every June scene in the Landsat 8 archive, but the composite space of all 10 acquisitions is less obviously linear because significant image-to-image variability exists in air temperature. Right: Correlation between coincident S, V and T images for each date. The observed (+) correlation between S and T is stronger in every case than the well-known (-) correlation between V and T. Because the S vs T correlation is so strong, the S vs V and T vs V correlations are very similar.

Discussion

Application Examples

Figure 36 shows an example of *ET* estimation using the SVD+T approach on an image from 14 August 2016 in the study area. This image was acquired relatively late in the growing season. In this image, the majority of rice fields have closed canopies, and some are beginning to senesce. Orchards are generally in full leaf at this time, and row crops are in various stages of growth. Rice fields are easily identifiable from the SVD image (top) on the basis of their high *V* fraction, large field size, and relatively homogenous internal structure. Orchards generally have a lower *V* fraction and higher *S* fraction, due to the bare soil that is present between rows of trees. Native vegetation in the wildlife refuges and grasslands is generally senescent at this time of year, resulting in low *V* fractions and high *S* fractions. Settlements show considerable complexity, generally resulting in high *S* and *D* fractions.

Variations in *V* and *T* images are manifest in the *EF* and *Mo* images (center and bottom, respectively). *EF* shows the highest values in the rice fields, and the lowest values in the dry grasslands and fallow fields, consistent with physical expectations. Wildlife refuges show substantial internal structure due to their complex land cover mosaic of water, native plants, and managed vegetation. Orchards and row crops show intermediate *EF* values. In contrast, the *Mo* image reveals different spatial patterns. Considerably more internal structure is evident in the rice-growing region in the *Mo* image than the *EF* image, consistent with spatial variations in field maturity. Rice in the western portion of this scene was planted earlier than in the east, resulting in more rapid senescence and reduced *Mo* in the west relative to the east. The spatial structure in the wildlife refuges observed in the *EF* image is greatly diminished in the *Mo* image, where the region is characterized by relatively homogenous low *Mo* values.

Figure 37 presents in greater spatial detail a 24 × 24 km spatial subset, as indicated by the white box in Figure 36. The image shown in Figure 37 was collected earlier in the growing season, on 19 June 2013. The false color image (panel A), together with the coincident thermal image (panel B), allow for broad discrimination among land cover types. The cold, black-to-green large rectilinear fields correspond to flooded paddies with early-stage rice growing in them. Warmer, brighter areas along the Sacramento River channel correspond to row crops and orchards growing in sandier soils. The settlement of Willows, CA is present in the northwest corner of the image, with a complex reflectance signature and elevated temperatures relative to the surrounding agricultural landscape. A wildlife preserve is also present in the southwest corner of the image, characterized by a complex reflectance and temperature mosaic. SVD fractions (panel C) quantify this diversity through the amplitude variations of three continuous fields.

*NDVI**, *NDVI**^{2}, and *V* are shown in panels D through F. Relative to *V*, *NDVI** underestimates the vegetative cover in the settlement and wildlife preservation areas, and overestimates it in some areas of rice agriculture. The overestimation in the rice is even more severe for *NDVI**^{2}, although the underestimation in the wildlife refuge and settlement areas appears to be less severe. These differences in estimates of fractional vegetation cover then map onto estimates of *EF* (panels G through I) and *Mo* (panels J through L) using each metric. The overall spatial pattern of *EF* does not have extreme variations from metric to metric, although prominent differences are evident within the region of rice agriculture, as well as in the settlement. *Mo* estimates, on the other hand, are wildly variable. While the spatial pattern of *Mo* estimated using *V* appears to match the physical properties of the landscape mosaic, *Mo* estimated using the spectral indices does not appear to capture even the prominent differences

between the dry wildlife refuge and settlement, and the flooded rice paddies. The differences in *EF* and *Mo* estimates illustrate the potential sensitivity of *ET* estimation to the vegetation metrics, and the opportunity for improvement in current estimates that use the SVD approach. While we have used apparent brightness temperature and top of atmosphere reflectance to illustrate the effects of air temperature, future applications could make use of atmospherically corrected surface reflectance and surface temperature Landsat products provided by the USGS.

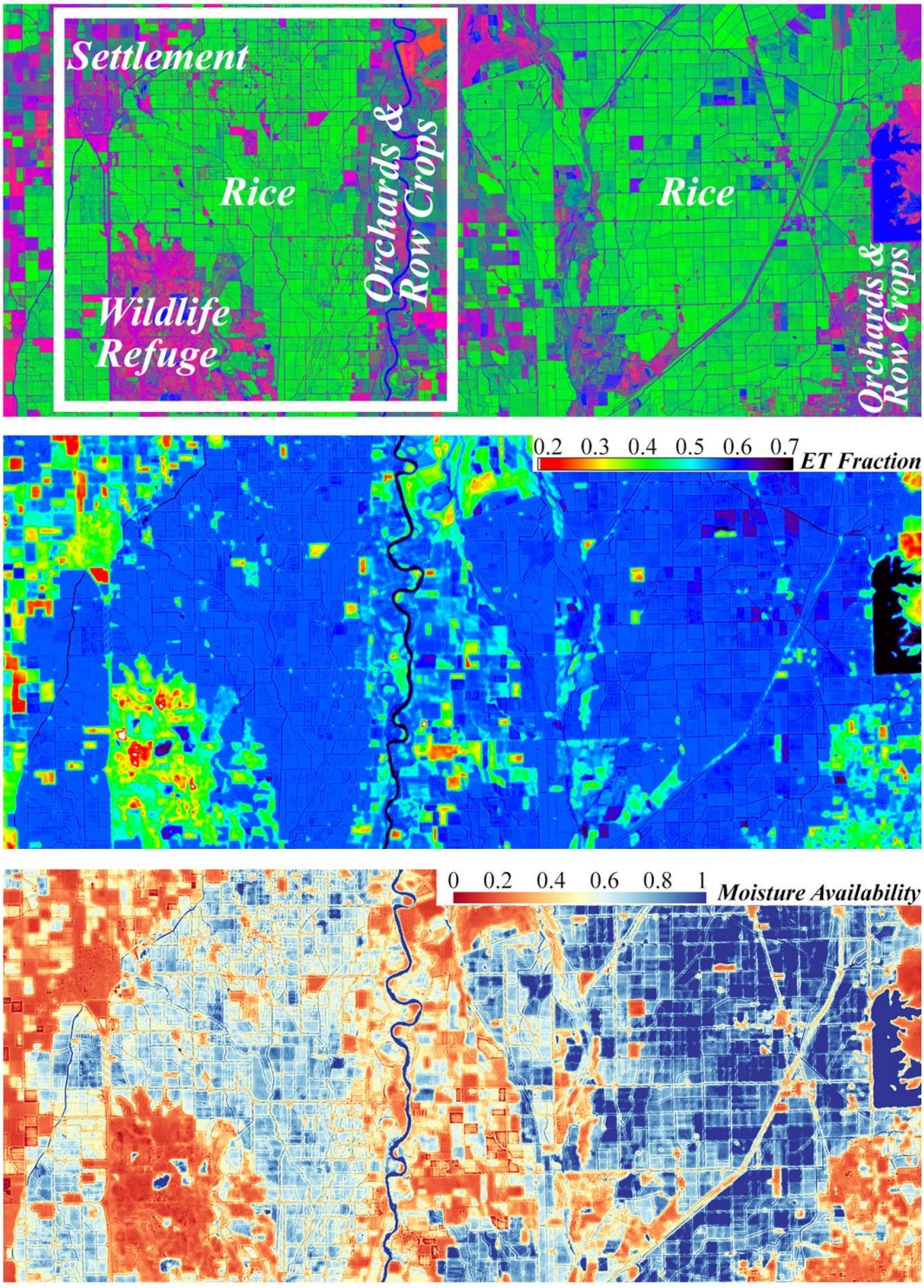

Figure 36. S, V & D fractions, along with EF & Mo, for a sample 15 × 50 km area imaged on August 14, 2016. Flooded paddies have high V and high Mo and EF. Fields in the western half of

the image were planted earlier than in the east and have started to senesce, resulting in lower Mo. Orchards have low EF and Mo. The wildlife refuge is complex, with both high and low EF and Mo. Landsat 8 resolves heterogeneity both within individual fields as well as across the valley. The white box shows the spatial subset used for Figure 37.

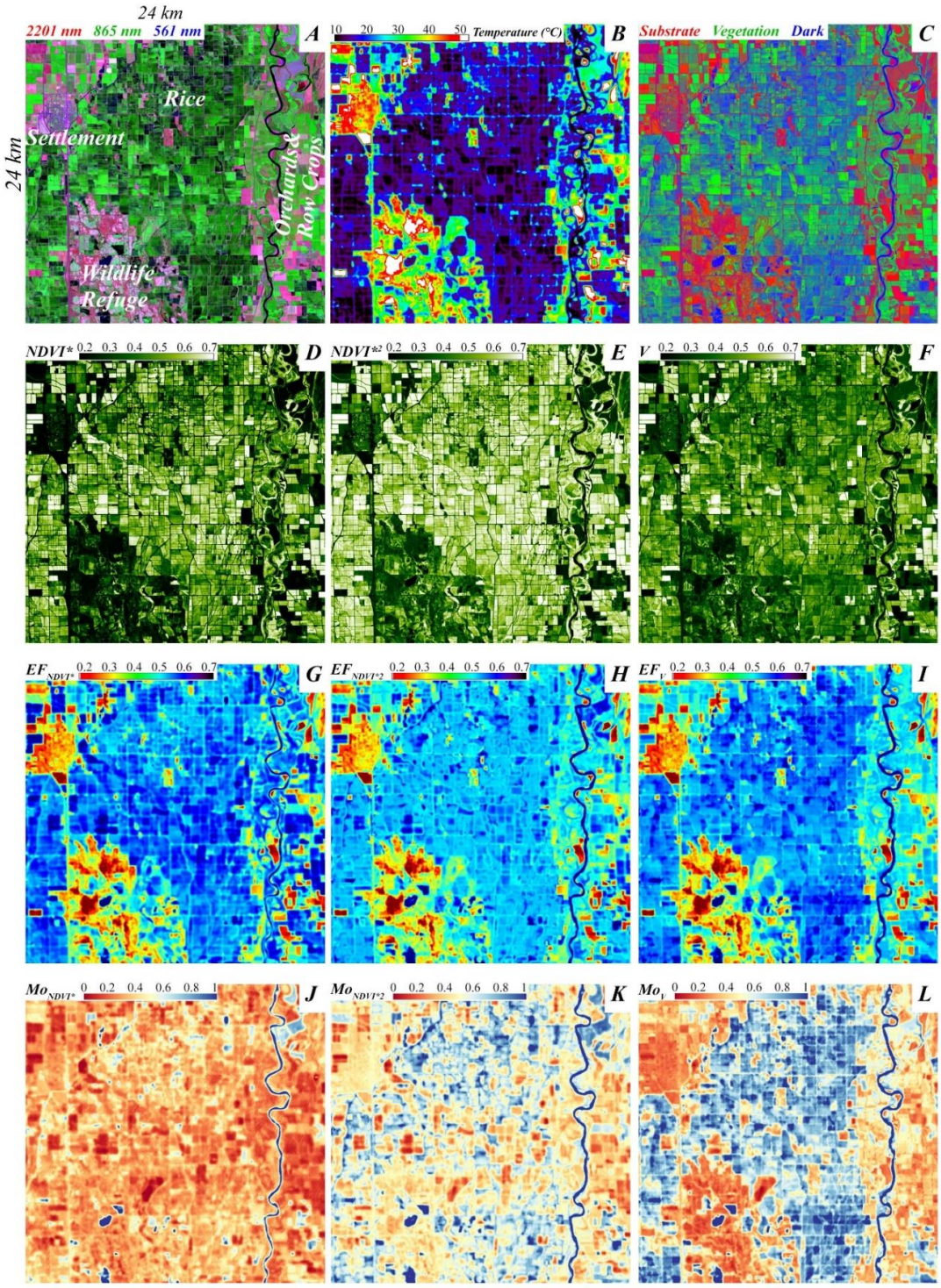

Figure 37. Example ET comparison. Landsat 8 collected coincident optical (A) and thermal (B) imagery on June 19, 2013. SVD fraction image (C) reveals substantial spatial heterogeneity in

agricultural and preserved lands. NDVI (D) and NDVI*2 (E) images show substantial differences from each other and from V (G). EF estimates using the three vegetation metrics (G-I) show similar overall patterns, but notable differences within agricultural areas. Differences in Mo (J-L) estimates are even more profound.*

Evaluation

One reason this analysis uses the Triangle Method is because both *EF* and *Mo* are relative measures of *ET*, providing information about the spatial distribution of total *ET* and soil moisture, but not absolute estimates of actual *ET* flux. This aligns with the goal of the study to provide a novel conceptual framework, within which *ET* models can be understood and harmonized—rather than proposing a particular predictive model. We principally focus on the relative distributions of data and model parameters across images, in order to (1) show the effect that differences in vegetation metric can have on even simple *ET* models, and (2) to show the differences and consistencies between *S* and *D* fractions, observed *T*, and estimated *EF* and *Mo*.

Despite these caveats, however, comparison of remotely sensed estimates with ground observations of relevant variables can still provide valuable insights. Ideally, direct field measures of actual *ET* from flux towers and/or lysimeters would be available to provide local calibration and validation constraints. To our knowledge, no such data are available for our region during the 2013–2018 time period that we considered. This unfortunately precludes direct validation.

Agricultural meteorological data do exist in the area, however, in the form of a network of standardized weather stations maintained by the California Irrigation Management Information System (CIMIS). CIMIS stations measure a wide range of micrometeorological

variables, including wind speed and direction, air temperature and humidity, solar radiation, and soil temperature. These data are used to provide standardized estimates of *ET*-relevant derived quantities, including reference *ET* (ET_o). Fortunately, four CIMIS stations are situated within our study area, and two more (Davis and Woodland) are immediately to the south (Figure 38).

The plots at the bottom of Figure 38 compare the time series of CIMIS-measured soil temperature (green) and air temperature (red) in comparison to Landsat-estimated brightness temperature (black) for nine pixels closest to each of the four CIMIS stations located within the study area. While some discrepancies do exist, the Landsat temperatures estimates generally track the upper bound of the CIMIS air temperature to within 3–5 °C. Differences in the accuracy with which Landsat measurements track different stations are likely due to differences in the siting of each station, particularly the spatial homogeneity and land cover of the surrounding landscape.

Figure 39 illustrates the relative ability of *EF* and *Mo* estimates based on *V*, *NDVI**, and $NDVI^{*2}$ to track ground observations. Every available cloud-free Landsat 8 scene in 2017 and 2018 was processed with the same global $NDVI_{max}$, $NDVI_{min}$, T_{max}, and T_{min} values that were used for the rest of the analysis. *EF* and *Mo* values for maximally vegetated pixels were then selected from the distributions of ($V/NDVI^*/NDVI^{*2}$) vs (*EF*/*Mo*) to represent the conditions that are present at well-watered, densely vegetated CIMIS stations. *EF* estimates were compared against CIMIS-derived ET_o (*L*) and *Mo* estimates were compared against (inverted) CIMIS-measured soil temperature (*R*). *EF* estimates using *V* track ET_o more closely than *EF* estimates using *NDVI**. *EF* estimated using $NDVI^{*2}$ shows high amplitude peaks and oscillations throughout the growing season, which are not present in ground observations. Moderately strong positive

correlations (0.7 to 0.9) between *EF* estimates and individual station ET_o records are observed for all metrics. While individual correlations are statistically significant (in all cases, $p < 0.001$ compared to null hypothesis of 0 correlation), the differences between the correlations are not ($p > 0.1$ in all cases).

Mo estimates show a similar pattern when compared against ground-based soil *T* measurements. When the SMA-derived *V* fraction is used, *Mo* estimates track the seasonal cycle of soil *T* remarkably closely. In contrast, *Mo* estimates using *NDVI** and $NDVI^{*2}$ overestimate *Mo* at the beginning and end of the growing season. This is in accord with the known superiority of *V* over *NDVI* in situations with sparse (early season) or senescent (late season) vegetation. Again, moderately strong positive correlations are observed between *Mo* estimates and individual station Soil *T* records for all metrics. Again, individual correlations are statistically significant (in all cases, $p < 0.001$ compared to null hypothesis of 0 correlation) but differences between the correlations are not ($p > 0.1$ in all cases). While admittedly indirect, this comparison to the available ground measurements provides additional evidence supporting the improvement, using the SMA-derived *V* fraction over transformed spectral indices like *NDVI** and $NDVI^{*2}$.

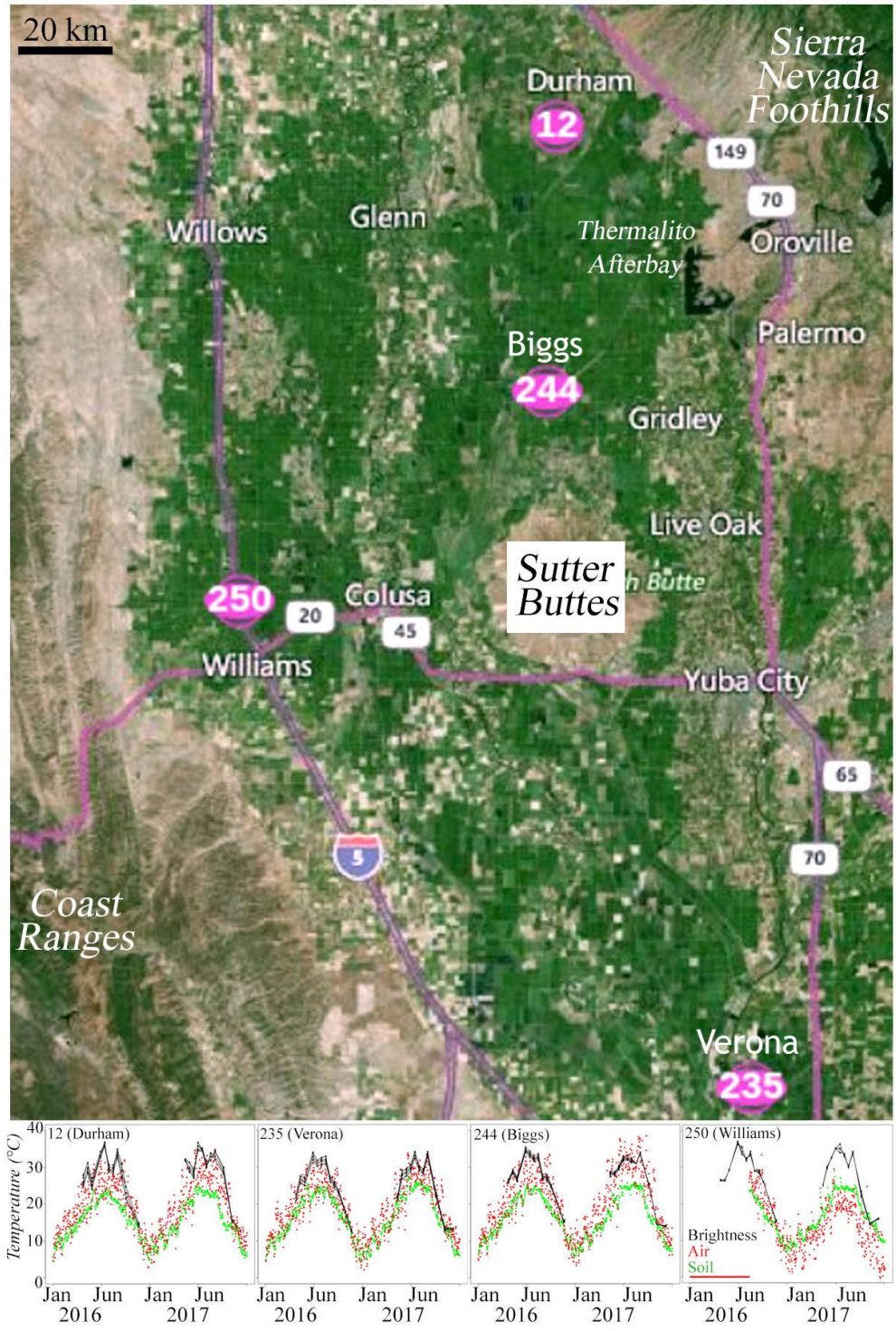

Figure 38. Four met stations are maintained in the study area by the California Irrigation Management Information System (CIMIS). Two more stations exist just to the south of the area.

Air temperatures (red) are generally higher and more variable than soil (green). Durham, Verona, & Biggs records are generally similar, with Landsat-observed brightness temperatures (black) at the warm bound of the envelope of air temperatures. The Williams station (installed mid 2016) has substantially lower air, but similar soil and brightness temperatures, to the other stations.

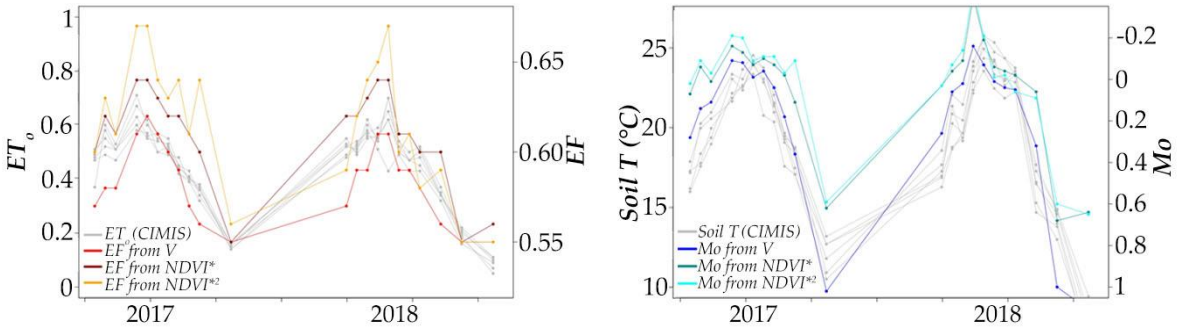

Figure 39. Comparison to ground observations. EF *(L) and* Mo *estimates (R) from maximally-vegetated pixels from all cloud-free observations from 2017 and 2018 are compared against CIMIS data. Strong seasonality is evident in al observations.* EF *from SMA-derived* V *fraction tracks CIMIS-estimated* ET_o *more accurately than* EF *from* NDVI*. EF *from* NDVI*^{2} *shows pronounced oscillations which are not present in the CIMIS data.* Mo *from SMA-derived* V *fraction tracks soil* T *much more accurately than* Mo *from* NDVI* *or* NDVI*^{2}. Mo *estimated using the spectral indices does not capture the curvature of the seasonal peak, likely as a result of effects of soil background reflectance in pixels with sparse (early season) and senescent (late season) vegetation.*

ET Partitioning

A recent global analysis has shown the partitioning of *ET* into its primary subcomponents of transpiration (leaf water to air), soil evaporation (soil moisture to air), and interception evaporation (plant surface water to air) to vary widely between common *ET* models (Talsma et al., 2018a). Further work (published in this Special Issue) specifically shows *NDVI* to be the input parameter resulting in the greatest sensitivity of total *ET* estimates generated by the Priestley–Taylor Jet Propulsion Laboratory (PT-JPL) *ET* model, with substantial nonlinearity (Talsma et al., 2018b). As mentioned in (Talsma et al., 2018b), nonlinearities in model formulation may explain this result. In addition, we suggest that another factor potentially contributing to this sensitivity could be the generally nonlinear relationship between the model input parameter (*NDVI*), and the physical quantity that it is intended to represent (fractional vegetation abundance). This hypothesis could be easily investigated through trials with the simple replacement of *NDVI* with SMA-estimated *V*. If the hypothesis is supported and improvement is seen, replacement of *NDVI* with *V* could offer a straightforward pathway towards *ET* model improvement requiring minimal effort.

This opportunity is not unique to the PT-JPL model. Many *ET* model formulations assume a simple relationship between a biogeophysical landscape quantity, such as fractional vegetation abundance and a spectral index. A robust body of previous work (partially reviewed in the Background section above) has shown SMA to outperform spectral indices in a wide range of environments and spatial resolutions, especially in the case of broadband multispectral imagery. SMA also has the advantage of being grounded in a straightforward physical basis, and it accounts for the effects of soil reflectance, moisture content, and shadow explicitly. In general, it is reasonable to expect that the relationship between the true subpixel areal abundance of land

cover and the estimate given by SMA to be more accurate, and scale more linearly, than the estimate that is given by a normalized difference index. Given the ease with which SMA can be implemented into multispectral image processing workflows, and the current prevalence of spectral vegetation indices in *ET* models, this presents a substantial opportunity for the improvement of remote sensing-based estimation of *ET*.

Despite their considerable advantages, the linear scaling properties of SMA-derived land cover fractions alone are not likely to resolve all scaling nonlinearities in *ET* estimation. The effects of other nonlinearities in the *ET* estimation process, such as surface roughness, are significant, and they can be observed in cases where vegetation parameters scale accurately. The recent work of (Ramírez-Cuesta et al., 2019) observes one such system. Using the METRIC model to estimate *ET* from an open-canopy olive orchard, Ramirez-Cuesta et al. find scaling discrepancies in sensible and latent heat fluxes of up to 24% and 15%, respectively. These differences could not be attributed to albedo or vegetation parameterization of the METRIC model. This work serves to highlight the complexity of the *ET* estimation problem, and the need for further work on characterizing the relationship between the spatial configuration of the landscape and the scaling of the *ET* estimates.

Thermal EM Selection

ET estimation methods that rely on the regional *V* vs *T* relation are generally sensitive to the selection of hot and cold thermal endmembers (Long et al., 2011; Long and Singh, 2013; Timmermans et al., 2007). As noted by (Carlson, 2013), the hot & cold EMs fundamentally set SVAT model boundary conditions, and thus constrain the distribution of possible *ET* outcomes. Because of this, *ET* models rooted in the *V* vs *T* relation can fundamentally only be as accurate and as consistent as the thermal EMs used in their formulation.

The SVD approach provides users with additional information about potential thermal EMs by providing two additional quantities relating to the land cover of the pixel. This information could be especially useful when considering the choice of hot EM, a particularly important and sensitive point, as noted by (Timmermans et al., 2007). The two parameters of spectral vegetation index and brightness temperature alone are generally insufficient to reliably distinguish between such widely variable materials as asphalt (or other low albedo anthropogenic surfaces), dry NPV (standing or cut crop litter, senesced grass), dry low albedo soil, and dry high albedo soil. However, by adding the *S* and *D* fraction information, these materials can be readily distinguished using their position in a 4-dimensional parameter space. This enhanced ability to discriminate between potential hot EM materials could support attempts to improve the consistency and accuracy of thermal EM selection.

Clustering in Fraction vs ET Parameter Space

The structure of the SVD fraction vs *ET* parameter spaces is a key component of this analysis. Both broad consistencies and illuminating differences are present between images in each space. Clustering in these spaces, indicative of landscape subsets with similar land cover and *ET* combinations, can be useful for mapping distinct land cover types. For example, the flooded rice paddies common in the study area are shown in Figures 3–6 as occupying a distinct position in each of the *S, V,* and *D* vs *T, EF* and *Mo* spaces. The position of these paddies relative to the other points in the space migrates throughout the growing season, resulting in a set of trajectories that are characteristic of rice paddies that are distinct from those of other types of crops, grasslands, or non-agricultural vegetation.

Clustering in the feature space is also the foundation for discrete image classification. By contributing an additional (although not independent) set of basis vectors for the multispectral

feature space, the *ET* parameter estimates offer an additional opportunity to help the statistical classification algorithms to resolve distinctions between the spectral–thermal properties of different land covers. Especially when approached from a multitemporal framework (Sousa and Small, 2019), this information could potentially be used to improve image classification algorithms used for the mapping and monitoring of both human-modified and wilderness landscapes.

The SVD Approach as a Unifying Framework

The bivariate parameter spaces shown in Figures 2–7, and the examples shown in Figures 8 and 9, illustrate the value of SMA with globally standardized SVD EMs as a unifying framework for two complementary approaches to *ET* investigation: the *V* vs *T* relationship and the α vs *T* relationship. Figure 30, Figure 31, and Figure 32 illustrate the *ET*-specific advantages of using *V* over the currently used metrics, such as *NDVI** and $NDVI^{*2}$, on the basis of the enhanced clustering and structure in the *V* vs *T*, *EF*, and *Mo* distributions. These advantages, in addition to previously demonstrated scaling and background suppression properties, advocate for the use of SMA-derived *V* fraction in *ET* studies.

In addition to *V*, the SVD+T approach simultaneously retrieves information on two other factors influencing *ET*; fractional soil exposure and soil moisture. The left and center columns of Figure 34 show this information from the *D* fraction to be highly similar to (inverted) broadband shortwave albedo ($\rho < -0.98$ for all scenes). The right column of Figure 34 and Figure 35 show that *S* fractions are strongly linearly related to *T*, at least in the June imagery in this study area. While this relationship does have a strong physical basis, more investigation is warranted, to confirm its generality in other environments and seasons. However, the agricultural and soil complexity in the Sacramento Valley suggest that the relationship may hold in other agricultural

environments. By synthesizing the contributions of both vegetation abundance and albedo, the SVD+T approach presents a unified framework for considering two of the main branches of the *ET* literature.

The focus of this analysis on a single study area may beg the question of the generality of the results. While the persistence of the feature space structure over several years is encouraging, it does not guarantee that the method will perform as well in other environments. However, the global analysis of (Small, 2006) did find a remarkable similarity of structure in the SVD fraction vs *T* spaces of 24 diverse urban-rural gradients spanning a very wide range of environments and land cover types. While the abundance of impervious surface in those environments complicates interpretation in terms of *ET*, a simple comparison of the SVD vs *T* spaces from (Small, 2006) with those in this analysis shows obvious similarities. The strong linearity of the *S* vs *T* space observed in the California study area is not a general feature in the global analysis, although it does appear in some examples containing abundant agriculture (e.g., Calgary, Essen & Cairo). An intercomparison of a diverse sample of agricultural areas worldwide is the focus of a separate study.

Finally, the clustering that is apparent in the *S, V,* & *D* fractions versus *T*, Mo,* and *EF* spaces suggests that these spaces could provide the basis for either continuous or discrete classifications of crop types and growth stages for agricultural monitoring. This approach could be particularly effective when combined with spatiotemporal analysis of phenological information derived from multitemporal observations, as proposed by (Sousa and Small, 2019). In addition, once planned global hyperspectral missions become a reality, the SVD framework could also be integrated with targeted narrowband approaches such as that of (Marshall et al., 2016).

Conclusions

The primary purpose of this study is to demonstrate the potential for spectral mixture analysis (SMA) based on globally standardized substrate, vegetation, and dark (SVD) endmembers (EMs) to provide a comprehensive, integrated framework for *ET* parameter estimation. The SVD approach yields complementary continuous field estimates of the subpixel fractional abundance of each EM. *V* fraction is an accurate, linearly scalable metric for vegetation abundance. *D* fraction is the linear complement to albedo. The linear tradeoff between *S* and *D* fractions provides information about the soil and NPV exposure, tillage conditions, and moisture content. Using the Triangle Method as an example model, the results of this analysis show substantially enhanced clustering in both the *ET* fraction (*EF*) and moisture availability (*Mo*) estimates, based on the *V* fraction, compared to the generally used *NDVI** or $NDVI^{*2}$. Replacing *NDVI*-based vegetation metrics with the standardized vegetation fraction eliminates a known nonlinearity and allows for pixel-based fractions to be downscaled and vicariously validated with higher resolution imagery when available. *EF* and *Mo* that are estimated using *V* also track field measurements of reference *ET* & soil temperature more closely than *EF* & *Mo* estimated using *NDVI** or $NDVI^{*2}$. Using the coefficients of (Liang, 2001), we show the *D* vs *T* relationship to be very similar to broadband shortwave albedo (α) vs *T*. Finally, we show *S* to have a consistent linear relationship with *T*, at least in this study area during peak growing and insolation season. SMA allows globally standardized *S*, *V*, and *D* fractions to be estimated simultaneously, with high accuracy and at trivial computational cost. The implications of such a unified framework for the standardization and accuracy improvement of *ET* models could be considerable.

5. Mapping and Monitoring Rice Agriculture with Multisensor Temporal Mixture Models

Abstract

Rice is the staple food for more than half of humanity. Accurate prediction of rice harvests is therefore of considerable global importance for food security and economic stability, especially in the developing world. Landsat sensors have collected coincident thermal and optical images for the past 35+ years, and so can provide both retrospective and near-realtime constraints on the spatial extent of rice planting and the timing of rice phenology. Thermal and optical imaging capture different physical processes, and so provide different types of information for phenologic mapping. Most analyses use only one or the other data source, omitting potentially useful information. We present a novel approach to the mapping and monitoring of rice agriculture which leverages both optical and thermal measurements. The approach relies on Temporal Mixture Models (TMMs) derived from parallel Empirical Orthogonal Function (EOF) analyses of Landsat image time series. Analysis of each image time series is performed in two stages: 1) spatiotemporal characterization, and 2) temporal mixture modeling. *Characterization* evaluates the covariance structure of the data, culminating in the selection of temporal endmembers (EMs) representing the most distinct phenological cycles of either vegetation abundance or surface temperature. *Modeling* uses these EMs as the basis for linear TMMs which map the spatial distribution of each EM phenological pattern across study area. The two metrics we analyze in parallel are 1) fractional vegetation abundance (F_v) derived from spectral mixture analysis (SMA) of optical reflectance, and 2) land surface temperature (LST) derived from brightness temperature (T_b). These metrics are chosen on the basis of being straightforward to compute for any (cloud-free) Landsat 4-8 image in the global archive. We demonstrate the method using a 90 × 120 km area in the Sacramento Valley of California.

Satellite T_b retrievals are corrected to LST using a standardized atmospheric correction approach and pixelwise fractional emissivity estimates derived from SMA. LST and T_b time series are compared to field station data in 2016 and 2017. Uncorrected T_b is observed to agree with the upper bound of the envelope of air temperature observations to within 3°C on average. As expected, LST estimates are 3 to 5°C higher. Soil T, air T, T_b and LST estimates can all be represented as linear transformations of the same seasonal cycle. The 3D temporal feature spaces of F_v and LST clearly resolve 5 and 7 temporal EM phenologies, respectively, with strong clustering distinguishing rice from other vegetation. Results from parallel EOF analyses of coincident F_v and LST image time series over the 2016 and 2017 growing seasons suggest that TMMs based on single year F_v datasets can provide accurate maps of crop timing, while TMMs based on dual year LST datasets can provide comparable maps of year-to-year crop conversion. We also test a partial-year model midway through the 2018 growing season to illustrate a potential real-time monitoring application. Field validation confirms the monitoring model provides an upper bound estimate of spatial extent and relative timing of the rice crop accurate to 89%, even with an unusually sparse set of usable Landsat images.

Introduction

Rice agriculture is critical for global food security. Much of the developing world relies on rice production for subsistence and/or commercial purposes. Rice is the largest food source for the world's poor, and more than half of the world's population relies on rice as its staple food (Muthayya et al., 2014). In terms of nutrition, rice provides 21% of global human per capita energy and 15% of per capita protein. More land area is used for rice production than any other agricultural crop (Global Rice Science Partnership, 2013). Predictability of global and regional rice production has obvious and significant implications for the management of both human and

natural systems. For these predictions to be accurate, yield models must be provided with inputs of abundant, accurate observations in order to constrain fundamental variables such as planted area and timing of key phenological transitions (e.g. (Bolton and Friedl, 2013)). Similar biogeophysical observations can also address concerns important to commercial growers like optimization of the use of water (Anderson et al., 2012) and nutrient additives (Wilcox et al., 1994); assessment of extent and severity of weeds (Shaw, 2005), pests (Luther et al., 1997), and diseases (MacDonald et al., 1972); and independent verification of alternative cropping practices (Bricklemyer et al., 2007).

One cost effective tool to provide these observations is the spatiotemporal analysis of satellite imagery. Free global decameter (10 to 100 m) resolution multispectral optical and thermal imagery already exists through the Landsat program, with data extending back to the early 1980s (Wulder et al., 2012). The Landsat program has been supplemented since 2015 by the addition of the optical-only Sentinel-2 constellation (Drusch et al., 2012). Additional hectometer (100 to 1000 m) resolution imagery is available through the MODIS, VIIRS, and Sentinel-3 programs. The global archive of meter to hectometer resolution optical satellite imagery is expected to continue to grow into the future as further missions are planned in both the public and private sectors. This rich set of observations—with global coverage—can facilitate both retrospective and prospective analyses for a wide range of agricultural applications.

Rigorous characterization of plant life cycles and cropping practices is required in order to confidently relate satellite measurements to crop conditions. In recent decades, significant effort has been devoted – and much success has been achieved – in studying and improving rice agriculture around the world (Khush, 2003). As a result, rice is one of the best-understood crops

on Earth from an agronomic perspective. Despite this progress, significantly less work has been done to characterize how the biogeophysical progression of the land surface characteristic of rice agriculture is recorded by optical and thermal satellite imagery. To date, most applications of satellite imagery for rice agriculture have focused on discrete classification and mapping of rice extent (e.g. (Gumma et al., 2015; Kontgis et al., 2015; Nguyen et al., 2016; Torbick et al., 2011; Wang et al., 2015)), rather than on a physical understanding of how the land surface properties and processes that characterize the phenological cycle of rice crops are manifest in satellite observations. This physically-based strategy is the approach taken in this study.

An obvious distinction between rice and most other crops is that rice is often (but not always) grown in paddies. In paddy rice, this fundamental difference results in substantial evaporative cooling and near-complete absorption in optical infrared wavelengths early in the cropping cycle, neither of which are generally present for non-rice crops in the same landscape. Imaging by satellites at both optical VSWIR (Visible through Shortwave Infrared, 0.4–2.5 μm) and TIR (Thermal Infrared, 8–14 μm) wavelengths results in both 1) lower TIR temperature measurements, and 2) lower overall VSWIR albedo relative to non-rice crops. Because the biogeophysical signal manifests in both VSWIR and TIR wavelength regimes, the evolution of the rice crop throughout a growing season occupies a more unique trajectory in the combined geophysical parameter space comprised of both VSWIR and TIR than in the space of either parameter alone. This provides an opportunity to improve the accuracy of crop-specific maps of rice based on optical imagery alone by supplementing with thermal image time series, illustrating the added value of the thermal satellite sensors and the importance of continuity in intercalibrated satellite thermal image collection.

This analysis presents a straightforward, physically-based approach for the mapping and monitoring of rice agriculture. Using the Sacramento Valley of California as our example area, we apply the methodology of spatiotemporal characterization and modeling, first described in detail by (Small, 2012), to the special case of a parallel analysis of the twin data streams from coincident Landsat 8 OLI (Operational Land Imager) and TIRS (Thermal Infrared Sensor) image time series. The resulting VSWIR and TIR data spaces each characterize complementary features of the biogeophysical evolution of the agricultural landscape. Using endmembers (EMs) that represent distinct temporal trajectories, independently derived from each data stream, we demonstrate the method by mapping both the timing and presence/absence of rice crops across 2 years. Finally, we also show the seasonal evolution of the landscape in Temperature vs Vegetation (TV) space. This suggests more detailed investigation into the spatiotemporal analysis of evapotranspiration (ET) as an attractive avenue for future work, as also proposed by (Sousa and Small, 2018b), to potentially directly address several of the outstanding research questions identified by the recent NRC Decadal Survey (Fisher et al., 2017).

While a considerable body of literature exists on mapping rice from optical satellite imagery, to our knowledge, previous work has generally focused on applying a variety of complex statistical algorithms to VSWIR data, usually without using thermal information. Some previous studies have included thermal data into their algorithms, but rarely in a physically-based way. The approach presented here explicitly integrates multitemporal thermal and optical measurements to discriminate between distinct phenological cycles, resulting in an improved quantitative understanding of land surface processes and coincident energy fluxes. Additional benefits include relative mathematical simplicity and a direct grounding in biogeophysical processes.

Background – Study Area

Regional Thermal Setting

Figure 40 shows the study area in regional context using a tri-temporal thermal composite image. The northern portion of the Great Central Valley of California (area within and around the white box) is one of the most productive rice growing regions on Earth. Land use in the valley is dominated by intensive agricultural production of a wide range of commodity and specialty crops. The Sacramento Valley is characterized by Köppen Climate *Csa* (Hot Summer Mediterranean). The vast majority of precipitation is delivered between the late fall and the early spring, with summers being characterized by dry, hot days with sparse cloud cover. A wide range of soil types exist in California, sometimes distinguishable on the basis of VSWIR reflectance (Sousa and Small, 2018a). Clay-rich soils are common in the northern portion of the valley, providing a nearly ideal natural substrate to support the standing water commonly used in intensive rice agriculture. Water in the region is highly controlled through a network of government-run water projects. Effectively all summer agriculture in the Central Valley is irrigated using a combination of water captured by reservoirs located in the surrounding foothills and pumped from wells.

The colors on Figure 40 illustrate at a glance the typical thermal evolution of the region over the first half of the calendar year. In this figure, the blue, green, and red channels of the image represent land surface temperatures (LSTs) in January, May, and August of 2016, respectively. No locations are bright blue because the landscape is universally colder in January than in May or August. The Mojave Desert appears as yellow (red + green) because its temperature (bottom time series) generally mimics the annual cycle of solar insolation. In contrast, the Basin and Range takes longer to heat and maps with a more reddish hue. High

elevations in the Sierra Nevada and Coast Ranges appear as dark red because seasonal snowpack results in low winter temperatures that then rapidly rise once the snowpack melts in late spring/early summer. Agriculture in the Central Valley and Snake River Plain appears green because surface temperature in the May image is generally elevated due to the low thermal inertia of bare, dry fields. Once crops have grown, however, the associated evapotranspiration (ET) significantly cools the landscape during the August image. This can be seen explicitly in the time series of typical annual thermal phenologies for Central Valley Rice from the MODIS sensor. In comparison, fields in the Central Valley left fallow, and the grasslands on the foothills of the Sierra Nevada and Coast Ranges, show annual thermal cycles more similar to the desert than the adjacent agricultural fields. Coastal areas, dominated by the thermal inertia of the Pacific Ocean and inundated in fog for much of the year, have a much lower amplitude annual thermal cycle. Inland lakes show somewhat more variability, but still are characterized by relatively cool, stable LSTs, therefore appearing dark.

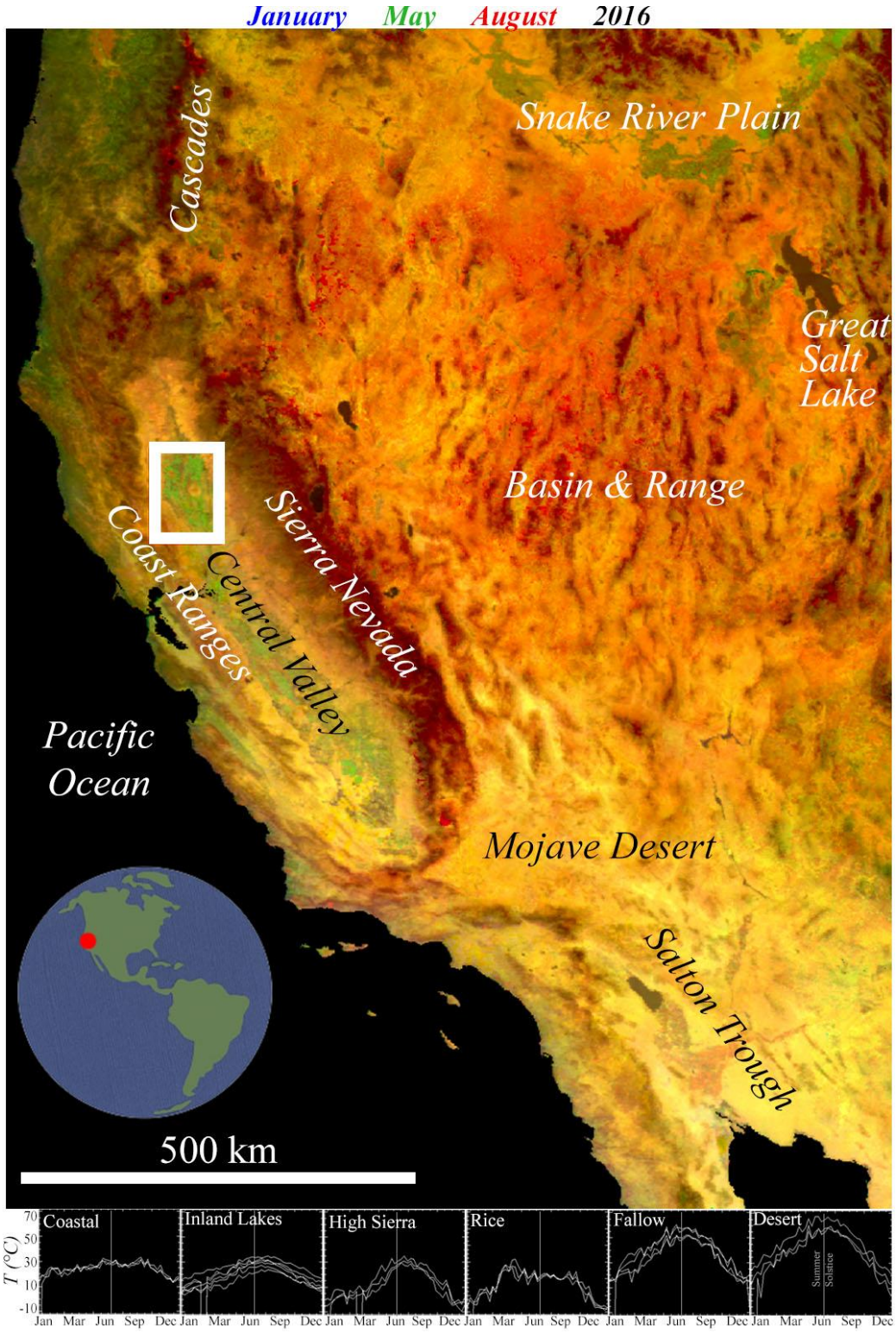

Figure 40. Thermal Phenology of the Western United States of America. The Central Valley lies between the Pacific Ocean and the hyperarid Basin & Range and Mojave Desert. Arid regions

appear red or yellow due to summer heating. Sierra Nevada and Cascades mountains appear dark red due to seasonal snowpack. Central Valley agriculture appears green because evapotranspiration (ET) of dense summer crops results in substantial August cooling. Example time series of annual temperature cycle shown for 6 biogeophysical regions.

Rice in the Sacramento Valley

The Great Central Valley of California is comprised of two major units: the northerly Sacramento Valley and the southerly San Joaquin Valley. The climate and soil of the Sacramento Valley are well suited to rice production: clay-rich soils which are easily able to support paddy water dominate much of the valley floor and hot, dry summers provide a supportive growing environment for the rice plant with minimal risk of mid- or late-season rains damaging the crop. As a result, rice yields in the region are some of the highest in the world, with average yields now exceeding 9000 kg/ha (8000 lbs/acre). California is a major rice-growing region, producing 75% of the medium grain and 98% of the short grain rice grown in the United States. California grows more rice than any U.S. state other than Arkansas, which dominates in long grain rice production. Of the rice production in California, approximately 95% occurs in the Sacramento Valley, mainly in Colusa, Sutter, Butte, and Glenn counties. For a concise yet thorough background on the history and current state of rice production in California, see (Geisseler and Horwath, 2013).

Rice fields in the Sacramento Valley are generally arrayed on a rectilinear grid. Most exceptions to this layout are commonly due to drainage and water management features such as river channels, abandoned creeks, and flood bypasses. Field sizes are variable, and generally laid out according to sections (1 × 1 mi; ≈ 1.6 × 1.6 km). Sections are generally subdivided into smaller units. Quarter sections (0.5 × 0.5 mi, ≈ 800 × 800 m) are very common, but 1/8 (≈ 400 ×

800 m) and 1/16 sections (≈ 400 × 400 m) are also common. The smallest rice field we observe is 1/32 section (≈ 200 × 400 m). While the size of the largest rice field we observe is 1 section, homogenous regions of adjacent fields with similar planting times can span large portions of the valley floor, forming regions of nearly uninterrupted rice on the order of 15 × 15 km.

The same clear, dry summer climate that supports rice production in the Sacramento Valley also benefits satellite imaging. This is reflected in the data archive, as over 10 cloud-free satellite imaging acquisitions were acquired for every growing season since the launch of Landsat 8 in 2013. When present, smoke from summer wildfires hinders satellite imaging. However, wildfires in California are most common in late summer, after the rice crop has been planted and established, and high frequency imaging is less critical for crop monitoring. These factors, combined with the economic productivity of the California rice crop and the abundance of ground-based observational data, suggest the Sacramento Valley as a nearly ideal location to characterize the evolution of rice agriculture in the geophysical parameter space relevant to multitemporal optical and thermal satellite imaging.

Materials and Methods

Data Acquisition & Preprocessing

Landsat data were downloaded using the USGS Global Visualization Viewer (GloVis) web tool (http://glovis.usgs.gov/) (USGS, 2018). The Landsat 8 satellite images the Earth simultaneously using both the Operational Land Imager (OLI) and the Thermal Infrared Sensor (TIRS) instruments. OLI collects data in 9 channels in the 0.4—2.3 µm optical wavelength range. The OLI data used in this study are from bands 2 through 7, all collected at 30 m spatial resolution. OLI data were calibrated from digital number (DN) to exoatmospheric reflectance using the standard calibration procedures described in the Landsat Data Users Handbook (USGS,

2016b). Where indicated, 30 m OLI data were subsequently convolved with a 21 × 21 low pass Gaussian blurring filter to mimic the coarser spatial resolution of the TIRS sensor.

The TIRS instrument collects data at 100 m resolution in 2 channels at thermal infrared wavelengths (10–13 μm). TIRS data were converted from DN to radiance using the standard procedures described in the Landsat Data Users Handbook, then atmospherically corrected using the approach described in Section 2.3 below, as proposed by (Barsi et al., 2003). All TIRS data used in this study were from Band 10 because standardized atmospheric correction coefficients for Band 11 are not yet available using this approach.

MODIS data used for illustration and comparison were downloaded using the USGS EarthExplorer website (http://earthexplorer.usgs.gov/) and the MODIStools R package (Busetto and Ranghetti, 2016). Where indicated, the MOD11 LST and Emissivity product was used to generate phenology curves for illustration purposes. Meteorological station data were downloaded from the California Irrigation Management Information System (CIMIS) website at https://cimis.water.ca.gov/. All data used in this analysis are freely available to the public.

Spectral Mixture Analysis of Optical Data

Spectral mixture analysis (SMA; (Adams et al., 1986; Gillespie et al., 1990; Smith et al., 1985)) is a well-established, physically-based image processing technique which represents the multispectral reflectance of each pixel as an area-weighted linear sum of endmember (EM) reflectance spectra. The technique is based on constrained least squares inversion of a system of mixing equations, which can be written in the following form:

$$F_S E_{S,\lambda_i} + F_V E_{V,\lambda_i} + F_D E_{D,\lambda_i} = R_{\lambda_i}$$

where F_S, F_V, F_D, are the relative subpixel areal abundances of the *S*, *V*, and *D* EMs; $E_{S,\lambda i}$, $E_{V,\lambda i}$, $E_{D,\lambda i}$, are the reflectances of the *S*, *V*, and *D* EMs at each wavelength; and $\lambda_i \in$ {482 nm; 561 nm; 655 nm; 865 nm; 1609 nm; 2201 nm}, corresponding to the center wavelengths of bands 2–7 of Landsat 8 OLI, respectively. Often, a unit sum constraint is imposed due to the physically-based expectation that subpixel areal abundances should sum to unity. In this analysis, this constraint was used and given a weight = 1.

SMA is sensitive to the EMs used, but global analyses of multispectral Landsat (Small, 2004; Small and Milesi, 2013) and Sentinel-2 (Small, 2018) data, as well as regional analysis of a diverse set of hyperspectral AVIRIS flight lines (Sousa and Small, 2018a), show that the Earth's ice-free land surface is generally well represented by 3 generic EMs: Substrate (S; rock and soil), Vegetation (V; illuminated photosynthetic foliage), and Dark (D; water and shadow). In addition to providing estimates of fractional vegetation cover which are linearly scalable (Christopher Small, 2001; Small and Milesi, 2013) and more accurate than vegetation indices (Elmore et al., 2000; Smith et al., 1990), SMA based on these globally standardized EMs simultaneously provides estimates of the subpixel abundance of S and D materials with root-mean-square misfits < 0.05 for > 97% of 100,000,000 spectral mixtures from every ice-free biome on Earth (Small and Milesi, 2013).

This study is rooted in the relationships between the annual phenological cycles of the rice crop and other vegetation (agricultural and indigenous), seasonal variations in soil moisture (from precipitation and irrigation), evaporation and transpiration of water, and the combined impact of all these factors on surface temperature. Understanding of these relationships is facilitated by conversion of the optical reflectances measured by OLI to fractional abundance of the global S, V and D EMs. For each of the 22 Landsat images used in this study, estimates of

the areal abundance of S, V, and D materials were derived by SMA based on the standardized global EMs of (Sousa and Small, 2017a). The output of this SMA is a set of three complementary time series of fraction images. Each fraction image time series shows the evolution of the abundance of S, V or D materials over the course of the 22 cloud-free overpasses of the study area in 2016 and 2017. In this study, we focus on the vegetation time series, but this approach also provides information on soil, water, and shadow, which are incorporated in a separate study.

Emissivity Estimation

Thermal imaging sensors measure radiance in one or more wavelength ranges, which can then be converted to an estimate of the apparent brightness temperature (T_b) of the emitting target. However, in order to convert apparent T_b into an estimate of actual LST, the emissivity (ε) of the target must be known (or assumed). Global, time-averaged ε estimates exist at 100 m scales (Hulley et al., 2015), but could introduce obvious errors in the agricultural landscape investigated here due to large seasonal variations in land cover. Daily global ε estimates are also now available at 1 km resolution (Hulley et al., 2014). While some fields in the study area are large enough to be oversampled by 1 km emissivity products, many are not. Combining temperature and emissivity measurements with an order of magnitude difference in spatial resolution would at minimum require accurate linear scaling. While spatial scaling of emissivity (and temperature) has been shown using both modeling and microbolometer experiments to be linear for small subpixel temperature differences, increasing nonlinearity is expected as subpixel temperature differences increase (Heasler et al., 2007; McCabe et al., 2008; Shi, 2011). Subpixel temperature differences in the study area used in this analysis (e.g. between adjacent bare vs flooded fields on a summer day) can be on the order of 40°C.

For these reasons, we generate pixel-specific ε estimates using SMA. Because SMA estimates the fraction of the area within each pixel covered by each land cover type, and representative ε values can be associated with each spectral EM material, SVD fraction images can be used to generate physically-based pixelwise aggregate emissivity estimates. We estimate the emissivity of the land surface at each Landsat pixel assuming the following simple linear mixing relation:

$$\varepsilon_{Mixed\ Pixel} = f_S\varepsilon_S + f_V\varepsilon_V + f_D\varepsilon_D$$

where f_s, f_v, and f_d are the fractional areal abundance of substrate, vegetation, and dark materials within each pixel; ε_S, ε_V, and ε_D are EM ε values for Substrate (dry soil), Vegetation, and Dark (water); and $\varepsilon_{Mixed\ Pixel}$ is the overall emissivity of the mixed pixel. The values used for ε_S, ε_V, and ε_D were 0.92, 0.96 and 1.0, respectively, taken from average values of a wide range of Earth materials reported in (Rubio et al., n.d.).

Atmospheric Correction of Thermal Data

Atmospheric effects can cause particularly pernicious errors in thermal satellite imaging because light at thermal wavelengths can be absorbed and re-emitted strongly within the atmosphere. Atmospheric correction models attempt to remove the effects of absorption, scattering and emission along the two-way path (for VSWIR) or one-way path (for TIR) of radiation through the atmosphere. However, atmospheric correction accuracy is dependent upon the abundance and quality of ancillary data, as well as the choice of model used. In many rice growing regions, field data to constrain atmospheric corrections are sparse or unavailable.

A recently developed Atmospheric Correction Parameter Calculator webtool provides standardized thermal atmospheric correction parameters for Landsat images using commercial

MODTRAN software and atmospheric profiles from the National Centers for Environmental Prediction (NCEP). Atmospheric correction parameters were computed for the center of the study area using this online tool, found at: https://atmcorr.gsfc.nasa.gov/ (accessed 5 December, 2018). This procedure uses standardized atmospheric profiles derived from National Centers for Environmental Prediction (NCEP) reanalysis and commercial Moderate Resolution Atmospheric Transmission (MODTRAN) radiative transfer software. This approach has been validated to yield a temperature bias of less than 0.5 ± 0.8 °C compared to results from two independent Landsat calibration/validation teams at the NASA Jet Propulsion Lab and Rochester Institute of Technology (Barsi et al., 2005). This tool has the benefit of providing a globally standardized approach to thermal atmospheric correction. This is particularly important for the case of rice mapping, where the quality and quantity of ancillary meteorological variable can be highly variable from basin to basin.

As described in (Barsi et al., 2003), space-reaching radiance and surface-leaving radiance may be related using the following expression:

$$L_{TOA} = \tau\varepsilon L_T + L_u + (1-\varepsilon)L_d$$

where τ is the atmospheric transmission, ε is the emissivity of the land surface, L_T is the radiance of a blackbody target of kinetic temperature T (i.e. LST), L_u is the upwelling radiance, L_d is the downwelling radiance and L_{TOA} is the space-reaching radiance. The web tool gives estimates of τ, L_u, and L_d; pixelwise ε was computed using the methodology described in Section 2.3; and L_{TOA} is the radiance measured by TIRS. This equation can be rearranged to solve for L_T:

$$L_T = \frac{L_{TOA} - L_u - (1-\varepsilon)L_d}{\tau\varepsilon}$$

This quantity was then used as the estimate of LST for the remainder of the analysis.

Effect of emissivity estimation and atmospheric correction

Figure 41 shows the effect of the atmospheric correction and pixelwise ε estimation on two representative scenes: one with a hot, low τ atmosphere (top row) and another with a cold, high τ atmosphere (bottom row). The estimated τ coefficients are 0.79 and 0.96, respectively, the most extreme values of the 22 scenes from 2016 and 2017 used in this study. The left column shows the effect of applying the atmospheric correction assuming uniform ε = 1, and the center column shows the effect of applying the atmospheric correction and estimating pixelwise mixed ε using SMA. Histograms of all three levels of correction for all image pixels in the field area are shown in the right column.

For the hot atmosphere, the effect of the atmospheric correction is essentially to act as a multiplicative linear transformation, decreasing the temperature of deep lakes by about 5 °C, increasing the temperature of rice paddies by about 2–5 °C and increasing the temperature of bare soil by about 5-9 °C. For the cold, high τ atmosphere, the effect is much smaller (less than 0.5 °C across all land cover types). The image-wide effect of the atmospheric correction is linear because the same linear coefficients are applied uniformly across the study area. In contrast, using pixelwise mixed ε introduces a more dispersive transformation because geographically explicit information is introduced. For the hot, low τ atmosphere, the overall amplitude of the atmospheric correction with pixelwise emissivity is approximately 10°C for bare soil, 4–6 °C for rice paddies, and 2–4 °C for deep lakes. The effects are reduced for the cold atmosphere, with temperature estimates for bare soil increasing by 2–5 °C, rice paddies by 0–2 °C, and deep lakes by 0–1 °C.

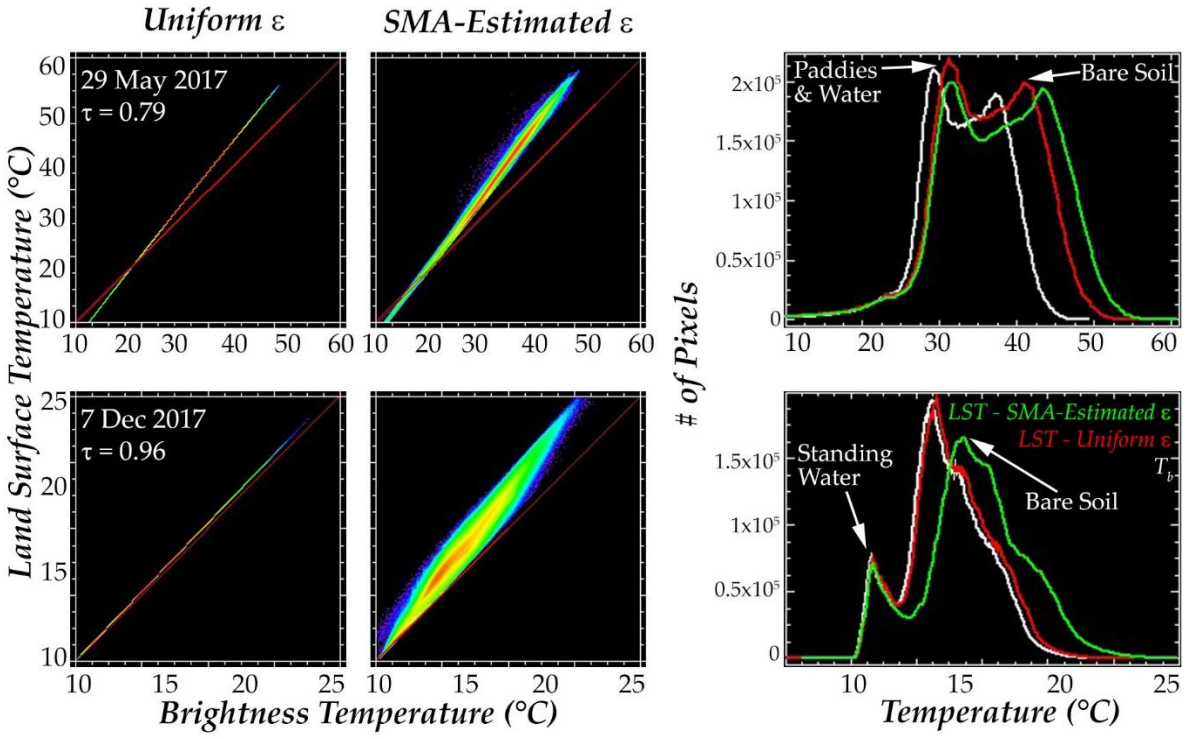

Figure 41. Effect of atmospheric correction and emissivity estimation on temperature estimates. In the case of a relatively low τ atmosphere and high insolation (top row, τ = 0.79), atmospheric correction increases T of rice paddies by about 2 °C and bare field about 4 °C. In the case of a high τ atmosphere with low insolation (bottom row, τ = 0.96), atmospheric correction changes T estimates by less than 0.5 °C. Using pixelwise ε estimates in the May image results in an additional 0.5 °C increase for paddies and a 2 to 3 °C increase for bare soil. In the December image, pixelwise ε results in no change in standing water but a 2 to 2.5 °C increase for bare soil.

Additional insight into the relationship between radiative and kinetic temperature can be derived from comparison of satellite-derived LST versus field temperature data. In this study area, this can be achieved using measurements from the California Irrigation Management Information System (CIMIS). CIMIS maintains an extensive network of field observations of meteorological data throughout the agricultural regions of California. Figure 42 shows a map of

the 4 station locations within the area of the white box from Figure 40. The stations bound the region dominated by rice agriculture (darker green) to the north, south and west. The stations are sited in agricultural microenvironments and include a comprehensive suite of air and soil temperature, rainfall, and wind measurements. These measurements are expected to be representative of the atmospheric and near surface conditions throughout the study area.

In Figure 42, daily time series of soil temperature (green) and air temperature (red) are plotted for the time of the Landsat 8 overpass for each of the stations, along with Landsat-derived T_b (gray) and LST (black) for each of the 9 pixels in a 3 × 3 box surrounding the station location. The variability in agreement between the field and satellite temperatures is likely related to variations in microclimate due to differences in the siting of each station. While all four stations are immediately surrounded by irrigated pasture, the Durham and Verona pastures are situated within a matrix of tree and row crops, while the Williams and Biggs pastures are surrounded by rice and/or wetlands. It is possible that the more saturated surface hydrology surrounding the Biggs and Williams sensors introduces atmospheric boundary layer effects that impact temperature retrievals. These local effects would not be captured by the atmospheric correction procedure used in this analysis.

As expected, in all cases the effect of the atmospheric correction is to increase the estimate of LST relative to the uncorrected T_b measurements. The magnitude of the increase is between 0.5 and 4°C, depending on atmospheric transmission. Interestingly, while these corrections do amount to an overall bias shift of the LST time series 1 to 5 °C, they do not affect the relative spatiotemporal structure of time series or appreciably impact the amplitude of the annual cycle.

Regardless of these complexities, it is clear that the shape and rough amplitude of the Landsat LST time series generally agree with the station data, in some cases remarkably closely. With the exception of the anomalous 2017 Williams data, the amplitude of the difference between the field air temperature measurements and the satellite LST measurements is generally much smaller than the amplitude of the seasonal cycle. As expected, the LST is considerably higher than the soil T because the latter integrates over a depth of several cm of soil and is much less sensitive to the higher skin temperature of the soil surface. In all cases, the timing of the annual cycles of soil T, air T, T_b, and LST agree, suggesting that TIRS effectively captures the essential features of the thermal phenology.

Spatiotemporal Analysis and Temporal Mixture Models

Our approach to the quantitative analysis of satellite image time series is implemented in two stages: *characterization* and *modeling*. The two stages are summarized briefly below. Each stage is also presented separately in the Results section. For detailed background, explanation, and examples of implementation of the method, please see (Small, 2012; Sousa and Small, 2017b).

Characterization involves Empirical Orthogonal Function (EOF) analysis. EOF analysis is a general tool which can be applied to any image time series. For the purposes of this study, the time series of interest are sequential maps of fractional vegetation cover, F_v, and LST. EOF analysis considers each image time series as a matrix with each geographic pixel occupying a row and each time step occupying a column. A satellite image time series therefore contains a large (generally $> 10^6$) number of rows and a much smaller (generally $< 10^3$) number of columns. In the case of our study area, the number of rows is 12×10^6 (3000×4000 pixels) and the number of columns is 22 for the 2016 + 2017 analyses and 11 for the 2016-only analyses. EOF

analysis is based on the Principal Component (PC) transform (Pearson, 1901) which computes the covariance (or correlation) matrix of the data, then decomposes that matrix into its corresponding eigenvalue and eigenvector pairs. The eigenvectors show the dominant modes of uncorrelated spatial and temporal variance in the dataset, and the eigenvalues quantify the fraction of total variance associated with each mode. For more background on EOF analysis, see (Bretherton et al., 1992; Menke and Menke, 2016, chap. 8; Preisendorfer, 1988; von_Storch and Zwiers, 1999).

Characterization continues with the examination of the transformed spatiotemporal data in this new, optimized space, referred to as the Temporal Feature Space (TFS). The low order projections of the TFS are depicted graphically using scatterplots of the spatial PCs in conjunction with time series of the corresponding temporal EOFs. The most distinct temporal patterns (i.e. phenologies) occupy apexes of the data cluster in the TFS. The temporal patterns of the geographic pixels associated with these apexes are identified as temporal endmembers (tEMs). In the case of linear mixing, binary mixtures of these patterns occupy sharp edges between the apexes. Pixels in the interior of the point cloud can be represented as combinations of all the EM time series.

Once the temporal EMs are selected, the analysis proceeds to the *modeling* phase. By direct analogy to spectral mixture modeling, this analysis uses linear Temporal Mixture Models (TMMs, (Lobell and Asner, 2004; Piwowar et al., 1998)) which have the virtue of relative mathematical simplicity and straightforward physical interpretation. Linear TMMs model every pixel time series as a linear combination of a small number of tEM time series. The tEMs to be used are identified during the characterization phase of the analysis. Inversion of the mixture model unmixes each pixel time series to yield an estimate of the relative contribution (fraction)

20 km
Sierra Nevada Foothills
Durham
12
149
Willows
Glenn
Thermalito Afterbay
Oroville
Biggs
244
Palermo
Gridley
Live Oak
Sutter Buttes
250
Colusa
Butte
Williams
Yuba City
65
5
70
Coast Ranges
Verona
235
Temperature (°C)
40
30
20
10
0
12 (Durham)
235 (Verona)
244 (Biggs)
250 (Williams)
Air
Soil
Landsat T_b
Landsat LST
Jan Jun Jan Jun
2016 2017

Figure 42. The primary rice producing region of California. The annual thermal cycle is captured by met stations maintained by the California Irrigation Management Information System (CIMIS). Air temperatures (red) are generally higher and more variable than soil (green). Durham, Verona, & Biggs records are similar. The Williams station (installed mid 2016) has substantially lower air, but similar soil and brightness temperatures, to the other stations. Landsat Tb (black) generally records at the warm bound of the envelope of air T. Landsat LST is higher than Tb in all cases.

of each tEM to each pixel time series in the dataset. The result is a set of continuous maps showing the relative contribution of each tEM pattern at each point in space. The meaning of the model result is therefore straightforward (quantitative description of similarity to each tEM), and the model inversion is mathematically transparent (ordinary least squares inversion of an overdetermined system of linear equations). This approach also has the benefit of generality, as no portion of the analysis imposes assumptions specific to particular geophysical variables or sensing modalities. The only implicit assumption is that spatiotemporal variance represents potentially useful information.

While this method has been shown to be effective in analyses using single geophysical variables (e.g. (Lobell and Asner, 2004; Piwowar et al., 1998; Small, 2012; Sousa and Small, 2017b)), to our knowledge it has not yet been applied to coincident observations of reflectance and temperature. This study examines the implications and potential utility for parallel application of this spatiotemporal analysis methodology to the case of coincident LST and F_v image time series for the practical purpose of mapping and monitoring rice agriculture.

Results

The parallel analysis presented here requires additional characterization before the EOF analysis to examine and compare the spatiotemporal patterns present in each data stream. Sections 3.1 and 3.2 show this initial step. Section 3.3 then presents the characterization as described in the Methods section, and Section 3.4 presents the results of the modeling step. Finally, Section 3.5 presents a potential application for near-realtime monitoring and results of field validation.

Vegetation Phenology

Figure 43 demonstrates a representative annual phenological progression of the region using a series of land cover fraction (first and third columns) and LST (second and fourth columns) images from the calendar year 2016. The subpixel fraction images use the colors Red, Green, and Blue to correspond to relative abundance of substrate (soil or non-photosynthetic vegetation), photosynthetic vegetation, and dark materials (shadow or water) for a given time. These relative abundances are computed using the 3-endmember spectral mixture model described in the Methods section. Each image is enhanced identically, so colors are directly comparable. Soils generally appear as red, photosynthetic vegetation as bright green, and standing water as blue. As vegetation senesces, its reflectance spectrum grades toward that of the substrate endmember, resulting in orange and yellow colors on the fraction images. Images are only shown from April through November, because winter months are generally covered in cloud and rice is not grown at this time.

Rice is generally grown in the clay rich soils to the east and west of the Sacramento and Feather River channels. The rice growing area can be visually identified as the area of standing

water (dark blue/black) in the May 26 image. This is due to the rice crop phenology, summarized as follows:

Many, but not all, rice fields are flooded during winter (November through February or March) to provide habitat for migrating birds. In April, the flooded fields are drained, and all rice fields are plowed in preparation for the rice crop. Rice fields are then generally flooded in May and seeded by airplane into standing water. The rice then greens up during the summer months and begins to senesce in September, continuing to senesce and being harvested through September and October. By November, the harvest is complete. After harvest, some fields are left bare and others are flooded for winter bird habitat, and the cycle begins again. For more information on the rice cropping calendar in this region, see http://www.rice.ucanr.edu/ or http://www.calrice.org/

While rice dominates the landscape, other vegetation also exists. The foothills of the Sierra Nevada, Coast Ranges, and Sutter Buttes largely host rainfed grasslands used for grazing. The phenology of these regions is nearly opposite that of rice agriculture, because the grasslands are green during winter and generally senesced during the summer months. In addition, a wide range of other row crops and orchards are grown in the valley with a diversity of cropping systems and phenologies. Settlements also occupy a small portion of the landscape, hosting an even more complex mixture of evergreen and deciduous trees, shrubs, and grasses.

The time series in the lower right of Figure 43 show typical phenological progressions of rice crops (solid) versus native grassland (dashed) in terms of both vegetation abundance (green) and temperature (red). As expected from the image time series, the vegetation abundance curves for the rice and grassland pixels are nearly 180° out of phase. Rice has a strong peak in vegetation abundance during the summer growing season, and also a minor peak during the

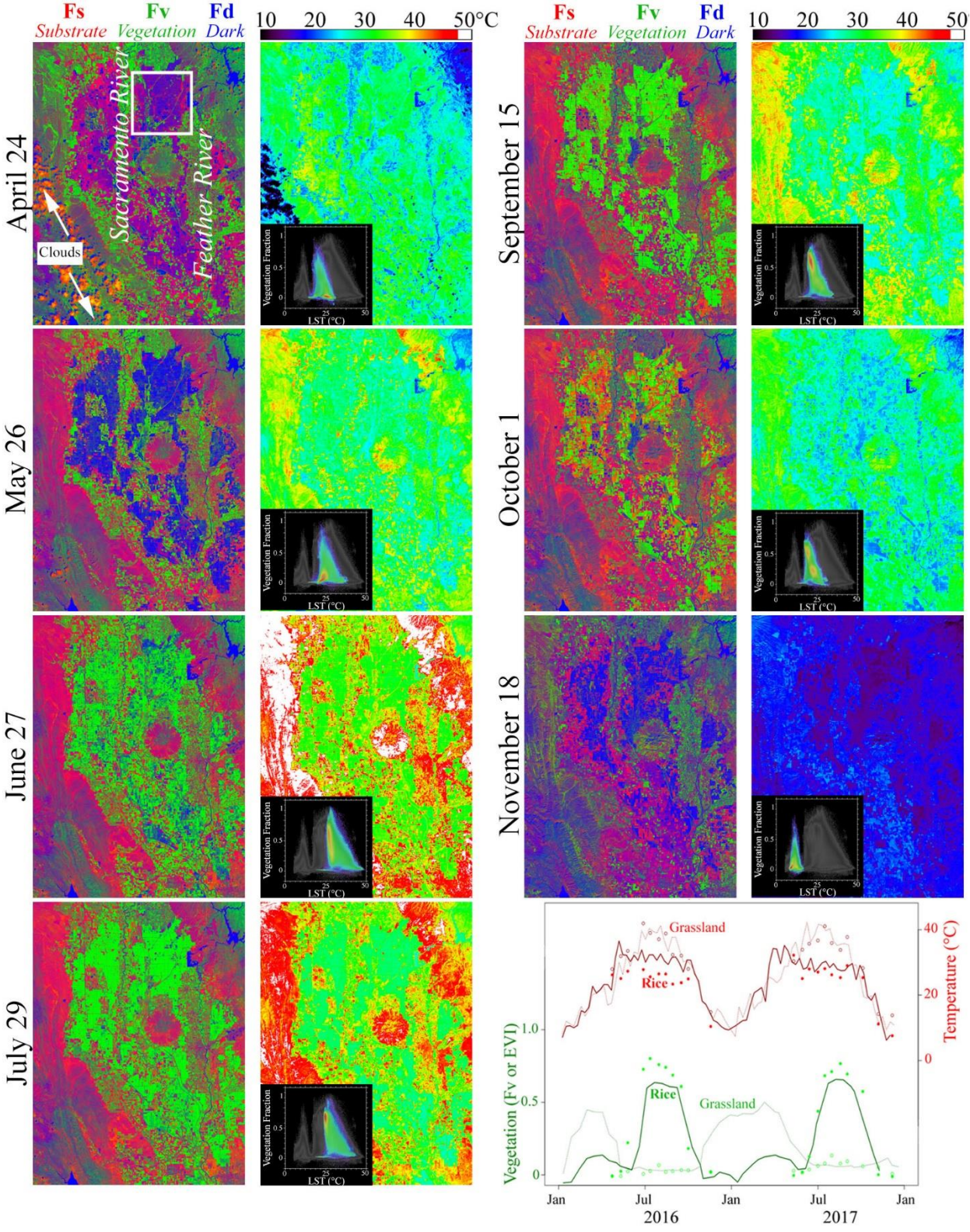
Fs
Substrate
Fv
Vegetation
Fd
Dark
10 20 30 40 50°C
April 24
May 26
June 27
July 29
September 15
October 1
November 18
Sacramento River
Feather River
Clouds
Vegetation Fraction
LST (°C)
Grassland
Rice
Vegetation (Fv or EVI)
Temperature (°C)
Jan
Jul
Jan
Jul
Jan
2016
2017

Figure 43. Multisensor evolution of land cover and temperature. Image time series shows Landsat EM fraction abundance (Fs, Fv, and Fd; 1st and 3rd columns) and LST (2nd and 4th columns). Fraction images show bare fields (dark red, mixture of Fs and Fd) prepared in Apr, flooded (dark blue, high Fd) in May, greening up from Jun to Sep (from dark green to bright green, tradeoff between Fd and Fv), senescing and being harvested (orange and yellow, tradeoff between Fv and Fs) in Oct and Nov. Thermal images are dominated by the seasonal cycle, with amplitude modulated by ET. Dry grasslands and fallow fields can reach summer LST of 20 °C greater than flooded rice fields. In winter, differences in LST between land covers are reduced. Inset plots show LST (X) vs Fv (Y) for each scene (in color) relative to all 22 scenes from 2016+2017 (in grayscale). White box on the Apr image indicates the area used for the characterization shown in Figure 44 and Figure 45. Inset time series shows comparison between Landsat Fv + LST (dots) and MODIS EVI + Land Surface Temperature composites (lines).

winter fallow season, presumably from non-rice vegetation growing in flooded fields. The grassland pixels have very low amounts of photosynthetic vegetation during the hot and dry summer months because they are rainfed, but reach broad peaks during the winter rainy season of comparable but somewhat smaller amplitude than the agriculture. In Figure 43, dots correspond to Landsat F_v and LST observations and continuous curves correspond to MODIS EVI and LST time series. The benefit of using both MODIS and Landsat for purposes of this illustration is evident, in that there were no cloud-free Landsat images available over a 3-month period during the wintertime, but sufficient usable MODIS images were acquired to produce composites approximating the full annual time series.

Thermal Phenology

The fundamental physical process driving the thermal phenology of the region is the sinusoidal seasonal insolation curve, with an annual minimum at the winter solstice. However, the biogeophysical properties of the landscape modify this insolation curve in both space and time. For instance, grassland achieves a much greater summer temperature than rice because the land surface dominated by dry soil and non-photosynthetic vegetation (or absence of vegetation) has low thermal inertia, and can support very little evapotranspirative cooling. On the other hand, rice agriculture is not only irrigated but grown in standing water for much of the summer, resulting in substantial cooling both from evaporation of the paddy water below the canopy and transpiration of the respiring and photosynthesizing vegetation. This results in a relatively stable LST during the summer months, yielding a flatter top to the temperature curve.

The phenological progression of the thermal image time series complements that of the fraction image time series. In late April, the only prominent spatial patterns in the thermal field are due to elevation, rivers and lakes, and transient clouds. However, as the spring progresses into summer, clear differences emerge between rice and grassland areas. In the September and October images, differences within the region of rice agriculture become apparent, likely on the basis of evapotranspiration decreasing at variable rates as some fields senesce sooner than others, and some fields are drained before others to prepare for harvest. Once the fields are harvested, differences between land cover types are greatly reduced. In fall, the remaining vegetation can be somewhat warmer than its dry surroundings due to the greater heat capacity of its leaf water.

Finally, the scatterplots inset on the thermal images show the relationship between LST (x-axis) and F_v (y-axis) for every pixel in the image. These scatterplots are an alternate coordinate system with which to understand the dataset. The scatterplots are color-coded so

warmer colors represent more pixels and cooler colors represent fewer pixels. The grayscale background silhouette of the full multitemporal point cloud shows the composite space of all the images together. Because so many pixels in the image correspond to rice agriculture, they generally form the largest cluster in Temperature vs Vegetation (TV) space and are represented by warmer colors. In April, for instance, rice fields are recently plowed so they are cool and unvegetated, and the corresponding warm colored cluster plots at the bottom center of the space. In May, the fields are flooded and become even cooler, but remain unvegetated, so the cluster moves to the left in TV space. In late June, fields vary widely from just planted (late crop) to nearly mature (early crop), resulting in a wide range of F_v. ET cools the crop so its temperature does not change appreciably, resulting in a vertically elongated cluster. For the rest of the summer, the fields do not change appreciably in vegetation abundance or temperature, so the cluster is stable until fields are drained and begin to senesce (September), resulting in the cluster elongating toward higher temperatures. Harvest of the rice crop results in a stepwise change of the TV properties of a rice field. The separation of the point cloud into two distinct clusters of approximately equal size (harvested & unharvested) in the October 1 image agrees with 2016 USDA estimates that 54% of the California rice crop was harvested by October 9 (Childs, 2016). By mid-November, rice harvest is complete, and the landscape shifts into its winter state. Interestingly, the few usable winter images that exist plot in a nearly disjoint portion of the vegetation temperature space, suggesting that the spatial relationship between vegetation and temperature during winter may be dominated by fundamentally different physical processes than during summer.

Characterization – EOF analysis and tEM selection

The preceding figures can be summarized by the following set of observations:

1. The thermal phenology of rice agriculture is substantially different in amplitude and shape from other land cover types in the region;
2. The parallel evolution of both thermal and vegetation phenology can be explained in terms of the surface hydrologic cycle and growth cycle of the multiple phases of rice crops;
3. The spatiotemporal variations in LST have substantial differences from those of the vegetation abundance, despite their interdependence; and
4. The spatiotemporal variations in both LST and F_v can be explained using fundamental physical principles.

Put together, observations 1, 2 and 3 suggest that including Landsat LST in a phenological analysis could add information that is not present using vegetation abundance alone. Observation 4 suggests that such a phenological analysis could be based on straightforward physical principles with a bare minimum of model complexity.

One potential approach to this mapping problem is the spatiotemporal analysis method of (Small, 2012). A primary benefit of this approach is that it imposes no assumptions about the functional form of the phenology, but rather characterizes the temporal patterns based on the data itself. Other benefits to the method are its simplicity, robustness, and generalizability, as well as its ability to generate results with straightforward physical meaning. Because they are based on physical principles and easily identified tEMs representing known phenologies, maps derived from linear model inversion provide a degree of uniqueness of solution that is almost never provided by discrete thematic classifications which are based on ad hoc selection of land cover classes and training data.

In order to use this approach with a dual data stream, two decisions must be made. The first decision is whether to incorporate both streams into a single analysis or to analyze each in parallel. We present the results of parallel characterization method here because it is conceptually simpler and achieves the objectives of the current study. The combined

characterization and analysis of thermal and vegetation phenology lends itself naturally to the study of ET dynamics, and is the focus of a separate study.

The second decision is whether to analyze the two years together or separately. Because significant benefits can result from either approach, we present results of both in Figure 44 and Figure 45, respectively. Because the two single-year characterizations yielded similar results, we present only the 2016 results as characteristic of both years of the dataset.

For each case, we begin by first conducting an EOF analysis of the relevant image time series. We choose unnormalized (covariance-based) rotations in each instance. Normalized (correlation-based) rotations were also investigated, but the resulting feature spaces were less informative. In each case, over 65% of the variance is represented in the first 3 dimensions of the data. While this number is low enough to suggest that informative structure may be present in the higher dimensions of the dataset, the three low-order dimensions capture the most relevant phenological patterns necessary to distinguish rice from other crops and to characterize its seasonal and interannual variability.

Figure 44 and Figure 45 summarize the characterization stage of the parallel analyses for single year (2016) and dual year (2016 + 2017) time series, respectively. Characterization is based on the 24 × 24 km subset shown in the white box in Figure 43. We use this spatial subset because it is dominated by rice agriculture with a wide range of crop timing. In every case, the loadings of the first 3 spatial PCs are shown as scatterplots. These scatterplots represent the location of each geographic pixel in the image time series in a 3-dimensional space, known as the Temporal Feature Space (TFS), in which the axes represent the relative contributions of the first 3 EOFs (uncorrelated temporal patterns of maximum variance). Clusters in this space correspond to sets of geographic pixels with similar temporal trajectories over the course of the

two years of the study. Apexes in the space correspond to temporal endmembers (tEMs), pixels with the most distinctive temporal patterns in the image time series. Pixel time series lying inside a convex hull connecting the tEMs can be represented as linear combinations of the tEM time series.

Figure 44 shows a comparison of the TFS for image time series of both F_v and LST for the year 2016. The TFS of the F_v image time series shows four distinct apexes representing the tEMs: Early Rice, Late Rice, Wetlands/Evergreen, and Water/Fallow. Time series of F_v corresponding to these tEMs are shown in the lower right. All 4 tEMs are clearly distinct on the PC 3 vs 2 scatterplot. The point cloud in this scatterplot forms a cross shape, with the axis between tEMs 1 and 2 corresponding to phenological timing and the axis between tEMs 3 and 4 corresponding to overall vegetation abundance. The Water/Fallow tEM forms the sharpest corner, as expected given the small amount of variability expected in the F_v of water bodies and fallow fields through time. Early and Late tEMs are less sharp but still clearly defined, indicating substantial variability in the timing of the phenological signal. However, the Early and Late clusters are also visibly distinct, indicating two clear phenological groups. The Wetlands tEM is the most diffuse, as expected given the wide range of vegetation types, hydrological regimes, and land management strategies for wetlands in the area.

The TFS of the LST image time series shows substantially more clustering than that of the F_v time series. This indicates that more pixels have more similar LST trajectories than F_v trajectories. At least 7 tEMs are identifiable. The most distinct from each other are Water (EM 4; blue) and fallow fields (3; gray). Water time series are particularly distinctive as their very low PC 2 and very high PC 1 and 3 values position them as disjoint from the remainder of the dataset. The remainder of the space partitions into a) differences in timing of rice phenology, and

b) differences between rice, non-rice agriculture, and wetlands. Wetlands (EM6) occupy the corner of the point cloud closest to water, and also form an axis grading into fallow fields (EM3). The Fallow-Wetland axis is nearly orthogonal to the Early-Late axis of rice phenology, most clearly seen in the PC 1 vs 3 projection. Non-rice agriculture (EM5) plots on a continuum between the Early Rice and Fallow tEMs. Finally, double cropping (D) is clearly identifiable in both the F_v and LST feature spaces. Few fields in the spatial subset used for this rotation practice double cropping, so this tEM is sparsely populated.

Figure 45 shows a characterization of the dual year 2016+2017 image time series. In both time series, the early/late phase information that dominated the single year time series is suppressed (though still present), and the structure of the TFS is dominated by year-to-year differences in crop presence or absence. In the F_v space, both Wetlands (EM4; green) and Water/Fallow (EM5; blue) are still clear tEMs. The largest cluster, however, is now that of fields cropped in both 2016 and 2017 (EM3; red). This cluster is clearly distinct from the small cluster of fields cropped in 2017 only (EM2; gray) and the much larger cluster of fields cropped in 2016 only (EM1; yellow). The fact that the 2016-only cluster is much larger than the 2017-only cluster is concordant with official USDA estimates of 42,000 fewer acres of California rice planted in 2017 than 2016 due to higher prices for competing commodities and severe early season flooding (Childs and Skorbiansky, 2017; NASS, 2017).

The dual year LST space again shows more clustering and overall complexity than the corresponding F_v space. At least 6 tEMs are identifiable. Again, the greatest distinction exists between water and fields that are fallow in both years (F/F). Water time series are again particularly distinctive as their very low PC 1 and PC 3 values position them as disjoint from the

remainder of the dataset. The remainder of the space partitions into a) differences in timing of phenology for fields under rice cultivation in both years, and b) the presence and absence of a

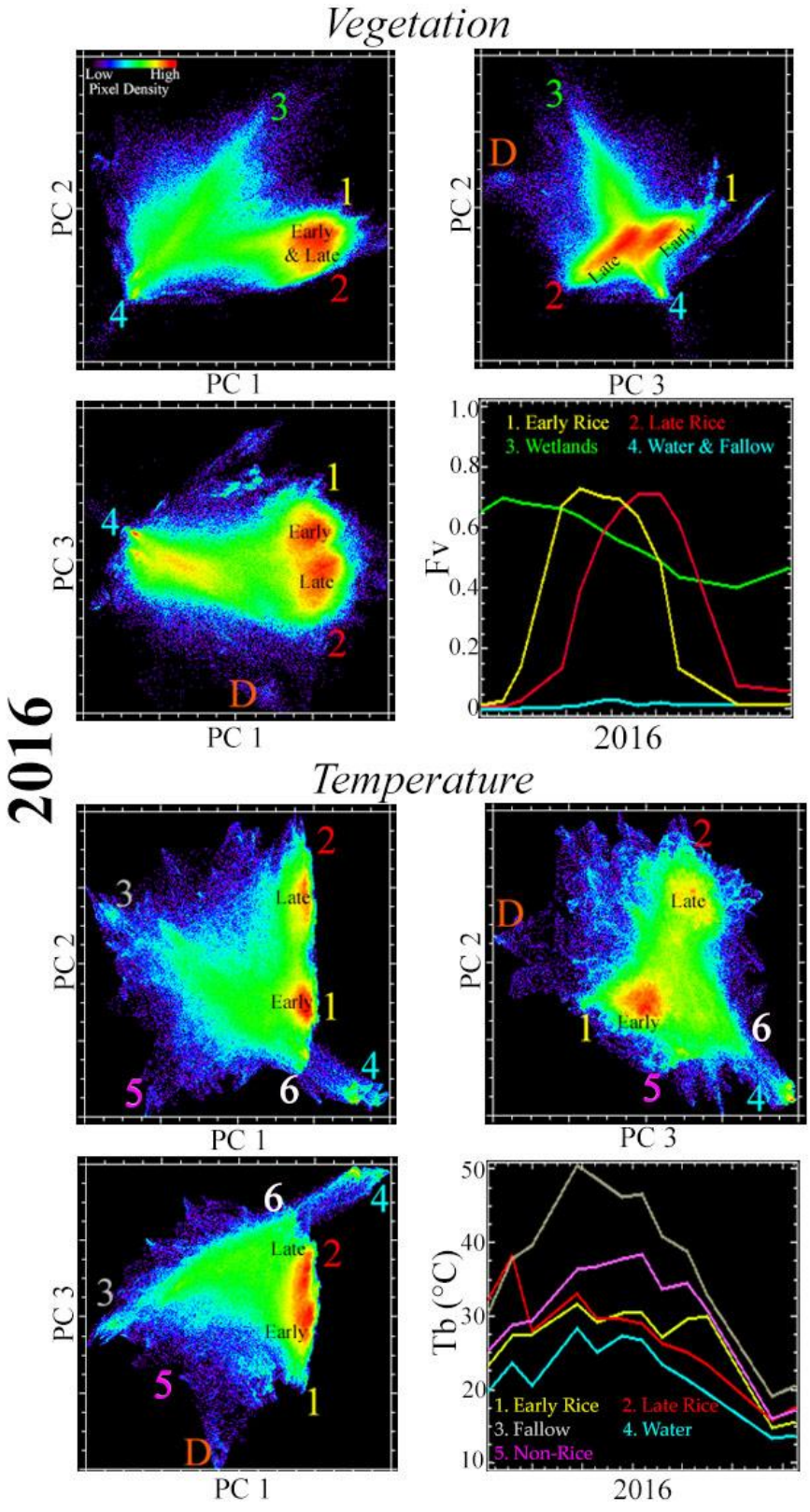
2016
Vegetation
Low
High
Pixel Density
PC 2
PC 1
PC 3
Early
& Late
Late
Early
1. Early Rice
2. Late Rice
3. Wetlands
4. Water & Fallow
Fv
2016
Temperature
Tb (°C)
1. Early Rice
2. Late Rice
3. Fallow
4. Water
5. Non-Rice

Figure 44. F_v vs LST 2016 temporal feature space (TFS) comparison. Each TFS highlights different aspects of the biogeophysical system. F_v discriminates between early and late cropping, but cannot distinguish rice from other crops with similar timing. LST clearly distinguishes rice from other crops, but misses the late season variability captured by F_v. These differences are reflected in EMs. F_v EMs correspond to Early Rice (1), Late Rice (2), Wetlands (3) and Water & Fallow (4). EMs of the LST space include Early and Late Rice (3 & 2) and also differentiate between water (4) and fallow (1). Non-rice agriculture (5) and wetlands (6) are distinct in LST but not F_v. Double cropping (D, Orange, EMs not shown) is also obvious with LST. Overall, the LST TFS is more complex and clustered than the F_v TFS.

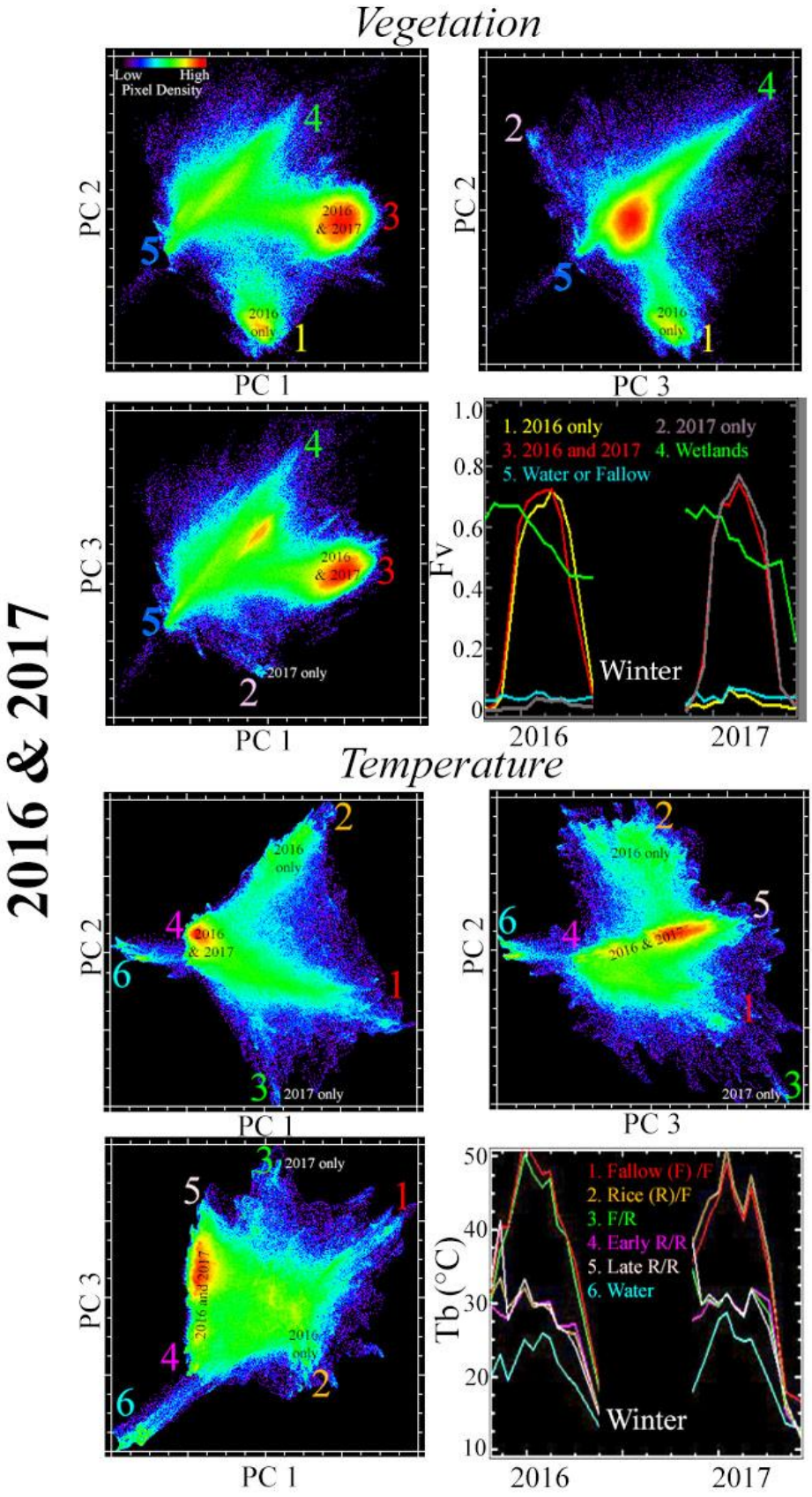
2016 & 2017
Vegetation
Low
High
Pixel Density
PC 2
PC 1
PC 3
2016 & 2017
2016 only
2017 only
1. 2016 only
2. 2017 only
3. 2016 and 2017
4. Wetlands
5. Water or Fallow
Fv
Winter
2016
2017
Temperature
6
Tb (°C)
1. Fallow (F) /F
2. Rice (R)/F
3. F/R
4. Early R/R
5. Late R/R
6. Water

Figure 45. Joint 2016 & 2017 F_v vs LST TFS comparison. When both years are analyzed together, intra-year signals (time of planting) are nested inside inter-year signals (crop conversion). EMs for both F_v & LST clearly differentiate between fields planted only in one year vs both years vs neither year. Again, LST shows more clustering than F_v, suggesting that, for rice agriculture in this location, a greater number of distinct spatially coherent temporal trajectories exist in LST time series than F_v time series. Early and late cropping remain as distinct EMs in LST, but do not in F_v.

rice crop in each year. The axis corresponding to phenology is nearly orthogonal to the axis corresponding to presence/absence of crop in each year. The potential utility of this information is discussed below.

While information about the phase of the rice is clearly present in both single year datasets, the F_v space tEMs capture more end-of-season variability than the LST tEMs. This could be due to gradual browning of the top canopy layer over weeks to months (resulting in progressive decline in F_v over the second half of the growing season) being accompanied by continual cooling by ET of the green vegetation and paddy water below (resulting in minimal change of LST). However, the LST dataset clearly shows enhanced ability to discriminate between rice and non-rice crops, likely due to early season paddy water producing a unique signature in LST but not F_v. For the dual year characterization, both F_v and LST clearly discriminate between areas cropped both years versus each individual year, but again LST shows superior ability to discriminate between rice and non-rice crops. Clearly, analyzing both datasets in parallel may yield substantial benefit over only using one, especially given that the two are co-acquired in all standard Landsat image acquisitions.

Modeling

As described in the Methods section, tEMs selected from each TFS were then used as the basis for two separate linear temporal mixture models. These models were then inverted to produce maps of thermal and vegetation phenology. Figure 46 shows the result of these inversions. In this figure, the saturation of each color corresponds to the similarity of each pixel to each of the tEM time series. Greater saturation implies greater similarity to the corresponding tEM (or binary mixtures for subtractive colors), while less saturation implies less similarity of the corresponding pixel to any of the tEMs. The latter is associated with higher model misfit, and is expected for pixels with phenologies not included in the model. Individual fields are clearly identifiable as either very early (pure green), very late (pure blue) or a mixture of the two (dark cyan). Intrafield heterogeneity in phenology is also clearly present in some cases, showing portions of individual fields growing faster than other portions. The potential utility of Landsat's ability to resolve intrafield spatiotemporal variability is discussed below. Overall, RMS misfits were comparable but somewhat higher for the F_v ($\mu = 0.15$, 90% < 0.25) than the LST ($\mu = 0.07$, 90% < 0.12) models. While these model misfit values are higher than generally observed for spectral mixture models, this is expected given the phenological complexity of the landscape and the relatively low number of tEMs used.

The right column shows the result of a 3 tEM temporal mixture model of 2016 + 2017 thermal phenology showing crops in both years (cyan), only 2016, magenta, or neither (dark yellow/orange). The unique temporal signature of rice thermal phenology allows it to be readily identified from other types of agriculture, which map as dull colors corresponding to combinations of tEMs. Field-to-field variations in the similarity of each pixel time series to the tEMs are present, likely due to a combination of soil moisture during the fallow year and/or

greenup phase during the cropped year. Some intrafield variability is also present, likely for similar reasons.

While the F_v TMM maps crop timing with high accuracy, it does not explicitly distinguish between rice and non-rice agriculture. As a result, non-rice agriculture maps in a variety of ways, potentially mimicking rice, depending on its phenological characteristics. Fortunately, the thermal image time series can explicitly capture the phenological signature of rice by leveraging the large early-season difference between cold, flooded, recently planted rice fields and hot, dry, recently planted non-rice fields. Interpreting the two of these phenology maps together therefore provides maximum information about both the location and timing of rice agriculture.

Near-Realtime Monitoring & Field Validation

To illustrate one potential application of this methodology, we present the results of a TMM generated in the middle of the current (2018) growing season. 2018 presents an unusually challenging case for the model, because only the first part of the growing season is available, with only 2/3 as many usable images as the same period in 2016 and 2017. This is due to the prevalence of cloud cover in many spring images and smoke plumes from multiple severe wild fires in late summer images. Through the end of July, only 4 usable thermal images were collected, in comparison to 6 images through the end of July for each of the 2016 and 2017 growing seasons.

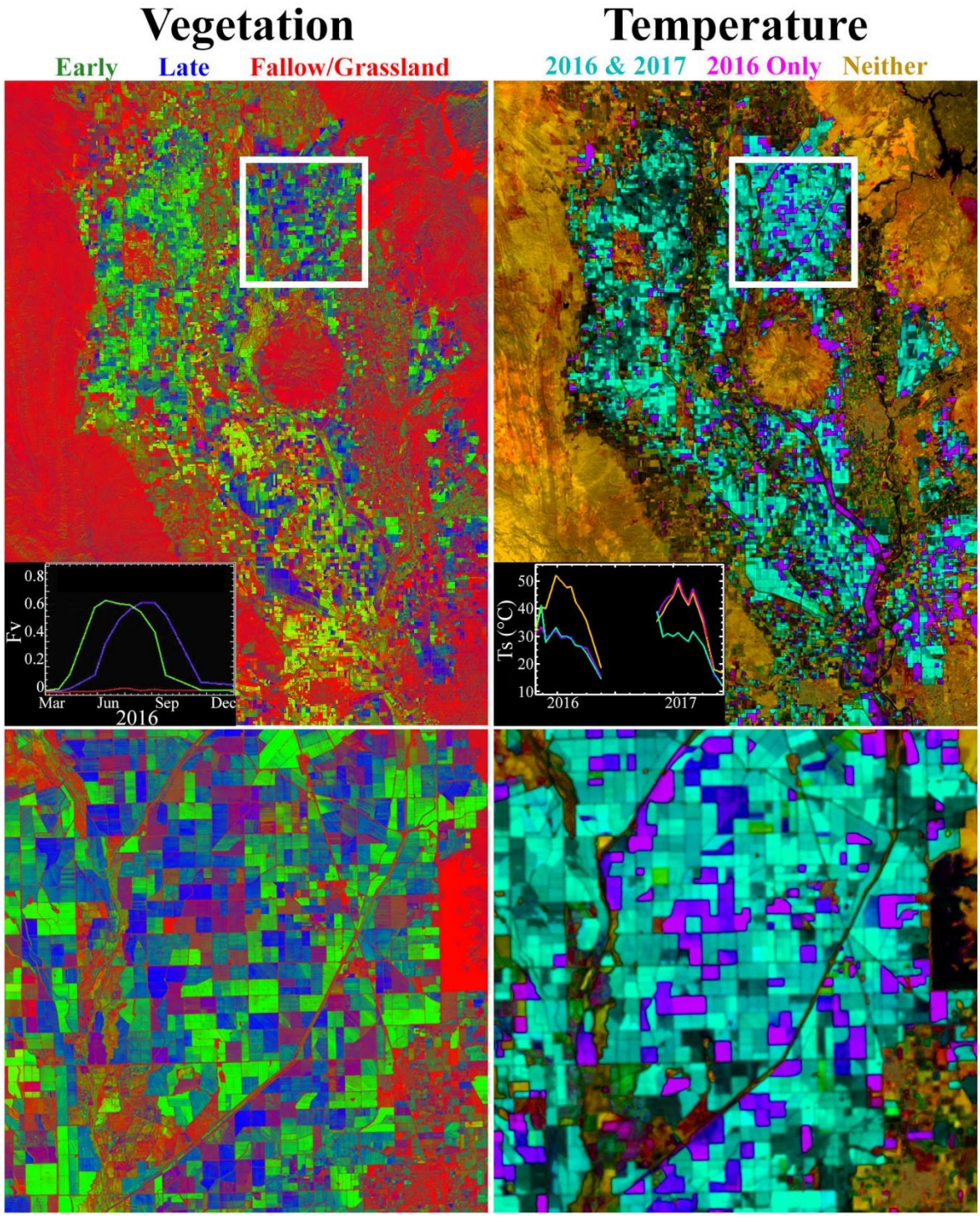

Figure 46. Temporal mixture model comparison. Each pixel time series can be modeled as a simple linear mixture of the EM time series derived from each TFS. Resulting EM fraction images can then be rendered as maps of temporal patterns. The EMs in the 2016 Fv TFS clearly

separate phenologic phase shifts, resulting in a map (L column) of early (green) versus late (blue) versus bare/grassland (red) crops for the 2016 growing season. The TMM based on Fv cannot distinguish between rice and non-rice crops with the same phenological timing. The EMs of the 2016+2017 LST TFS discriminate between rice and non-rice because the flooded rice paddies are significantly colder than the bare fields present before non-rice crops are planted. The dual-year LST TMM (R column) shows year-to-year crop transitions. Fields planted with rice in both years (cyan) are clearly distinct from those planted only in 2016 (magenta), and those bare or grassland in both years (orange). The top row shows a regional map, while the bottom row shows a 24x24 km spatial subset (area within box) at full pixel resolution. Time series of the EMs displayed in each model are inset.

Figure 47 shows false color composite and thermal image time series for these 4 images. The false color composite images show a clear difference in crop timing between the rice growing areas in the eastern versus western portions of the valley, with the dividing line located approximately at the Sacramento River channel in the north and the Sutter Bypass in the south. The wide range of planting times in 2018, and the overall unusually late crop, is due to complex water management circumstances. Because of the relatively dry winter and associated low reservoir levels, uncertainty existed in early spring about expected water allocations. Heavy April rains then boosted allocations, but also forced farmers to wait for the clay-rich soils to dry before it was possible to bring tractors onto the fields for leveling. The fields which had already been prepared could be flooded and planted on time, but those which had not were forced to plant significantly later than usual. This is described in brief by (Linquist, 2018)' and expected

impacts of this situation are broadly described by (Childs and Skorbiansky, 2018).

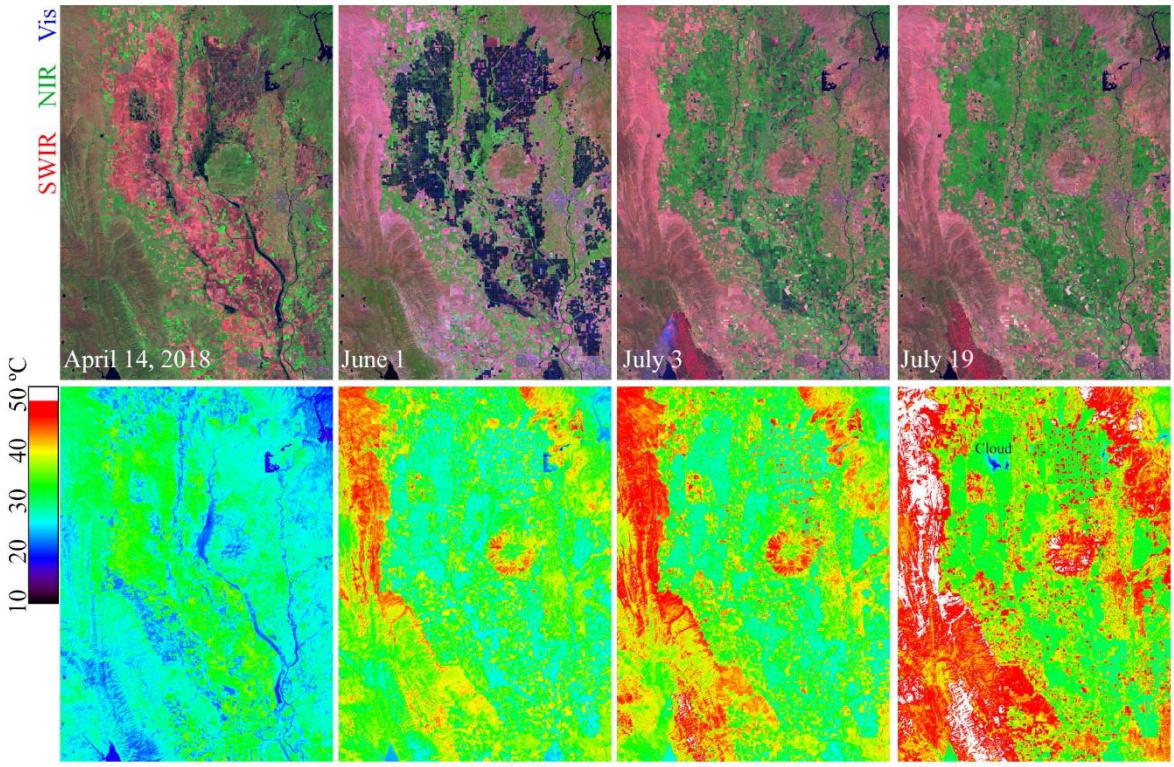

Figure 47. 2018 stress test. 2018 presents a difficult case for a monitoring model because unusually frequent cloud contamination results in only 4 usable images through July. Relatively low reservoir levels combined with unusually heavy April rains during the time of field preparation resulted in an unusually wide range of planting dates. In the April image, the western part of the valley is clearly drier than the eastern part of the valley. This resulted in earlier planting & green-up in the east, visible in the June & July images. Some fields were never planted at all, resulting in the checkerboard pattern in the July thermal imagery particularly prominent north of the Sutter Buttes.

A TMM condenses the information from these 4 LST images into a single map, shown in Figure 48. In this model, red corresponds to grasslands and fallow fields, green corresponds to early rice, and blue corresponds to water and non-rice crops. Despite the limited data availability

in 2018, and the fact that this map is produced mid-season with no data on senescence or harvest, the areas growing rice are clearly identifiable. The broad east-west dichotomy in planting date described by (Linquist, 2018) is evident in the discrepancy between bright and dull green map color. Field validation with 1650 km of driving transects, 8500 field photos, and 380 field spectra verifies that 527 of 592 fields (89%) are correctly mapped as rice. Validation details are given in the appendix.

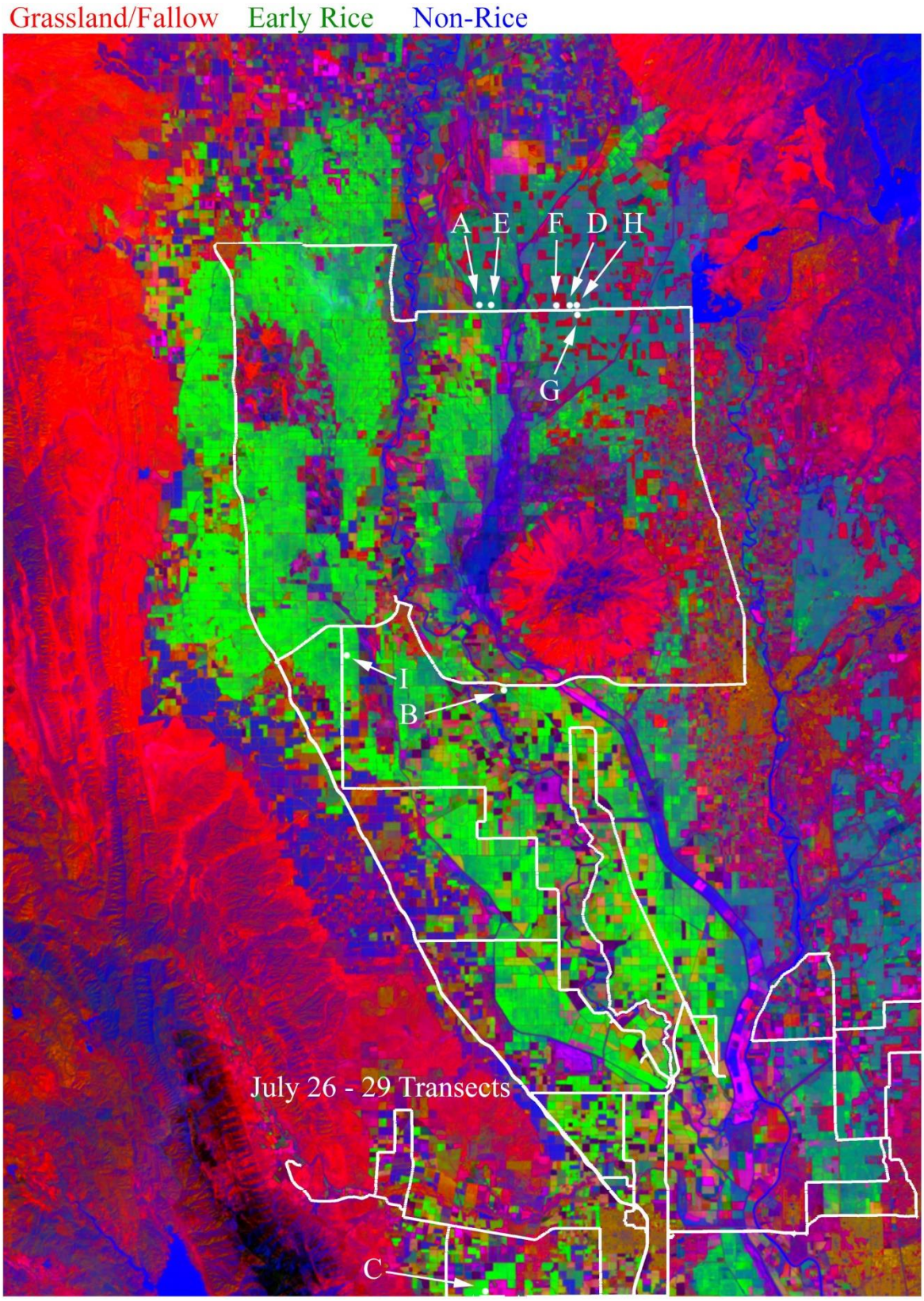
Grassland/Fallow
Early Rice
Non-Rice
A
E
F
D
H
G
I
B
July 26 - 29 Transects
C

Figure 48. Mid-season TMM for 2018. Despite only 4 images from the first half of the 2018 season, the LST-based TMM discriminates rice from non-rice, as well as between early (bright green) and late (dark green) rice crops. Field validation was conducted July 25 - 29, 2018 using over 1650 km of driving transects, 8500 field photos, and 380 reflectance spectra. False negatives (rice mapped by the model as non-rice) are rare (< 1%), but false positives (non-rice mapped as rice) occur at a rate of 11%, generally in field that were fully green and/or heavily irrigated at the time when rice paddies are flooded. Labeled white circles (A-I) correspond to locations of field spectra in Figure 50.

Discussion

The topological structure of the low order temporal feature spaces provides a detailed yet intuitive characterization of the thermal and vegetation phenology of the 2016 and 2017 rice crops in the Sacramento Valley. The clearly distinct temporal endmembers spanning the feature space correspond to distinctive and easily verified land cover phenologies with straightforward interpretations in terms of vegetation abundance and LST at decameter scales. The degree of separation of the temporal endmembers, and the fact that they bound almost all the pixels in the feature spaces, allows them to be used as the basis for useful linear mixture models that can be inverted to yield pixel scale similarity metrics for each temporal endmember. The resulting endmember fraction maps provide continuous field estimates of both vegetation and thermal phenology of multiple rice crops as well as other land cover types. While the continuous field maps provide the most information on the spatiotemporal evolution of the rice crops, the clear presence of distinct clusters within the temporal feature spaces shows that the continuous field maps could be easily discretized into thematic classifications if necessary. The spatiotemporal clustering highlights clear distinctions between the multiple phases of rice cropping, as well as

from other land cover types with different phenologies. It is important to note that continuous fraction land cover models can be used to accurately represent compositionally discrete land cover (like agriculture) with no loss of generality, but the converse is not true. Discrete thematic classifications cannot accurately represent the far more common diversity of continuously varying land cover properties present in most landscapes.

The ability to rigorously map and monitor the state of rice agriculture with optical satellite imagery has a wide range of potential implications:

Harvest Forecasts

In many regions of the world, the prediction of rice harvest is hindered by inaccurate estimates of basic information. While providing accurate estimates of yield from satellite imagery can be difficult because of the range of factors that can contribute to the harvest, it is likely that constraints on fundamental variables such as planting date and total area under cultivation could be improved with the joint VSWIR+TIR temporal mixture model approach presented here. In particular, TMMs based on single-year time series show the potential to map crop timing, and dual-year time series show the potential to identify changes in the location and overall abundance of planted fields. This could improve one set of inputs to complex yield models, which also rely on a significant amount of additional ancillary information, as well as work synergistically with other rice crop monitoring systems such as the methodologies proposed by (Boschetti et al., 2009; Nelson et al., 2014; Torbick et al., 2011).

Intra-field Variability: Weed and Nutrient Management

Examination of decameter image time series from sensors such as Landsat and Sentinel reveals considerable intra-field heterogeneity in the time series of green-up and senescence.

These within-field variations likely arise as a result of imperfections in field leveling, flooding, and drainage; variability in weed and nutrient management; and heterogeneity in planting density. The information present in these variations could be leveraged using active management strategies for precision agriculture. In conjunction with unmanned autonomous vehicles, localized application of fertilizer and herbicide could be targeted to areas of concern with a potentially significant reduction in environmental impact and cost to the grower. The growing prevalence of VNIR hyperspectral imaging sensors has the potential to contribute significantly to these problems by discriminating between individual absorption features, such as those captured by the field spectra shown in Figure 50 of the Appendix.

Pest Management

Some pests require proximity in order to transmit from one field to another. Large, interconnected regions growing similar crops may provide transmission opportunities for these pests. Transmission could be minimized by a basin-scale management approach based upon strategic disruption of spatial networks of agriculture. Accurate crop-specific maps could provide a useful input into a network-based approach to understanding agricultural landscape evolution, as explored in (Sousa and Small, 2016).

Evapotranspiration and Water Use

ET has been shown to be remarkably consistent for rice fields throughout the growing season (Linquist et al., 2015). Indeed, the relative stability of the LST and area of illuminated photosynthetic vegetation of rice fields are a part of the reason why the joint VSWIR+TIR mapping approach is so well-suited to rice in particular. This is shown explicitly in the spatiotemporal composite TV space for all 22 images in the 2016-2017 time series, shown in

Figure 49.

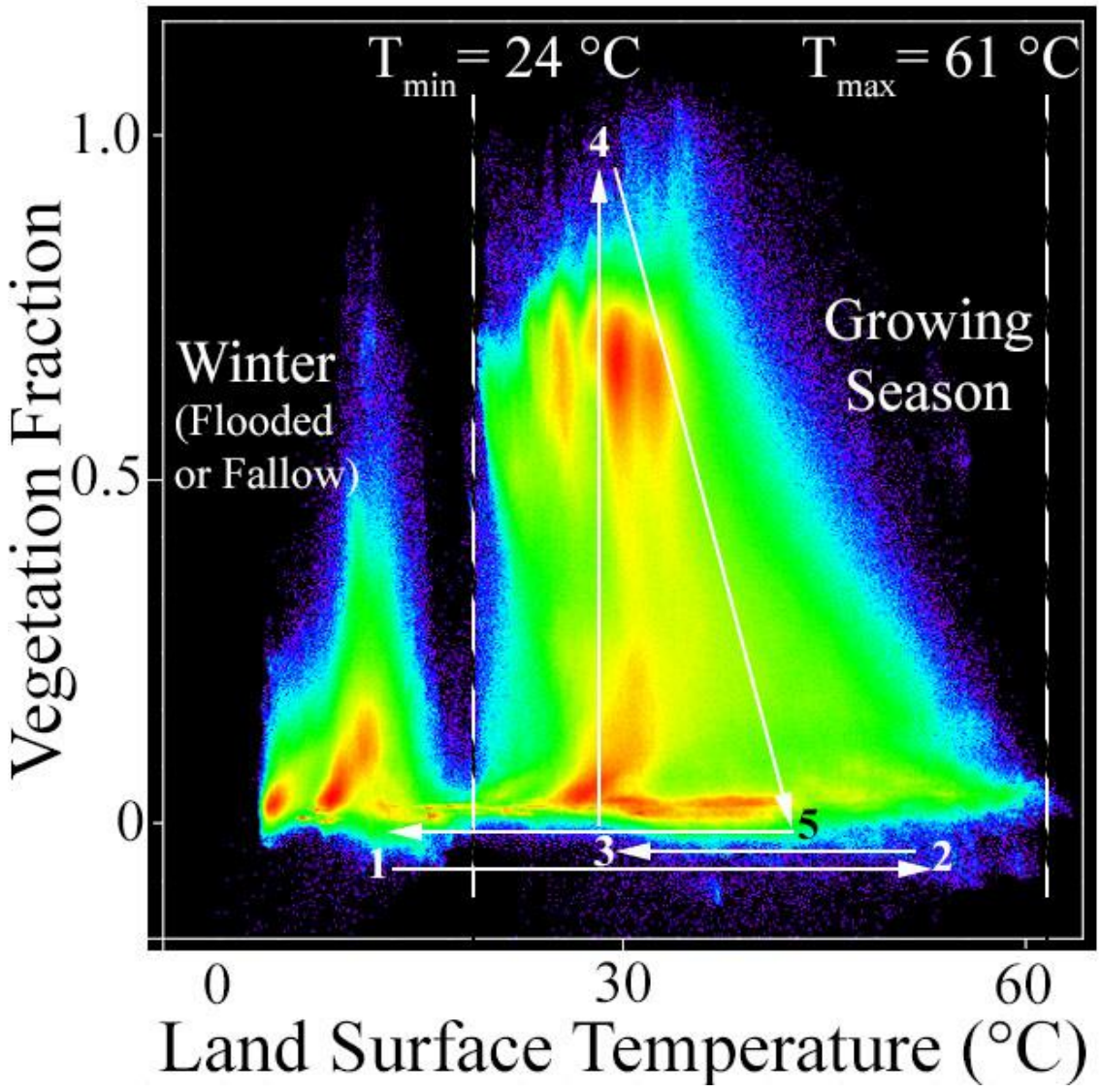

Figure 49. Relationship between vegetation and soil LST throughout the study period. A clear gap is present between the soils during the summer growing season (higher LST) and winter fallow season (lower LST). Physical bounds to growing season temperatures are easily recognizable, yielding straightforward values for Tmin and Tmax as defined by Carlson et al., 1994. Schematic rice phenological trajectory shown with white arrows. Rice fields are unvegetated and cold in winter (1). In spring, the fields are drained and leveled, remaining

unvegetated and sometimes reaching high temperatures due to the low heat capacity of dry soil. Fields are then flooded and planted (3), after which point the rice plants begin to grow until maturity (4). In late summer and early fall, plants senesce and then are harvested in mid-to-late fall (5). After harvest, many rice fields are then flooded again, returning them to their winter state (1).

The composite TV space shown in Figure 49 is particularly illuminating when viewed in relation to its subsets shown earlier in Figure 43. The wide range of LST values shown at near-zero F_v is primarily due to the substantial discrepancy between the relatively high heat capacity of water and the much lower heat capacity of dry soil (and synthetic surfaces like pavement and plastics). In contrast, the much more constrained range of values at high F_v values is likely a reflection of the thermal stability of dense, well-watered, respiring vegetation. The warm-colored clusters in this space represent groups of geographic pixels with similar TV properties. At low values of F_v, these are likely bare fields with similar moisture contents and tilling practices. In contrast, the clustering at high F_v values likely corresponds to rice fields imaged at different dates, with differences in water temperature resulting from fluctuations in air temperature due to changing weather within the growing season.

At least two additional features of this plot suggest potential avenues for future work through application to ET, following the Triangle Method introduced by (J. C. Price, 1990), further elaborated by (Carlson et al., 1994), and recently reviewed by (Carlson, 2007) with additional useful explanation in (Carlson, 2013). First, the remarkably straight edges suggest the Sacramento Valley may be particularly well-suited to this approach to ET mapping. This is likely due to a combination of large field sizes, prevalent irrigation, and dominance of agricultural land use across the landscape. Second, a clear division between the growing season and the winter is

also evident, suggesting the relationship between temperature and vegetation can be described as alternating between (at least) two physical regimes over the course of the year. Moving forward, the application of the spatiotemporal analysis methods described in this paper to image time series of quantities estimated by ET models has the potential to make progress toward all 5 of the requirements of the Path Forward outlined by the recent Decadal Survey (Fisher et al., 2017), especially viewed under the unifying framework of spectral mixture analysis, as proposed by (Sousa and Small, 2018b). Detailed intercomparison of ET estimates from this and other ET models presents an attract avenue for future work.

View Angle and Flooding Presence

Because rice is an erectophile plant, small differences in off-nadir viewing geometry can produce significant differences in its overall bidirectional reflectance distribution function (BRDF). Specifically, the background of paddy water or soil is most pronounced when nadir-looking and rapidly exits the field of view when viewed off-nadir. Sufficient data now exist to quantify this effect at various stages throughout the rice life cycle. Understanding the size of this effect has the potential to determine at what stages of development the flooding or drying of the substrate below the rice can be accurately determined, with potential implications for the verification of alternative cropping practices such as alternate flooding and draining of fields.

Integration of New Data Streams

Finally, recent missions such as the ECOsystem Spaceborne Thermal Radiometer Experiment (ECOSTRESS), as well as the planned launch of hyperspectral missions such as NASA's Surface Biology and Geology (SBG) and DLR's EnMap, have the potential to substantially enhance the ability of the scientific community to map and monitor rice agriculture. During crop growth, VSWIR imaging spectroscopy has been shown to provide information

about biomass (Gnyp et al., 2014) and foliar chemistry such as nitrogen and cellulose (LaCapra et al., 1996), and multispectral thermal measurements are expected to provide improved measures of evapotranspiration (Wong et al., 2017). Hyperspectral measurements have also been shown to be potentially useful for detecting physiological stress in rice due to soil heavy metal content (Liu et al., 2011), fungal infections (Liu et al., 2008), and insect infestations (Yang et al., 2007). When fields are fallow, hyperspectral measurements are expected to provide improved soil characterization (Castaldi et al., 2016; Stoner and Baumgardner, 1981). It is possible that when this information is incorporated in temporal mixture models, it could potentially provide useful added information about the presence, timing, and spread of pathogens across a landscape; the need for fertilizer application; and/or water consumption and stress across rice and non-rice agricultural landscapes.

Conclusions

The combined spatiotemporal analysis of decameter scale VSWIR and thermal imaging shows considerable promise for improvements in the mapping and monitoring of rice agriculture. Characterization of single-year time series of the agriculture-dominated Sacramento Valley of California readily yields information about early/late crop planting, while dual-year characterization provides information about year-to-year crop conversion. Surprisingly, considerably more clustering is evident in the LST image time series than in the F_v image time series, in both single- and dual-year cases. Investigation of the temporal feature spaces suggests that F_v time series data show particular promise for estimating crop timing, while LST appears particularly well suited for distinguishing rice from other crops. Example monitoring results from the 2018 growing season show considerable promise for near-realtime mapping of rice phenology using partial-season TMMs. Field validation based on over 1650 km of driving

transects and 8500 field photos confirms that mid-season monitoring models can provide an accurate upper bound estimate (< 1% false negatives; 11% false positives) of the spatial extent and relative timing of the rice crop, even under conditions of relative data scarcity (only 4 images total for 2018, with only 1 capturing flooded and unplanted rice paddies). These results could have potential implications for food security, precision agriculture, pest management, and ET.

Appendix: Field Validation

The TMM for the 2018 growing season shown in Figure 48 is validated with over 1650 km of field transects collected between July 26 and 29 (white lines), including over 8500 field photos and 380 VNIR reflectance spectra. Field spectra are mapped as white dots and will be discussed further in Figure 50. Comparison of field photos to map output shows the model to produce < 1% false negatives (i.e. fields planted as rice but not captured by the model). However, approximately 11% of fields in the model were identified as false positives (i.e. fields in which rice was not planted, but mapped by the model as rice). The reason for the prevalence of false positives in the 2018 model is straightforward, as only 1 image captures the rice in the phase in which it is dominated by standing water. Because the thermal signature of standing water can sometimes be similar to that transpiring vegetation and wet soil, the thermal time series of any crop which was bare in mid-April but already fully green (or fallow and saturated) by June 1 could mimic that of the rice. This thermal mimicking is expected to be less severe in years with better data availability, and could also potentially be resolved by building a more complex model in which both F_v and LST are used. However, for the purposes of simplicity and illustration of the method outlined in this work, we defer a detailed examination of the strengths and weaknesses of more complex models to a future study.

VNIR field spectra were collected with an ASD HandHeld2 field spectrometer on July 29. Wildfires were active in the Coast Ranges to the west and north of the study area from mid-July through late August, 2018. As a result, substantial atmospheric contamination was present during field spectra collection. These effects are evident in satellite images collected before, during, and after the field campaign. When compared to both same-day Sentinel-2 spectra (corrected with the ESA Sen2Cor algorithm) and Landsat 8 spectra from August 4, 2018

(corrected with the NASA/USGS LaSRC algorithm), the field measurements yielded higher reflectance across all wavelengths than the satellite spectra. We interpret this as resulting from substantial indirect illumination by haze from the fires, view angle discrepancies due to the field spectrometer being held slightly off-nadir, and the unavoidable difference in measurement distance between the Spectralon white standard (used for calibration) and the distance from the rice canopy necessary to sample a representative mixture of foliage and exposed paddy water (or soil). Fortunately, however, the phenological progression can be captured by relative differences in reflectance between wavelengths. In order to facilitate comparison of spectral shapes, the overall amplitudes of the field spectra were adjusted by simple multiplicative scaling using constants in the range 0.5 to 0.8.

Figure 50 shows the corrected field spectra at full spectral resolution (thin gray) and the mean spectrum (thin black) for reference, as well as these spectra convolved with the broadband spectral response functions of the VNIR bands of the Landsat 8 OLI sensor (thick blue). These are shown in comparison to the actual observed Landsat 8 spectra from the August 4 Landsat 8 image (thick gold). In some cases (A–C), the agreement between the synthetic and observed Landsat spectra is remarkably good, even despite the significant atmospheric problems discussed above and the nearly 1 week between field and satellite data collection. In other cases, the spectral shape at visible wavelengths is distorted (D–F) or there is an overall loss of contrast (G–I) in the satellite spectra. These imperfections are likely due a combination of 1) changes in the state of the atmosphere in the 10s of seconds between field calibration to white standard and collection of reflectance spectra, and 2) the inability of the atmospheric correction model to capture the complex scattering and absorption effects of the smoke plumes.

In addition to the comparison with broadband observations, field spectra show subtle features which are not captured by multispectral instruments. Changes in absorption depth in the visible red are likely due to chlorophyll b and other plant pigments. In addition, changes in the curvature at the base of the red edge (0.69–0.71 μm), as well as variations in slope at the top of the red edge (0.8–0.9 μm) have the potential to be leveraged in future work for investigations into nutrient stress and phenological progression of plant functional traits.

Finally, sample field photos showing rice at a variety of stages are shown in Figure 51. In late July, 2018, rice in the Sacramento Valley was observed in a range of maturity stages (photos A–C). The prevalence of weeds widely varied among fields (D and E). Abundant waterfowl (F) could be observed feeding in the rice fields. Viewed from above, weedy rice fields (G) were clearly distinct from weed-free fields (H). Substantial standing water background was observed in nadir-looking photos. The importance of view angle can be clearly seen when comparing (H) and (I), as rice fields of this age are fully opaque when viewed obliquely but not when viewed from nadir. A broad diversity of other agricultural land covers was also present in the valley, including sunflowers (J), fruit and nut orchards (K), rice straw (L), bare soil (M), alfalfa (N) and tomatoes (O).

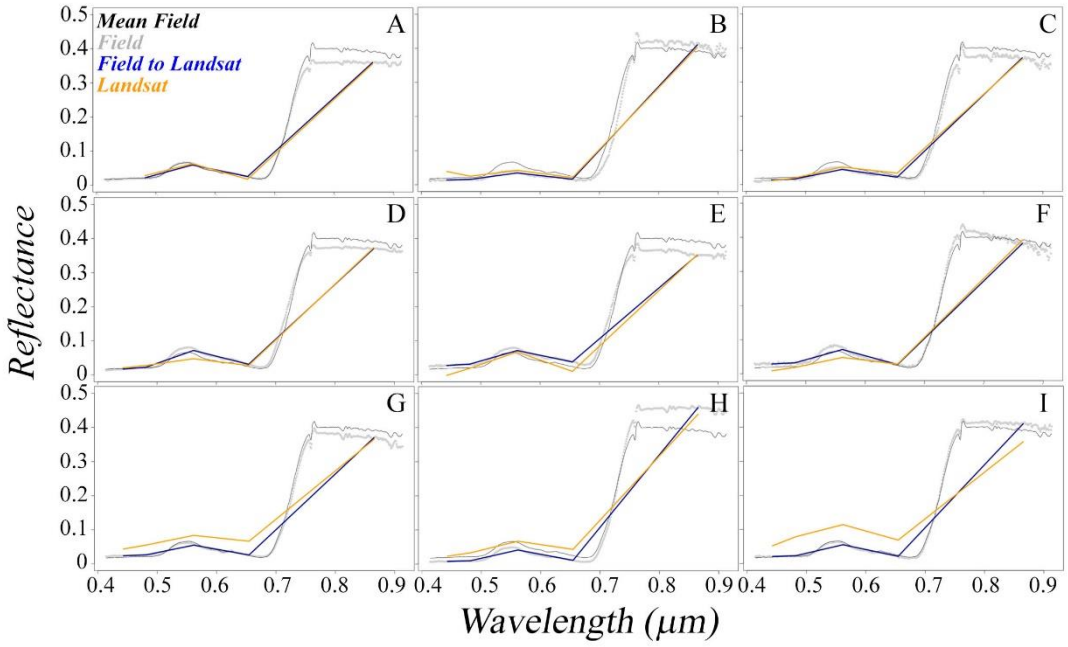

Figure 50. Comparison of field and satellite spectra. Continuous field spectra (light gray) were collected on July 28 and 29 at 9 rice fields, then convolved to bands 2-5 of the Landsat 8 OLI sensor (blue). These are then compared with actual Landsat spectra from the same locations imaged on August 4 (gold). The Landsat spectra were atmospherically corrected with the standard LaSRC atmospheric correction. In some cases (A-C) the synthetic and observed Landsat spectra agree remarkably well, especially given the pervasive atmospheric effects due to fires present during both the days of field measurement and satellite overpass and the nearly 1 week of time elapsed. In other cases (D-F), the overall ranges of the spectra are similar but the shape in the visible is notably distorted. In yet other cases (G-I), loss of contrast is observed, likely due to aerosol contamination incompletely corrected by the LaSRC model. Locations of field spectra are shown in Figure 48.

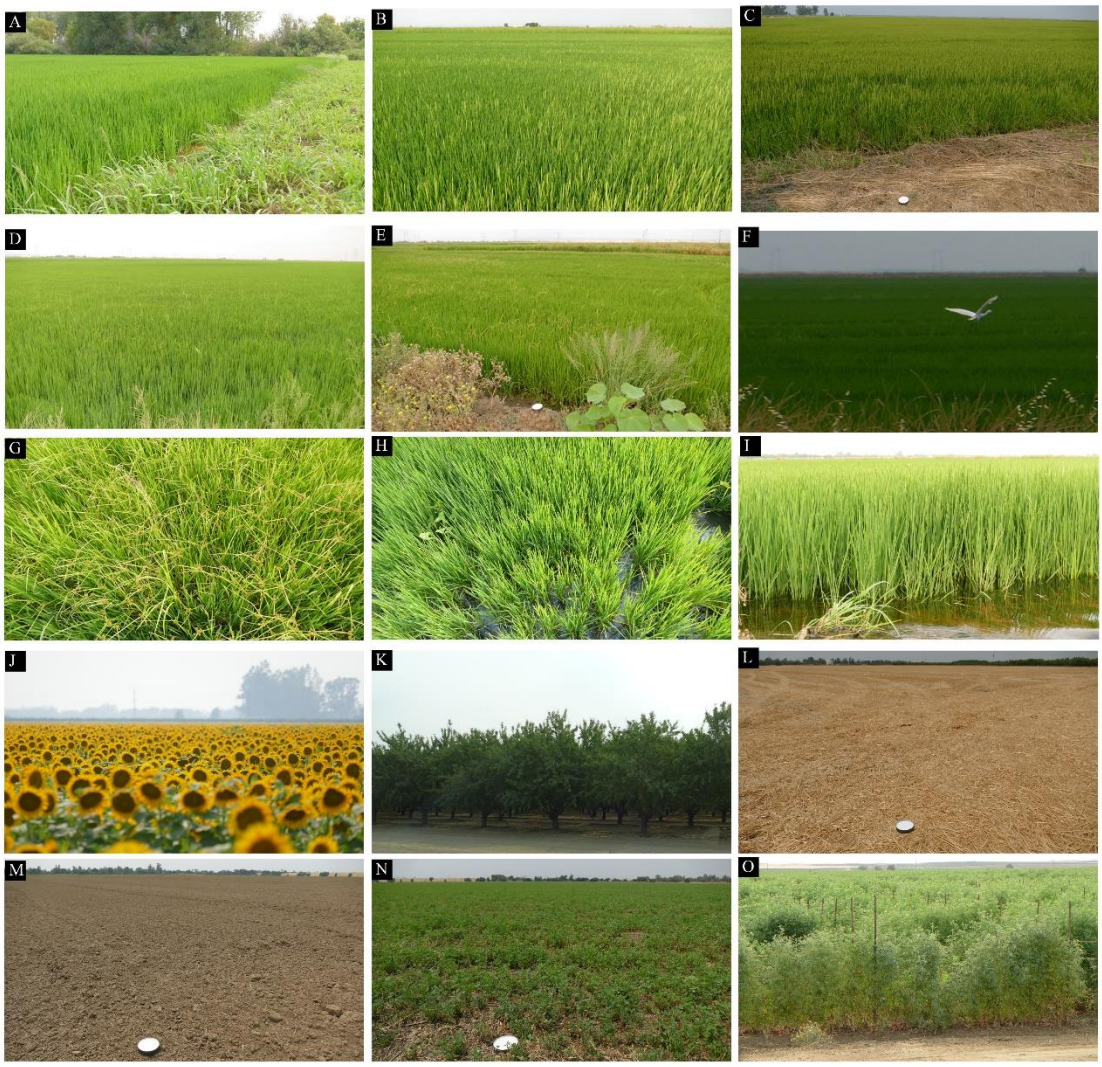

Figure 51. Photos from July 2018 field validation campaign. In late July, rice was present in a wide range of stages from not yet headded (A) to partially and fully headded (B and C). Weeds were visibly present at a range of abundances in some fields (D and E). Waterfowl (F) continue to hunt in the rice paddies during the growing season. Viewed from near nadir, weeds (G) and standing water below the rice plants (H) are clearly visible. The importance of view angle is clearly evident when comparing these photos to side-on photos like I. A wide range of other agricultural land covers is present in the valley, including sunflowers (J), fruit and nut orchards (K), wheat stubble (L), bare fields (M), alfalfa (N) and heirloom tomatoes (O).

6. Spatial Structure and Scaling of Agricultural Networks

Abstract

Considering agricultural landscapes as networks can provide information about spatial connectivity relevant for a wide range of applications including pollination, pest management, and ecology. At global scales, spatial networks of agricultural land use inferred from land cover products are well-described by power law rank-size distributions. However, regional analyses of agricultural land use typically focus on subsets of the total global network. In this paper, we seek to address the following questions: Does the globally observed scale-free property of agricultural networks hold over smaller spatial domains? Can similar properties be observed at kilometer to meter scales? Does the observed scale-free structure persist as agricultural networks evolve over the growing season? We analyze 9 intensively cultivated Landsat scenes on 5 continents with a wide range of vegetation distributions. We find that networks of vegetation fraction within the domain of each of these Landsat scenes exhibit substantial variability – but generally still possess similar scaling properties to the global distribution of agriculture. We also find similar results when comparing Landsat and Sentinel-2 imagery for 3 agricultural regions in Europe, as well as in an IKONOS image of an agricultural region of China. To illustrate an application of spatial network analysis, we show an example of network disruption. We compare two networks with similar rank-size distributions that behave differently when nodes are progressively removed. We suggest that treating agricultural land cover as spatial networks can provide a straightforward way of characterizing the connectivity and evolution of complex spatial distributions of agriculture across a wide range of landscapes and at spatial scales relevant for practical agricultural applications.

Introduction

The spatial distribution of agriculture in a landscape can provide information which is complementary to the properties of individually treated fields or political units. Pollination, insect diversity, and other ecosystem services are reliant on the spatial connectivity of an agricultural landscape (Diekötter et al., 2008; Ricketts et al., 2007). Outbreaks of pests and pathogens can sometimes be contained by breaking spatial adjacency between cropped areas (Gilligan, 2008). The ecology of native species populations can be altered by habitat fragmentation of natural landscapes by agriculture (Dixo et al., 2009; Luoto et al., 2003). However, the diversity of agricultural landscapes around the globe demands a tool which is flexible enough to accommodate a wide range of spatial distributions and connectivity patterns. Network theory provides the basis for a conceptually simple model which can represent a variety of processes with complex spatial structure.

Globally, maps of cropland extent have been observed to display an unexpected consistency in their size distributions (Small and Sousa, 2016). Despite considerable disagreement when compared directly in the same locations, 4 different global agriculture products possess the property that the sizes of contiguous patches of agricultural land diminish at the same rate that their frequency increases (Figure 52). This property implies (nearly) uniform distributions of total agricultural area across a wide range of spatial scales. This implies that the sum of the area of the largest segments is equal to the sum of the area of the smallest segments, which is equal to the sum of the segments of any arbitrary size interval in between. The consistency of this observation across the 4 products is especially surprising given the substantial differences in the input data, assumptions, and algorithms used in each of the 4 products. The

consistency of the observation at global scales begs the question of whether this pattern can also be observed at finer spatial scales.

The property of diminishing magnitude with increasing number is common in nature and is often referred to as a power law relationship. Power law relationships are also a defining characteristic of many networks – often referred to as "scale-free" because of the implied self-similarity and lack of a characteristic scale. Because networks are capable of representing processes with complex spatial structure (e.g. as reviewed by (Barthélemy, 2011)), and because many networks (such as those in (Barabasi and Albert, 1999)) display similar power law relationships to those observed for agriculture on the global scale, we suggest that networks may be a useful tool to characterize agricultural landscapes and provide insight into processes reliant on agricultural connectivity.

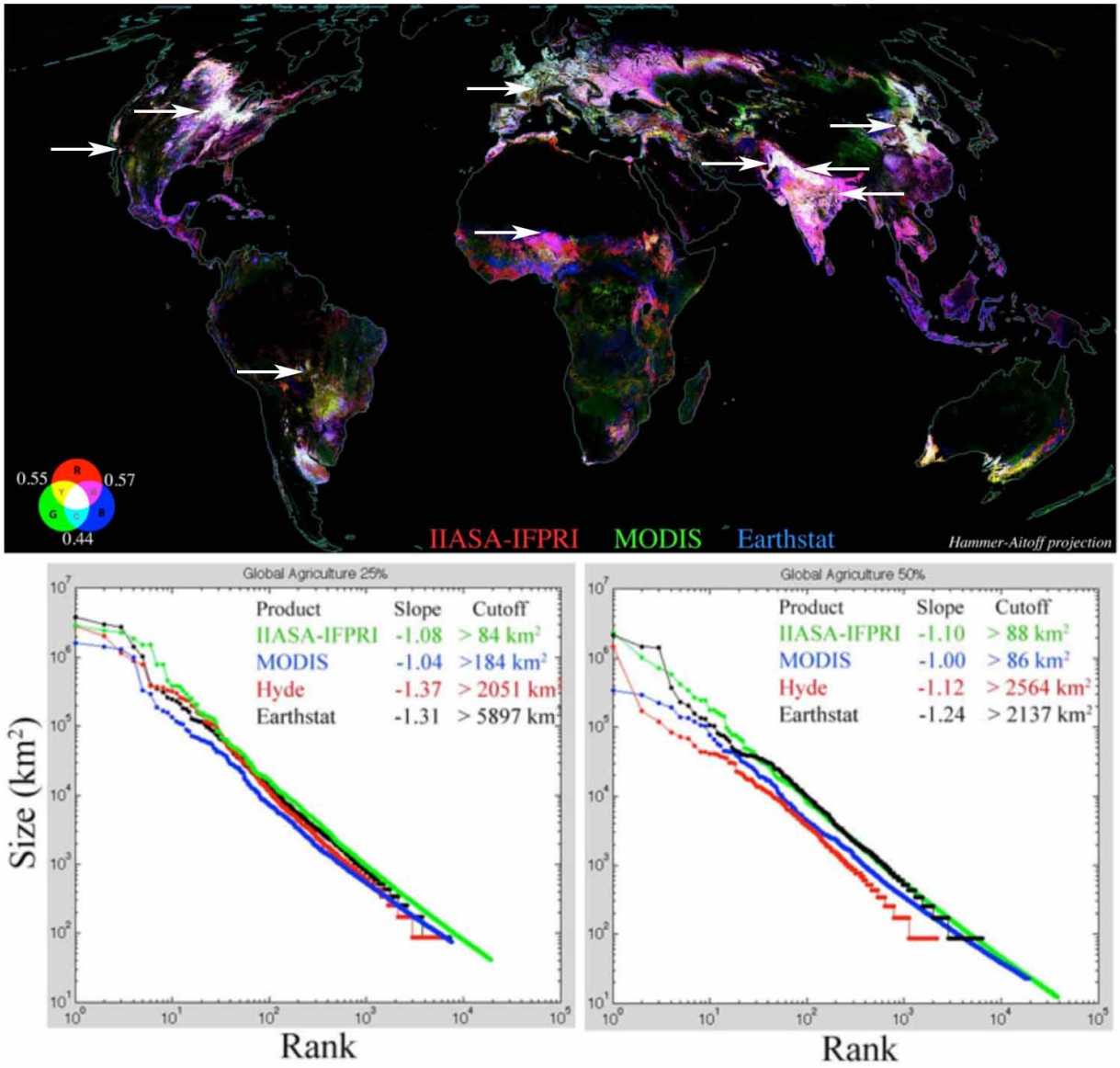

Figure 52. Global comparison of agricultural land cover products (top) and corresponding rank size distributions of agricultural land area (bottom). Areal fractions of land under cultivation for three global products shown as red, green, and blue brightness. Pairwise spatial correlations between products shown in lower left corner of the map quantify agreement. Segmenting each continuous fraction map at >25% and >50% thresholds produces binary maps. Rank size distributions of contiguous areas of agricultural land cover for each product have similar slopes over 4 orders of magnitude in size. Power law fits to each rank size distribution yield slopes near

-1. Size cutoffs estimate lower bound of power law behavior. Small cutoffs for the IASA-IFPRI and MODIS products indicate that the power law fits all but the smallest segments, while the larger cutoffs in the HYDE and Earthstat products result from quantization of smaller segments due to their coarser 10 x 10 km resolution. Slopes near -1 indicate that areas of agricultural land cover diminish in size at the same rate they increase in number. The implication is that the total area of agricultural land cover is nearly uniform across a wide range of segment sizes. This figure is adapted from Small and Sousa (2016).

Several remote sensing studies have used power laws to describe fire size distributions. For instance, (Hantson et al., 2015) studied the global distribution of fire sizes using a 2° grid and found that a power law model successfully fit 93% of grid cells with significant fire activity. Similarly, (Malamud et al., 2005) studied wildfires across the conterminous United States and found robust power law fits in 18 different ecoregions. (Kumar et al., 2011) use these established power law relationships to estimate fire biomass and radiative energy.

Studies of a wide range of other phenomena in the natural sciences also find power law behavior. Desert vegetation in the Kalahari was found by (Scanlon et al., 2007) to follow a robust power law distribution across 1.5 orders of magnitude. Horizontal cloud sizes were found by (Wood and Field, 2011) to be well represented by power laws from sizes ranging from 0.1 km to at least 1500 km. Earthquakes (famously described by (Gutenberg and Richter, 1955)), wind profiles (as characterized by (Hsu et al., 1994)), and landslide area (characterized by (Guzzetti et al., 2002)) provide but a few of the myriad other cases in which power laws have been used to describe Earth processes. Interested readers may find more detailed descriptions of similar processes in references such as (Turcotte, 1997) and (Sornette, 2006).

The goal of this paper is to investigate the question of whether the globally observed scaling property of agricultural land cover holds over smaller areas and at spatial scales relevant to the questions of pollination, pathogen transmission, and ecology. Specifically, we seek to assess the robustness of the global scaling relationship at the decameter spatial scale for a set of diverse agricultural landscapes spanning 5 continents. To our knowledge, the investigation of heavy-tailed size distributions of contiguous patches of agriculture has not yet been performed in the literature. We ultimately seek to answer the question: Do the size distributions of agricultural landscapes already observed at global scales maintain similarity to true power laws at spatial scales resolving individual fields? This question has direct relevance to several agricultural applications because of the implications for spatial connectivity of agricultural networks at scales where interventions are feasible.

Background

Rank-size Plots and Heavy-Tailed Distributions

Some processes in nature tend to produce objects or events that cluster around one characteristic size, with large deviations from this value being relatively infrequent. However, other processes produce objects or events that can take on a wide range of sizes – sometimes varying over several orders magnitude. When viewed as realizations of random variables, distributions which can take on a wide range of values are said to be *heavy tailed*. In a heavy tailed distribution, concepts from Gaussian statistics such as mean and standard deviation have little utility since the random variable deviates highly from that of a Gaussian (i.e., extreme events are much more common than predicted by a Gaussian distribution). Several types of heavy-tailed distribution which have been invoked by different authors to describe natural phenomena include the Weibull (e.g. wind speed, (Seguro and Lambert, 2000)), log-normal (e.g.

distribution of chemical concentrations, (Limpert et al., 2001)) and power law (e.g. city size, (Auerback, 1913; Lotka, 1941; Zipf, 1942)) distributions.

In the case of phenomena characterized by heavy tailed distributions, rank-size plots can be an intuitive tool for displaying both the magnitude and frequency of observations. Because such processes often span several orders of magnitude, such plots are typically displayed on logarithmic axes. Such a visualization scheme can be desirable because of its conceptual simplicity and minimum of assumptions about the form of the data. In the case where a rank-size plot is linear on logarithmic axes, the power law distribution is often considered a likely candidate for the underlying process. A power law distribution is defined by a constant factor and an exponent. If a set of features is distributed according to a power law, the slope of the rank-size plot in log-log space is related to the power law exponent α by the following expression from (Li, 2002):

$$slope = -\frac{1}{\alpha - 1}$$

Nonparametric statistical methods have been developed to determine the power law of best fit, the portion of the distribution most likely to be power law, and confidence intervals using Monte Carlo and the Kolmogorov-Smirnoff goodness-of-fit statistic. For an excellent description of these tools and their application to a wide range of datasets, see Clauset et al. (2009). When observations are binned logarithmically, a rank-size distribution with a slope of -1 (corresponding to a power law exponent of -2) corresponds to a uniform distribution across scales (Small et al., 2011).

Importantly, linearity of the rank-size plot alone does not rule out the possibility of other similar heavy tailed distributions describing the data equally well – or even better (Clauset et al.,

2009). For this reason, in this paper we only use power law fitting as a convenient way to quantify the degree of linearity and slope of the rank-size plots. We remain noncommittal about the ultimate form of the underlying probability density function and suggest more rigorous analysis as a direction for future work on this topic.

Scale-Free Networks and Constrained Networks

The most basic pieces of networks are *nodes* and *links*. Nodes are connected to each other by links. Depending on the network, some nodes may be linked to many other nodes, some may be linked to only a few, and some nodes may not linked to any other nodes at all. Each set of interconnected nodes is called a *component*. Within each component, all nodes are connected to each other either directly or indirectly (i.e. through other nodes within the same component). No node within one component can be linked to a node within another component. A *network* is a set of components. In many networks, all nodes are linked to each other (directly or indirectly) to form a single "giant" component (Newman, 2010). Other networks have many components.

In a network, each node has a certain number of links. The frequency distribution of the number of links per node is called the degree distribution of the network. In some networks, the degree distribution can be well-characterized by a power law. These networks are called scale-free networks. For these networks, when the distribution of degree sizes versus rank (ordinal number: 1 = largest, 2 = second largest, 3 = third largest, …) is plotted on logarithmic axes, the result is linear. The slope of this line can vary substantially for different networks (Barabasi and Albert, 1999; Clauset et al., 2009). The wide range of degrees necessary for a power law distribution is possible in some cases because many networks have no limit (or some very large limit) to the number of links that each node can have. Networks are already used in the field of landscape ecology under the term graph theory (Cantwell and Forman, 1993; Gardner et al.,

1992; McIntyre et al., 2014; Urban and Keitt, 2001). For a general review of network theory, see (Albert and Barabási, 2002; Newman, 2010).

In this paper we treat landscapes as networks of land cover. The spatial domain of interest determines the total possible spatial extent of the network it contains. As the network grows within the rectangular grid of the domain, each pixel is treated as a potential node. In this paper, a pixel becomes a node of a spatial network if it satisfies a single criterion: subpixel vegetation abundance above the threshold of analysis. We consider two pixels to be directly linked if they are spatially adjacent to each other. For this reason, nodes in land cover networks on a regular rectangular grid (as is the case in this study) have a maximum number of direct links (Steinwender, 2002). Because we use the Queen's case for connectivity (all immediate neighbors including diagonals), this number is 8. In this case, the parameter of interest is not the degree distribution but the component size distribution, as the sizes of each component (spatially contiguous patch of agricultural land) can possess a wide range of values. The rank-size plots used in this paper show the distribution of component sizes in a single network. We refer to the particular type of spatial network defined in this way as a *bounded spatial network* (Small and Sousa, 2015).

(Small and Sousa, 2016) show that four land cover products which seek to map agricultural land use at the global scale exhibit empirical component size distributions characterized by linearity in logarithmic space and slope of -1, despite differences in spatial patterns (Figure 52, from (Small and Sousa, 2016)). This result holds across a wide range of analysis thresholds (described in more detail below). This suggests that agriculture may be well characterized as a scale-free spatial network on the global scale. Other types of land cover

products have also been found to exhibit similar properties on the global scale (Small and Sousa, 2015).

Scale-free networks have been shown to result from two simple conditions: network growth and preferential attachment (Barabasi and Albert, 1999). Preferential attachment is sometimes described as “rich get richer”– i.e., new nodes to attach more frequently to existing nodes with greater numbers of links, or to components with a greater number of nodes, than to their less connected counterparts. The networks we consider fill space on a surface. This generates a mechanism for preferential attachment because the surface has finite area and larger components naturally have larger perimeters to which new nodes can link. If new nodes are generated randomly in space, components with larger perimeters will exhibit preferential attachment – without the need for a situation-specific mechanism for preference. To the extent that components with larger sizes (i.e. areas) also have larger perimeters, a mechanism for preferential attachment is inherent to bounded spatial networks on a surface. For more detailed background and mechanism, see (Small and Sousa, 2015).

Data & Methods

To quantify the scaling properties of different agricultural landscapes, we choose images that are dominated by agricultural land cover and then use the following procedure. Beginning with raw Landsat data, we first calibrate from DN to radiance to exoatmospheric reflectance. We then estimate vegetation fraction (F_v) at each pixel using the standardized global endmembers from (Small and Milesi, 2013), generating a continuous field of sub-pixel vegetation abundance.

Sentinel data are processed by first resampling all 12 bands to 10 m resolution and then unmixing into Substrate, Vegetation, and Dark components. Subpixel vegetation fraction from

this unmixing is then used for subsequent network analysis. Sentinel-2 spectral unmixing is performed using local SVD endmembers since global Sentinel-2 endmembers are not currently available. As noted previously (Small and Milesi, 2013), local substrate EMs can differ substantially from the global EMs and produce systematic differences in fraction estimates between global and local EMs. These differences are most prominent in substrate fraction estimates.

We then segment the F_v images at several different fraction thresholds with the ENVI segmentation algorithm, using the Queen's case of 8 neighbors including diagonals. The ENVI segmentation algorithm finds spatially contiguous groups of pixels which all obey the rule used for segmentation. In this case, the rule used is F_v above a given threshold. All spatially adjacent pixels with F_v above this threshold are labeled with the same segment number. We use the Queen's case as our metric for spatial adjacency in order to provide the most liberal estimate of connectivity. We use a minimum segment size of 8100 m^2 (9 Landsat pixels or 81 Sentinel-2 pixels) to account for spatial autocorrelation of the input imagery and avoid large numbers of spurious detections. Allowing smaller segments in Sentinel imagery has the effect of resolving the characteristic field size of the landscape and is discussed in (Small and Sousa, 2016). The segmentation algorithm produces a map of segments corresponding to spatially contiguous patches of vegetation (for each threshold). The agricultural network is thus composed of all pixels in the image for which the following two conditions are true: (1) F_v of the pixel is above the given threshold and (2) the pixel is spatially adjacent (directly or indirectly) to at least 8 other pixels which also have F_v above the given threshold.

Next, we calculate the total area of each segment (for each threshold). The resulting segment size maps (for each threshold) provide both the size distributions and a depiction of the

spatial network structure. Segment areas are then sorted into a descending list and plotted against ordinal number (i.e. rank) on logarithmic axes.

A wide range of thresholds was applied in each case and results were compared. Figure 53 shows the typical progression of a rank-size distribution at full resolution for an example region in northern California. Images of the spatial structure of the network are shown for several different thresholds, with inset size distributions. Segment sizes are color coded on both the image and the rank-size plot. At a threshold of 100% subpixel vegetation abundance, all pixels fall below the threshold and there is no network. As the threshold is lowered, more pixels are included in the network and form components (contiguous patches). At this phase the components correspond to individual fields or groups of closely spaced fields with high F_v. Continuing to lower the threshold eventually results in connection of more and more components into larger contiguous areas as pixels with lower F_v are added to the network. Eventually enough pixels become part of the network that components begin connecting to form much larger components. Eventually the larger components superconnect and form one massive unit. If the threshold continues to be lowered to negligible F_v, the entire spatial domain of the image becomes part of the network. For more detail on the general methodology used to segment continuous fields, see (Small et al., 2011; Small and Sousa, 2015).

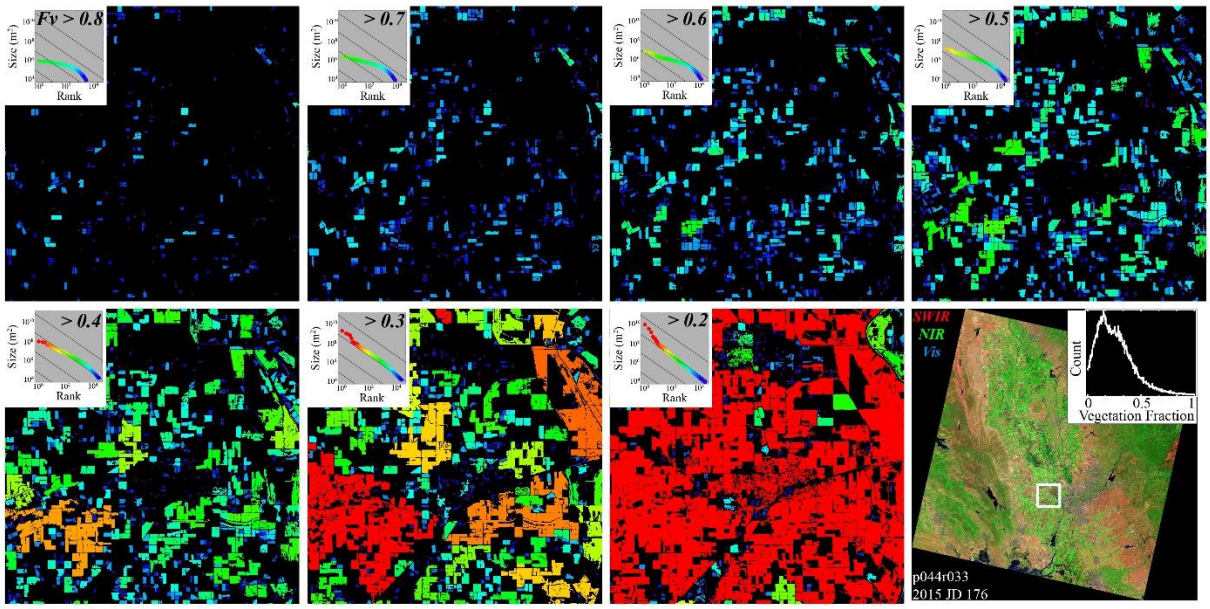

Figure 53. Illustration of network progression with threshold. This 1000 x 1000 pixel subscene of Landsat vegetation fraction was thresholded at successive values (upper left of each image). Insets show size distributions for each threshold. At threshold of Fv > 0.8, only a few fields emerge as part of the network and the size distribution is nearly flat. As the threshold decreases, more fields are included and adjacent fields connect. The size distribution steepens and loses its curvature. This continues until the size distribution becomes straight (near Fv > 0.3 in this case). After this point, further lowering of the threshold results in a majority of segments superconnecting into a small number of very large segments. This progression is typical of the other vegetation fraction images in this paper.

Disruption of agricultural networks was performed by sequential erosion using a morphological operator. For each iteration of the analysis, segment area maps were converted into binary maps indicating presence or absence of agriculture. These binary maps were then convolved with a 3 x 3 pixel Gaussian filter. Any pixel with a full set of 8 agricultural neighbors was unchanged, but any pixel with one or more non-agricultural neighbor decreased in value. A

threshold of 1 was then applied and segment areas were recaluclated. This produced the effect of removing every pixel in the image on the boundary of the network. The output of one erosional step was then used as the input for the next step.

Power law exponents were fit using the statistically robust algorithm described by (Clauset et al., 2009) and converted to slopes of the size distributions using the relation given in Eq. 1. Power law fits are also characterized by size cutoffs describing how far the power law properties plausibly extend down the lower tail of the distribution. Cutoffs were determined using the same algorithm by choosing the minimum of the Kolmogorov-Smirnoff (KS) statistic for sets of points extending sequentially farther into the lower tail of the distribution. Significance was estimated using a Monte Carlo approach to generate 1000 synthetic datasets and calculating the KS goodness-of-fit for each. Using this approach, large p values represent plausible power law fits. We use the suggestion of (Clauset et al., 2009) in presenting significant power law fits as those with $p > 0.1$, which is a stricter test than accepting as plausible distributions with $p > 0.05$.

While significant p values indicate that a power law distribution cannot be ruled out, they do not decisively show it to be a better fit than other heavy tailed distributions such as log-normal. Comparison of power law versus log-normal and Weibull distributions was performed by computing the Likelihood Ratio for each fit to each distribution. In all 27 cases, the power law gave a better fit (i.e. yielded a higher Likelihood value) than either the log-normal or Weibull distributions. However, despite outperforming both of the other two heavy tailed distributions, we remain non-committal about the true form of the underlying distributions being a strict power law. More information would be required to substantiate this claim than is available at the present time, and rigorous statistical testing of the power law hypothesis could be

a useful avenue for future work. In this paper, we simply use the power law as a convenient metric of linearity of the rank-size distributions in logarithmic space.

The data used in this study were (1) Landsat TM/ETM+/OLI scenes selected from diverse agricultural regions across 5 continents, (2) Sentinel-2 scenes selected from 3 agricultural regions in Europe, and (3) one IKONOS scene of an intensively cultivated region in Anhui, China. All Landsat scenes were acquired from the USGS Earth Resources Observation and Science Center (www.glovis.usgs.gov). All Sentinel scenes were acquired from the ESA SciHub web portal (www.scihub.copernicus.eu). For Landsat and IKONOS data, we use UTM equal area projections at the native resolution of the sensor. For Sentinel-2 data, we resample all 12 bands to the 10 m resolution native to the Sentinel-2 VNIR sensor in UTM equal area projection. Landsat scenes in this analysis are referred to by their WRS-2 path and row identifiers: i.e. scene p029r030 corresponds to Path 29, Row 30 (South Dakota).

The scenes were chosen to represent a diverse set of landscapes dominated by extensive agriculture, spanning a range of field sizes, climate zones, phenologies, and land management practices. A wide range of crops are represented, including regions dominated by one or two grains (e.g. rice and/or wheat) as well as regions producing a balance of both commodity and specialty crops. The 9 Landsat scenes used in this study were selected quasi-randomly from the Landsat archive to meet the criteria of: lack of cloud cover, diversity of agricultural practices, and range of hydrologic and climatic milieu. They were selected quasi-randomly in time to represent a range of stages of the phenologic cycle. We do not claim that these 9 scenes fully sample the global distribution, but rather suggest that their results represent a diverse set of potential endmembers of the global distribution of agricultural landscapes.

Figure 54 shows false color composites of the 9 Landsat scenes used for this analysis. Spatial configuration of agriculture across scenes varies widely from nearly wall-to-wall coverage (e.g. South Dakota and North China) to regions strongly limited in spatial extent by irrigation (e.g. Salton Trough and Indus). A range in extent of sectioning of the landscape by roads and rivers is apparent. Field size varies widely both across scenes and within scenes. Scenes were chosen at varying stages of the annual cycle, from soon after planting to maximum greenness. All scenes contain some non-agricultural vegetation ranging from tropical forest to desert shrubs – but all are dominated by agriculture. The Bavaria scene contains several forest patches, but all are managed forests so are effectively part of the agriculture/silviculture mosaic.

The spatial extent and abundance of non-agricultural vegetation varies from scene to scene. While the presence of some non-cultivated vegetation violates the assumption made in the analysis that networks of vegetation fraction strictly represent networks of agricultural activity, we have attempted to choose regions dominated by extensive cropland. We also suggest that, for some applications such as species migration and pollination, vegetation networks may be closer to the phenomenon of interest than strict definitions of cropland. Further, while considerable uncertainty exists as to the definition of cropland in global agriculture maps (reviewed in (Small and Sousa, 2016)), subpixel vegetation abundance represents a physically meaningful quantity which can be directly compared across widely varying landscapes. While using F_v as a general proxy for agriculture would not be valid in many landscapes, we hold that its properties of simplicity and consistency justify its use in the examples chosen in the context of this analysis.

Analysis

Landsat

Figure 55 shows Rank-Size plots for 3 different thresholds for each of the 9 Landsat scenes from Figure 54. F_V distribution for each scene is inset with the three thresholds indicated using vertical arrows. Histograms vary widely from scene to scene in central tendency, dispersion, and number of modes, reflecting differences between the landscapes described above. Thresholds are adjusted accordingly from scene to scene to capture similar positions in the distribution. Horizontal arrows on the rank-size plots indicate the cutoff for power law fit that maximized the goodness-of-fit criterion. Italicized thresholds and slopes have p values > 0.1, indicating a statistically plausible power law fit. The statistical significance of the fit is not critical for the purposes of this analysis because we use the power law exponent as a tool to quantify the slope of the rank-size plot, not as an assertion of the generating process itself. We include the goodness-of-fit result for the benefit of readers inclined to favor the power law mechanism.

Figure 56 shows Rank-Size slope estimates for several thresholds for each of the 9 Landsat scenes. Error bars indicate 95% confidence. As the threshold is successively lowered, rank-size slopes generally increase toward more negative values. This corresponds to an increase in overall network size and in the size of individual components, consistent with the network growth mechanism proposed in (Small and Sousa, 2015). Prominent exceptions to this rule correspond to cases of severe non-Gaussianity of the vegetation histogram, e.g. bimodality in the Mato Grosso and North China Landsat scenes and a broad, asymmetric shoulder in the South Dakota scene. Slopes near -1 indicate that segments decrease in size at roughly the same rate that they increase in frequency. Slopes pass through a value of -1 for 8 of the 9 scenes considered

here. The two scenes with slopes consistently shallower than -1, Indus and Salton Trough, are characterized by exponential-like F_v histograms with a mode of $F_v \approx 0$.

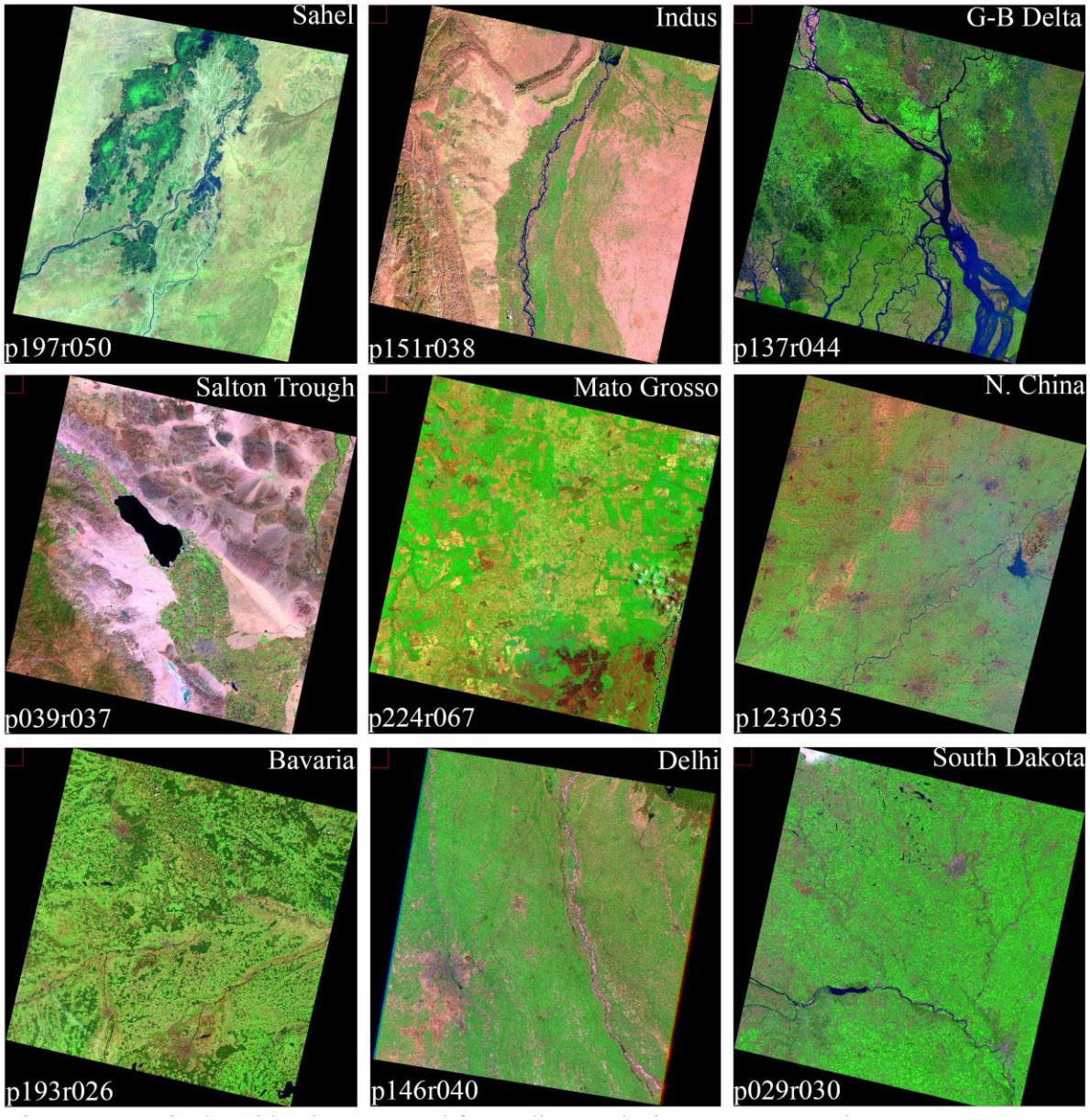

Figure 54. Agricultural landscapes used for scaling analysis. Scenes were chosen to represent a diverse set of landscapes characterized by agricultural extensification and intensification. A range of field sizes, competing land uses, climate zones, and land management practices is depicted.

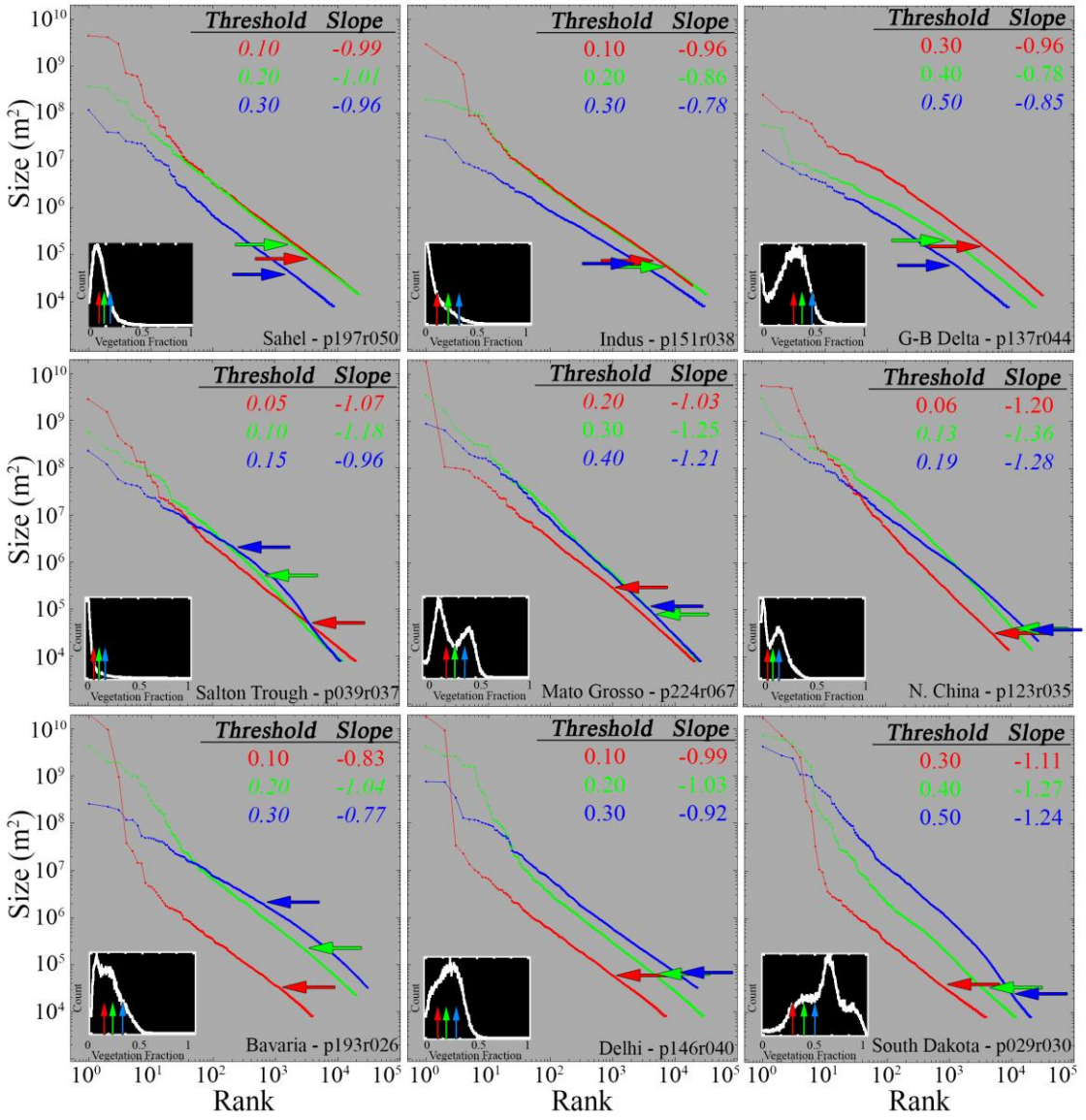

Figure 55. Rank-Size distributions for vegetation fraction from the 9 Landsat scenes shown in Figure 54. Inset shows vegetation fraction histogram for each Landsat scene, with arrows indicating the segmentation thresholds. Rank-Size distributions for each scene illustrate the sensitivity of the network structure to threshold. Distributions of vegetation fraction are different for each landscape but most scenes have linear rank size distributions with slopes near -1 and giant components forming as thresholds approach the median vegetation fraction.

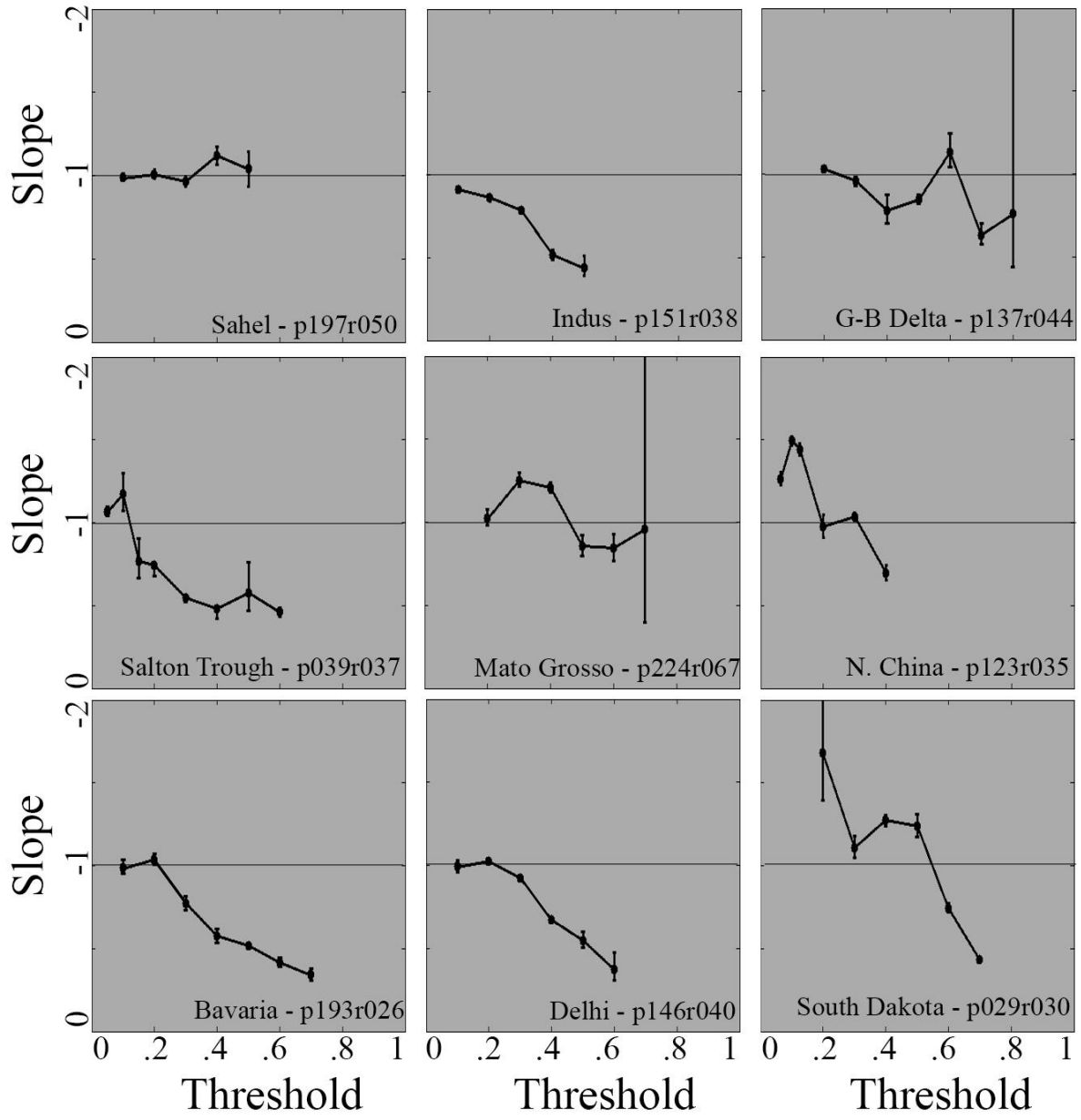

Figure 56. Slope of Rank-Size distribution versus threshold for the nine Landsat scenes used in Figure 54 and Figure 55. Local landscape properties vary from scene to scene, resulting in a wide range of vegetation fraction distributions. These distributions control the progression of slope of the size distributions.

Sentinel-2

Figures 39-41 show network structure intercomparisons between Landsat and Sentinel-2 for three 30 km x 30 km agricultural landscapes in Europe. In Figure 57, we examine an agricultural basin in Abbruzzo, Italy imaged on successive days in December, 2015. The segment size image of the agricultural network (middle row) reveals a range of spatial patterns of contiguous photosynthetic agriculture, from isolated small fields to clusters of closely spaced fields with separators which are not resolved by either 30 m Landsat or 10 m Sentinel-2 sensors. However, close visual inspection reveals several cases where fields grouped together in Landsat imagery are broken apart in Sentinel imagery – and vice versa. This is possible because increasing spatial resolution can have (at least) two processes working in opposite directions: ability to resolve narrow connectors which do not emerge above threshold in coarse resolution imagery (enhancing connectivity) and ability to resolve narrow separators which are presented in coarse resolution imagery as a mixed pixel above threshold (reducing connectivity). Which of these processes dominates varies based on the local geometry of the segment at play.

In Figure 58, we examine a subset of the agriculture/silviculture mosaic in Bavaria used in the global analysis of Figures 36-38. In this case, we examine the agricultural network over a range of nearly 25 years and 17 days offset in the phenological cycle. As a result, the overall greenness of the landscape is notably different, although the spatial arrangement of fields is generally stable. The segment size images reveal the breakup and connection of segments as a result of interannual, phenological, and resolution-based differences in the images. In spite of these differences, the rank-size distributions of segment areas remain remarkably consistent.

Figure 59 shows a region in Centre-Val de Loire, France 1 year and 14 days apart. In both cases, the agricultural network is dominated by large segments, identifiable both by visual

inspection of the segment area images and by rank-size slopes steeper than -1. Loci of closely spaced fields which dominate the landscape appear to be generally stable in their position, but the connectivity between them varies. While the spatial positions of the largest components shift due to this variation in connectivity, the rank-size plots again remain remarkably stable.

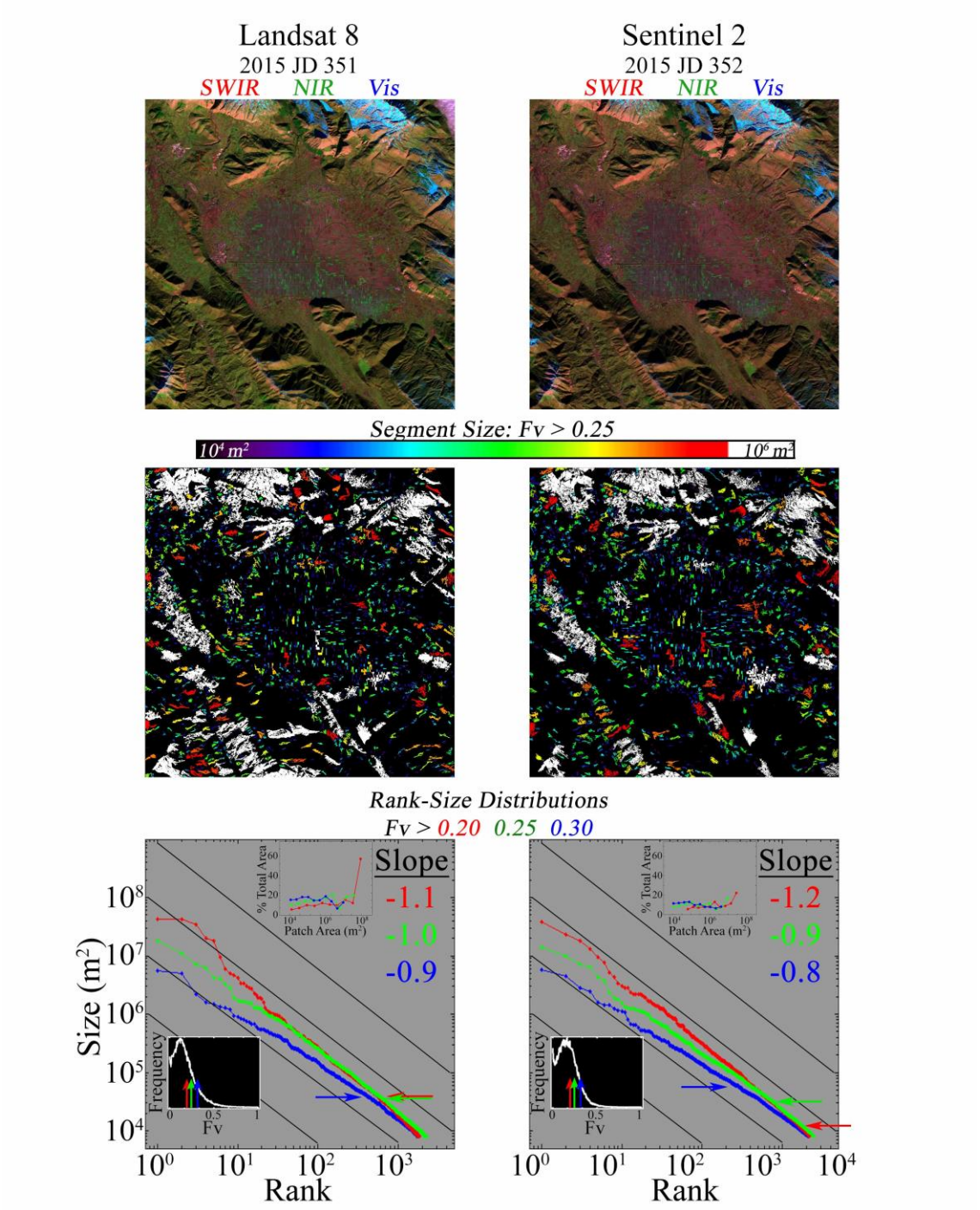

Figure 57. Comparison of Landsat- and Sentinel-derived networks from a 30 km x 30 km agricultural region in Abbruzzo, Italy. 1:1 lines shown on the rank-size curves in black. Inset histograms show vegetation fraction (lower left) and total area by segment size (upper right) distributions.

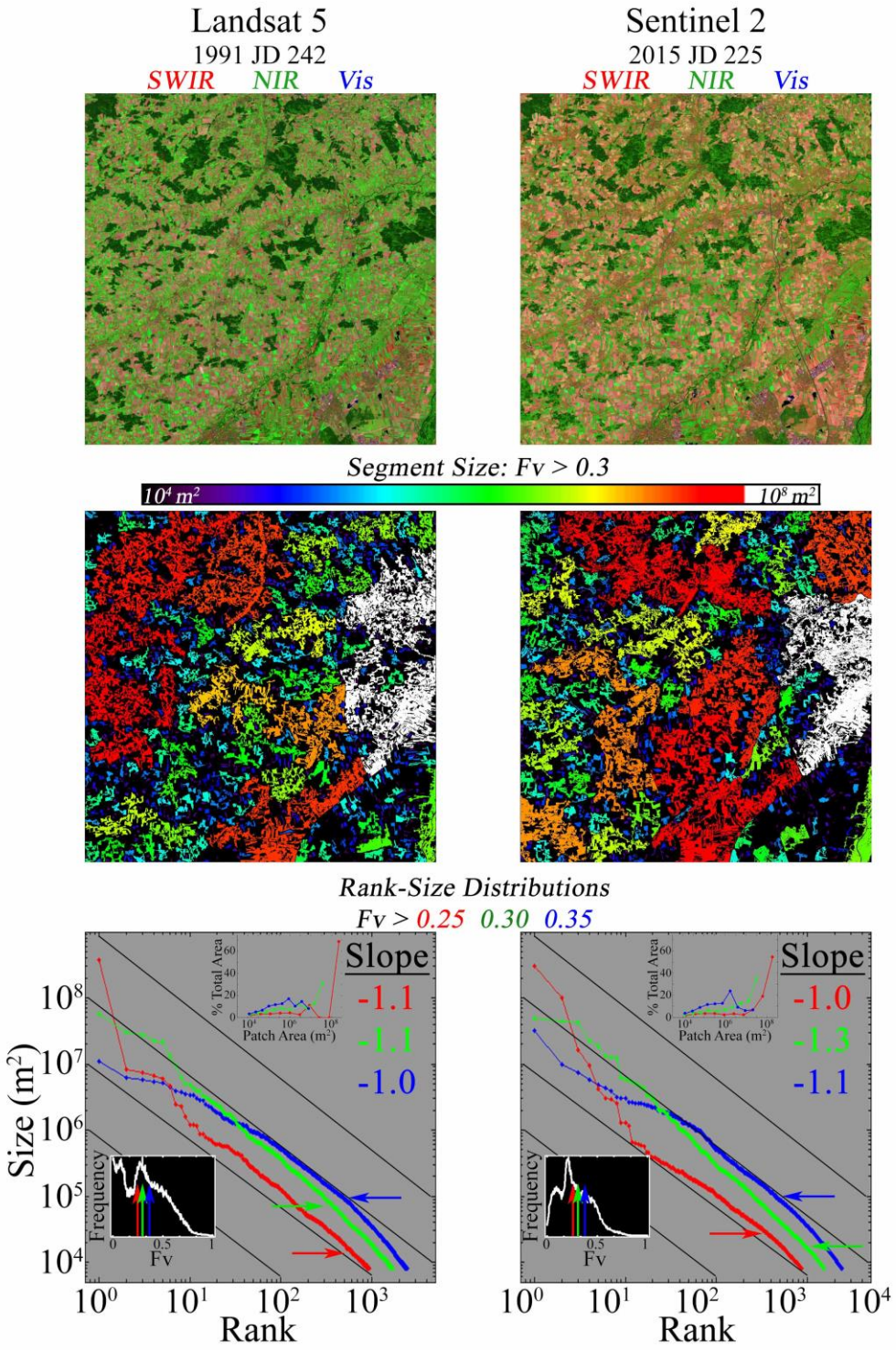

Figure 58. Same as Figure 57, but for a 30 km x 30 km agricultural region in Bavaria, Germany.

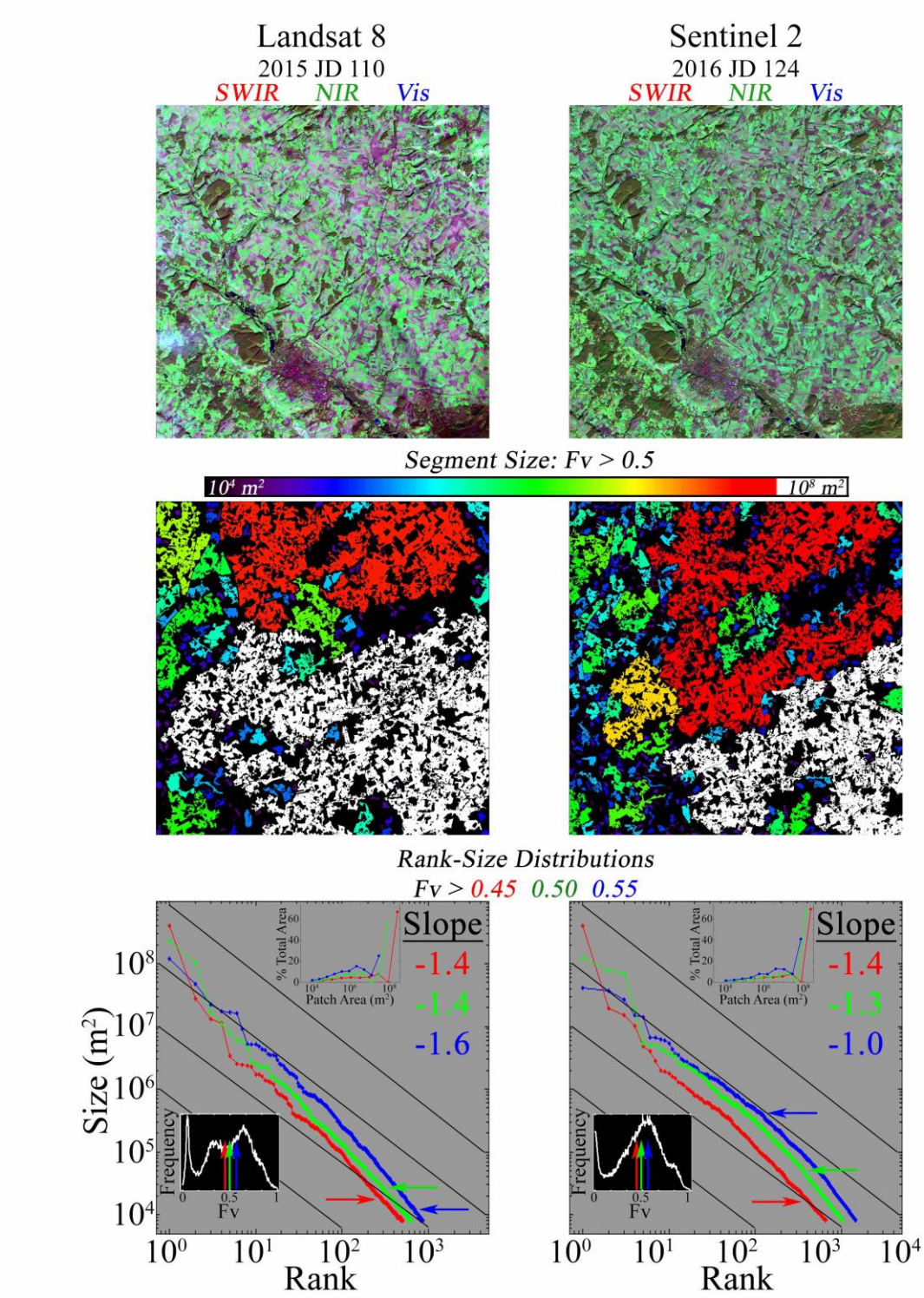

Figure 59. Same as Figure 57 and Figure 58, but for a 30 km x 30 km agricultural region in Centre-Val de Loire, France.

IKONOS

Figure 60 shows the procedure of successive thresholding when repeated for a ~39 km^2 IKONOS image in Anhui, China. The 4-band image was unmixed into SVD fractions using local endmembers. Successive thresholding was then applied to the F_v image. Segment area maps for four representative thresholds demonstrating the progression of the network are shown in the top 4 panels. The progression of the IKONOS size distributions with changing threshold (bottom right panel) is similar to that of the Landsat scene shown in Figure 53. At high thresholds IKONOS size distributions have high curvature and shallow slopes. The slope of the size distribution steepens as the threshold is reduced and the lower-tail power law cutoff gradually moves up the distribution. Curvature is even more pronounced than for Landsat at this phase. Once a threshold near 0.3 is reached, however, the size distribution loses most of its curvature and becomes linear. The slope of the size distribution crosses -1 at this point and the lower-tail cutoff rapidly moves deep into the lower tail of the distribution. As the threshold is decreased below this level, the network superconnects into a few giant components. The total number of segments (i.e. maximum rank) begins to decrease and the bottom of size distribution moves to the left. These properties are all similar to those observed for the Landsat and Sentinel scenes in previous figures.

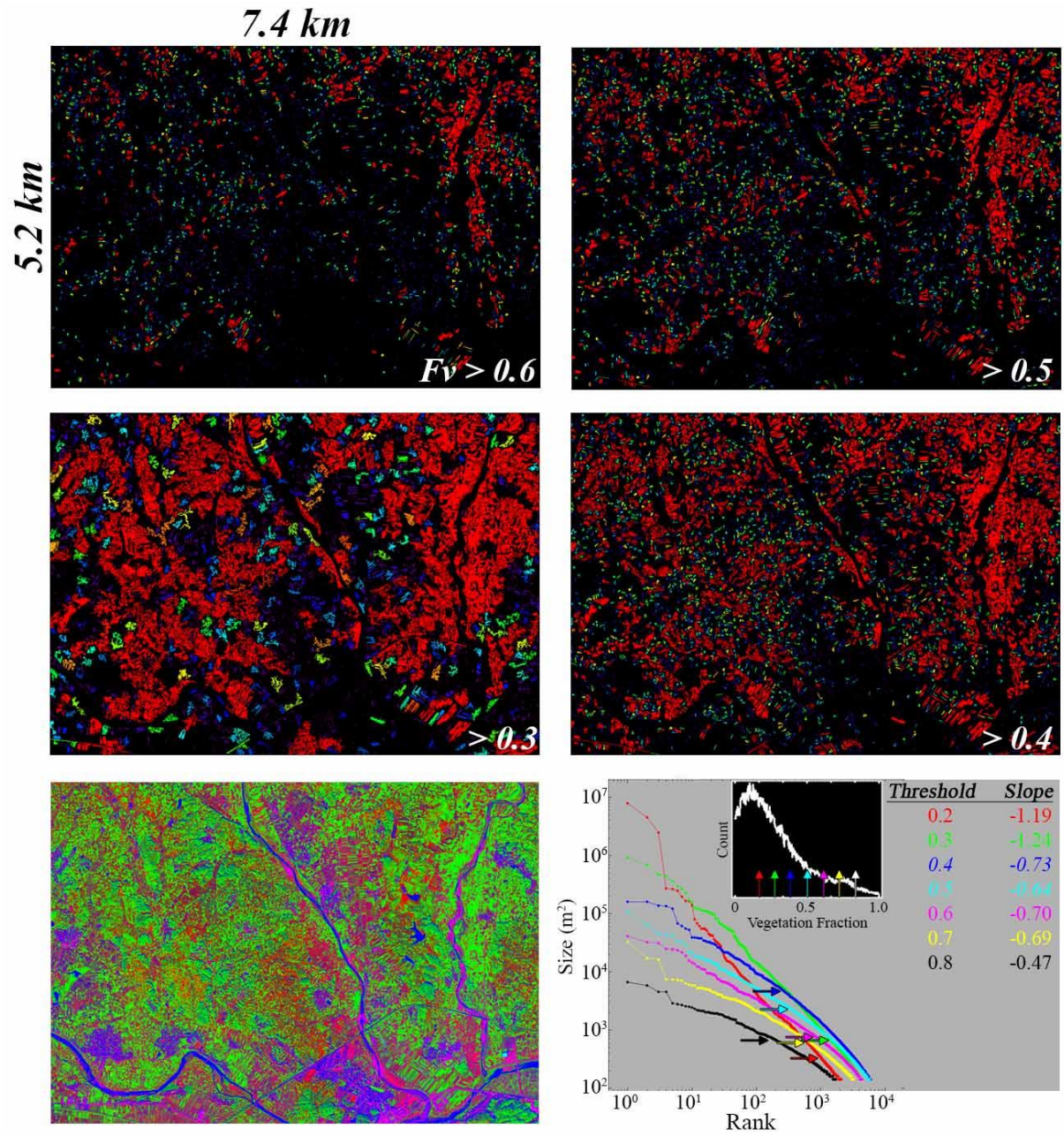

Figure 60. Successive thresholding of vegetation fraction for a 39 km² IKONOS image of Anhui, China. Rank-Size plots show a similar succession to those from Landsat in previous figures.

Practical Example – Disruption by Node Removal

Figure 61 shows how two agricultural networks can respond differently to disruption by sequentially reducing the area of each component. In each iteration of this process, all segments in the image are simultaneously reduced in size by removing one pixel width from around the boundary. We refer to this type of disruption as “erosion”. This process has the potential to remove segments from the network by shrinking them below the 9 pixel threshold. It also has the potential to break a small number of large segments into a large number of smaller segments (i.e. making little pieces out of big pieces) by separating dense intra-segment clusters which are only connected by narrow “bridges”.

We disrupt two agricultural networks in this way: one in the Salton Trough (p039r037) and one in South Dakota (p029r030). The upper tails of the rank-size distributions are shown in detail for successive numbers of erosional steps. The Salton Trough network (top) maintains the structure of its rank-size distribution through 7 erosional iterations, while the largest segments in the South Dakota network (bottom) rapidly dissociate into components with area approximately 2 orders of magnitude smaller, resulting in a drastic shallowing of the slope of the size distribution. This is a consequence of the differences in spatial structure and fractal dimension of the two networks.

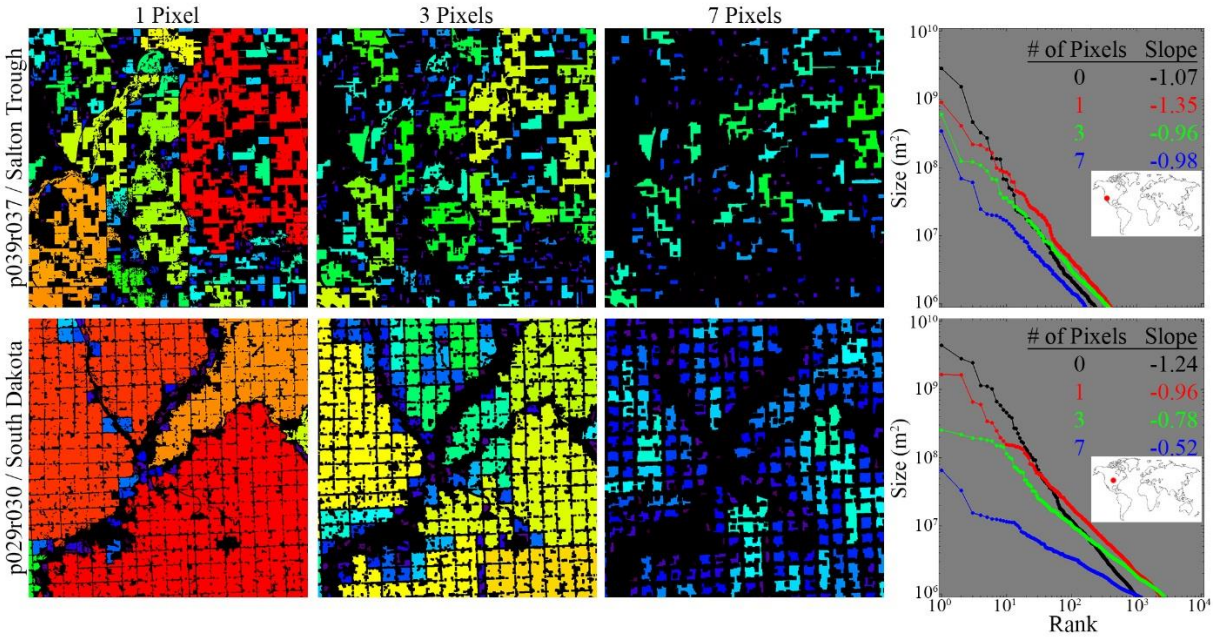

Figure 61. Disruption of agricultural networks by erosion. Images show a 1000 x 1000 pixel subset of segment area maps derived from full Landsat scenes. In each step, all boundary pixels are removed from the network, akin to removing rings of an onion. Regular rectilinear patterns correspond to real features of the landscape (i.e. roads) which often serve to guide the erosion process. As pixels are removed, the upper tail of the size distribution may maintain a slope near -1 (top) or flatten considerably (bottom), depending on the spatial structure of the network. Networks with size distributions which maintain their slope in the face of erosional perturbations may be more robust to disruption. Whether this form of network stability is desirable or undesirable depends on the application.

Discussion

Considerable range exists in the slope and curvature of the size distributions shown in Figure 55 – but the similarities are much more surprising than the differences. Indeed, we find it remarkable that there is any similarity at all given the diversity of landscapes (Figure 54) and of

vegetation abundance distributions (histogram insets of Figure 55) from which they are derived. While it is clear that none of the 9 size distributions here exactly resembles the global size distribution in Figure 52, it is similarly clear that none of the 9 landscapes used in this study comes close to fully sampling the diversity or scope of agriculture at global scales. Furthermore, because the differences between size distributions emerge from the differences in landscapes, these differences can be diagnostic in characterizing the variability in spatial distributions of agriculture across widely variable landscapes. From a network perspective, a diversity of size distributions implies a diversity of network structures.

Several potential explanations exist for the differences in rank-size distributions shown in Figure 55. Some Landsat scenes, such as the Salton Trough and Indus scenes, feature heavily irrigated agricultural landscapes in which cropland is tightly clustered around the hydrologic distribution network. This clustering impacts the rank size distribution and corresponding power law fit. All scenes feature some variable amount of human settlement, and some scenes such as North China, Delhi, and South Dakota feature spatially extensive conurbations which visibly disrupt the agricultural landscape. The extent to which these populated areas influence the spatial pattern of the agricultural land in the scene impacts the rank-size distribution of agricultural land.

Furthermore, the scenes range widely in levels of agricultural development, from smallholder farms (e.g. G-B Delta and Delhi), to industrial scale production (e.g. Salton Trough and South Dakota). While our analysis captures clusters of agriculture rather than individual fields, the distribution of field sizes contributes to the size of these clusters and thus the rank-size distribution. Major non-agricultural curvilinear and rectilinear features (e.g. rivers and roads) also cross-cut all of the scenes, providing a plethora of subscene background geometries which break apart some contiguous segments and encourage others to grow together. Finally, a wide

range of climate zones from tropical (G-B Delta and Mato Grosso) to hyperarid (Salton Trough and Indus) impact the background landscape mosaic within which the contiguous agricultural land for each scene is embedded. A detailed investigation of the way in which these (and other) factors generate the differences in rank-size distributions could provide a rich subject for future work.

Some of the size distributions in Figure 55 cannot plausibly be described as power laws. Some exhibit power law behavior that truncates in the middle of the distribution. Others show statistically plausible power law behavior extending deep into the lower tail of the distribution. We suggest that the important characteristic of the size distributions is not presence or absence of statistically defensible power law behavior, but rather that every distribution shown here is similarly heavy tailed. Every size distribution shows many more small patches than large patches, and nearly all distributions show that when ordered by area patches become smaller and more frequent at similar rates – implying the total area sum of patches at any size is nearly equal to the total sum at any other size. This property corresponds to a slope near -1 on the plots in Figure 55. Further, Figure 56 shows that many of the distributions vary with threshold in a predictable way: starting at high threshold (right side of the plots), the size distribution increases in slope as the threshold drops and the components grow (moving right to left on the plot) until reaching linearity near -1. At this point, a giant component emerges and dominates the network.

As the threshold is dropped even further, more and more of the remaining patches become connected into the giant component, reducing the total number of segments until every pixel in the entire domain is superconnected. The variations in progression of network structure with threshold are related to the fraction distributions, but the gross structure described above occurs in a consistent way across a wide range of conditions. A similar progression is also shown

for the IKONOS image (Figure 60) over a much smaller spatial domain. Similar progressions have even been observed in some random spatial networks and a general mechanism for the process been proposed (Small and Sousa, 2015). Despite this observed commonality, some of the distributions shown here vary with changing threshold in a more complex way than described above. This discrepancy often corresponds to severe non-Gaussianity in the F_v histogram. Detailed analysis of this complexity will be the subject of further study.

Landsat – Sentinel-2 intercomparisons provide an opportunity to make note of several important limitations of spatial network analysis for agricultural landscapes. A primary challenge, long recognized, is in the definition of "agriculture" as observed by remote sensing. In this study we use vegetation fraction because it is a physically meaningful quantity which has been shown to be consistent across sensors and scalable across spatial resolution. However, it cannot distinguish between anthropogenically-driven vegetation (i.e. agriculture, including silviculture) and natural vegetation. When scenes are pre-selected to be dominated by agriculture, as they have been in this study, this problem is minimized – but not completely eliminated. Inspection of the hillslopes around the agriculturally-dominated caldera in the Abbruzzo scene provides one example of this scenario.

Phenology provides another challenge which can be highly complex in agricultural landscapes. Network analysis of any single image provides a single snapshot of that landscape in time. As is apparent from Figure 55 and Figure 56, temporal variability on the order of weeks can substantially alter the spatial connectivity of an agricultural landscape. Complete network-based analyses intended for practical applications must account for the phenology of the landscapes which they observe, as spatially-dependent processes are often temporally-dependent as well. As quantified by single-image vegetation fraction, landscapes possess a temporal

progression of connectivity structures – of which the power law phase may be short-lived. We find it remarkable that so many agricultural networks, even when undersampled so extensively in both time and space, still display this unique structure which is so similar to that of the global network.

Analysis of two seemingly similar agricultural landscapes by network erosion shown in Figure 61 demonstrates one potential application of the concepts presented in this paper. In one case (Salton Trough), power law behavior with slope near -1 is persistent even after removal of many pixels and considerable reduction of the total size of the network. In another case (South Dakota), the power law behavior of the network is much less robust. Removal of only a few pixels drastically reduces the sizes of the largest components (by a factor of ~100), rapidly breaking apart the largest segments of the network into much smaller disconnected components. This is clearly a result of the sectioning of the landscape by the regular grid of the road network. One could imagine a landscape which is more sensitive to small perturbations as being more easily disruptable – either a dangerous characteristic (as in the case of pollinator pathways) or a desirable one (as in the case of quarantining disease outbreaks). Understanding the robustness of the structure of an agricultural network to disruption could provide application-specific insight into practical methods for disrupting (or preventing disruption of) connectivity across an agricultural landscape.

Another possible application, not shown in this analysis, is to use multitemporal observations to constrain the growth and attenuation of agricultural networks in a landscape throughout the complete phenological cycle. As the agricultural mosaic evolves through time, different crops are planted, green up, senesce, and are harvested at different times of year. Taken together, the combination of the spatial distribution of these crops and their corresponding

phenology time series govern the complete spatiotemporal agricultural network of a landscape. The diagnostic property of an agricultural landscape may be not just the network as observed at any one time but rather the robustness of the network properties throughout the course of the year. For instance, effective pollination may require an agricultural network to remain in a particularly interconnected state for a certain length of time. Crops may be particularly susceptible to disease outbreaks at one particular time of year. Native species may be more sensitive to disruptions of habitat in migration season than at other times of year. Furthermore, network adaptation to catastrophic environmental stresses such as drought or widespread disease outbreaks may be easily characterized. Finally, multitemporal network studies – like all of the analyses performed in this paper – have the added benefit of being easily performed nearly anywhere on Earth using simple methodologies and freely available remotely sensed observations.

Conclusion

This thesis begins with a consideration of the microscale physics of the evaporation of water from porous media. Chapter 1 presents laboratory experiments documenting the joint optical and thermal evolution of drying sands. As expected, all of the samples demonstrated the same overall stages of drying, regardless of composition or grain size. However, systematic variations were also observed among the drying trajectories that were consistent with systematic variations in the physical properties of the samples. The effect of reflectance and emissivity due to variations in composition was observed to be 2-5x greater than the effect of grain size. Run-to-run variability was greater for the thermal measurements than the optical measurements, but compositional and grain size effects exceeded run-to-run variability in nearly every case. The results of this chapter suggest that for the drying of sands, reflectance-based differences in heating may dominate grain-sized based differences in hydrologic properties (e.g. capillarity, conductivity), at least in the 125-1000 □m grain size range. A set of hypotheses is developed addressing the potential to leverage differences in optical and thermal skin depths to infer the slope of the vertical water gradient at a particular stage in the drying process. If these hypotheses are validated by future experimental studies, a new method of characterizing near-surface hydrological properties of porous media using only remotely sensed measurements could be developed.

Chapter 2 then addresses the question of information loss between narrowband hyperspectral reflectance measurements (like those made in Chapter 1), and broadband multispectral measurements (like those used throughout Chapters 3-6). Satellite-based multispectral sensors like Landsat comprise the current and historical multispectral archive, but several future hyperspectral satellite missions are currently under development. Potential

differences between multispectral and hyperspectral observations of substrates (soil, rock, and non-photosynthetic vegetation) are of particular relevance to this thesis. A comparative analysis of coincident hyperspectral AVIRIS and multispectral Landsat image pairs is presented. The information content of the two datasets is compared using the dimensionality and topology of the spectral feature spaces. The results indicate that a surprising fraction of the information content of the hyperspectral dataset is carried over into the multispectral dataset, at least when quantified using variance as the metric for information content. This is consistent with the hypothesis that the dominant absorption features common to substrate materials are sufficiently broad to be effectively captured by multispectral sensors. The results of Chapter 2 suggest that the much of the signal present in the narrowband laboratory reflectance measurements made in Chapter 1 can be reasonably expected to extend into the broadband domain for applications such as those presented in Chapters 3 through 6 – an encouraging finding for the remote sensing of ET.

Spectral mixture analysis is used as the tool of choice for inferring land surface properties from optical satellite imagery. However, in order for this approach to be used to mix data collected by the current Landsat 8 sensor and the older sensors onboard Landsat 4-7, the global spectral mixture model must first be cross-calibrated. Chapter 3 presents this cross-calibration, allowing data to be used interchangeably throughout the entire Landsat 4-8 archive. In addition, a potential theoretical explanation is advanced to explain the observed superior scaling properties of fractional vegetation abundance derived from this method relative to spectral indices. The results of Chapter 3 provide practical tools which can be used as the basis for future ET applications, such as those presented in Chapters 4 through 6.

Chapter 4 presents a framework for applying SMA to ET studies based on satellite imaging. Each of the Substrate, Vegetation and Dark (SVD) endmembers is examined relative to

the parameters of Moisture Availability and ET Fraction, as estimated by the Triangle Method. As expected, SMA-estimated vegetation fraction is observed to possess superior scaling properties to spectral vegetation indices. Perhaps the most interesting of the results is the apparently robust linear relation observed between the S fraction and EF, with clear potential connection to the laboratory results of Chapter 1.

Chapter 5 examines the relative utility of optical and thermal Landsat image time series for the mapping and monitoring of rice agriculture. SMA-derived vegetation fraction was used as the optical metric, based on the endmembers developed in Chapter 3, and surface temperature was used as the thermal metric. The information content of each dataset was visually explored using the temporal feature space, and parallel temporal mixture models were used to map the extent of rice agriculture. Thermal-based models were observed to outperform optical-based models in mapping rice presence/absence, but optical-based models outperformed thermal-based models in mapping the timing of rice phenology.

Chapter 6 is broadest in scope, focusing on the spatial structure of networks of agricultural land cover. A consistent scaling relationship is observed for nine widely varying agricultural landscapes at 30 m resolution. This relationship was observed to be remarkably similar to that observed at kilometer resolution in a previous global study of forests, agriculture, and human settlements. Potential implications of the spatial structure of seasonally evolving networks of agricultural land cover were discussed.

The results of this thesis are particularly relevant given that they come at a time of rapidly increasing data availability. Open access to the entire Landsat archive, along with rigorous intercalibration, enables 35+ year retrospective studies. The ongoing integration of the combined Landsat + Sentinel constellation is currently reducing the nominal revisit time of decameter

optical imaging from 16 to 5 days. An increasing wealth of airborne hyperspectral data is available online, and several hyperspectral satellite missions are expected to be operationalized in the near future.

This increase in observational capacity suggests that the implications of this thesis are likely to increase in scope in the coming years. At laboratory scales, a promising path forward is identified which may result in a new metric to quantify near-surface hydrological properties of porous media from optical and thermal remote sensing. At landscape scales, the steps made toward more accurate ET estimation may become increasingly relevant as the new intercalibrated Harmonized Landsat Sentinel (HLS) product is developed, allowing for seamless intermixing of these two data streams. For agricultural and environmental applications, temporal mixture models offer increasing promise as revisit time is reduced and temporal aliasing becomes less severe. Finally, the agricultural network analysis offers perhaps the most novel path forward, with potentially far-reaching implications for scaling constraints on ET estimation based on a new approach to the geophysical analysis of land cover.

References

Adams, J.B., Smith, M.O., Johnson, P.E., 1986. Spectral mixture modeling: A new analysis of rock and soil types at the Viking Lander 1 site. J. Geophys. Res. Solid Earth 91, 8098–8112.

Albert, R., Barabási, A.-L., 2002. Statistical mechanics of complex networks. Rev. Mod. Phys. 74, 47–97. https://doi.org/10.1103/RevModPhys.74.47

Allen, R.G., Tasumi, M., Morse, A., Trezza, R., 2005. A Landsat-based energy balance and evapotranspiration model in Western US water rights regulation and planning. Irrig. Drain. Syst. 19, 251–268. https://doi.org/10.1007/s10795-005-5187-z

Allen, R.G., Tasumi, M., Trezza, R., 2007. Satellite-based energy balance for mapping evapotranspiration with internalized calibration (METRIC) Model. J. Irrig. Drain. Eng. 133, 380–394.

Anderson, M., Allen, R.G., Morse, A., Kustas, W.P., 2012. Use of Landsat thermal imagery in monitoring evapotranspiration and managing water resources. Remote Sens. Environ. 122.

Anderson, M., Kustas, W., Norman, J., Hain, C., Mecikalski, J., Schultz, L., GonzÃ¡lez-Dugo, M., Cammalleri, C., D'Urso, G., Pimstein, A., 2011. Mapping daily evapotranspiration at field to continental scales using geostationary and polar orbiting satellite imagery. Hydrol. Earth Syst. Sci. 15, 223–239.

Anderson, M., Norman, J., Mecikalski, J.R., Torn, R.D., Kustas, W.P., Basara, J.B., 2004. A multiscale remote sensing model for disaggregating regional fluxes to micrometeorological scales. J. Hydrometeorol. 5, 343–363.

Anderson, M.C., Norman, J.M., Diak, G.R., Kustas, W.P., Mecikalski, J.R., 1997. A two-source time-integrated model for estimating surface fluxes using thermal infrared remote sensing. Remote Sens. Environ. 60, 195–216.

Ångström, A., 1925. The Albedo of Various Surfaces of Ground. Geogr. Ann. 7, 323–342 CR–Copyright © 1925 Swedish Societ. https://doi.org/10.2307/519495

Asner, G.P., Knapp, D.E., Boardman, J., Green, R.O., Kennedy-Bowdoin, T., Eastwood, M., Martin, R.E., Anderson, C., Field, C.B., 2012. Carnegie Airborne Observatory-2: Increasing science data dimensionality via high-fidelity multi-sensor fusion. Remote Sens. Environ. 124, 454–465. https://doi.org/10.1016/J.RSE.2012.06.012

Auerback, F., 1913. Das Gesetz der Bevölkerungskonzentration. Petermanns Geogr. Mitt. 59, 74–76.

Bablet, A., Vu, P.V.H., Jacquemoud, S., Viallefont-Robinet, F., Fabre, S., Briottet, X., Sadeghi, M., Whiting, M.L., Baret, F., Tian, J., 2018. MARMIT: A multilayer radiative transfer model of soil reflectance to estimate surface soil moisture content in the solar domain (400–2500 nm). Remote Sens. Environ. 217, 1–17. https://doi.org/10.1016/J.RSE.2018.07.031

Baldocchi, D., Krebs, T., Leclerc, M.Y., 2005. "Wet/dry Daisyworld": a conceptual tool for quantifying the spatial scaling of heterogeneous landscapes and its impact on the subgrid variability of energy fluxes. Tellus B Chem. Phys. Meteorol. 57, 175–188.

https://doi.org/10.3402/tellusb.v57i3.16538

Barabasi, A.-L., Albert, R., 1999. Emergence of scaling in random networks. Science 286, 509–12. https://doi.org/10.1126/SCIENCE.286.5439.509

Barsi, J.A., Barker, J.L., Schott, J.R., 2003. An Atmospheric Correction Parameter Calculator for a single thermal band earth-sensing instrument, in: 2003 IEEE International Geoscience and Remote Sensing Symposium. Proceedings (IEEE Cat. No.03CH37477). IEEE, pp. 3014–3016. https://doi.org/10.1109/IGARSS.2003.1294665

Barsi, J.A., Schott, J.R., Palluconi, F.D., Hook, S.J., 2005. Validation of a web-based atmospheric correction tool for single thermal band instruments, in: Butler, J.J. (Ed.), . International Society for Optics and Photonics, p. 58820E. https://doi.org/10.1117/12.619990

Barthélemy, M., 2011. Spatial networks. Phys. Rep. 499, 1–101. https://doi.org/10.1016/J.PHYSREP.2010.11.002

Bastiaanssen, W., Menenti, M., Feddes, R.A., Holtslag, A.A.M., 1998. A remote sensing surface energy balance algorithm for land (SEBAL). 1. Formulation. J. Hydrol. 212–213, 198–212. https://doi.org/10.1016/S0022-1694(98)00253-4

Bastiaanssen, W., Noordman, E.J.M., Pelgrum, H., Davids, G., Thoreson, B.P., Allen, R.G., 2005. SEBAL Model with Remotely Sensed Data to Improve Water-Resources Management under Actual Field Conditions. J. Irrig. Drain. Eng. 131, 85–93. https://doi.org/10.1061/(ASCE)0733-9437(2005)131:1(85)

Baumgardner, M.F., Silva, L.F., Biehl, L.L., Stoner, E.R., 1986. Reflectance Properties of Soils. Adv. Agron. 38, 1–44. https://doi.org/10.1016/S0065-2113(08)60672-0

Ben-Dor, E., Chabrillat, S., Demattê, J.A.M., Taylor, G.R., Hill, J., Whiting, M.L., Sommer, S., 2009. Using Imaging Spectroscopy to study soil properties. Remote Sens. Environ. 113, S38–S55. https://doi.org/10.1016/J.RSE.2008.09.019

Boardman, J., 1993. Automating spectral unmixing of AVIRIS data using convex geometry concepts, in: Summaries of the 4th Annual JPL Airborne Geoscience Workshop. NASA-JPL, Pasadena, CA, pp. 11–14.

Boardman, J.W., Green, R.O., 2000. Exploring the spectral variability of the Earth as measured by AVIRIS in 1999, in: AVIRIS 2000 Workshop. NASA-JPL, Pasadena, California, USA.

Bolton, D., Friedl, M., 2013. Forecasting crop yield using remotely sensed vegetation indices and crop phenology metrics. Agric. For. Meteorol.

Boschetti, M., Stroppiana, D., Brivio, P., Bocchi, S., 2009. Multi-year monitoring of rice crop phenology through time series analysis of MODIS images. Int. J. Remote Sens. 30, 4643–4662.

Bretherton, C.S., Smith, C., Wallace, J.M., 1992. An Intercomparison of Methods for Finding Coupled Patterns in Climate Data. J. Clim. 5, 541–560. https://doi.org/10.1175/1520-0442(1992)005<0541:AIOMFF>2.0.CO;2

Bricklemyer, R.S., Lawrence, R.L., Miller, P.R., Battogtokh, N., 2007. Monitoring and verifying agricultural practices related to soil carbon sequestration with satellite imagery. Agric. Ecosyst. Environ. 118, 201–210. https://doi.org/10.1016/J.AGEE.2006.05.017

Brown, D.J., Shepherd, K.D., Walsh, M.G., Dewayne Mays, M., Reinsch, T.G., 2006. Global soil characterization with VNIR diffuse reflectance spectroscopy. Geoderma 132, 273–290. https://doi.org/10.1016/J.GEODERMA.2005.04.025

Brunsell, N., Anderson, M., 2011. Characterizing the multi–scale spatial structure of remotely sensed evapotranspiration with information theory. Biogeosciences 8, 2269–2280. https://doi.org/10.5194/bg-8-2269-2011

Brunsell, N., Gillies, R., 2003a. Scale issues in land–atmosphere interactions: implications for remote sensing of the surface energy balance. Agric. For. Meteorol. 117, 203–221. https://doi.org/10.1016/S0168-1923(03)00064-9

Brunsell, N., Gillies, R., 2003b. Length Scale Analysis of Surface Energy Fluxes Derived from Remote Sensing. J. Hydrometeorol. 4, 1212–1219. https://doi.org/10.1175/1525-7541(2003)004<1212:LSAOSE>2.0.CO;2

Busetto, L., Ranghetti, L., 2016. MODIStsp : An R package for automatic preprocessing of MODIS Land Products time series. Comput. Geosci. 97, 40–48. https://doi.org/10.1016/j.cageo.2016.08.020

Cantwell, M.D., Forman, R.T.T., 1993. Landscape graphs: Ecological modeling with graph theory to detect configurations common to diverse landscapes. Landsc. Ecol. 8, 239–255. https://doi.org/10.1007/BF00125131

Carlson, T.N., 2013. Triangle Models and Misconceptions. Int. J. Remote Sens. Appl. 3, 155–158.

Carlson, T.N., 2007. An Overview of the "Triangle Method" for Estimating Surface Evapotranspiration and Soil Moisture from Satellite Imagery. Sensors 7, 1612–1629. https://doi.org/10.3390/s7081612

Carlson, T.N., Boland, F.E., 1978. Analysis of urban-rural canopy using a surface heat flux/temperature model. J. Appl. Meteorol. 17, 998–1013.

Carlson, T.N., Gillies, R., Perry, E., 1994. A method to make use of thermal infrared temperature and NDVI measurements to infer surface soil water content and fractional vegetation cover. Remote Sens. Rev. 9, 161–173. https://doi.org/10.1080/02757259409532220

Carlson, T.N., Ripley, D.A., 1997. On the relation between NDVI, fractional vegetation cover, and leaf area index. Remote Sens. Environ. 62, 241–252.

Carter, C., Liang, S., 2018. Comprehensive evaluation of empirical algorithms for estimating land surface evapotranspiration. Agric. For. Meteorol. 256–257, 334–345. https://doi.org/10.1016/J.AGRFORMET.2018.03.027

Castaldi, F., Palombo, A., Santini, F., Pascucci, S., Pignatti, S., Casa, R., 2016. Evaluation of the potential of the current and forthcoming multispectral and hyperspectral imagers to estimate soil texture and organic carbon. Remote Sens. Environ. 179, 54–65.

https://doi.org/10.1016/J.RSE.2016.03.025

Chander, G., Markham, B., 2003. Revised Landsat-5 TM radiometric calibration procedures and postcalibration dynamic ranges. IEEE Trans. Geosci. Remote Sens. 41, 2674–2677. https://doi.org/10.1109/TGRS.2003.818464

Childs, N., 2016. Rice Outlook: October 14, 2016.

Childs, N., Skorbiansky, S.R., 2018. Rice Outlook: July 16, 2018.

Childs, N., Skorbiansky, S.R., 2017. Rice Outlook: July 14, 2017.

Choudhury, B.J., Ahmed, N.U., Idso, S.B., Reginato, R.J., Daughtry, C.S., 1994. Relations between evaporation coefficients and vegetation indices studied by model simulations. Remote Sens. Environ. 50, 1–17.

Clauset, A., Rohilla Shalizi, C., J Newman, M.E., 2009. Power-Law Distributions in Empirical Data. SIAM Rev. 51, 661–703. https://doi.org/10.1137/070710111

Crist, E.P., Cicone, R.C., 1984. A Physically-Based Transformation of Thematic Mapper Data---The TM Tasseled Cap. IEEE Trans. Geosci. Remote Sens. GE-22, 256–263. https://doi.org/10.1109/TGRS.1984.350619

Diekötter, T., Billeter, R., Crist, T.O., 2008. Effects of landscape connectivity on the spatial distribution of insect diversity in agricultural mosaic landscapes. Basic Appl. Ecol. 9, 298–307. https://doi.org/10.1016/J.BAAE.2007.03.003

Dixo, M., Metzger, J.P., Morgante, J.S., Zamudio, K.R., 2009. Habitat fragmentation reduces genetic diversity and connectivity among toad populations in the Brazilian Atlantic Coastal Forest. Biol. Conserv. 142, 1560–1569. https://doi.org/10.1016/J.BIOCON.2008.11.016

Drusch, M., Del Bello, U., Carlier, S., Colin, O., Fernandez, V., Gascon, F., Hoersch, B., Isola, C., Laberinti, P., Martimort, P., Meygret, A., Spoto, F., Sy, O., Marchese, F., Bargellini, P., 2012. Sentinel-2: ESA's Optical High-Resolution Mission for GMES Operational Services. Remote Sens. Environ. 120, 25–36. https://doi.org/10.1016/J.RSE.2011.11.026

Elmore, A.J., Mustard, J.F., Manning, S.J., Lobell, D.B., 2000. Quantifying vegetation change in semiarid environments: precision and accuracy of spectral mixture analysis and the normalized difference vegetation index. Remote Sens. Environ. 73, 87–102.

Ershadi, A., McCabe, M.F., Evans, J.P., Walker, J.P., 2013. Effects of spatial aggregation on the multi-scale estimation of evapotranspiration. Remote Sens. Environ. 131, 51–62. https://doi.org/10.1016/J.RSE.2012.12.007

Farahani, H.J., Howell, T.A., Shuttleworth, W.J., Bausch, W.C., 2007. Evapotranspiration: Progress in Measurement and Modeling in Agriculture. Trans. ASABE 50, 1627–1638. https://doi.org/10.13031/2013.23965

Fisher, J.B., Melton, F., Middleton, E., Hain, C., Anderson, M., Allen, R., McCabe, M.F., Hook, S., Baldocchi, D., Townsend, P.A., Kilic, A., Tu, K., Miralles, D.D., Perret, J., Lagouarde, J., Waliser, D., Purdy, A.J., French, A., Schimel, D., Famiglietti, J.S., Stephens, G., Wood, E.F., 2017. The future of evapotranspiration: Global requirements for ecosystem

functioning, carbon and climate feedbacks, agricultural management, and water resources. Water Resour. Res. 53, 2618–2626. https://doi.org/10.1002/2016WR020175@10.1002/(ISSN)1944-9208.COMHES1

Fisher, J.B., Whittaker, R.J., Malhi, Y., 2011. ET come home: potential evapotranspiration in geographical ecology. Glob. Ecol. Biogeogr. 20, 1–18. https://doi.org/10.1111/j.1466-8238.2010.00578.x

Flood, N., 2014. Continuity of Reflectance Data between Landsat-7 ETM+ and Landsat-8 OLI, for Both Top-of-Atmosphere and Surface Reflectance: A Study in the Australian Landscape. Remote Sens. 6, 7952–7970. https://doi.org/10.3390/rs6097952

Galleguillos, M., Jacob, F., Prévot, L., French, A., Lagacherie, P., 2011. Comparison of two temperature differencing methods to estimate daily evapotranspiration over a Mediterranean vineyard watershed from ASTER data. Remote Sens. Environ. 115, 1326–1340.

Gardner, R.H., Turner, M.G., Dale, V.H., O'Neill, R. V., 1992. A Percolation Model of Ecological Flows. Springer, New York, NY, pp. 259–269. https://doi.org/10.1007/978-1-4612-2804-2_12

Gaston, K.J., 2000. Global patterns in biodiversity. Nature 405, 220–227. https://doi.org/10.1038/35012228

Geisseler, D., Horwath, W.R., 2013. Rice Production in California. Davis.

Gerace, A., Montanaro, M., 2017. Derivation and validation of the stray light correction algorithm for the thermal infrared sensor onboard Landsat 8. Remote Sens. Environ. 191, 246–257. https://doi.org/https://doi.org/10.1016/j.rse.2017.01.029

Gillespie, A.R., Smith, M.O., Adams, J.B., Willis, S.C., Fischer, A.F., Sabol, D.E., 1990. Interpretation of residual images: spectral mixture analysis of AVIRIS images, Owens Valley, California, in: Annual JPL Airborne Visible/Infrared Imaging Spectrometer (AVIRIS) Workshop. pp. 54–90.

Gilligan, C.A., 2008. Sustainable agriculture and plant diseases: an epidemiological perspective. Philos. Trans. R. Soc. B Biol. Sci. 363, 741–759. https://doi.org/10.1098/rstb.2007.2181

Global Rice Science Partnership, 2013. Rice Almanac, 4th Edition: Source Book for One of the Most Important Economic Activities on Earth. Los Banos, Philippines.

Gnyp, M.L., Miao, Y., Yuan, F., Ustin, S.L., Yu, K., Yao, Y., Huang, S., Bareth, G., 2014. Hyperspectral canopy sensing of paddy rice aboveground biomass at different growth stages. F. Crop. Res. https://doi.org/10.1016/j.fcr.2013.09.023

Green, A.A., Berman, M., Switzer, P., Craig, M.D., 1988. A transformation for ordering multispectral data in terms of image quality with implications for noise removal. IEEE Trans. Geosci. Remote Sens. 26, 65–74. https://doi.org/10.1109/36.3001

Green, R., Boardman, J., 2000. Exploration of the relationship between information content and signal-to-noise ratio and spatial resolution in AVIRIS spectral data, in: 2000 AVIRIS Workshop. Pasadena, CA.

Green, R.O., Eastwood, M.L., Sarture, C.M., Chrien, T.G., Aronsson, M., Chippendale, B.J., Faust, J.A., Pavri, B.E., Chovit, C.J., Solis, M., Olah, M.R., Williams, O., 1998. Imaging Spectroscopy and the Airborne Visible/Infrared Imaging Spectrometer (AVIRIS). Remote Sens. Environ. 65, 227–248. https://doi.org/10.1016/S0034-4257(98)00064-9

Gumma, M.K., Mohanty, S., Nelson, A., Arnel, R., Mohammed, I.A., Das, S.R., 2015. Remote sensing based change analysis of rice environments in Odisha, India. J. Environ. Manage. 148, 31–41. https://doi.org/10.1016/J.JENVMAN.2013.11.039

Gutenberg, B., Richter, C.F., 1955. Magnitude and Energy of Earthquakes. Nature 176, 795–795. https://doi.org/10.1038/176795a0

Gutman, G., Ignatov, A., 1998. The derivation of the green vegetation fraction from NOAA/AVHRR data for use in numerical weather prediction models. Int. J. Remote Sens. 19, 1533–1543.

Guzzetti, F., Malamud, B.D., Turcotte, D.L., Reichenbach, P., 2002. Power-law correlations of landslide areas in central Italy. Earth Planet. Sci. Lett. 195, 169–183. https://doi.org/10.1016/S0012-821X(01)00589-1

Hantson, S., Pueyo, S., Chuvieco, E., 2015. Global fire size distribution is driven by human impact and climate. Glob. Ecol. Biogeogr. 24, 77–86. https://doi.org/10.1111/geb.12246

Hapke, B., 2012. Theory of reflectance and emittance spectroscopy. Cambridge University Press.

Heasler, P.G., Foley, M.G., Thompson, S.E., 2007. Consequences of Mixed Pixels on Temperature Emissivity Separation. PNNL-16330. Richland, WA (United States). https://doi.org/10.2172/1133253

Holden, C.E., Woodcock, C.E., 2016. An analysis of Landsat 7 and Landsat 8 underflight data and the implications for time series investigations. Remote Sens. Environ. 185, 16–36. https://doi.org/10.1016/J.RSE.2016.02.052

Hsu, S.A., Meindl, E.A., Gilhousen, D.B., Hsu, S.A., Meindl, E.A., Gilhousen, D.B., 1994. Determining the Power-Law Wind-Profile Exponent under Near-Neutral Stability Conditions at Sea. J. Appl. Meteorol. 33, 757–765. https://doi.org/10.1175/1520-0450(1994)033<0757:DTPLWP>2.0.CO;2

Huete, A.., 1988. A soil-adjusted vegetation index (SAVI). Remote Sens. Environ. 25, 295–309. https://doi.org/10.1016/0034-4257(88)90106-X

Huete, A., Didan, K., Miura, T., Rodriguez, E.P., Gao, X., Ferreira, L.G., 2002. Overview of the radiometric and biophysical performance of the MODIS vegetation indices. Remote Sens. Environ. 83, 195–213. https://doi.org/http://dx.doi.org/10.1016/S0034-4257(02)00096-2

Hulley, G., Veraverbeke, S., Hook, S., 2014. Thermal-based techniques for land cover change detection using a new dynamic MODIS multispectral emissivity product (MOD21). Remote Sens. Environ. 140, 755–765. https://doi.org/10.1016/J.RSE.2013.10.014

Hulley, G.C., Hook, S.J., Abbott, E., Malakar, N., Islam, T., Abrams, M., 2015. The ASTER Global Emissivity Dataset (ASTER GED): Mapping Earth's emissivity at 100 meter spatial scale. Geophys. Res. Lett. 42, 7966–7976. https://doi.org/10.1002/2015GL065564

Idso, S.B., Jackson, R.D., Reginato, R.J., 1977. Remote-Sensing of Crop Yields. Science (80-.). 196, 19 LP-25.

Idso, S.B., Jackson, R.D., Reginato, R.J., Kimball, B.A., Nakayama, F.S., 1975. The dependence of bare soil albedo on soil water content. J. Appl. Meteorol. 14, 109–113.

Jackson, R.D., Idso, S.B., Reginato, R.J., Pinter Jr, P.J., 1981. Canopy temperature as a crop water stress indicator. Water Resour. Res. 17, 1133–1138.

Jackson, R.D., Reginato, R.J., Idso, S.B., 1977. Wheat canopy temperature: a practical tool for evaluating water requirements. Water Resour. Res. 13, 651–656.

Jiang, L., Islam, S., 1999. A methodology for estimation of surface evapotranspiration over large areas using remote sensing observations. Geophys. Res. Lett. 26, 2773–2776.

Johnson, P.E., Smith, M.O., Taylor-George, S., Adams, J.B., 1983. A semiempirical method for analysis of the reflectance spectra of binary mineral mixtures. J. Geophys. Res. Solid Earth 88, 3557–3561.

Kalma, J.D., McVicar, T.R., McCabe, M.F., 2008. Estimating land surface evaporation: A review of methods using remotely sensed surface temperature data. Surv. Geophys. 29, 421–469.

Kauth, R.J., Thomas, G.S., 1976. The Tasseled Cap - a graphic description of the spectral-temporal development of agricultural crops as seen by Landsat, in: Proceedings of the Symposium on Machine Processing of Remotely Sensed Data. Purdue University, West Lafayette, Indiana, p. 4B41-4B51.

Khush, G., 2003. Productivity Improvements in Rice. Nutr. Rev. 61, S114–S116. https://doi.org/10.1301/nr.2003.jun.S114-S116

Knight, E., Sensing, G.K.-R., 2014, undefined, n.d. Landsat-8 operational land imager design, characterization and performance. mdpi.com.

Kontgis, C., Schneider, A., Ozdogan, M., 2015. Mapping rice paddy extent and intensification in the Vietnamese Mekong River Delta with dense time stacks of Landsat data. Remote Sens. Environ. 169, 255–269. https://doi.org/10.1016/J.RSE.2015.08.004

Kou, L., Labrie, D., Chylek, P., 1993. Refractive indices of water and ice in the 065- to 25-μm spectral range. Appl. Opt. 32, 3531. https://doi.org/10.1364/AO.32.003531

Kumar, S.S., Roy, D.P., Boschetti, L., Kremens, R., 2011. Exploiting the power law distribution properties of satellite fire radiative power retrievals: A method to estimate fire radiative energy and biomass burned from sparse satellite observations. J. Geophys. Res. 116, D19303. https://doi.org/10.1029/2011JD015676

Kustas, W.P., Norman, J.M., Anderson, M.C., French, A.N., 2003. Estimating subpixel surface temperatures and energy fluxes from the vegetation index-radiometric temperature relationship. Remote Sens. Environ. 85, 429–440.

LaCapra, V.C., Melack, J.M., Gastil, M., Valeriano, D., 1996. Remote sensing of foliar chemistry of inundated rice with imaging spectrometry. Remote Sens. Environ. 55, 50–58.

https://doi.org/10.1016/0034-4257(95)00185-9

Lee, C.M., Cable, M.L., Hook, S.J., Green, R.O., Ustin, S.L., Mandl, D.J., Middleton, E.M., 2015. An introduction to the NASA Hyperspectral InfraRed Imager (HyspIRI) mission and preparatory activities. Remote Sens. Environ. 167, 6–19. https://doi.org/10.1016/J.RSE.2015.06.012

Lekner, J., Dorf, M., 1988. Why some things are darker when wet. Appl. Opt. 27, 1278–1280.

Li, G., Jing, Y., Wu, Y., Zhang, F., Li, G., Jing, Y., Wu, Y., Zhang, F., 2018. Improvement of Two Evapotranspiration Estimation Models Using a Linear Spectral Mixture Model over a Small Agricultural Watershed. Water 10, 474. https://doi.org/10.3390/w10040474

Li, J., Roy, D.P., Li, J., Roy, D.P., 2017. A Global Analysis of Sentinel-2A, Sentinel-2B and Landsat-8 Data Revisit Intervals and Implications for Terrestrial Monitoring. Remote Sens. 9, 902. https://doi.org/10.3390/rs9090902

Li, W., 2002. Zipf's law everywhere. Glottometrics 5, 14–21.

Liang, S., 2001. Narrowband to broadband conversions of land surface albedo: I. Algorithms. Remote Sens. Environ. 76, 213–238.

Limpert, E., Stahel, W.A., Abbt, M., 2001. Log-normal Distributions across the Sciences: Keys and CluesOn the charms of statistics, and how mechanical models resembling gambling machines offer a link to a handy way to characterize log-normal distributions, which can provide deeper insight into variability and probability—normal or log-normal: That is the question. Bioscience 51, 341–352. https://doi.org/10.1641/0006-3568(2001)051[0341:lndats]2.0.co;2

Linquist, B., 2018. Planting Progress for Rice, 2018 [WWW Document]. UC Rice Blog. URL http://ucanr.edu/blogs/blogcore/postdetail.cfm?postnum=27403

Linquist, B., Snyder, R., Anderson, F., Espino, L., Inglese, G., Marras, S., Moratiel, R., Mutters, R., Nicolosi, P., Rejmanek, H., Russo, A., Shapland, T., Song, Z., Swelam, A., Tindula, G., Hill, J., 2015. Water balances and evapotranspiration in water- and dry-seeded rice systems. Irrig. Sci. 33, 375–385. https://doi.org/10.1007/s00271-015-0474-4

Liu, M., Liu, X., Ding, W., Wu, L., 2011. Monitoring stress levels on rice with heavy metal pollution from hyperspectral reflectance data using wavelet-fractal analysis. Int. J. Appl. Earth Obs. Geoinf. 13, 246–255. https://doi.org/10.1016/J.JAG.2010.12.006

Liu, Z., Huang, J., Tao, R., 2008. Characterizing and Estimating Fungal Disease Severity of Rice Brown Spot with Hyperspectral Reflectance Data. Rice Sci. 15, 232–242. https://doi.org/10.1016/S1672-6308(08)60047-5

Lobell, D.B., Asner, G.P., 2002. Moisture Effects on Soil Reflectance. Soil Sci. Soc. Am. J. 66, 722. https://doi.org/10.2136/sssaj2002.7220

Lobell, D.B.D., Asner, G.G.P., 2004. Cropland distributions from temporal unmixing of MODIS data. Remote Sens. Environ. 93, 412–422.

Long, D., Singh, V.P., 2013. Assessing the impact of end-member selection on the accuracy of

satellite-based spatial variability models for actual evapotranspiration estimation. Water Resour. Res. 49, 2601–2618.

Long, D., Singh, V.P., Li, Z.-L., 2011. How sensitive is SEBAL to changes in input variables, domain size and satellite sensor? J. Geophys. Res. Atmos. 116. https://doi.org/10.1029/2011JD016542

Lotka, A., 1941. The law of urban concentration. Science (80-.). 94.

Lucke, R.L., Corson, M., McGlothlin, N.R., Butcher, S.D., Wood, D.L., Korwan, D.R., Li, R.R., Snyder, W.A., Davis, C.O., Chen, D.T., 2011. Hyperspectral Imager for the Coastal Ocean: instrument description and first images. Appl. Opt. 50, 1501. https://doi.org/10.1364/AO.50.001501

Luoto, M., Rekolainen, S., Aakkula, J., Pykälä, J., 2003. Loss of Plant Species Richness and Habitat Connectivity in Grasslands Associated with Agricultural Change in Finland. AMBIO A J. Hum. Environ. 32, 447–452. https://doi.org/10.1579/0044-7447-32.7.447

Luther, J.E., Franklin, S.E., Hudak, J., Meades, J.P., 1997. Forecasting the susceptibility and vulnerability of balsam fir stands to insect defoliation with Landsat Thematic Mapper data. Remote Sens. Environ. 59, 77–91. https://doi.org/10.1016/S0034-4257(96)00108-3

MacDonald, R., Bauer, M., Allen, R., Clifton, J., Erickson, J., Landgrebe, D., 1972. Results of the 1971 corn blight watch experiment, LARS Technical Reports.

Malamud, B.D., Millington, J.D.A., Perry, G.L.W., 2005. Characterizing wildfire regimes in the United States. Proc. Natl. Acad. Sci. U. S. A. 102, 4694–9. https://doi.org/10.1073/pnas.0500880102

Markham, B.L., Helder, D.L., 2012. Forty-year calibrated record of earth-reflected radiance from Landsat: A review. Remote Sens. Environ. 122, 30–40.

Marshall, M., Thenkabail, P., Biggs, T., Post, K., 2016. Hyperspectral narrowband and multispectral broadband indices for remote sensing of crop evapotranspiration and its components (transpiration and soil evaporation). Agric. For. Meteorol. 218–219, 122–134. https://doi.org/https://doi.org/10.1016/j.agrformet.2015.12.025

Matthias, A.D., Fimbres, A., Sano, E.E., Post, D.F., Accioly, L., Batchily, A.K., Ferreira, L.G., 2000. Surface roughness effects on soil albedo. Soil Sci. Soc. Am. J. 64, 1035–1041.

McCabe, M.F., Balick, L.K., Theiler, J., Gillespie, A.R., Mushkin, A., 2008. Linear mixing in thermal infrared temperature retrieval. Int. J. Remote Sens. 29, 5047–5061. https://doi.org/10.1080/01431160802036474

McCabe, M.F., Wood, E.F., 2006. Scale influences on the remote estimation of evapotranspiration using multiple satellite sensors. Remote Sens. Environ. 105, 271–285. https://doi.org/10.1016/J.RSE.2006.07.006

McIntyre, N.E., Wright, C.K., Swain, S., Hayhoe, K., Liu, G., Schwartz, F.W., Henebry, G.M., 2014. Climate forcing of wetland landscape connectivity in the Great Plains. Front. Ecol. Environ. 12, 59–64. https://doi.org/10.1890/120369

Menenti, M., Bastiaanssen, W., Van Eick, D., El Karim, M.A.A., 1989. Linear relationships between surface reflectance and temperature and their application to map actual evaporation of groundwater. Adv. Sp. Res. 9, 165–176.

Menke, W., Menke, J., 2016. Environmental data analysis with MatLab.

Merlin, O., Chirouze, J., Olioso, A., Jarlan, L., Chehbouni, G., Boulet, G., 2014. An image-based four-source surface energy balance model to estimate crop evapotranspiration from solar reflectance/thermal emission data (SEB-4S). Agric. For. Meteorol. 184, 188–203.

Michel, S., Gamet, P., Lefevre-Fonollosa, M.-J., 2011. HYPXIM — A hyperspectral satellite defined for science, security and defence users, in: 2011 3rd Workshop on Hyperspectral Image and Signal Processing: Evolution in Remote Sensing (WHISPERS). IEEE, pp. 1–4. https://doi.org/10.1109/WHISPERS.2011.6080864

Miralles, D.G., De Jeu, R.A.M., Gash, J.H.C., Holmes, T.R.H., Dolman, A.J., 2011. Magnitude and variability of land evaporation and its components at the global scale. Hydrol. Earth Syst. Sci. 967–981.

Miralles, D.G., van den Berg, M.J., Gash, J.H., Parinussa, R.M., de Jeu, R.A.M., Beck, H.E., Holmes, T.R.H., Jiménez, C., Verhoest, N.E.C., Dorigo, W.A., Teuling, A.J., Johannes Dolman, A., 2013. El Niño–La Niña cycle and recent trends in continental evaporation. Nat. Clim. Chang. 4, 122.

Miralles, D.G., Van Den Berg, M.J., Teuling, A.J., De Jeu, R.A.M., 2012. Soil moisture-temperature coupling: A multiscale observational analysis. Geophys. Res. Lett. 39. https://doi.org/10.1029/2012GL053703

Mishra, N., Helder, D., Barsi, J., Markham, B., 2016. Continuous calibration improvement in solar reflective bands: Landsat 5 through Landsat 8. Remote Sens. Environ. 185, 7–15. https://doi.org/10.1016/J.RSE.2016.07.032

Montanaro, M., Gerace, A., Lunsford, A., Reuter, D., 2014. Stray Light Artifacts in Imagery from the Landsat 8 Thermal Infrared Sensor. Remote Sens. . https://doi.org/10.3390/rs61110435

Moran, M.S., Clarke, T.R., Inoue, Y., Vidal, A., 1994. Estimating crop water deficit using the relation between surface-air temperature and spectral vegetation index. Remote Sens. Environ. 49, 246–263.

Morfitt, R., Barsi, J., Levy, R., Markham, B., Micijevic, E., Ong, L., Scaramuzza, P., Vanderwerff, K., Morfitt, R., Barsi, J., Levy, R., Markham, B., Micijevic, E., Ong, L., Scaramuzza, P., Vanderwerff, K., 2015. Landsat-8 Operational Land Imager (OLI) Radiometric Performance On-Orbit. Remote Sens. 7, 2208–2237. https://doi.org/10.3390/rs70202208

Muthayya, S., Sugimoto, J.D., Montgomery, S., Maberly, G.F., 2014. An overview of global rice production, supply, trade, and consumption. Ann. N. Y. Acad. Sci. 1324, 7–14. https://doi.org/10.1111/nyas.12540

NASS, 2017. 2017 Acreage Report.

Nelson, A., Setiyono, T., Rala, A.B., Quicho, E.D., Raviz, J. V., Abonete, P.J., Maunahan, A.A., Garcia, C.A., Bhatti, H.Z.M., Villano, L.S., Thongbai, P., Holecz, F., Barbieri, M., Collivignarelli, F., Gatti, L., Quilang, E.J.P., Mabalay, M.R.O., Mabalot, P.E., Barroga, M.I., Bacong, A.P., Detoito, N.T., Berja, G.B., Varquez, F., Wahyunto, Kuntjoro, D., Murdiyati, S.R., Pazhanivelan, S., Kannan, P., Mary, P.C.N., Subramanian, E., Rakwatin, P., Intrman, A., Setapayak, T., Lertna, S., Minh, V.Q., Tuan, V.Q., Duong, T.H., Quyen, N.H., Van Kham, D., Hin, S., Veasna, T., Yadav, M., Chin, C., Ninh, N.H., Nelson, A., Setiyono, T., Rala, A.B., Quicho, E.D., Raviz, J. V., Abonete, P.J., Maunahan, A.A., Garcia, C.A., Bhatti, H.Z.M., Villano, L.S., Thongbai, P., Holecz, F., Barbieri, M., Collivignarelli, F., Gatti, L., Quilang, E.J.P., Mabalay, M.R.O., Mabalot, P.E., Barroga, M.I., Bacong, A.P., Detoito, N.T., Berja, G.B., Varquez, F., Wahyunto, Kuntjoro, D., Murdiyati, S.R., Pazhanivelan, S., Kannan, P., Mary, P.C.N., Subramanian, E., Rakwatin, P., Intrman, A., Setapayak, T., Lertna, S., Minh, V.Q., Tuan, V.Q., Duong, T.H., Quyen, N.H., Van Kham, D., Hin, S., Veasna, T., Yadav, M., Chin, C., Ninh, N.H., 2014. Towards an Operational SAR-Based Rice Monitoring System in Asia: Examples from 13 Demonstration Sites across Asia in the RIICE Project. Remote Sens. 6, 10773–10812. https://doi.org/10.3390/rs61110773

Newman, M., 2010. Networks: An Introduction. Oxford University Press, Oxford.

Nguyen, D.B., Gruber, A., Wagner, W., 2016. Mapping rice extent and cropping scheme in the Mekong Delta using Sentinel-1A data. Remote Sens. Lett. 7, 1209–1218. https://doi.org/10.1080/2150704X.2016.1225172

Nieto, H., Kustas, W.P., Torres-Rúa, A., Alfieri, J.G., Gao, F., Anderson, M.C., White, W.A., Song, L., Alsina, M. del M., Prueger, J.H., McKee, M., Elarab, M., McKee, L.G., 2018. Evaluation of TSEB turbulent fluxes using different methods for the retrieval of soil and canopy component temperatures from UAV thermal and multispectral imagery. Irrig. Sci. 1–18. https://doi.org/10.1007/s00271-018-0585-9

Olson, D.M., Dinerstein, E., Wikramanayake, E.D., Burgess, N.D., Powell, G.V.N., Underwood, E.C., D'amico, J.A., Itoua, I., Strand, H.E., Morrison, J.C., Loucks, C.J., Allnutt, T.F., Ricketts, T.H., Kura, Y., Lamoreux, J.F., Wettengel, W.W., Hedao, P., Kassem, K.R., 2001. Terrestrial Ecoregions of the World: A New Map of Life on EarthA new global map of terrestrial ecoregions provides an innovative tool for conserving biodiversity. Bioscience 51, 933–938. https://doi.org/10.1641/0006-3568(2001)051[0933:teotwa]2.0.co;2

Palacios-Orueta, A., Ustin, S.L., 1998. Remote Sensing of Soil Properties in the Santa Monica Mountains I. Spectral Analysis. Remote Sens. Environ. 65, 170–183. https://doi.org/10.1016/S0034-4257(98)00024-8

Palacios-Orueta, A., Ustin, S.L., 1996. Multivariate statistical classification of soil spectra. Remote Sens. Environ. 57, 108–118. https://doi.org/10.1016/0034-4257(95)00250-2

Pearson, K., 1901. LIII. On lines and planes of closest fit to systems of points in space. London, Edinburgh, Dublin Philos. Mag. J. Sci. 2, 559–572.

Petropoulos, G., Carlson, T., Wooster, M., Islam, S., 2009. A review of Ts/VI remote sensing based methods for the retrieval of land surface energy fluxes and soil surface moisture. Prog. Phys. Geogr. 33, 224–250.

Philpot, W., 2010. Spectral reflectance of wetted soils, in: Proceedings of ASD and IEEE GRS 2. pp. 1–12.

Piwowar, J.M., Peddle, D.R., LeDrew, E.F., 1998. Temporal mixture analysis of arctic sea ice imagery: a new approach for monitoring environmental change. Remote Sens. Environ. 63, 195–207.

Preisendorfer, R.W., 1988. Principal component analysis in meteorology and oceanography. Elsevier, Amsterdam.

Price, J., 1990. On the information content of soil reflectance spectra. Remote Sens. Environ. 33, 113–121. https://doi.org/10.1016/0034-4257(90)90037-M

Price, J.C., 1997. Spectral band selection for visible-near infrared remote sensing: spectral-spatial resolution tradeoffs. IEEE Trans. Geosci. Remote Sens. 35, 1277–1285. https://doi.org/10.1109/36.628794

Price, J.C., 1994. Band selection procedure for multispectral scanners. Appl. Opt. 33, 3281. https://doi.org/10.1364/AO.33.003281

Price, J.C., 1990. Using spatial context in satellite data to infer regional scale evapotranspiration. IEEE Trans. Geosci. Remote Sens. 28, 940–948.

Price, J.C., 1975. Information content of Iris spectra. J. Geophys. Res. 80, 1930–1936. https://doi.org/10.1029/JC080i015p01930

Ramírez-Cuesta, J.M., Allen, R.G., Zarco-Tejada, P.J., Kilic, A., Santos, C., Lorite, I.J., 2019. Impact of the spatial resolution on the energy balance components on an open-canopy olive orchard. Int. J. Appl. Earth Obs. Geoinf. 74, 88–102. https://doi.org/10.1016/J.JAG.2018.09.001

Ricketts, T.H., Williams, N.M., Mayfield, M.M., 2007. Connectivity and ecosystem services: crop pollination in agricultural landscapes.

Roberts, D.A., Smith, M.O., Adams, J.B., 1993. Green vegetation, nonphotosynthetic vegetation, and soils in AVIRIS data. Remote Sens. Environ. 44, 255–269. https://doi.org/10.1016/0034-4257(93)90020-X

Roberts, Y.L., Pilewskie, P., Kindel, B.C., 2011. Evaluating the observed variability in hyperspectral Earth-reflected solar radiance. J. Geophys. Res. Atmos. 116, n/a-n/a. https://doi.org/10.1029/2011JD016448

Roerink, G.J., Su, Z., Menenti, M., 2000. S-SEBI: A simple remote sensing algorithm to estimate the surface energy balance. Phys. Chem. Earth, Part B Hydrol. Ocean. Atmos. 25, 147–157.

Rouse, J., Haas, R.H., Schell, J.A., Deering, D.W., 1974. Monitoring vegetation systems in the Great Plains with ERTS, in: Freden, S.C., Mercanti, E.P., Becker, M.A. (Eds.), Third Earth Resources Technology Satellite-1 Symposium- Volume I: Technical Presentations. NASA SP-351. NASA, Washington, D.C., p. 309.

Roy, D.P., Kovalskyy, V., Zhang, H.K., Vermote, E.F., Yan, L., Kumar, S.S., Egorov, A., 2016. Characterization of Landsat-7 to Landsat-8 reflective wavelength and normalized difference

vegetation index continuity. Remote Sens. Environ. 185, 57–70. https://doi.org/10.1016/J.RSE.2015.12.024

Rubio, E., Caselles, V., Environment, C.B.-R.S. of, 1997, undefined, n.d. Emissivity measurements of several soils and vegetation types in the 8–14, μm Wave band: Analysis of two field methods. Elsevier.

Sadeghi, M., Babaeian, E., Tuller, M., Jones, S.B., 2017. The optical trapezoid model: A novel approach to remote sensing of soil moisture applied to Sentinel-2 and Landsat-8 observations. Remote Sens. Environ. 198, 52–68. https://doi.org/10.1016/J.RSE.2017.05.041

Scanlon, T.M., Caylor, K.K., Levin, S.A., Rodriguez-Iturbe, I., 2007. Positive feedbacks promote power-law clustering of Kalahari vegetation. Nature. https://doi.org/10.1038/nature06060

Schott, J., Gerace, A., Woodcock, C., Wang, S., Zhu, Z., Wynne, R., Blinn, C., 2016. The impact of improved signal-to-noise ratios on algorithm performance: Case studies for Landsat class instruments. Remote Sens. Environ. 185, 37–45.

Seguro, J.V., Lambert, T.W., 2000. Modern estimation of the parameters of the Weibull wind speed distribution for wind energy analysis. J. Wind Eng. Ind. Aerodyn. 85, 75–84. https://doi.org/10.1016/S0167-6105(99)00122-1

Shafroth, P.B., Brown, C.A., Merritt, D.M., 2010. Saltcedar and Russian olive control demonstration act science assessment, Scientific Investigations Report 2009-5247. Reston, VA.

Sharma, V., Kilic, A., Irmak, S., 2016. Impact of scale/resolution on evapotranspiration from Landsat and MODIS images. Water Resour. Res. 52, 1800–1819. https://doi.org/10.1002/2015WR017772

Shaw, D.R., 2005. Translation of remote sensing data into weed management decisions. Weed Sci. 53, 264–273. https://doi.org/10.1614/WS-04-072R1

Shi, Y., 2011. Thermal infrared inverse model for component temperatures of mixed pixels. Int. J. Remote Sens. 32, 2297–2309. https://doi.org/10.1080/01431161003698252

Singer, R.B., 1981. Near-infrared spectral reflectance of mineral mixtures: Systematic combinations of pyroxenes, olivine, and iron oxides. J. Geophys. Res. Solid Earth 86, 7967–7982.

Singer, R.B., McCord, T.B., 1979. Mars-large scale mixing of bright and dark surface materials and implications for analysis of spectral reflectance, in: Lunar and Planetary Science Conference Proceedings. pp. 1835–1848.

Small, C., 2018. Multisource imaging of urban growth and infrastructure using Landsat, Sentinel and SRTM, in: NASA Landsat-Sentinel Science Team Meeting. Rockville, MD.

Small, C., 2012. Spatiotemporal dimensionality and Time-Space characterization of multitemporal imagery. Remote Sens. Environ. 124, 793–809.

Small, C., 2006. Comparative analysis of urban reflectance and surface temperature. Remote Sens. Environ. 104, 168–189.

Small, C., 2004. The Landsat ETM+ spectral mixing space. Remote Sens. Environ. 93, 1–17. https://doi.org/http://dx.doi.org/10.1016/j.rse.2004.06.007

Small, C., 2001. Estimation of urban vegetation abundance by spectral mixture analysis. Int. J. Remote Sens. 22, 1305–1334.

Small, C., 2001. Multiresolution analysis of urban reflectance, in: IEEE/ISPRS Joint Workshop on Remote Sensing and Data Fusion over Urban Areas (Cat. No.01EX482). IEEE, Rome, Italy, pp. 15–19. https://doi.org/10.1109/DFUA.2001.985717

Small, C., Elvidge, C.D., Balk, D., Montgomery, M., 2011. Spatial scaling of stable night lights. Remote Sens. Environ. 115, 269–280. https://doi.org/10.1016/J.RSE.2010.08.021

Small, C., Milesi, C., 2013. Multi-scale standardized spectral mixture models. Remote Sens. Environ. 136, 442–454.

Small, C., Sousa, D., 2016. Humans on Earth: Global extents of anthropogenic land cover from remote sensing. Anthropocene 14. https://doi.org/10.1016/j.ancene.2016.04.003

Small, C., Sousa, D., 2015. Spatial Scaling of Land Cover Networks.

Small, C., Steckler, M., Seeber, L., Akhter, S.H., Goodbred, S., Mia, B., Imam, B., 2009. Spectroscopy of sediments in the Ganges–Brahmaputra delta: Spectral effects of moisture, grain size and lithology. Remote Sens. Environ. 113, 342–361.

Smith, M.O., Johnson, P.E., Adams, J.B., 1985. Quantitative determination of mineral types and abundances from reflectance spectra using principal components analysis. J. Geophys. Res. Solid Earth 90, C797–C804.

Smith, M.O., Ustin, S.L., Adams, J.B., Gillespie, A.R., 1990. Vegetation in deserts. I. A regional measure of abundance from multispectral images. Remote Sens. Environ. 31, 1–26.

Smits, K.M., Cihan, A., Sakaki, T., Illangasekare, T.H., 2011. Evaporation from soils under thermal boundary conditions: Experimental and modeling investigation to compare equilibrium- and nonequilibrium-based approaches. Water Resour. Res. 47. https://doi.org/10.1029/2010WR009533

Smits, K.M., Ngo, V. V., Cihan, A., Sakaki, T., Illangasekare, T.H., 2012. An evaluation of models of bare soil evaporation formulated with different land surface boundary conditions and assumptions. Water Resour. Res. 48. https://doi.org/10.1029/2012WR012113

Smits, K.M., Sakaki, T., Howington, S.E., Peters, J.F., Illangasekare, T.H., 2013. Temperature Dependence of Thermal Properties of Sands across a Wide Range of Temperatures (30–70°C). Vadose Zo. J. 12, 0. https://doi.org/10.2136/vzj2012.0033

Smits, K.M., Sakaki, T., Limsuwat, A., Illangasekare, T.H., 2010. Thermal Conductivity of Sands under Varying Moisture and Porosity in Drainage–Wetting Cycles. Vadose Zo. J. 9, 172. https://doi.org/10.2136/vzj2009.0095

Sornette, D., 2006. Critical phenomena in natural sciences: chaos, fractals, selforganization and

disorder: concepts and tools. Springer Science & Business Media.

Sousa, D., Small, C., 2019. Mapping and Monitoring Rice Agriculture with Multisensor Temporal Mixture Models. Remote Sens. 11, 181. https://doi.org/https://doi.org/10.3390/rs11020181

Sousa, D., Small, C., 2018a. Multisensor analysis of spectral dimensionality and soil diversity in the great central valley of California. Sensors (Switzerland) 18. https://doi.org/10.3390/s18020583

Sousa, D., Small, C., 2018b. Spectral Mixture Analysis as a Unified Framework for the Remote Sensing of Evapotranspiration. Remote Sens. 10, 1961. https://doi.org/10.3390/rs10121961

Sousa, D., Small, C., 2017a. Global cross-calibration of Landsat spectral mixture models. Remote Sens. Environ. 192. https://doi.org/10.1016/j.rse.2017.01.033

Sousa, D., Small, C., 2017b. Coupled Spatiotemporal Characterization of Monsoon Cloud Cover and Vegetation Phenology. arXiv:1706.09216 [physics.geo-ph].

Sousa, D., Small, C., 2016. Spatial structure and scaling of agricultural networks. Remote Sens. Environ. 184. https://doi.org/10.1016/j.rse.2016.07.038

Steinwender, J., 2002. Graph-theoretic Issues in Remote Sensing and Landscape Ecology, in: Environmental Communication in the Information Society - Proceedings of the 16th Conference. IGU/ISEP, Wien, pp. 546–552.

Stoner, E.R., Baumgardner, M.F., 1981. Characteristic Variations in Reflectance of Surface Soils1. Soil Sci. Soc. Am. J. 45, 1161. https://doi.org/10.2136/sssaj1981.03615995004500060031x

Storey, J., Choate, M., Lee, K., Storey, J., Choate, M., Lee, K., 2014. Landsat 8 Operational Land Imager On-Orbit Geometric Calibration and Performance. Remote Sens. 6, 11127–11152. https://doi.org/10.3390/rs61111127

Stuffler, T., Kaufmann, C., Hofer, S., Förster, K.P., Schreier, G., Mueller, A., Eckardt, A., Bach, H., Penné, B., Benz, U., Haydn, R., 2007. The EnMAP hyperspectral imager—An advanced optical payload for future applications in Earth observation programmes. Acta Astronaut. 61, 115–120. https://doi.org/10.1016/J.ACTAASTRO.2007.01.033

Sun, H., 2016. A Two-Source Model for Estimating Evaporative Fraction (TMEF) Coupling Priestley-Taylor Formula and Two-Stage Trapezoid. Remote Sens. . https://doi.org/10.3390/rs8030248

Talsma, C.J., Good, S.P., Jimenez, C., Martens, B., Fisher, J.B., Miralles, D.G., McCabe, M.F., Purdy, A.J., 2018a. Partitioning of evapotranspiration in remote sensing-based models. Agric. For. Meteorol. 260–261, 131–143. https://doi.org/10.1016/J.AGRFORMET.2018.05.010

Talsma, C.J., Good, S.P., Miralles, D.G., Fisher, J.B., Martens, B., Jimenez, C., Purdy, A.J., 2018b. Sensitivity of Evapotranspiration Components in Remote Sensing-Based Models. Remote Sens. 10, 1601. https://doi.org/10.3390/rs10101601

Thompson, D.R., Boardman, J.W., Eastwood, M.L., Green, R.O., 2017. A large airborne survey of Earth's visible-infrared spectral dimensionality. Opt. Express 25, 9186. https://doi.org/10.1364/OE.25.009186

Tian, J., Philpot, W.D., 2015a. Relationship between surface soil water content, evaporation rate, and water absorption band depths in SWIR reflectance spectra. Remote Sens. Environ. 169, 280–289. https://doi.org/10.1016/J.RSE.2015.08.007

Tian, J., Philpot, W.D., 2015b. Relationship between surface soil water content, evaporation rate, and water absorption band depths in SWIR reflectance spectra. Remote Sens. Environ. 169, 280–289. https://doi.org/10.1016/j.rse.2015.08.007

Tian, J., Philpot, W.D., 2015c. Relating water absorption features to soil moisture characteristics, in: Pagano, T.S., Silny, J.F. (Eds.), . International Society for Optics and Photonics, p. 96110M. https://doi.org/10.1117/12.2188478

Timmermans, W.J., Kustas, W.P., Anderson, M.C., French, A.N., 2007. An intercomparison of the surface energy balance algorithm for land (SEBAL) and the two-source energy balance (TSEB) modeling schemes. Remote Sens. Environ. 108, 369–384.

Torbick, N., Salas, W.A., Hagen, S., Xiangming Xiao, 2011. Monitoring Rice Agriculture in the Sacramento Valley, USA With Multitemporal PALSAR and MODIS Imagery. IEEE J. Sel. Top. Appl. Earth Obs. Remote Sens. 4, 451–457. https://doi.org/10.1109/JSTARS.2010.2091493

Townshend, J.R.G., Goff, T.E., Tucker, C.J., 1985. Multitemporal dimensionality of images of normalized difference vegetation index at continental scales. IEEE Trans. Geosci. Remote Sens. GE-23, 888–895.

Turcotte, D.L., 1997. Fractals and chaos in geology and geophysics. Cambridge University Press.

Twomey, S.A., Bohren, C.F., Mergenthaler, J.L., 1986. Reflectance and albedo differences between wet and dry surfaces. Appl. Opt. 25, 431–437.

Urban, D., Keitt, T., 2001. Landscape Connectivity: A Graph-Theoretic Perspective. Ecology 82, 1205–1218. https://doi.org/10.1890/0012-9658(2001)082[1205:LCAGTP]2.0.CO;2

USGS, 2018. USGS Global Visualization Viewer (GloVis) [WWW Document]. URL https://glovis.usgs.gov/

USGS, 2016a. Provisional LaSRC Product Guide, Version 3.3, in: Http://Landsat.Usgs. Gov/Documents/Provisional_lasrc_product_guide.Pdf.

USGS, 2016b. Landsat 8 Data Users Handbook, Version 2.0. Sioux Falls, SD.

Vanderborght, J., Fetzer, T., Mosthaf, K., Smits, K.M., Helmig, R., 2017. Heat and water transport in soils and across the soil-atmosphere interface: 1. Theory and different model concepts. Water Resour. Res. 53, 1057–1079. https://doi.org/10.1002/2016WR019982

Vogelmann, J.E., Gallant, A.L., Shi, H., Zhu, Z., 2016. Perspectives on monitoring gradual change across the continuity of Landsat sensors using time-series data. Remote Sens.

Environ. 185, 258–270. https://doi.org/10.1016/J.RSE.2016.02.060

von_Storch, H., Zwiers, F.W., 1999. Statistical Analysis in Climate Research. Cambridge University Press, Cambridge UK.

Wang, J., Xiao, X., Qin, Y., Dong, J., Zhang, G., Kou, W., Jin, C., Zhou, Y., Zhang, Y., 2015. Mapping paddy rice planting area in wheat-rice double-cropped areas through integration of Landsat-8 OLI, MODIS, and PALSAR images. https://doi.org/10.1038/srep10088

Wang, L., Good, S.P., Caylor, K.K., 2014. Global synthesis of vegetation control on evapotranspiration partitioning. Geophys. Res. Lett. 41, 6753–6757. https://doi.org/10.1002/2014GL061439

Wei, Q., Bioucas-Dias, J., Dobigeon, N., Tourneret, J.-Y., 2015. Hyperspectral and Multispectral Image Fusion Based on a Sparse Representation. IEEE Trans. Geosci. Remote Sens. 53, 3658–3668. https://doi.org/10.1109/TGRS.2014.2381272

Wilcox, C., Frazier, B., Ball, S., 1994. Relationship between soil organic carbon and Landsat TM data in Eastern Washington. Photogramm. Eng. Remote Sens. 60, 777–781.

Wong, A., Jin, Y., He, R., Hulley, G., Fisher, J., Lee, C.M., Rivera, G., Hook, S.J., Medellin-Azuara, J., Kent, E.R., Paw U, K.T., Gao, F., Lund, J.R., 2017. Mapping Evapotranspiration in the Sacramento San Joaquin Delta using simulated ECOSTRESS Thermal Data: Validation and Inter-comparison. Am. Geophys. Union, Fall Meet. 2017, Abstr. #H11M-04.

Wood, R., Field, P.R., 2011. The Distribution of Cloud Horizontal Sizes. J. Clim. 24, 4800–4816. https://doi.org/10.1175/2011JCLI4056.1

Woodcock, C., Strahler, A., 1987. The factor of scale in remote sensing. Remote Sens. Environ.

Wulder, M. a., Masek, J.G., Cohen, W.B., Loveland, T.R., Woodcock, C.E., 2012. Opening the archive: How free data has enabled the science and monitoring promise of Landsat. Remote Sens. Environ. 122, 2–10. https://doi.org/10.1016/j.rse.2012.01.010

Wulder, M.A., White, J.C., Woodcock, C.E., Belward, A.S., Cohen, W.B., Fosnight, E.A., Shaw, J., Masek, J.G., Roy, D.P., 2016. The global Landsat archive: Status, consolidation, and direction. Remote Sens. Environ. 185, 271–283. https://doi.org/10.1016/J.RSE.2015.11.032

Wulf, H., Mulder, T., Schaepman, M., Keller, A., Jörg, P., 2014. Remote sensing of soils, academia.edu. Zurich, Switzerland.

Yang, C.-M., Cheng, C.-H., Chen, R.-K., 2007. Changes in Spectral Characteristics of Rice Canopy Infested with Brown Planthopper and Leaffolder. Crop Sci. 47, 329. https://doi.org/10.2135/cropsci2006.05.0335

Yang, J., Wang, Y., 2011. Estimating evapotranspiration fraction by modeling two-dimensional space of NDVI/albedo and day–night land surface temperature difference: A comparative study. Adv. Water Resour. 34, 512–518. https://doi.org/https://doi.org/10.1016/j.advwatres.2011.01.006

Zhang, H., Voss, K.J., 2006. Bidirectional reflectance study on dry, wet, and submerged particulate layers: effects of pore liquid refractive index and translucent particle

concentrations. Appl. Opt. 45, 8753. https://doi.org/10.1364/AO.45.008753

Zhang, Y., Peña-Arancibia, J.L., McVicar, T.R., Chiew, F.H.S., Vaze, J., Liu, C., Lu, X., Zheng, H., Wang, Y., Liu, Y.Y., Miralles, D.G., Pan, M., 2016. Multi-decadal trends in global terrestrial evapotranspiration and its components. Sci. Rep. 6, 19124.

Zhou, Y., Feng, L., Hou, C., Kung, S.-Y., 2017. Hyperspectral and Multispectral Image Fusion Based on Local Low Rank and Coupled Spectral Unmixing. IEEE Trans. Geosci. Remote Sens. 55, 5997–6009. https://doi.org/10.1109/TGRS.2017.2718728

Zipf, G., 1942. The unity of nature, least-action, and natural social science. Sociometry 48–62.